Precious metal, Lu-Hf, and Re-Os geochemistry of the metasomatized lithospheric mantle: implications for subcrustal precious metal mobilization and MARID petrogenesis

by

Jason C Hinde

A thesis submitted in partial fulfillment of the requirements for the degree of

Master of Science

Department of Earth and Atmospheric Sciences
University of Alberta

Abstract

The connection between metasomatism - the change in chemical composition of a rock via interaction with a fluid or melt - and the formation of metalliferous ore deposits in the Earth's crust is well established. Similarly, it is now accepted that the Earth's lithospheric mantle has experienced significant metasomatism following large-scale melt depletion events. Despite the recognition of the importance of this process in the transfer of metals, the ability of mantle metasomatism to mobilize precious metals (the PGE and other HSE) and the extent to which they are concentrated in mantle metasomes is poorly constrained. A better understanding of the distribution and abundance of precious metals in areas of the mantle that have experienced metasomatism as well as the agents of this alteration is required to more critically evaluate models that link metal lode in crustal ore deposits to materials derived from the SCLM. In addition, unravelling the petrogenesis of exotic metasomes (MARID xenoliths) interpreted as crystallization products of mantle-derived melts provides a clearer picture of their original precious metal characteristics and new insights into enriched source regions within the lithospheric mantle.

Here we present new major, trace, and precious metal element geochemistry at both the mineral (silicate, oxide, and BMS phases; via EPMA and LA-ICP-MS) and whole rock (via XRF and ID-ICP-MS) scales from a series of modally metasomatized mantle xenoliths from the Kaapvaal craton in Southern Africa and the Lherz Massif in the French Pyrenees in order to better characterize the effects of metasomatism on precious metal distribution in the mantle. We also provide the first published set of whole rock Re-Os isotope data (via ID-ICP-MS and N-TIMS)

for a series of MARID xenoliths, which combined with *in situ* zircon U-Pb, Lu-Hf isotope results (via LASS-ICP-MS), provide new constraints on MARID petrogenesis and the source regions of their parental magmas.

Lithophile trace element mass balance calculations show that strongly metasomatized mantle xenoliths display significant deficiencies (up to 80%) in LILE that can be accounted for by the presence of trace phases and pervasive kimberlite metasomatism. Additionally, mass balance modelling indicates that mantle BMS fail to completely account for the whole rock precious metal budget, especially in more intensely metasomatized samples, and a combination of BMS and micro-scale PGE-rich alloys is required to completely characterize precious metal abundance. Several of our peridotite samples show PPGE enrichment (6.25 ppb Pd in the GPP xenolith and 29.0 ppb Pt in the PP xenolith) similar to primary magmas associated with the formation of basalt-hosted PGE deposits. However, conflicting evidence from BMS and whole rock data make determining the source of enrichment challenging.

MARID xenoliths display differing Os isotope signatures (γOs = -12 to 116; n = 4). Two-component mixing between a "pure" MARID composition and depleted lithospheric peridotite show that these contrasting signatures are a result of variable interaction with wall rock peridotite during MARID formation. The highly radiogenic γOs composition of pure MARID samples indicate that their parental magmas are derived from an ancient, subduction-related source region.

In situ zircon U-Pb data from MARID sample AJE-2422 yields $^{238}U/^{206}Pb$ ages ranging from 86.2 to 125.9 Ma (n = 18) with prominent modes at 90.6 Ma, 94.6 Ma, and 125.8 Ma indicating that MARID zircon growth in the Kaapvaal craton lithosphere occurred over a temporally extended period that coincides with major occurrences of Mesozoic intraplate magmatism. Lu-Hf

isotopes from the same sample revealed a consistently enriched signature (average εHf_i = -17.3 ± 0.5; n = 18) across the wide temporal span recorded in U-Pb ages. This signature is isotopically distinct from archetypal kimberlites and shows good agreement with published results for South African orangeites and lamproites. We interpret this as strong evidence for the presence of an orangeite-like magma during the crystallization of a MARID assemblage. We envisage a simplified geological model for the formation of MARID-veined lithosphere where isotopically enriched slabs subducted during the Namaqua-Natal orogeny (~1.1 Ga), or potentially mantle pyroxenites associated with this event, were selectively melted during Mesozoic plume activity leading to a protracted period of orangeite-like magmatism that variably stalled and crystallized in the lithospheric mantle under open-system conditions.

Preface

This thesis is an original work by Jason Hinde. No part of this thesis has been previously published.

Acknowledgements

This project was supported by the Diamond Exploration Research Training School (DERTS) with additional funding provided by Canada's Natural Sciences and Engineering Research Council (NSERC) and a Society of Economic Geologists' (SEG) graduate student fellowship awarded to the author. Several samples in this work were generously donated from the University of Cape Town's Mantle Room by Dr. Philip Janney.

I would like to thank the tireless and patient support of my supervisor Graham Pearson, who was always encouraging, supportive, and available to guide me in the right direction. I also want to thank Hélène Legros for editing my manuscripts and helping me be a better scientific writer. Hélène, Yan Luo, Chiranjeeb Sarkar, and Sarah Woodland were all incredible resources for completing the LA-ICP-MS and ID-ICP-MS laboratory work and data reduction, especially during COVID shutdowns, and this thesis would not have been possible without their hard work. Thank you to Andrew Locock, who helped guide me through my first forays into analytical work with extensive knowledge and patience. A sincere thank you to Mark Labbe for his help in thin section preparation.

Finishing a graduate thesis post-March 2020, often in isolation and away from family and friends, was a rewarding but often challenging experience. I want to thank my friends, Nikita, Gaby, Brandon, and Avni for helping me keep my sanity and making my time in Edmonton worthwhile. I learned a tremendous amount from working alongside such bright and motivated people. Thank you to my parents for listening to my late-night, incoherent ramblings over the phone as I tried to sort out the next steps of my project. Lastly and most importantly, to my wife Kathleen, even in the roughest of rough patches, you always managed to make me feel like this was all worth doing.

Table of Contents

List of Tables

List of Figures

Chapter 1: Introduction

1.1 Project Rationale and Objectives

The subcontinental lithospheric mantle (SCLM) is a geochemically heterogeneous reservoir that has provided geoscientists with much of our current knowledge about the composition of the deeper Earth. The SCLM plays a key role in the preservation of ancient crust (cratons) and is host to some of the world's largest and most important ore deposits including major diamond producing kimberlite pipes and the PGE-rich Bushveld Complex. Geochemical studies of the primary magmas that form these deposits indicate that their precious metal content may be partially derived from a metasomatically enriched lithospheric mantle (e.g., Griffin *et al*. 2013; Holwell 2019). Other studies contest these models, suggesting that there is little direct evidence of precious metal enriched lithospheric mantle (Maier *et al*. 2000; Arndt 2013). This lack of evidence is in part due to the sparsity of research constraining the effects of metasomatism on ore forming elements in the upper mantle (see text in Section 2.1.1 for previous research). This thesis aims to address this knowledge gap by characterizing the precious metal abundance and distribution in a suite of modally metasomatized mantle xenoliths from both cratonic and non-cratonic settings.

In addition, the relationship between the formation of exotic metasomatic assemblages in the lithospheric mantle (i.e., mica-amphibole-rutile-ilmenite-diopside [MARID] xenoliths) and intraplate magmatism is poorly characterized. Contemporary research is often contradictory when describing the timing, petrogenetic mechanisms (open-system crystallization vs. metasomatic replacement) and parental magmas (kimberlite vs orangeite/lamproite) of these rare mantle samples (see text in Section 3.1.1 for previous research). We aim to better constrain the temporal and petrogenetic formation of MARID xenoliths using whole rock Re-Os isotopes combined with joint *in situ* zircon Lu-Hf, U-Pb isotopes.

Our study focuses on a suite of nine modally metasomatized mantle xenoliths from the Kaapvaal craton in Southern Africa and the Lherz Massif in the French Pyrenees. We aim to complete the following main objectives:

1. Use major and trace element data to evaluate the geochemical characteristics of modally metasomatized mantle samples. Expand on the results of previous works. (i.e., Fitzpayne *et al*., 2018; Fitzpayne *et al*., 2019; Fitzpayne *et al.,* 2020)
2. Determine the abundance (absolute concentrations) of precious metals in areas of the lithospheric mantle metasomatized by intraplate magmatism. Identify major host phases (e.g., sulphide, silicate, platinum group minerals (PGM)) of precious metals and their contribution to the whole rock budget.
3. Analyze variations in precious metal distribution and fractionation between different suites of metasomatized mantle rocks from different localities.
4. Use radiogenic isotope systematics (U-Pb; Re-Os; Lu-Hf) to further constrain the timing and petrogenesis of MARID rocks, their relationship to intraplate magmatism and the source regions of metasomatic agents in the lithospheric mantle.

This thesis is split into two main chapters. Chapter 2 characterizes precious metal abundance and distribution in the modally metasomatized lithospheric mantle and uses Re-Os isotopes to examine peridotite interaction with crystallizing MARID assemblages. Chapter 3 discusses the temporal and petrogenetic implications of zircon Lu-Hf, U-Pb characteristics in MARID xenoliths of the Kaapvaal craton. Each chapter represents a self-contained scientific report, with introductory information and previous research, methods, results, discussion, and conclusions. We recommend reading this thesis in the order it is presented, though early chapters occasionally reference conclusions made in later chapters. All references are presented in the bibliography section at the end of this document and supplementary data is presented in Appendix A-C.

1.2 Regional Geology

1.2.1 Evolution of the Kaapvaal Craton Lithosphere

The complex formation and subsequent modification of the Kaapvaal craton has been extensively characterized due in part to the large number of mantle xenoliths transported to the Earth's surface by kimberlites and related volcanism. Figure 1.2.1 outlines the key zones of

Southern Africa as they relate to modification of the SCLM. Geophysical studies, using seismic velocity changes, have demarcated most of these boundaries (e.g., James *et al*., 2001; Shirey *et al.,* 2002).

The Kaapvaal craton is an Archean cratonic nucleus preserving some of the world's oldest terrestrial rocks. Major crust formation began in the Paleoarchean (~3.7 Ga) and was followed by a protracted period of amalgamation and stabilization from ~3.1 Ga to 2.6 Ga (De Wit *et al*., 1992). Examination of a large database of Re-Os model ages in Kaapvaal peridotites by Pearson and Wittig (2014) showed significant spread, but indicated that the major melt extraction (and thus crust forming) event occurred between 3.0 and 2.7 Ga. This timing coincides with the suturing of the two main terrane blocks (at 2.9 Ga; Schmitz *et al*., 2004) of the Kaapvaal craton: the 3.55-3.05 Ga Witwatersrand Block to the east and the 3.15-2.9 Ga Kimberley Block to the west (De Wit *et al*., 1992). The Colesberg lineament remains as the surficial expression of the suturing event (Schmitz *et al.,* 2004; Figure 1.2.1).

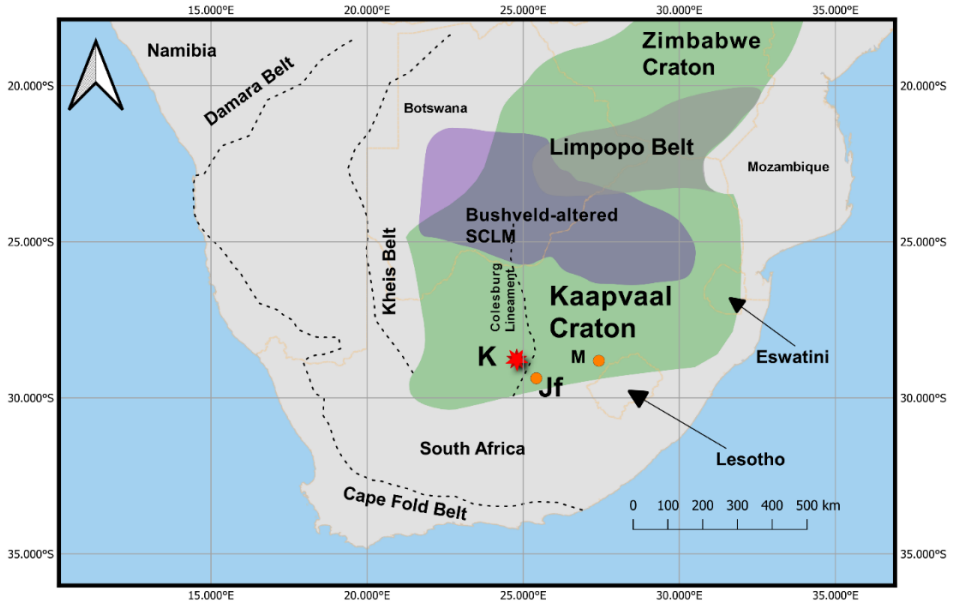

Figure 1.2.1: Map of Southern Africa highlighting important characteristics of the SCLM (reproduced after Pearson et al., 1998; Shirey et al., 2002; Aulbach et al., 2021). Kimberlite pipes that entrained samples analyzed in this study are marked as: K – Kimberley pipe cluster including De Beers and Bultfontein; Jf – Jagersfontein; M – Monastery. Country borders are marked as thin orange lines.

Another major suturing event in the Late Archean occurred during the amalgamation of the Zimbabwe Craton and the Kaapvaal (both together are known as the Kalahari Craton). The Limpopo Belt separates these two terranes (Roering *et al*., 1992; Figure 1.2.1). Although the majority of the craton was stabilized by ~2.6 Ga, accretion of mobile terranes occurred well into the Mesoproterozoic forming orogenic belts such as the Kheis-Magondi Belt (2.0 Ga; Griffin *et al*., 2003) and the Namaqua-Natal Belt (~1.1 Ga during the Kibaran orogeny; Jacobs *et al*., 2008). The Phanerozoic Cape Fold Belt bounds the craton to the south.

More importantly in the context of this work, these events had significant impact on the SCLM of the Kaapvaal craton, imposing geochemical constraints unique to Archean lithospheric mantle (summarized in Figure 1.2.2).

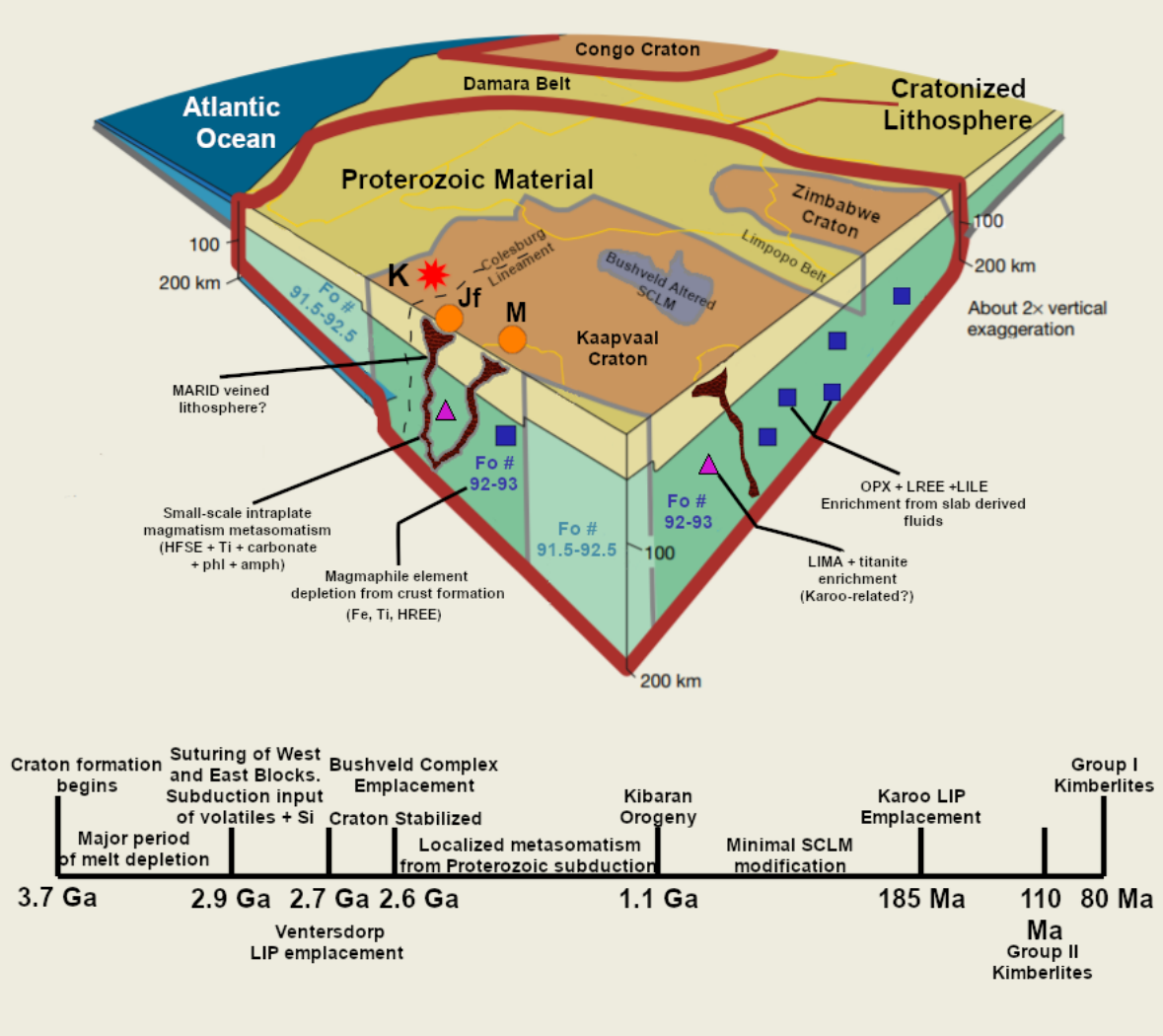

Figure 1.2.2: Schematic diagram of Southern Africa SCLM and timeline of major events in the Kaapvaal craton. Modified after Pearson et al., (2021). Elevated Fo # in Archean-aged Kaapvaal material highlights extreme degree of melt depletion. Squares and triangles illustrate the large-scale re-fertilization of the SCLM from differing sources. Intraplate magmatic pipes (red) display localized metasomatism and are exaggerated in size for illustrative purposes. Kimberlite pipes entraining samples analyzed in this study are labeled identically to Figure 1.2.1. Data for the timeline of major events was assembled from sources included in the main text.

The basaltic crust formation and cratonic stabilization events of the Archean led to extremely high degrees of partial melting of mantle material. The setting in which this occurred is debated, with some models invoking shallow, mid-ocean ridge (MOR) melting (e.g., Simon *et al*., 2007) and others suggesting high pressure, plume-related melting occurring at depth (e.g., Griffin *et al*., 2003). Regardless of the setting, the high degree of melting led to a peridotite residue unique in composition compared to younger SCLM (Figure 1.2.2). Magmaphile elements such as Fe, Al, and Ti were removed leading to elevated Mg #s. Additionally, incompatible elements and precious metals such as the PPGE were selectively partitioned into the melt and removed from the peridotite residue (Pearson *et al*., 2004; Holwell *et al*., 2019). Suturing of the west and east craton blocks at 2.9 GA led to the introduction of subducted material and the incorporation of associated volatile components rich in large-ion lithophile elements (LILE), and Si (Bell *et al*., 2005). This process is thought to be responsible for the OPX-rich nature of Kaapvaal peridotites (Simon *et al*., 2007). Subduction inputs continued throughout the Proterozoic further enriching the SCLM in associated volatiles (Richardson *et al*., 1990; Fitzpayne *et al*., 2019). Major igneous events intruded during this period such as the Ventersdorp large igneous province (LIP) (2.7 GA; Armstrong *et al*., 1991) and the PGE-rich Bushveld magmatic complex (2.6 GA; Buick *et al*., 2001) left their fingerprints on the SCLM in the form of low seismic velocities and renewed diamond growth (Aulbach *et al*., 2021). Both events are often attributed to mantle plume related melting (e.g., Hatton 1995), but the source of metals (especially in the Bushveld Complex) remains unclear. The Karoo LIP emplacement (~185 Ma; Duncan *et al*., 1997) is also associated with strongly metasomatized rocks bearing lindsleyite-mathasite (LIMA) and titanite minerals. Finally, Jurassic-Cretaceous orangeite and kimberlite magmatism locally metasomatized the SCLM, introducing a variety of components including clinopyroxene, phlogopite, amphiboles, HFSE, Ti, and carbonate (Simon *et al*., 2007). This process is also likely responsible for MARID veining at shallow lithospheric depths (~60-150 km; Dawson and Smith 1977; Gregoire *et al.,* 2002; Fitzpayne *et al*., 2018).

1.2.2 Intraplate Magmatism of the Kaapvaal Craton

As outlined above, intraplate magmatism is one of the most well studied aspects of the Kaapvaal craton. Specifically, the variably carbonated and alkali-rich variety often grouped together as "kimberlite magmatism" has been a critical window into the processes occurring in the Earth's mantle. This type of volcanic activity is not unique to the Kaapvaal craton, with ~ 3500 kimberlites identified on every continent spanning a wide temporal range (Giuliani and Pearson 2019). However, Kaapvaal kimberlites have received special attention primarily due to their diamondiferous character (Giuliani and Pearson 2019).

Locality	Classification	Emplacement Age	Associated Samples (this study)
Jagersfontein	Kimberlite	85.8 ± 1 Ma	JAG1
Monastery	Kimberlite	89.2 ± 0.2 Ma	17MON 004
Kimberley "Big Hole"	Kimberlite	86.5 ± 0.6 Ma	UIB-2, AJE-326
De Beers	Kimberlite	86.5 ± 0.6 Ma	AJE-335, KDB-20
Bultfontein	Kimberlite	88.4 ± 0.2 Ma	AJE-2422

Table 1.2.1: Summary characteristics of magmatic intrusions entraining samples from this study. Classifications and emplacement ages from Kjarsgaard *et al*., in press. Uncertainty is quoted as 2σ

In general, kimberlites have historically been divided into two groups: i) archetypal or "Group I" kimberlites and ii) orangeites or "Group II" kimberlites (Smith *et al*., 1985; Mitchell 1995). Archetypal kimberlites of the Kaapvaal craton are relatively petrographically and geochemically homogeneous (Tappe *et al*., 2021). They contain lower Ba/Nb, Th/Nb and La/Nb ratios than orangeites but higher Ce/Pb (Becker and Le Roex 2006). Moderately depleted to slightly enriched Sr-Nd-Hf isotopic compositions indicate source rocks located in the convecting mantle (Nowell *et al.,* 2004; Becker and Le Roex 2006; Figure 1.3.3). Kimberlite magmatism has

occurred in various "pulses" since ~ 1.8 Ga, with many of the diamondiferous pipes occurring roughly ~90 Ma including the famous Kimberley region pipes (Simon *et al*., 2007).

In contrast, orangeites are more temporally restricted, erupting between 200 and 110 Ma (Kjarsgaard *et al*., in press).

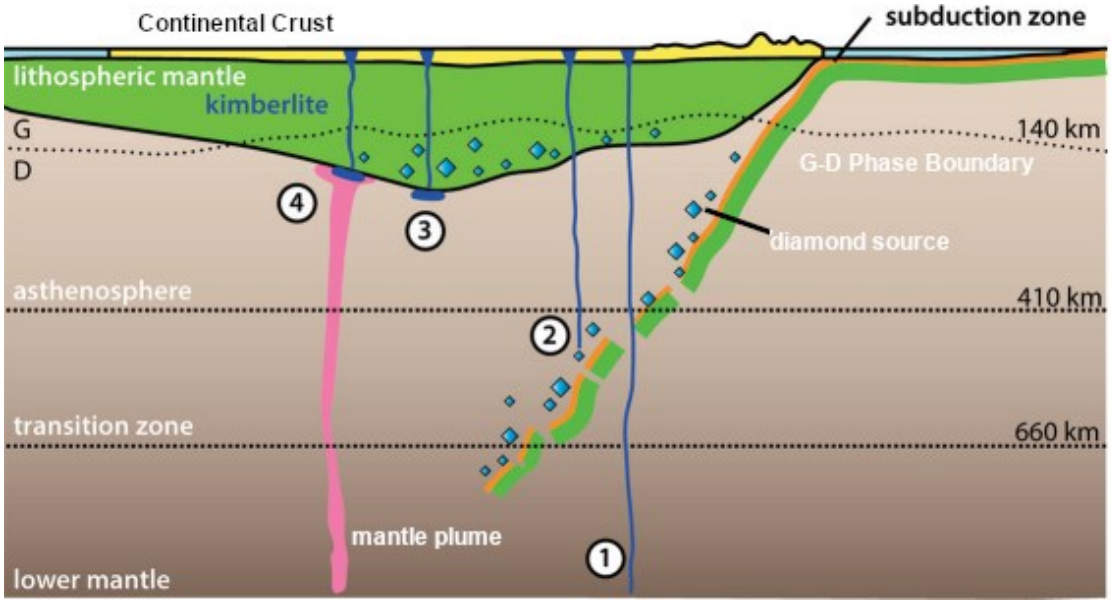

Figure 1.2.3.: Schematic diagram of the crust, SCLM, and convecting mantle illustrating possible source regions for archetypal kimberlite magmas. Modified after Pearson and Giuliani (2019) and Shirey et al., (2013). Possible source regions include 1) partial melting in the lower mantle 2) Partial melting in the transition zone as a response to subduction inputs 3) Partial melting at the lithosphere-asthenosphere boundary 4) Partial melting at the lithosphere-asthenosphere boundary driven in part by mantle plume activity.

Orangeites also show different geochemical characteristics compared to kimberlites with higher concentrations of LILE, Pb, and LREE (Becker and Le Roex 2006). In addition, Sr-Nd-Hf isotopes suggest an enriched source rock that has long been separated from the convecting mantle (Nowell *et al*., 2004; Becker and Le Roex 2006).

Five pipes have entrained mantle xenolith samples used for this study: Jagersfontein, Monastery, De Beers, Big Hole, and Bultfontein. The key characteristics and associated samples are summarized in Table 1.2.1. All of these pipes are archetypal kimberlites that erupted during the major pulse of diamondiferous magmatism roughly 90 Ma. Three of these pipes (Big Hole, De Beers, and Bultfontein) are part of the world-famous Kimberley cluster occurring over the younger Kimberley block on the west side of the Colesburg Lineament (Figure 1.2.1). Two of

the pipes (Jagersfontein and Monastery) intrude through the older Witwatersrand Block on the east side of the Colesburg Lineament (Figure 1.2.1). All five pipes intrude through on-craton Archean SCLM.

1.2.3 The Lherz Massif

Located in the French Pyrenees mountains, the Lherz Massif provides an opportunity to examine contrasting SCLM characteristics. The orogenic peridotites comprise ~40 discreet ultramafic bodies ranging in size from a few m^2 to 1 km^2 (Figure 1.2.4; Le Roux *et al*., 2007). These bodies are mainly composed of metasomatically re-fertilized lherzolite and refractory lenses of harzburgite (Figure 1.2.4; Le Roux *et al.,* 2007).

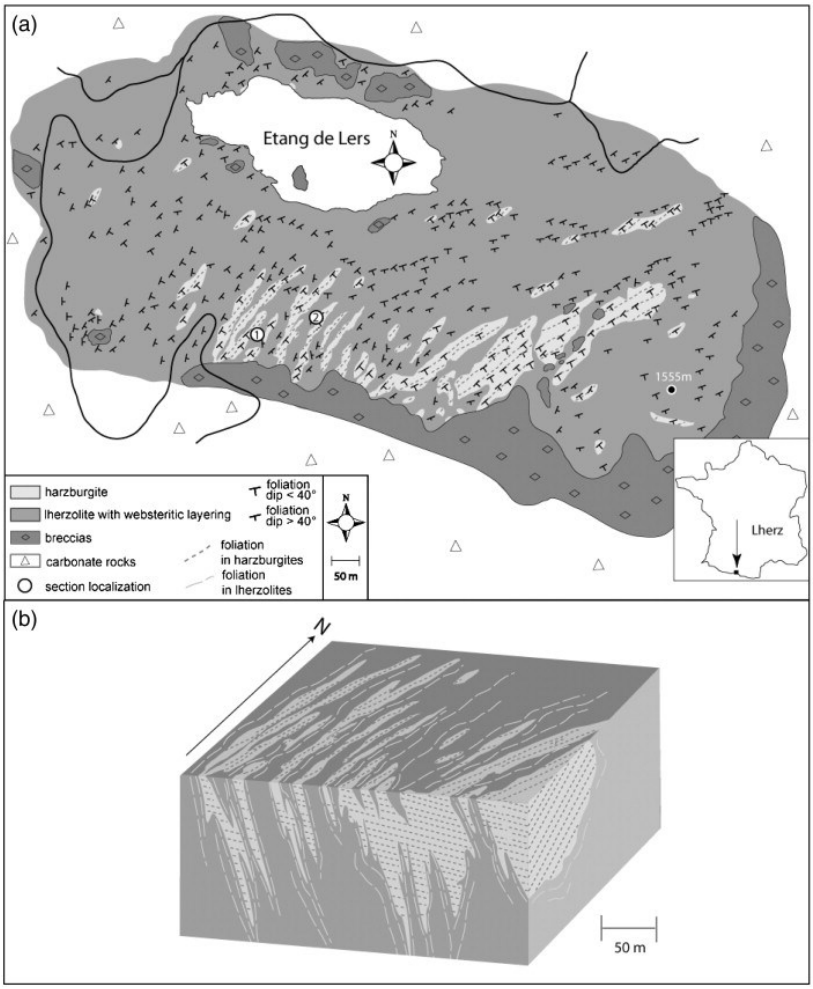

Figure 1.2.4: The Lherz Massif in a) plan view and b) block view from Le Roux et al., (2007). The compositional heterogeneity of the Lherz Massif is highlighted as a key characteristic used to decipher the process of mantle metasomatism.

Like all massif peridotites, the Lherz massif has been metamorphically altered by tectonic exhumation, showing high-T, low-P granulite facies metamorphism. The peridotites are embedded within carbonate rocks of Jurassic to Aptian age (the North Pyrenean Metamorphic Zone; Le Roux *et al*., 2007). Lherz SCLM is significantly younger, stabilizing during a major period of European crustal growth during the Paleoproterozoic (1.9 Ga; Burnham *et al*., 1998). It has also undergone a smaller degree of melt depletion with models estimating as much as 25% partial melting in the harzburgitic residua (Burnham *et al*., 1998).

Despite these differences, the Lherz SCLM shows a similarly complex metasomatic history to the Kaapvaal craton. Throughout the massif, the compositional (lherzolite vs. harzburgite) and geochemical (e.g., LREE depleted lherzolite and LREE enriched harzburgite) heterogeneity is attributed to large-scale re-fertilization from reactive percolation with mantle-derived melts (Le Roux *et al*., 2007; Le Roux *et al.,* 2008; Lorand *et al*., 2010). The major model for this refertilization process suggests that the Lherz SCLM represents a "fossilized" lithosphere-asthenosphere boundary in which asthenospheric melts infiltrated and reacted with refractory harzburgite to irregularly produce re-fertilized lherzolites (Le Roux *et al*., 2007). This process is thought to have occurred prior to Cretaceous tectonic exhumation, during the Late Paleozoic Variscan Orogeny (Le Roux *et al*., 2008). This process had a pronounced effect on the precious metal budget of the Lherz lithospheric mantle. The work of Lorand *et al.,* (2010) delineated two generations of BMS and PGM: a) refractory IPGE-rich BMS assemblage containing Pt-Ir-Os alloys representative of the depleted harzburgite protolith and b) Pd-rich metasomatic BMS containing low-T bismuthotellurides indicating re-fertilization processes in agreement with the model of Le Roux *et al*., (2007).

Similarly, Lherz SCLM has experienced localized metasomatism typified by the well-studied veins of hydrous amphibole pyroxenites and phlogopite amphibolites occurring within Lherz peridotites. These veins likely represent the high-pressure crystallization products of transitional alkali basalts (in the case of the amphibole pyroxenites) and basanitic magmas (in the case of phlogopite amphibolites) at depths of ~45 km (Fabriès *et al*., 2001). These melts are interpreted as a late-stage process generated from the partial melting of the already re-fertilized SCLM during Cretaceous tectonic exhumation (Fabriès *et al.,* 2001). In contrast to intraplate magmatism of the Kaapvaal craton, these hydraulically propagated veins display limited

geochemical infiltration into the host peridotites (Bodinier *et al.,* 1990; Bodinier *et al*., 2004). Little is known about the precious metal characteristics of Lherz amphibolite veins. Lorand (1989) showed that they are capable of carrying high concentrations of S (up to 1900 ppm) in the form of sulphides that co-crystallized in an immiscible melt. Only two samples (both amphibole pyroxenites) were analyzed for Pd and Ir contents in Lorand (1989) and both showed surprisingly high concentrations of both elements (2.0 and 3.2 ppb Ir; 11 and 7 ppb Pd; Lorand 1989). Here we expand the precious metal characterisation via a study of an amphibolite vein plus its lherzolite host.

Chapter 2: Precious Metal Inventory of the Metasomatized Lithospheric Mantle and Mantle-Derived Melts: Implications for Subcrustal Metal Mobilization

2.1 Introduction

2.1.1 Background and Objectives

The Earth's lithospheric mantle, being isolated from the homogenizing effects of convective flow, displays significant geochemical heterogeneity at both fine (mineral) and broad (km-sized massif bodies) scales (Bodinier and Godard 2003; Pearson *et al*., 2003). Two main processes are the drivers of this compositional spectrum: variable degrees of melt depletion during crustal formation events (e.g., Pearson *et al*., 1995; Pearson *et al*., 2004; Griffin and O'Reilly 2007) and secondary metasomatic refertilization (e.g., Harte 1983; Griffin *et al*., 1999). Metasomatism in the lithospheric mantle is primarily attributed to infiltrating melts and associated fluids of variable composition including: subducting slab derived fluids (Richards 2011), carbonatitic melts and CO_2-rich fluids (e.g., Griffin *et al*., 1996), kimberlite-like melts and fluids (including orangeites and lamproites; Gregoire *et al*., 2002; Simon *et al*., 2007; Fitzpayne *et al*., 2018, 2019) and larger fractions of silicate melts of broadly basaltic composition (e.g., Le Roux *et al*., 2007; Giuliani *et al*., 2014). The effects of refertilization range from "cryptic" or "stealth" metasomatism (i.e., LREE enrichment of clinopyroxene or precipitation of new clinopyroxene; Harte 1983; O'Reilly and Griffin 2013) to the modal addition of hydrous phases such as phlogopite and amphibole (Dawson and Smith 1977).

The suite of metasomatized mantle peridotites interpreted as products of interaction with kimberlite-like melts and related fluids are particularly well studied. Erlank *et al*., (1987) described a metasomatic series from unaltered garnet peridotite through garnet phlogopite peridotite (GPP), to phlogopite peridotite (PP), then to phlogopite potassic (K) richterite peridotite (PKP) as a result of progressive interaction with infiltrating kimberlite. These authors

also proposed that the suite of mica, amphibole, rutile, ilmenite, and diopside bearing MARID mantle xenoliths may be the result of the most extreme kimberlite metasomatism. Potassic metasomes such as the MARID and related PIC (phlogopite-ilmenite-clinopyroxene) rocks are now more commonly interpreted as complex crystallization products of stalled kimberlite-like melts in the lithospheric mantle, though the exact nature of their petrogenesis remains mysterious (Sweeney *et al*., 1993; Fitzpayne *et al*., 2018; Hoare *et al*., 2021; Chapter 3 of this study).

In general, the effects of metasomatism on the major element and lithophile trace element budget of upper mantle rocks has been extensively studied in a variety of settings. The high volume of metasomatized mantle xenoliths entrained in kimberlite pipes of the Kaapvaal craton in Southern Africa have shown a complex refertilization history (e.g., Griffin *et al*., 1999; Gregoire *et al*., 2003). Studies of the upper mantle via massif peridotites (e.g., the Lherz massif in the French Pyrenees) have revealed some similar metasomatic refertilization trends (e.g., Bodinier *et al*., 1990; Le Roux *et al.,* 2007). However, research into metasomatic effects on highly siderophile and strongly chalcophile elements (collectively referred to as precious metals in this study) are comparatively sparse (e.g., Morgan 1986; Lorand *et al.,* 2010; Alard *et al*., 2011; König *et al*., 2015; Harvey *et al*., 2015). Unlike lithophile trace elements which are mostly controlled by silicate and oxide phases, precious metals in the lithospheric mantle primarily reside in Cu-Fe-Ni base metal sulphides (BMS; Handler and Bennett 1999; Alard *et al*., 2000; Lorand *et al*., 2008; Lorand and Luguet 2016). However, precious metal mass balance calculations based on BMS phases often show poor agreement with whole rock data (particularly Au and Pt) suggesting that micro-scale platinum group minerals (PGM) and alloys create a strong "nugget effect" that can account for a significant proportion of the upper mantle PGE budget (e.g., Alard *et al*., 2000; Pearson *et al*., 2003; Ackerman *et al*., 2013). Silicate melts are capable of dissolving significant concentrations of sulfur (e.g., Schiano and Clocchiatti 1994) and thus metasomatism has the potential to significantly alter precious metal abundances and distribution in the lithospheric mantle (Pearson *et al*., 2003; Lorand and Luguet 2016).

The precious metal geochemistry of alkali-rich mantle derived melts (kimberlites, orangeites, and lamproites) are also poorly studied. The chondrite normalized patterns of platinum group elements plus rhenium for Kaapvaal craton kimberlites are relatively unfractionated with variable total abundances (McDonald *et al*., 1995; Maier *et al*., 2017). Orangeite data from the

Karelian craton show similar patterns to kimberlites, but the original precious metal signatures of kimberlite-like melts are likely obscured by significant mantle and crustal assimilation (Maier *et al*., 2017). Thus, the study of precious metal systematics in metasomes interpreted as crystallization products of these melts (i.e., MARID and PIC xenoliths) may provide a clearer picture of their ability to redistribute these elements.

Several researchers have suggested that a metasomatically enriched lithospheric mantle may play a role in the generation of some crustal precious metal deposits. (Richards 2011; Griffin *et al*., 2013; Giuliani *et al.,* 2015; Holwell *et al*., 2019). The most commonly invoked role for the upper mantle as a precious metal source is in the formation of layered mafic intrusion (LMI) nickel-PGE deposits such as the Bushveld Complex in Southern Africa and the Norilsk Deposit in Siberia (e.g., Richardson and Shirey 2008; Barnes *et al*., 2010; Begg *et al*., 2013). However, these models are contested, with other studies claiming that there is little direct evidence of a lithospheric mantle source and that other petrogenetic processes are responsible for ore formation (e.g., Maier *et al*., 2000; Arndt 2013).

Here we analyze the geochemistry of a series of modally metasomatized mantle xenoliths and alkali-rich metasomes from the Kaapvaal craton as well as an amphibole-veined lherzolite from the Lherz Massif in order to better understand the effects of metasomatism on the lithospheric mantle. We report precious metal abundances at both the mineral and whole rock scale to provide additional constraints on the major host phases for these elements and evaluate the enriched lithospheric mantle as a potential metal source for crustal ore deposits. We also report major and lithophile trace element results to expand the available data set on modally metasomatized xenoliths and evaluate further the results from previous studies (e.g., Fitzpayne *et al*., 2018, 2019, 2020). Finally, we present the first published set of Re-Os isotopic data for MARID xenoliths which further constrains their petrogenesis.

2.1.2 Samples and Previous Work

Seven xenoliths from the kimberlites of the Kaapvaal Craton and one outcrop sample from the Lherz Massif were analyzed for this study. Several samples were provided by Dr. Philip Janney of the University of Cape Town's Mantle Room while others were taken from collections at the University of Alberta. Samples consisted of a mixture of hand samples and thin sections. Table 2.1.1 summarizes the key characteristics of each sample in this study.

Sample	Sample Type	Analyzed in Fitzpayne *et al.*, (2018)?	Sample Provider	Locality	Rock Type	Rock Subtype	Analytical Techniques
JAG1	H.S.	No	University of Alberta	Jagersfontein	Metasomatized peridotite	Garnet phlogopite peridotite	EPMA LA-ICPMS XRF ID-ICPMS
17MON 004	H.S.	No	University of Cape Town	Monastery	Metasomatized peridotite	Phlogopite peridotite	EPMA LA-ICPMS XRF ID-ICPMS
LZM-001	H.S.	No	University of Alberta	Lherz Massif	Metasomatized peridotite	Veined spinel lherzolite	EPMA LA-ICPMS XRF ID-ICPMS
UIB-2	T.S.	No	University of Alberta	Kimberley "Big Hole"	Alkali-rich metasome	PIC	EPMA LA-ICPMS
AJE-326	H.S.	Yes	University of Cape Town	Kimberley "Big Hole"	Alkali-rich metasome	MARID	EPMA LA-ICPMS XRF ID-ICPMS
AJE-335	H.S.	Yes	University of Cape Town	De Beers	Alkali-rich metasome	MARID	EPMA LA-ICPMS XRF ID-ICPMS
AJE-2422	H.S.	Yes	University of Cape Town	Bultfontein	Alkali-rich metasome	MARID	EPMA LA-ICPMS LASS-ICPMS XRF ID-ICPMS
KDB-20	H.S.	No	University of Cape Town	De Beers	Alkali-rich metasome	MARID	EPMA LA-ICPMS XRF ID-ICPMS

Table 2.1.1: Summary of mantle-derived metasomatic rocks analyzed in this study. Rocks that were available as hand samples are indicated as H.S. while samples that were available only as thin sections are indicated as T.S.

We differentiate between modally altered peridotites (referred to as metasomatized peridotites) and metasomes interpreted as crystallization products of volatile-rich melts (i.e., MARID, PIC, and the Lherz amphibole vein collectively referred to as alkali-rich metasomes) to reflect their differing roles in the mantle lithosphere. The samples from the Kaapvaal craton were chosen to cover the spectrum of metasomatized xenoliths that have been recorded in volcanically entrained xenoliths (excluding PKP xenoliths). The sample from the Lherz Massif was chosen to compare precious metal mobility under contrasting styles of metasomatism in a different tectonic setting. The Lherz rock, a spinel lherzolite with a cm-scale amphibole vein, has the additional benefit of containing a pristine sample of an alkali-rich metasome within the host rock that allows direct

comparison of both geochemical characteristics. Sample classification was based on petrographic examination as well as geochemical constraints (i.e., delineating between MARID and PIC samples requires geochemical analysis).

Three samples in this work (AJE-326, AJE-335, AJE-2422; Table 2.1.1) have been previously analyzed in a series of studies examining the effects of kimberlite metasomatism on the lithospheric mantle (Fitzpayne *et al*., 2018; Fitzpayne *et al*., 2019; Fitzpayne *et al.,* 2020). Results from this project are compared to these works to verify geochemical characteristics of these samples. New data, including Re-Os isotopes and precious metal abundances, are also presented.

2.2 Analytical Methods

2.2.1 Sample Preparation and Petrography

Hand samples were cut into billets and sent for thin section preparation at Precision Petrographics (Langley, BC) and the University of Alberta's Thin Section Laboratory. Two 100 µm polished thick sections and one 30 µm polished thin section were made from each sample.

Initial petrographic analysis was conducted using optical microscopy on 30 µm polished thin sections. Primary mineral assemblages and dominant textures were noted and used to assist in classifying samples. Precise calculation of primary mineral abundances was conducted by obtaining high quality (4000 dots-per-inch) scans of each thin section using a modified Nikon Coolscan 9000 at the University of Alberta's Digital Imaging Facility (DIF). Point counting software Rock.AR (Larrea *et al.,* 2014) was used to determine precise modal abundances of the main minerals based on the following procedure: scans were converted to 2324 x 1379 pixel JPEG images and loaded into Rock.AR. A grid overlay combined with manual recognition of mineral phases was used to point count minerals that contribute to the primary assemblage (Figure 2.1.1). A cut-off of 1% was used to delineate accessory phases from major phases.

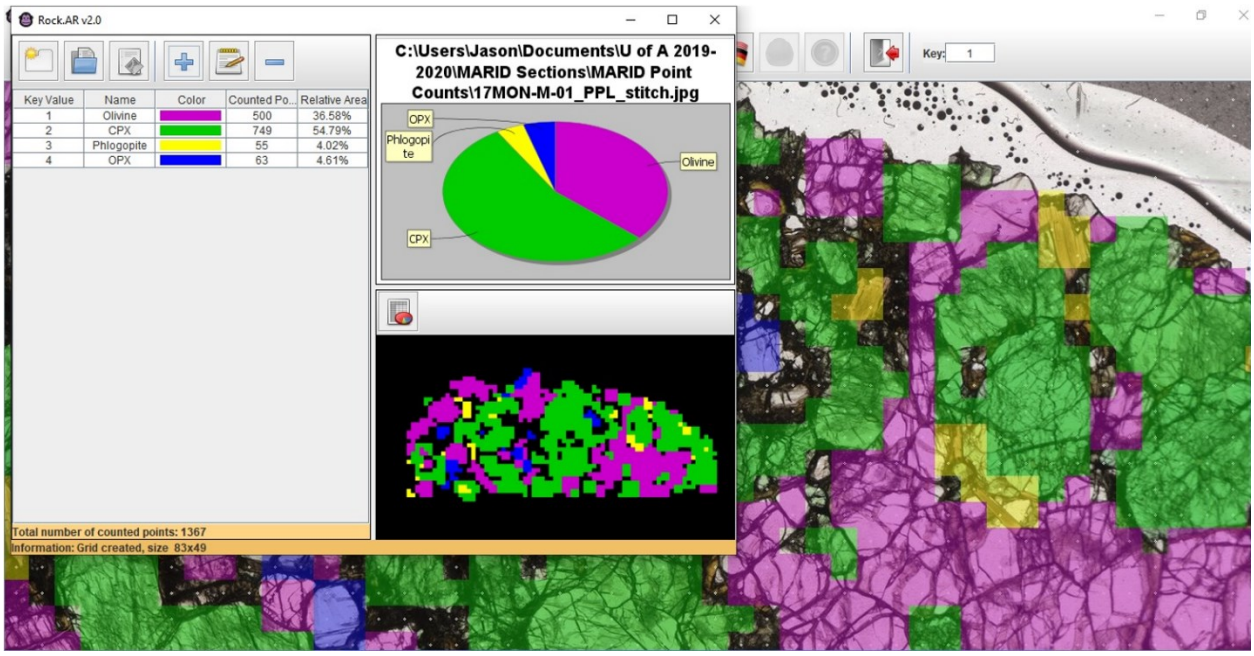

Figure 2.1.1: Image of RockAR GUI used to calculate modal abundances of primary phases in thin sections.

2.2.2 Electron Probe Microanalysis (EPMA)

Silicate and Oxide Phases

Major element concentrations in silicate and oxide mineral phases were analyzed via EPMA at the University of Alberta's Electron Microprobe Laboratory (EML). Data were collected using a model JEOL JXA-8900R microprobe. Analytical conditions included an accelerating voltage of 20 kV, a beam current of 20 nA, a spot-sized beam diameter (< 1µm), and between 20 and 40 s of on-peak and off-peak count time (Table 2.2.1). Mineral grains were analyzed *in situ* on polished, carbon coated thin sections. Major element compositions were acquired using wavelength-dispersive spectrometry (WDS) and calculated with Probe for EPMA software (Donovan *et al*., 2012). Standards for each element are outlined in Table 2.2.1. Data were collected across five analytical sessions.

Element	Line/Crystal	Calibration Standards	On Peak Time (s)	Off Peak Time (s)
Si	Ka/TAP	$CaMgSi_2O_6$ Diopside Wakefield, Fo90.5, Frank Smith Pyrope Garnet	40	40
Ca	Ka/PETH	$CaMgSi_2O_6$ Diopside Wakefield	40	40
Na	Ka/TAP	NaAlSi3O8 albite VA 131705	40	40
Fe	Ka/LIFH	Fe2SiO4 fayalite Rockport, FeTiO3 Ilmenite 96189	20	20
Mn	Ka/LIFH	Spessartine Little 3	20	20
K	Ka/PETH	KAlSi3O8 sanidine Itrongay	40	40
Ti	Ka/PET	TiO2 Rutile MTI, FeTiO3 Ilmenite 96189	30	30
Mg	Mg/TAP	CaMgSi2O6 diopside Wakefield, Fo90.5, Frank Smith Pyrope Garnet	40	40
Al	Ka/TAP	Frank Smith Pyrope Garnet, Plagioclase (labradorite) 115900,	40	40
Cr	Ka/PET	Cr2O3 chromium oxide Alfa	30	30
Ba	Lb/PET	BaSi2O5 Sanbornite, Fresno	30	30
Ni	Ka/LIFH	Ni nickel Alfa	20	20
Zn	Ka/LIFH	ZnAl2O4 gahnite H111989	20	20

Table 2.2.1: Summary of select analytical conditions and standards for the analysis of major elements in silicate and oxide phases

Major element weight percentages were quantified for SiO_2, CaO, Na_2O, FeO^T, MnO, K_2O, TiO_2, MgO, Al_2O_3, Cr_2O_3, BaO, NiO, ZnO ± H_2O using Probe for EPMA software (Donovan *et al*., 2012). Stoichiometric mineral formulae and oxide weight percentage were calculated separately for each mineral phase based on their number of cations (e.g., 3 cation slots for olivine). Amphibole (k-richterite, titanian pargasite) composition and formulae were processed using the ACES excel spreadsheet (Locock 2014).

Reported compositions for individual mineral grains are based on one analysis point per grain. Data were checked for acceptable stoichiometry and only minerals with total oxide weight percentage above 97.9% were used in the results.

Sulphide Phases

Major element concentrations in sulphide phases were analyzed via EPMA at the University of Alberta's Electron Microprobe Laboratory (EML). Data was collected using a model JEOL JXA-8900R microprobe. Analytical conditions included an accelerating voltage of 20 kV, a beam current of 20 nA, a spot-sized beam diameter (< 1µm), and between 20 and 40 s of on-peak and

off-peak count time (Table 2.2.2). Quantitative major element compositions were acquired using wavelength-dispersive x-ray spectroscopy (WDS) and calculated with Probe for EPMA software (Donovan *et al*., 2012).

Element	Line/Crystal	Calibration Standards	On Peak Time (s)	Off Peak Time (s)
As	La/LTAP	Gallium arsenide GaAs	40	40
S	Ka/PET	Iron disulfide FeS2	40	40
Fe	Ka/LLIF	Pyrrhotite Fe7S8	30	30
Cu	Ka/LLIF	Copper Cu	30	30
Co	Ka/LLIF	Cobalt Co	30	30
Zn	Ka/LLIF	Sphalerite ZnS	30	30
Ni	Ka/LLIF	Ni nickel Alfa	20	20
Si	Ka/LTAP	KAlSi3O8 sanidine Itrongay	20	20

Table 2.2.2: Summary of select analytical conditions and standards for the analysis of major elements in sulphide phases

2.2.3 Laser Ablation Inductively Coupled Plasma Mass Spectrometry (LA-ICP-MS)

Silicate and Oxide Phases

Trace element concentrations in silicate and oxide mineral phases were analyzed *in situ* via laser ablation inductively coupled plasma mass spectrometry (LA-ICP-MS) at the University of Alberta's Arctic Resources Laboratory. Data was collected using a Resolution Excimer 193 nm laser with thin sections loaded into a 2-volume Laurin-Technic S-155 ablation cell. The ablated material was passed to and analyzed by a Thermo Element-XR 2 mass spectrometer. Laser conditions included a repetition rate of 10 Hz, 26% attenuator value, a laser energy of 120 mJ, and a fluence of ~3.5 J/. Spot sizes varied from 50-285 µm depending on the size of the target mineral grain. Each analysis consisted of 60 seconds of background and washout time followed by 50 seconds of ablation time.

Silicate minerals were analyzed using Si as an internal standard (collected from EPMA analysis). 27 elements (^{45}Sc, ^{47}Ti, ^{57}Fe, ^{59}Co, ^{60}Ni, ^{85}Rb, ^{88}Sr, ^{89}Y, ^{90}Zr, ^{93}Nb, ^{137}Ba, ^{139}La, ^{140}Ce, ^{141}Pr, ^{146}Nd, ^{147}Sm, ^{153}Eu, ^{157}Gd, ^{159}Tb, ^{163}Dy, ^{165}Ho, ^{166}Er, ^{169}Tm, ^{172}Yb, ^{175}Lu, ^{178}Hf, ^{208}Pb) were calibrated using glass standard reference material (SRM) NIST 612 (Jochum *et al.,* 2011) as the primary standard and United States Geological Survey (USGS) doped synthetic basalt glass standard BIR-1G (Jochum *et al.,* 2005) as the secondary, quality-control standard. Six elements (^{63}Cu, ^{107}Ag, ^{185}Re, ^{106}Pd, ^{195}Pt, ^{197}Au) were calibrated using glass SRM NIST 610 (Jochum *et*

al., 2011) as the primary standard while ^{191}Ir used GSE-1G as the primary standard. Two of these elements, ^{106}Pd and ^{191}Ir, were only present in one available reference material and were not able to be quality-checked with a secondary standard. The remaining elements used USGS glass standard BHVO-2G and GSE-1G as secondary, quality control standards (Jochum *et al.,* 2005).

Oxide minerals were analyzed using ^{57}Fe as an internal standard (collected from EPMA analysis). 27 elements (^{29}Si,^{45}Sc, ^{47}Ti, ^{59}Co, ^{60}Ni, ^{85}Rb, ^{88}Sr, ^{89}Y, ^{90}Zr, ^{93}Nb, ^{137}Ba, ^{139}La, ^{140}Ce, ^{141}Pr, ^{146}Nd, ^{147}Sm, ^{153}Eu, ^{157}Gd, ^{159}Tb, ^{163}Dy, ^{165}Ho, ^{166}Er, ^{169}Tm, ^{172}Yb, ^{175}Lu, ^{178}Hf, ^{208}Pb) were calibrated using BHVO-2G as the primary standard with USGS basalt glass standard BCR-2G as the secondary, quality-control standard. ^{63}Cu, ^{107}Ag, ^{185}Re, ^{106}Pd, ^{191}Ir, ^{195}Pt, ^{197}Au were calibrated using the same approach as the silicate analyses.

During a run, samples were bracketed by the primary standard (n = 3) when the spot size was changed or after 10 sample points were analyzed. Within the sample brackets, one point of each secondary standard was included to ensure consistent data quality.

Primary and secondary reference analyses for silicate and oxide phases are summarized in figures included in Appendix A.1.1 and A.1.2. In general, measured results agree well with reference values. ^{195}Pt measurements in GSE-1G and BHVO-2G show significant deviation from reference values and generally poor repeatability between measurements (RSD of 154% and 80% respectively). In both cases, these results appear to be skewed by the presence of several outliers. It is unclear whether these are the result of a nugget effect within the reference material or the presence of an interfering species (e.g., ^{179}Hf^{16}O). ^{197}Au results in GSE-1G are higher than reference values (42.9% and 71.4% error in silicate and oxide calibration respectively) but show good repeatability (RSD of 9% and 15% in silicate and oxide calibration respectively). The elevated, repeatable Au concentrations may point to the presence of interfering species ^{181}Ta^{16}O formed during ablation. A further source of uncertainty is the lack of comprehensive accuracy and homogeneity studies conducted for precious metals in these reference materials.

Signal integration of the time-resolved LA-ICP-MS spectra was conducted using the Iolite 3 software package (Paton *et al.,* 2011) and the "Trace Elements" data reduction scheme (Woodhead *et al*., 2007). Signal spikes were avoided during the integration of time resolved signals.

To be considered for data quantification, unknown values must lie above the limit of quantification (LOQ) (LOQ $= \frac{10}{3}$LOD; Currie 1968; Equation 2.2.1). For plotting, all values below LOQ were replaced with $\frac{1}{2}$LOD. For tabulation and statistical analysis, unknown values below LOQ are marked as such and are not used for the calculation of descriptive statistics.

$$LOD = \frac{1}{S}\left[3 \times 1\sigma_b \times \sqrt{\frac{1}{n_b} + \frac{1}{n_a}}\right]$$

Equation 2.2.1: Formula for LOD where S = sensitivity (cps/ppm), 1σ = standard deviation of the background measurement, n_b = the number of measurements in the background selection and n_a is the number of measurements in the sample selection

	^{45}Sc	**^{47}Ti**	**^{57}Fe**	**^{59}Co**	**^{60}Ni**	**^{85}Rb**	**^{88}Sr**	**^{89}Y**	**^{90}Zr**	**^{93}Nb**
Mean LOQ (ppm)	0.2	2	6	0.07	1	0.09	0.05	0.009	0.6	18
Total Analyses	107	107	86	107	107	107	107	107	100	107
	^{137}Ba	**^{139}La**	**^{140}Ce**	**^{141}Pr**	**^{146}Nd**	**^{147}Sm**	**^{153}Eu**	**^{157}Gd**	**^{159}Tb**	**^{163}Dy**
Mean LOQ (ppm)	21	0.2	0.5	0.07	0.3	0.1	0.02	0.07	0.008	0.03
Total Analyses	107	107	107	107	107	107	107	107	107	107
	^{165}Ho	**^{166}Er**	**^{169}Tm**	**^{172}Yb**	**^{175}Lu**	**^{178}Hf**	**^{208}Pb**	**^{63}Cu**	**^{107}Ag**	**^{185}Re**
Mean LOQ (ppm)	0.009	0.02	0.004	0.02	0.004	0.1	0.1	0.09	0.02	0.003
Total Analyses	107	107	107	107	107	107	107	77	78	87
	^{106}Pd	**^{191}Ir**	**^{195}Pt**	**^{197}Au**						
Mean LOQ (ppm)	0.006	0.003	0.003	0.008						

Total Analyses	87	78	87	87

Table 2.2.3: Mean LOQ values for each LA-ICPMS analyte. All concentrations are in ppm. Total analyses vary based on phases present in samples and instrument error.

LOQ for analytes in silicate and oxide runs are < 1 ppm. Exceptions are ^{47}Ti, ^{57}Fe, ^{93}Nb, ^{137}Ba, all of which reach wt. % levels in various mineral phases and thus shift the LOQ to higher values. Most REE and precious metal elements have LOQ at the ppb level or one order of magnitude higher.

Sulphide Phases

Trace element concentrations in sulphides were analyzed *in situ* via LA-ICP-MS at the University of Alberta's Arctic Resources Laboratory. Data was collected using a Resolution Excimer 193 nm laser with thin sections loaded into a 2-volume Laurin-Technic S-155 ablation cell. The ablated material was by a Thermo Element XR high resolution mass spectrometer. Laser conditions included a fluence of 3.5 J/cm^2, 8 Hz repetition rate, 26% attenuator value, and a laser energy of 120 mJ. Spot sizes varied from 33-90 μm and were adjusted based on the size of the grains and the presence of unwanted phases within the mineral (serpentine, magnetite, other sulphides). Each analysis consisted of 90 seconds of background and washout time followed by 60 seconds of ablation time.

Base metal sulphides were analyzed using ^{57}Fe as an internal standard with unknown analysis points referencing data collected from EPMA analysis. HSEs (^{99}Ru, ^{103}Rh, ^{106}Pd, ^{192}Os, ^{193}Ir, ^{195}Pt, ^{197}Au) were calibrated using the synthetic pyrrhotite "Po726" as the primary standard (Sylvester *et al.,* 2005). United States Geological Survey (USGS) doped synthetic basalt glass standard GSE-1G and GSD-1G were used as secondary, quality-control standards to monitor instrument performance. All three of these reference materials contain Ir, Pt, and Au that were used to monitor data quality. Other elements of interest (^{29}Si, ^{59}Co, ^{60}Ni, ^{63}Cu, ^{107}Ag, ^{185}Re) were calibrated using GSE-1G as the primary standard with GSD-1G as a secondary, quality control standard. Only elements calibrated against the primary, matrix-matched standard Po726 are considered quantitative (^{99}Ru, ^{103}Rh, ^{106}Pd, ^{192}Os, ^{193}Ir, ^{195}Pt, ^{197}Au). Elements calibrated using the synthetic basalt glass standard GSE-1G as a primary standard (^{29}Si, ^{59}Co, ^{60}Ni, ^{63}Cu, ^{107}Ag, ^{185}Re) are considered semi-quantitative.

Sample runs were bracketed by Po726 (n = 3) and GSE-1G (n = 3) when the spot size was changed or after blocks of 10 sample points were analyzed. Within the sample brackets, one point of Po726, GSE-1G, and GSD-1D were analyzed to ensure consistent data quality. GSE-1G and GSD-1G standard reference concentrations were obtained from the online reference materials database GeoReM (Jochum *et al.,* 2005) while Po726 reference concentrations were obtained directly from the University of Alberta's Arctic Resources Laboratory.

Table 2.2.4 and Figure 2.3.1 summarizes the results of all primary and secondary reference analyses used to calibrate Ru, Rh, Pd, Os, Ir, Pt, and Au.

Reference Material	**^{99}Ru**	**^{103}Rh**	**^{106}Pd**	**^{1932}Os**	**^{193}Ir**	**^{195}Pt**	**^{197}Au**
Po726 (primary)							
Average Measured Value ($\bar{x}$)	36.7	40.3	44.4	42.4	43.2	36.9	46.4
Measured Uncertainty (1σ)	0.74	0.79	0.81	1.00	0.83	1.08	2.15
Reference Value	36.7	40.3	44.3	42.4	43.1	36.8	46.1
Reference Uncertainty (1σ)	0.3	0.1	0.4	1.4	0.3	0.4	2.2
Percent Error (%)	0	0	0.23	0	0.23	0.23	0.75
GSE-1G (secondary)							
Average Measured Value ($\bar{x}$)	-	-	-	-	43.6	34.4	9.44
Measured Uncertainty (1σ)	-	-	-	-	29.7	52.2	1.70
Reference Value	-	-	-	-	120	30	7
Reference Uncertainty (1σ)	-	-	-	-	-	-	4
Percent Error (%)	-	-	-	-	-63.7	14.6	34.8
GSD-1G (secondary)							
Average Measured Value ($\bar{x}$)	-	-	-	-	6.71	6.74	4.34
Measured Uncertainty (1σ)	-	-	-	-	0.60	0.62	0.93
Reference Value	-	-	-	-	12	6	4
Reference Uncertainty (1σ)	-	-	-	-	-	-	-
Percent Error (%)	-	-	-	-	-44.1	12.3	8.44

Table 2.2.4: Summary of LA-ICPMS results of primary and secondary reference material analyses for the calibration of Ru, Rh, Pd, Os, Ir, Pt, and Au. All values are in ppm. Blank reference uncertainties denote values without quoted uncertainty on GeoReM

Measured values from primary standard Po726 agree well with the published literature (Sylvester, 2008), falling within one standard deviations of accepted values (Table 2.2.4; Figure 2.2.1).

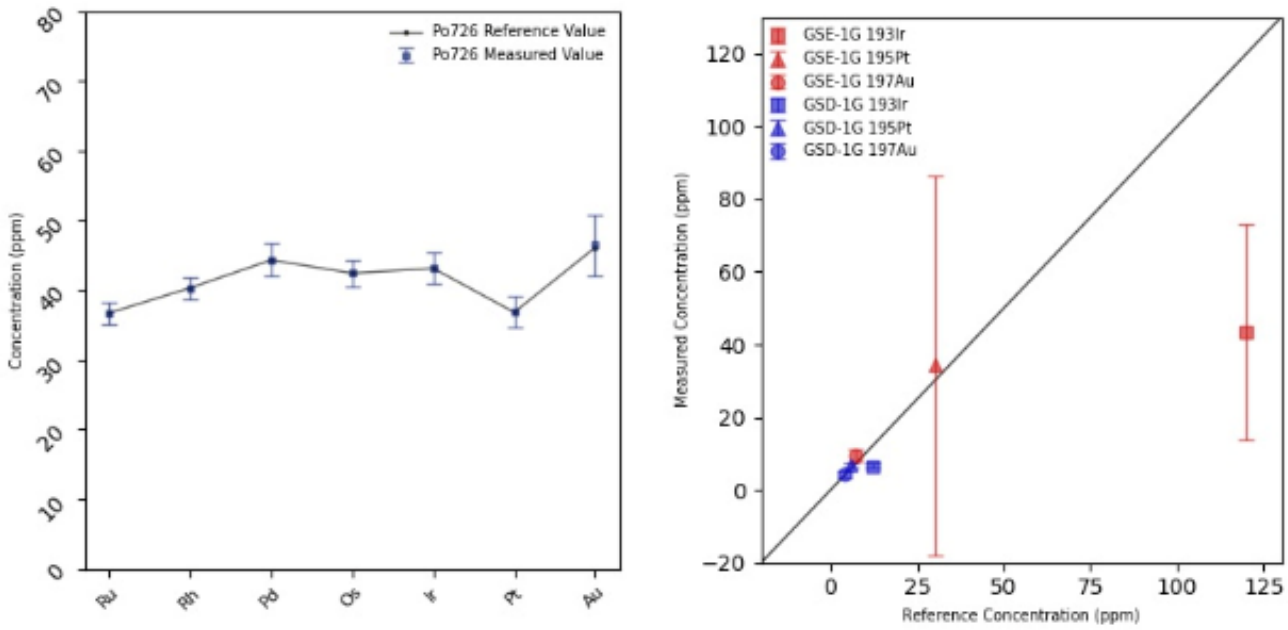

Figure 2.2.1: Summary figures of reference material LA-ICPMS analysis for HSE calibration. Left) Spider diagram of primary standard Po726. The gray line denotes reference concentrations while the blue squares mark the average measured concentrations of all analyses. Error bars are 1SD. Right) 1:1 diagram of secondary standards GSE-1G (red) and GSD-1G (blue). Deviations from the gray 1:1 line indicate concentrations that do not agree with accepted literature values. Error bars are 1SD

The mean value of ^{195}Pt in GSE-1G (34.4 ± 52.2 ppm) agrees closely with the accepted value but has very poor repeatability (151% RSD). ^{193}Ir is significantly lower than accepted values in both GSE-1G (43.6 ± 29.7 ppm) and GSD-1G (6.74 ± 0.60 ppm). However, there is no accepted uncertainty for ^{193}Ir or ^{195}Pt in either of these reference materials. As such, it is unclear whether the mis-match between our analyses and the reference data is caused by poor characterization of the glass reference materials, heterogeneity in their manufacture, and/or the larger contribution of HfO interferences the Ir and Pt mass spectra.

Table 2.2.5 and Figure 2.2.2 summarize the results of all primary and secondary reference analyses used to calibrate Si, Co, Ni, Cu, Ag, and Re.

Reference Material	^{29}Si	^{59}Co	^{60}Ni	^{63}Cu	^{107}Ag	^{185}Re
GSE-1G (primary)						
Average Measured Value ($\bar{x}$)	250919	380	439	379	200	78.9
Measured Uncertainty (1σ)	1552	2.22	6.39	4.72	3.39	1.43
Reference Value	251015	380	440	380	200	78.9
Reference Uncertainty (1σ)	-	20	30	40	20	7.7
Percent Error (%)	-0.04	0	-0.23	-0.23	0	0
Po 726 (secondary)						

Average Measured Value ($\bar{x}$)	-	-	-	-	-	-
Measured Uncertainty (1σ)	-	-	-	-	-	-
Reference Value	-	-	-	-	-	-
Reference Uncertainty (1σ)	-	-	-	-	-	-
Percent Error (%)	-	-	-	-	-	-
GSD-1G (secondary)						
Average Measured Value ($\bar{x}$)	256085	39.3	61.5	41.4	22.8	-
Measured Uncertainty (1σ)	4264	0.76	1.34	1.23	0.52	-
Reference Value	248691	40	58	42	23	-
Reference Uncertainty (1σ)	3739	2	4	2	3	-
Percent Error (%)	3.0	-1.84	6.04	-1.32	-0.8	-

Table 2.2.5: Summary of results of primary and secondary reference material analyses for the calibration of Si, Co, Ni, Cu, Ag, and Re. All values are in ppm. Blank reference uncertainties denote values without quoted uncertainty in GeoReM

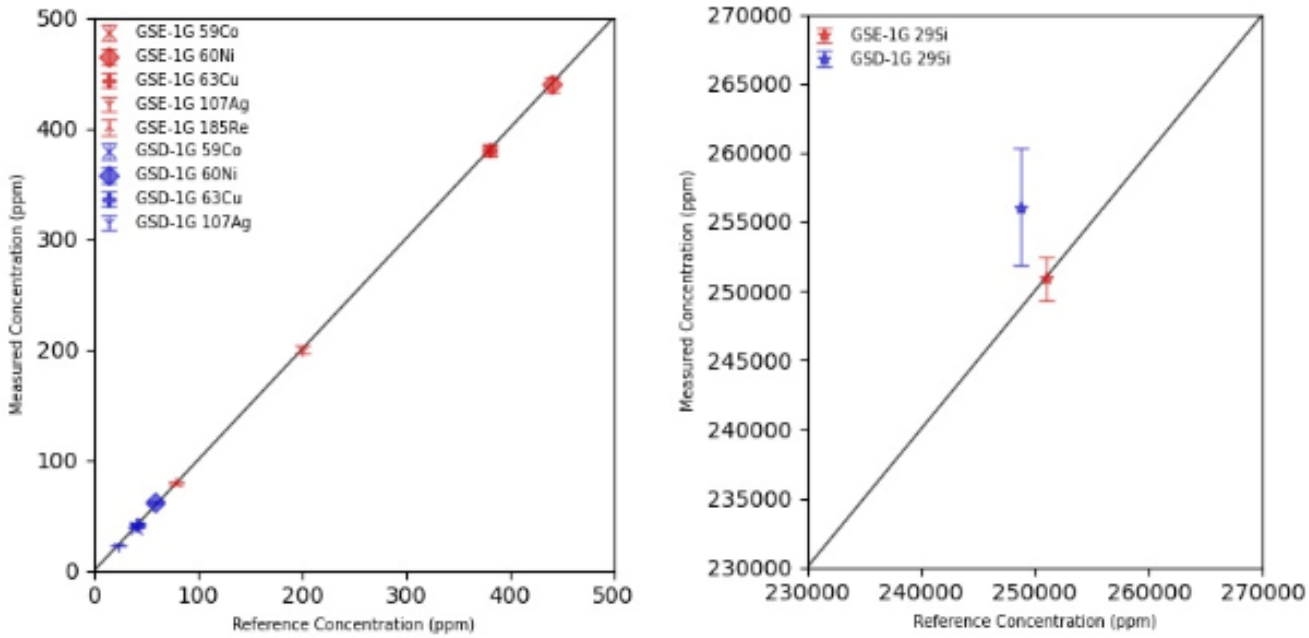

Figure 2.2.2: Summary 1:1 diagrams of primary standard GSE-1G (red) and secondary standard GSD-1G (blue) used to calibrate Si, Co, Ni, Cu, Ag, and Re during LA-ICP-MS analysis. Deviations from the gray 1:1 line indicate concentrations that do not agree with accepted literature values. Error bars are 1SD. Left) Co, Ni, Cu, Ag, Re and Right) Si

Measured values from primary standard GSE-1G agree well with the published literature (Jochum *et al*., 2005), falling within one standard deviations of accepted values (Table 2.2.5; Figure 2.2.2). Results from secondary standard GSD-1G fall within one standard deviation of accepted values. The exceptions to this are ^{29}Si (measured at ~3% above the reference value) and ^{185}Re (not present in GSD-1G).

Signal integration of the time-resolved LA-ICPMS spectra was conducted using the Iolite 3 software package and the "Trace Elements" data reduction scheme. Time-resolved signals were

carefully scrutinized and signal spikes were avoided for data integration and processing. Limits of detection (LOD) were calculated in Iolite 3 using Equation 2.3.1 based on the work of Longerich *et al*., (1996). To be considered for data quantification, unknown values must lie above the limit of quantification (LOQ) (Equation 2.2.1). For plotting, all values below LOQ were replaced with $\frac{1}{2}$LOD. For tabulation and statistical analysis, unknown values below LOQ are marked as such and are not used for the calculation of descriptive statistics.

	^{59}Co	**^{60}Ni**	**^{63}Cu**	**^{99}Ru**	**^{103}Rh**	**^{106}Pd**	**^{107}Ag**	**^{185}Re**	**^{192}Os**	**^{191}Ir**
Mean LOQ (ppm)	0.2	5.7	0.4	0.3	0.08	0.7	1.8	0.02	0.03	0.05
Total Analyses	34	34	34	34	34	34	34	34	34	34
	^{195}Pt	**^{197}Au**								
Mean LOQ (ppm)	0.1	0.08								
Total Analyses	34	34								

Table 2.2.6: Mean LOQ values for each LA-ICPMS analyte. All concentrations are in ppm.

All elements in sulphide runs have mean LOQ values below 1 ppm (Table 2.2.6). The exception to this is ^{60}Ni which reaches wt. % levels in most sulphide grains and thus shifts the LOQ to higher values. Several analytes (^{185}Re, ^{192}Os, ^{191}Ir, ^{197}Au) have mean LOQ in the 10's of ppb range while others are in the 100's of ppb range.

Due to the complex nature of mantle sulphide phases, we compared the concentrations of ^{60}Ni between EPMA and laser ablation analytical sessions to ensure a composition representative of the target mineral was obtained (Figure 2.2.3). A maximum deviation between the two values of 25% was used in order for the analysis to be considered representative. Most Ni concentrations returned from ablation are lower than their respective EPMA values. This is likely due in part to the semi-quantitative nature of the LA-ICP-MS Ni data (calibrated with GSE-1G) as well as the

inclusion of silicate material from serpentinized cracks within grains which dilutes the Ni signal. Only analytical points with less than 50,000 ppm Si were considered in the results.

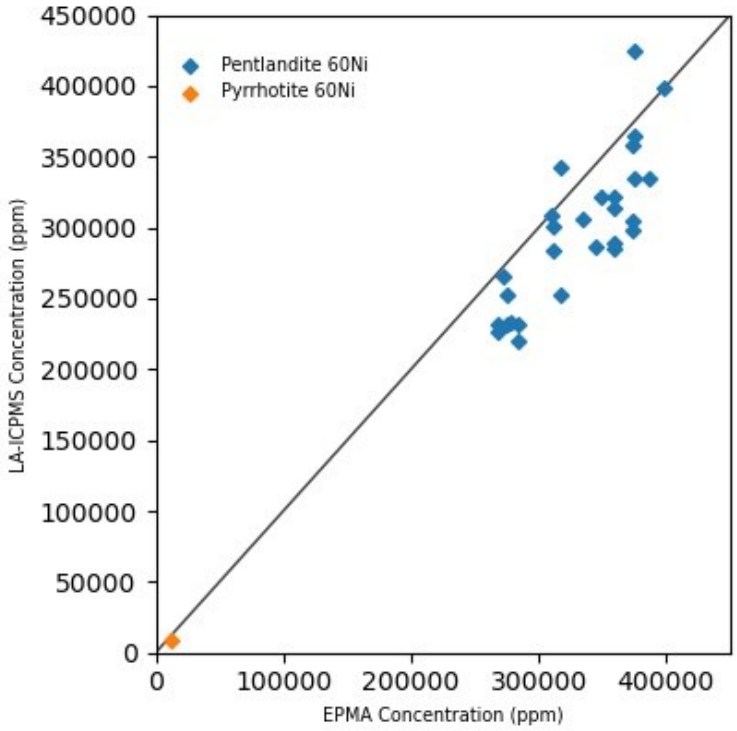

Figure 2.3.3: 1:1 diagram of Ni concentration from LA-ICPMS analysis vs internal calibration values from EPMA analysis. Deviations from the grey line indicate differences between LA-ICPMS and EPMA values.

Several mixed phases were ablated including heazlewoodite-pentlandite, chalcopyrite-pentlandite, and magnetite-pentlandite when the isolation of a single sulphide phase was not possible (similar to the methods of Lawley *et al.,* 2020). All mixed phase analyses are highlighted in Appendix B.2.2. We discuss the implications of mixed phase analysis as well as other analytical challenges in Section 2.4.1.

2.2.4 X-Ray Fluorescence (XRF)

Whole rock powders were prepared for bulk chemistry analysis with equipment provided by the University of Alberta. Samples were washed in a sonicator bath of deionized water for approximately 10 minutes and allowed to dry completely. Samples were pre-crushed with rubber mallets and paper wrapping before being added to an agate ball mill and pulverized until the powder was able to pass through an 80-mesh sieve screen. Prepared powders were analyzed for

major and trace elements at the X-Ray Laboratory at Franklin and Marshall College, Lancaster Pennsylvania according to methods viewable in Mertzman (2015) (briefly summarized here).

10 major elements (SiO_2, TiO_2, Al_2O_3, $Fe_2O_3^T$, MnO, MgO, CaO, Na_2O, K_2O, P_2O_5) were analyzed using a PANalytical 2404 X-ray fluorescence vacuum spectrometer equipped with a PW2540 X-Y sample handler and a 4 kW Rh super sharp X-ray tube. 0.4000 ± 0.0001 g of whole rock powder was mixed with 3.6000 ± 0.0002 of $Li_2B_4O_7$ and heated in a platinum crucible with a meeker burner until molten. Molten material was then quenched to a glass disk. Samples were calibrated using working curves based on rock standards from Abbey (1983) and Govindaraju (1994). Between 30 and 50 data points were collected for each working curve and elemental interference corrections were applied.

19 trace elements (Rb, Sr, Y, Zr, V, Ni, Cr, Nb, Ga, Cu, Zn, Co, Ba, La, Ce, U, Th, Sc, Pb) were analyzed using the same XRF setup described above. 7.0000 ± 0.0004 grams of whole rock powder was mixed with 1.4000 ± 0.0002 high purity copolywax powder for 10 minutes and then pressed (3 minutes at 50,000 psi) into a briquette. Samples were calibrated using the same method described above for major elements. The Rh Compton peak was used as a mass absorption correction for Group 1 elements.

2.2.5 Isotope Dilution Inductively Coupled Plasma Mass Spectrometry (ID-ICP-MS)

Samples were analysed for PGE abundances and Re-Os isotopes using isotope dilution techniques at the Arctic Resources Laboratory, University of Alberta. All samples are processed in a better than Class 100 ULPA-filtered clean lab with open samples handled in better than class 10 ULPA filtered combined laminar flow/exhaust hoods.

For each sample, approximately 1 g of whole rock powder (prepared according to the methods outlined in Section 2.2.4) and 10-20 mL of a PGE spike, isotopically enriched in ^{99}Ru, ^{106}Pd, ^{185}Re, ^{190}Os, ^{191}Ir, and ^{194}Pt, were added to 30 mL quartz glass vials. Inverse aqua regia (2 mL conc. HCl ; 5 mL conc. HNO_3) was added to the vials. All acids used in this study are of Fisher Trace Metal Grade further purified in Savillex Teflon cupola stills. The nitric acid is sparged after distillation to further reduce Os blank. The vials were closed with quartz lids and a semi-permeable Teflon seal, then heated to 260 °C at a containing pressure of ~130 bar for 16 hours in

an Anton-Paar high pressure asher system (HPA-S). This effectively digests residual PGE bearing phases whilst equilibrating the spike and sample, which compensates for any future loss of PGE/Os during chemistry. Os was separated from the other PGE using a $CHCl_3$ triple solvent extraction, back extracted into HBr (Cohen and Waters, 1996), and purified by micro-distillation (Birck et al., 1997). Following Os extraction, the aqua regia was dried before converting Re and the other PGEs to chloride form by drying repeatedly in HCl. Matrix separation was achieved using anion exchange chromatography modified from Pearson and Woodland (2000).

Os isotopes and abundances were measured using negative thermal ionization mass spectrometry (N-TIMS) on a Thermo Fisher Triton Plus at the ARL. A $Ba(OH)_2$ activator was used on all samples and standards. All samples in this study were analysed by peak hopping on a secondary electron multiplier (SEM). Mass fractionation was corrected to $^{192}Os/^{188}Os = 3.082614$. Accuracy and precision of the Os isotope analyses in this study was assessed by analyzing a DrOsS standard at the start and end of each measurement session and comparing this to the long term laboratory mean values of $^{187}Os/^{188}Os$ (0.16083 ± 0.00028; 2σ absolute; n = 39; 2σ relative = 1.8‰) which have been ascertained over several years through repeated measurements of the DrOsS standard. The mean $^{187}Os/^{188}Os$ for DrOsS standards measured in this study is identical within the stated level of precision, to the accepted value of 0.160924 ± 0.00004 (Luguet et al., 2008), hence the Os isotopic data are considered accurate at this level of precision. All samples are corrected for an Os blank of 40fg which comes primarily from the Pt filament material used (H-Cross).

PGE and Re abundances were measured on a Nu Attom ICP-MS at the ARL, using a standard peltier-cooled, cyclonic, glass spray chamber. Mass fractionation was corrected externally using synthetic 1 ppb PGE standards. Blank corrections are minor for Ir, Re, Ru, and Pd being on the order of 5pg/g or less. Blanks are slightly higher for Pt, typically in the order of 20pg/g. Blanks are calculated by passing spiked acids through the total procedure; asher digestion through anion chemistry, to acquire a realistic total procedural blank. As spike lost through the procedure will inflate the apparent “blank”, the blank estimates are considered maxima.

Accuracy of the PGE abundance measurements (including Os) was monitored by analysis of an OKUM standard alongside this sample set. Long term data and the OKUM standard measured

for this study overlaps previously published data for the OKUM standard within 2σ, and the data is considered accurate at this level of precision (Waterton *et al.* 2021).

All data was processed using in-house spread sheets developed specifically for PGE and Os isotopic analysis at ARL (Pedro Waterton, 2018, unpublished). The PGE spreadsheet uses a robust fashion outlier filter on primary signal intensity data (Median Absolute Deviates) and further incorporates oxide interference corrections, mass bias corrections, total procedural blank corrections, statistical analysis of the quality of standard reproducibility during the runs and quality of the spike to sample ratio achieved. In the Os isotopic sheet, errors are fully propagated including uncertainties in the measured Os and Re isotopic ratios, oxide and interference corrections, background correction (for the ICP-MS data) fractionation correction, spike unmixing calculations, spike isotopic composition and concentration, and long term variability in the DrOsS and PGE synthetic standards.

2.3 Results

2.3.1 Petrography

Thin section images of each sample are provided in Appendix C. Table 2.3.1 summarizes the modal abundances of primary phases organized by rock classification type while Table 2.3.2 summarizes observed sulphide phases and their major textures.

Rock Type and Sample Number	Ol	OPX	CPX	Gt	Spn	Phl	Krc	Prg	Ilm	Rut	Acc
Garnet Phlogopite Peridotite											
JAG1	43	26	8	22	-	1	-	-	-	-	Prg
Phlogopite Peridotite											
17MON 004	52	13	33	-	-	2	-	-	-	-	Chr
Spinel Lherzolite											
LZM-001 Host	71	15	8	-	3	-	-	3	-	-	-
LZM-001 Vein	-	-	-	-	-	10	-	90	-	-	Cal

Rock Type and Sample Number	Ol	OPX	CPX	Gt	Spn	Phl	Krc	Prg	Ilm	Rut	Acc
PIC											
UIB-2	-	-	54	-	-	28	-	-	18	-	Zir, apt, cal
MARID											
AJE-326	-	-	-	-	-	34	63	-	3	-	Cal, apt, Bar,OPX
AJE-335	-	-	13	-	-	85	-	-	>1%	2	pvsk
AJE-2422	-	-	-	-	-	22	69	-	6	2	Zir, cal
KDB-20	-	-	-	-	-	93	-	-	7	-	Pvsk, gt, ttn

Table 2.3.1: Summary modal abundances (in percentage) of primary phases in metasomatized mantle xenoliths from this study. Abbreviations: Ol – olivine, OPX – orthopyroxene, CPX – clinopyroxene, Gt – garnet, Spn – spinel, Phl – phlogopite, Krc – potassic richterite, Prg – pargasite, Ilm – ilmenite, Rut – rutile, Chr – chromite, Cal – calcite, Zir – zircon, Apt – apatite, Bar – barite, Pvsk – perovskite, Ttn – titantie

Rock Type and Sample Number	Phases Observed	Major Textures
Garnet Phlogopite Peridotite		
JAG1	Pentlandite; Heazlewoodite	Interstitial to grain boundaries; Overgrowths on pentlandite grains
Phlogopite Peridotite		
17MON 004	Pentlandite; Bornite; Pt-rich alloy	Interstitial to grain boundaries; Needle-like ingrowths in pentlandite; Sub-micron inclusions in pentlandite
Spinel Lherzolite		
LZM-001 Host + Vein	Pentlandite	Host: Enclosed in olivine and interstitial to olivine/opx. Vein: Enclosed within amphibole and phlogopite
PIC		
UIB-2	Pentlandite; Chalcopyrite; Pyrrhotite	Enclosed in CPX; Micron intergrowths of chalcopyrite-pentlandite
MARID		
AJE-326, AJE-335, AJE-2422, KDB-20	Pentlandite; Heazlewoodite; Chalcopyrite/Cu metal	Interstitial to grain boundaries; Cu-rich phases intergrown with pentlandite

Table 2.3.2: Summary of observed sulphide phases and their major textures in metasomatized mantle xenoliths from this study

JAG1: Garnet Phlogopite Peridotite (GPP)

Sample JAG1 is a fresh lherzolite composed of olivine, orthopyroxene, garnet, and clinopyroxene with minor phlogopite from the Jagersfontein Mine, South Africa. The sample displays a coarse texture with no visible foliation or shearing. Grain sizes average 3-10 mm and are subhedral-euhedral. Garnets are typically the largest mineral phase (5-8 mm) and lack the kelyphite rims that are common in many coarse-grained xenoliths (Winterburn *et al.,* 1990). Clinopyroxene is in high abundance (~8.5%) compared to average Kaapvaal craton GPP xenoliths (2-4%; Boyd and Nixon 1978). Olivine is the most abundant phase and commonly shows undulose extinction. Olivine grains are frequently fractured and filled with secondary serpentine. Primary phlogopites are tabular crystals ranging from 0.5-2.5 mm. and display alteration to chlorite or serpentine along cleavage planes.

Sulphide minerals in the GPP xenolith tend to occur in close spatial association with hydrous phases such as phlogopite (Appendix C). These grains primarily occur interstitial to grain boundaries (Type-i; Lorand and Luguet 2016), within serpentinized fractures of olivine, or as small (< 10 μm) crystals within serpentinized veins crosscutting the xenolith. Grains occuring interstitially or within olivine fractures range from less than 100 μm to 500 μm and are pentlandites that have largely been altered to heazlewoodite and magnetite (Figure 2.3.3 A). Pentlandite remnants are typically concentrated around the edges of these grains.

17MON 004: Phlogopite Peridotite (PP)

17MON 004 is a lherzolite comprised of olivine, clinopyroxene, orthopyroxene, and phlogopite with chromite being the primary oxide phase. The sample displays a coarse texture with no visible foliation or shearing. Infiltration channels (of fluid/melt?) altered portions of the xenolith leaving behind cryptocrystalline groundmass and occasional remnant cores of olivine and orthopyroxene grains (Appendix C). Olivine (1-7mm) is the most abundant phase and exhibits rare undulose extinction. Clinopyroxene (2-10 mm) abundance is anomalously high and varies widely between thin sections (21 – 55 % modal abundance). Clinopyroxene grains commonly display exsolution lamellae of orthopyroxene and co-genetic intergrowths of metasomatic phlogopite (Figure 2.3.2 F). This may indicate that a portion of the observed clinopyroxene has a metasomatic origin (e.g., Gregoire *et al.,* 2002). Chromite commonly shows spatial association

with clinopyroxene. Primary phlogopite occurs as tabular crystals (0.25-2mm) in textural equilibrium with nearby phases.

Sulphide minerals in the PP xenolith are large grains (typically ~ 500 µm) of well crystallized pentlandite (Figure 2.3.3 B). Grains are interstitial to clinopyroxene and olivine and are typically connected to networks of fractures in the mineral assemblage. In contrast to the GPP xenolith, low-T heazlewoodite alteration is not observed. Grain sizes range from 26 µm to over 700 µm with the majority being greater than 100 µm. Two pentlandite grains showed occasional, needle-like inclusions of bornite. Several micron-scale inclusions of a Pt-rich phase were observed in a large, well-formed pentlandite grain (Figure 2.3.1; Figure 2.3.3). These inclusions are generally less than 2 µm wide with an EDS spectra suggesting a composition of Pt metal or a Pt-(Fe,Ni) alloy phase (Appendix C).

Figure 2.3.1: Wavelength dispersive spectroscopy (WDS) image of Pt-rich "micro-nuggets" in 17MON 004 pentlandite

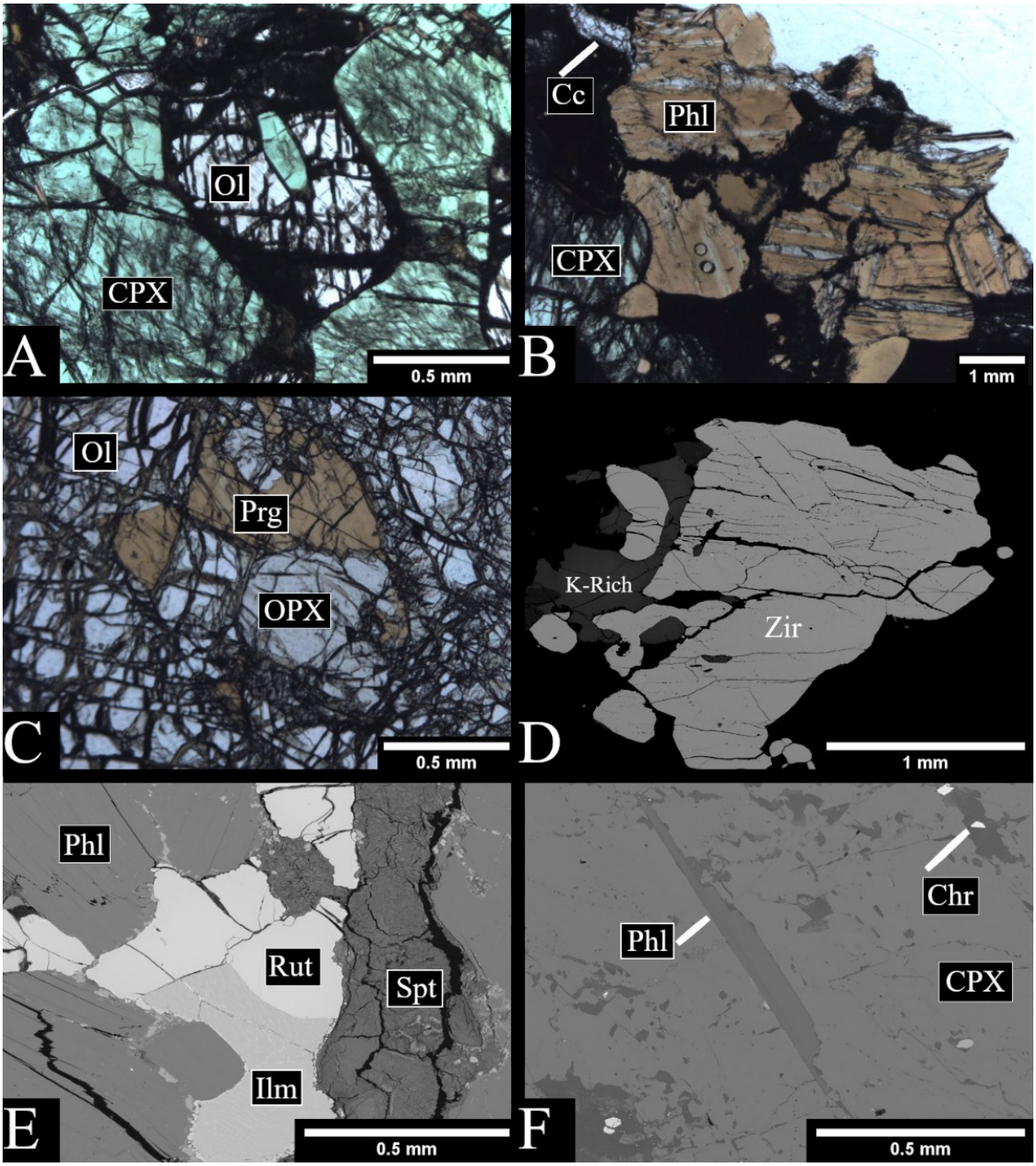

Figure 2.3.2: Optical microscopy and BSE images of select silicate and oxide phases in metasomatized xenoliths from this study. A) Coarse-grained olivine and diopside highlighting poikilitic texture in sample 17MON 004 (PPL). B) Phlogopite with calcite along cleavage planes in PIC xenolith UIB-2 (PPL). C) Thin titanian pargasite overgrowth on porphyroblastic olivine in spinel lherzolite LZM-001 (PPL). D) Large, subhedral zircon in MARID xenolith AJE-2422 (BSE). E) Co-crystallized ilmenite and rutile in MARID xenolith AJE-2422 (BSE) F) Phlogopite enclosed within clinopyroxene in sample 17MON 004 (BSE).

LZM-001: Veined Spinel Lherzolite

Sample LZM-001 is a spinel facies lherzolite with a 15 mm vein of coarsely crystallized amphibole + phlogopite that crosscuts the peridotite assemblage.

The LZM-001 lherzolite host is predominantly porphyroclastic olivine. Larger grains of olivine display undulose extinction that are absent in neoblasts. Orthopyroxene tends to occur in clusters of subhedral crystals while clinopyroxene is evenly distributed. Pargasite amphibole occurs infrequently (< 1%) as overgrowths on olivine (Figure 2.3.2 C), providing textural and mineralogical evidence that the veining agent has infiltrated and altered the lherzolite host. Pargasite grains are observed disseminated within the sample but are more frequent proximal to the vein boundaries. Spinel is the main aluminous phase and occurs as mm-scale anhedral grains in spatial association with orthopyroxene.

The 15 mm crosscutting vein has sharp, well-defined boundaries and is mainly composed of pargasite amphibole that increases in grain size towards the center of the vein (0.5 – 6 mm). Phlogopite occurs as small (< 1 mm) overgrowths on the edges of amphibole crystals as well as larger (3 mm), solitary crystals. Multiple thin (< 1 mm) veins of carbonate cut across the vein minerals and terminate at the border with the lherzolite host.

BMS grains within the host and vein of LZM-001 are pentlandites that do not show any low-T alteration. Pentlandite grains are more abundant within the vein of LZM-001 and range in size from 50 µm to 250 µm. Vein pentlandites are exclusively enclosed in silicate phases (type-e; Lorand and Luget 2016) with complex polyhedral shapes and smoothly curving grain boundaries common in pargasite-hosted grains (Figure 2.3.4 A). Pentlandite grains within the host lherzolite usually occur in interstitial spaces of fractured olivine grains. Polyhedral shapes occuring at the triple junction of olivine and orthopyroxene are common (Figure 2.3.4 B) and may indicate "wetting textures" of an immiscible sulphide melt adsorbing to the edges of pre-existing silicate phases (Lorand and Luget 2016). The host pentlandites are typically smaller than their vein counterparts and range in size from 50 µm to 210 µm.

UIB-2: Phlogopite-Ilmenite-Clinoyproxene (PIC)

Sample UIB-2 is a coarse-grained rock predominantly composed of clinopyroxene and ilmenite. Clinopyroxene ranges from 1-3 mm and is subhedral-anhedral. Similar to other xenoliths in this

study, UIB-2 shows evidence of infiltration from a potential fluid or melt (Appendix C). Clinopyroxene grains are partially dissolved leaving cryptocrystalline groundmass and occasional small remnant cores.

Phlogopite forms large (0.5-5 mm), tabular crystals that are unevenly distributed in clusters. Phlogopites grains frequently contain thin veinlets of calcite/apatite oriented along cleavage planes (Figure 2.3.2 B) and lack the serpentine-chlorite alteration observed in the GPP and PP xenoliths.

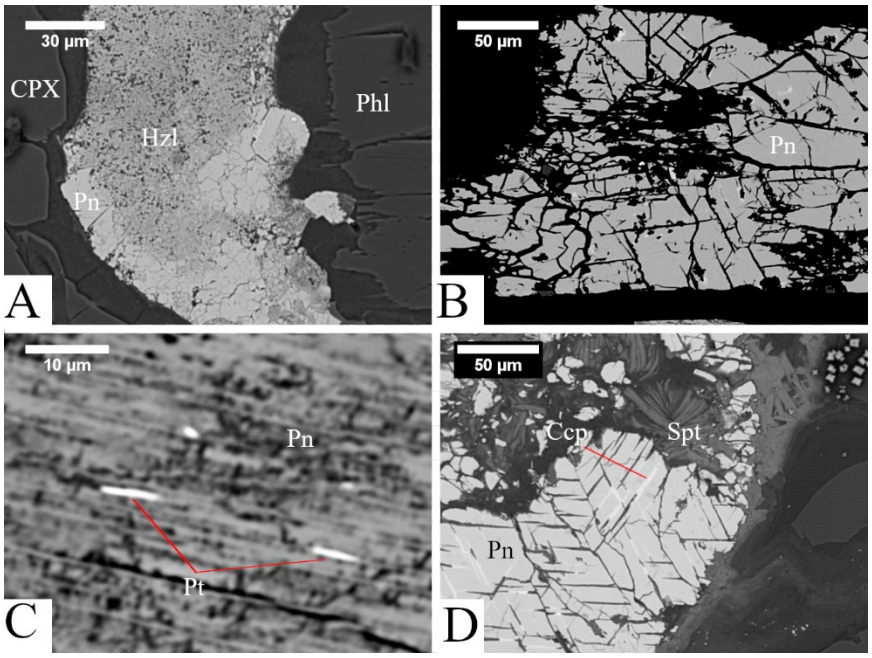

Figure 2.3.3: Back-scattered electron images of sulphides from samples JAG1 and 17MON 004. (A) JAG1- Large pentlandite (Pn) grain showing alteration to heazlewoodite (Hzl) towards the center. Grain located interstitial to phlogopite (Phl) and clinopyroxene (CPX). (B) 17MON 004- Well crystallized pentlandite showing distinct lack of low T alteration. (C) 17MON 004- Pt-rich "micro-nuggets" (Pt) in pentlandite. (D) 17MON 004 – Pentlandite with intergrowths of chalcopyrite (Ccp). Serpentine (Spt) fills fractured areas of the grain

Ilmenite (0.3 – 4 mm) is evenly distributed throughout the sample and occasionally displays minor intergrowths of rutile. Ilmenite infrequently occurs as small (<1mm) inclusions within clinopyroxene. Rutile also occurs as sub-mm inclusions inside clinopyroxene. We also observed several small (~10 µm) grains of un-zoned, euhedral zircons.

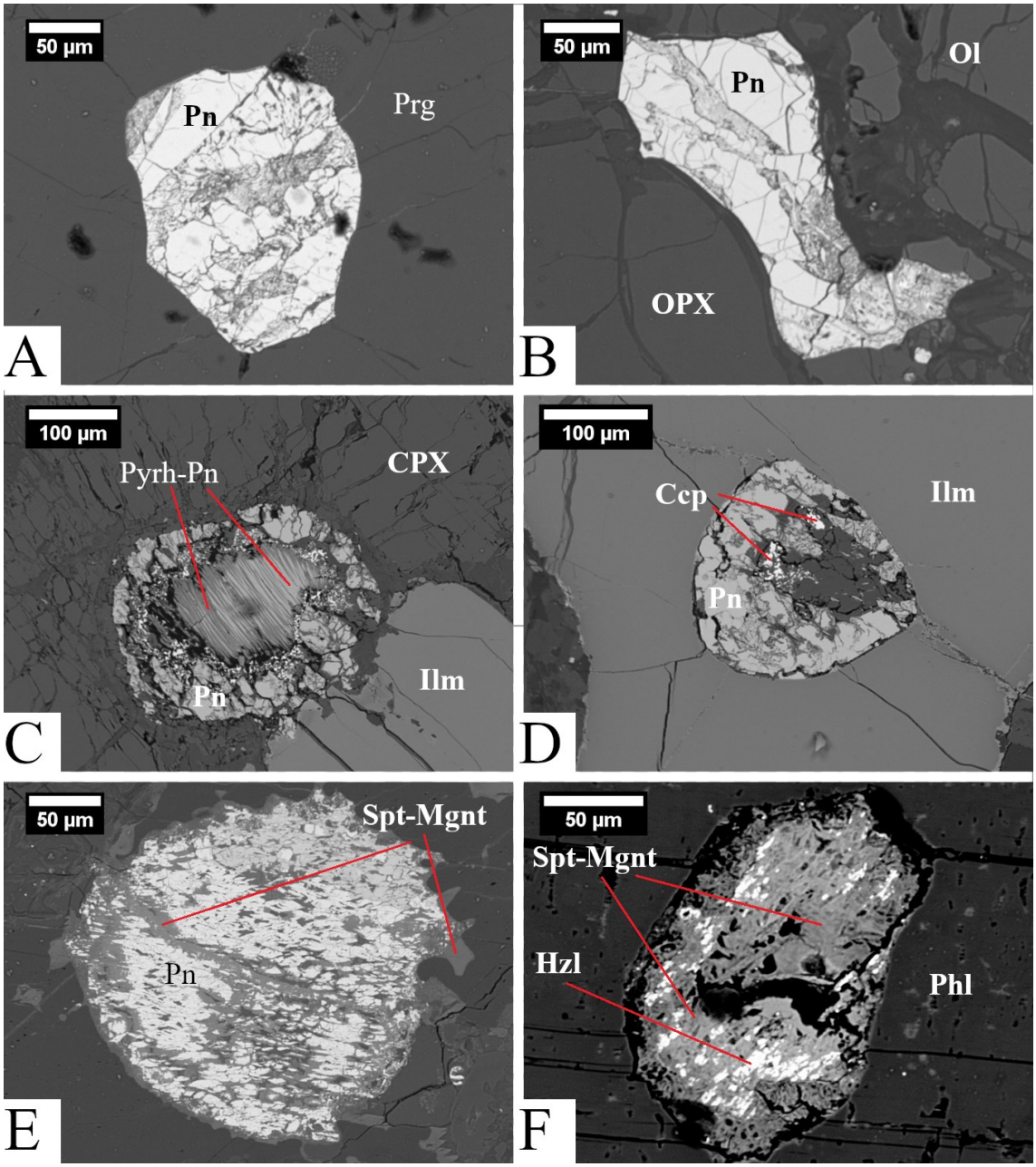

Figure 2.3.4: BSE images of sulphide grains in: (A) LZM-001 Vein – Pentlandite (Pn) enclosed within pargasite (Prg) (B) LZM-001 Host – Polyhedral pentlandite curving around grain boundary of orthopyroxene (OPX) (C) UIB-2 – pentlandite with pyrrhotite (Pyrh) exsolution at the junction of clinopyroxene (CPX) and ilmenite (Ilm) (D) UIB-2 - sulphide grain enclosed in ilmenite with pentlandite and minor chalcopyrite (Ccp) (E) AJE-326 – Pentlandite in serpentine near phlogopite grain boundaries. Grain displays alteration to serpentine-magnetite (Spt-Mgnt) in fractures (F) Heazlewoodite (Hzl) enclosed in phlogopite. Note the direct connection to cleavage planes of the phlogopite. Most of the grain has been overprinted by a serpentine-magnetite assemblage

The sulphides in the PIC xenolith range from 120 µm to 290 µm. Most grains are hosted within clinopyroxene with one grain observed within a large ilmenite crystal (Figure 2.3.4 D). Enclosed

sulphide grains are commonly surrounded by a network of fractures radiating through the host silicate or oxide crystal. Most grains are fractured and mixed with serpentine, magnetite or a combination of primary suphide and low-T alteration phases. One grain displays a thick rim of well crystallized pentlandite with a core of striped BMS caused by exsolution of pentlandite to pyrrhotite (Figure 2.3.4 C).

AJE-326: Mica-Amphibole-Rutile-Ilmenite-Diopside (MARID)

Sample AJE-326 is a coarse-grained MARID xenolith composed of k-richterite, phlogopite and ilmenite but no rutile or clinopyroxene. The modal abundances of these minerals agree with values from this sample in Fitzpayne *et al*., (2018). K-Richterite forms the largest grains (0.5-3 mm) and shows a poikilitic texture with phlogopite chadacrysts (Appendix C). Phlogopite also occurs as 0.1-1.5 mm subhedral grains that lack alteration to chlorite-serpentine. Ilmenite in sample AJE-326 ranges in size from 0.5-1 mm and lacks rutile intergrowths. Several areas show evidence of fluid/melt infiltration similar to other xenoliths in this study (cryptocrystalline groundmass + remnant cores of primary minerals).

Sulphide grains in AJE-326 show two populations. The first population contains large (> 100 μm) interstitial grains of pentlandite that are strongly altered to a low-T assemblage of heazlewoodite, serpentine, and magnetite. Figure 2.3.4 (E) shows a ~ 0.5 mm grain from this population. Remnant fragments of the original pentlandite are commonly surrounded by low-T minerals. The second population is small (< 100 μm) anhedral grains of heazlewoodite commonly found in areas where there is evidence of fluid/melt infiltration. This second population is unlikely to be part of the original mantle BMS assemblage and may have precipitated from the infiltrating fluid/melt. We do not consider this population further.

AJE-335: MARID

Sample AJE-335 is a coarse-grained MARID xenolith with no visible foliation. It is composed of phlogopite, clinopyroxene, rutile, and ilmenite with no amphibole. The modal abundances calculated here agree with values from this sample in Fitzpayne *et al*., (2018). Phlogopite is the dominant mineral phase (~85%) and it occurs as euhedral-subhedral grains ranging in size from 0.5-3.5 mm. Clinopyroxene grains are subhedral-anhedral and occur in mm-scale patches (Appendix C). Clinopyroxene grains in AJE-335 have spongy rims which suggests they have

been altered by an infiltrating fluid or melt (Carpenter *et al*., 2002). Ilmenite and rutile typically form subhedral, sub-mm grains interstitial to phlogopite. These two phases are commonly intergrown (Figure 2.3.2 E).

Sulphide grains are rare in AJE-335. Only two grains larger than 50 μm were observed and both showed degradation to a low-T mineral assemblage of serpentine/magnetite/heazlewoodite (e.g., Figure 2.3.4 F). Most sulphides are interstitial to silicate grains with the exception of one 150 μm grain enclosed in phlogopite (Figure 2.3.4 F).

AJE-2422: MARID

Sample AJE-2422 is a coarse-grained MARID xenolith with no fabric/shearing. It is composed of k-richterite, phlogopite, ilmenite, and rutile with no clinopyroxene. The modal abundance of primary phases calculated here is significantly different than values from this sample in Fitzpayne *et al*., (2018). K-richterite is the dominant phase (69.1%) in this study compared to phlogopite being the dominant silicate mineral (86%) in Fitzpyane *et al*., (2018). This extreme phase heterogeneity is commonly observed in MARID xenoliths (e.g., Dawson and Smith 1977; Gregoire *et al*., 2002) and highlights the difficulty in determining a typical "bulk MARID" composition (Fitzpayne *et al*., 2018).

K-richterite occurs as subhedral-euhedral grains ranging in size from 0.5-3.5 mm. They show good 45° amphibole cleavage (Appendix C) and minor serpentinization in fracture planes. Phlogopite occurs in mm-scale patches of euhedral-subhedral, tabular grains ranging in size from 0.1-0.5 mm. Phlogopite also occasionally occurs poikilitically enclosed by k-richterite. Ilmenite and rutile in AJE-2422 consistently occur as co-crystallized grains in close proximity to each other. Ilmenite grains show small "stringers" of intergrown rutile while rutile grains do not contain ilmenite intergrowths (Appendix C). AJE-2422 also contains five mm-scale subhedral zircon grains in textural equilibrium with other primary phases (Figure 3.1.1 D). Zircons are analyzed in greater detail in Chapter 3 of this study.

Similar to other MARID xenoliths in this study, sulphide grains in AJE-2422 are compositionally variable on the micron scale and show extreme alteration to low-T mineral assemblages. Occasional small grains (~75 μm) of pentlandite occur interstitial to silicate phases and usually contain significant serpentine/magnetite. Sample AJE-2422 contains a higher proportion of Cu-

sulphides (chalcocite/chalcopyrite/bornite) which occur as discrete grains or needle-like intergrowths within Fe-Ni sulphides. Several small (~20 μm) grains of Cu metal were also observed near a cluster of Cu-sulphides.

KDB-20: MARID

Sample KDB-20 is a small (~3 cm) MARID xenolith that is in direct contact with volcanic material from the host kimberlite (Appendix C). The contact between kimberlite and MARID material is often diffuse with large portions of the MARID xenolith being disturbed by an infiltrating fluid/melt. This results in the outer portion (~0.5 cm) of the xenolith being largely amorphous, cryptocrystalline groundmass. The center portion is dominantly composed of subhedral-euhedral phlogopite (0.1-1 mm) with minor amounts of subhedral ilmenite (0.1-0.5 mm). There is no rutile, amphibole, or clinopyroxene in sample KDB-20.

Sulphides within KDB-20 are exclusively heazlewoodite and are found in both the kimberlite and MARID portion of the sample as well as within the amorphous zone affected by melt infiltration. Only heazlewoodite grains in the MARID portion of the sample are considered in the results of this study. MARID heazlewoodites are small, rounded grains (~30-50 μm) that occur interstitial to phlogopite. Heazlewoodite grains often occur intergrown with small needles of phlogopite indicating that they may have precipitated from the same fluid/melt (Appendix C).

2.3.2 Major Element Mineral Chemistry

Tabulated major element mineral chemistry for silicate and oxide mineral phases are presented in Appendix B.0.1 while sulphide phases are presented in Appendix B.0.2

Silicate and Oxide Phases

Olivines in the different suites of metasomatized peridotites are distinguished by their concentration of FeO^T and Mg numbers (100 * Mg/ Mg + Fe). Olivine Mg number is representative of the bulk rock in peridotites and commonly used as an index of melt depletion or metastomatic reenrichment (e.g., Pearson *et al*., 2003). The least modally metasomatized xenolith in this study (GPP – JAG1) contains olivine with the highest average Mg # (91.17 ± 0.06) while the most modally altered sample (PP- 17MON 004) has the lowest (88.4 ± 0.01). The Lherz spinel lherzolite sample is intermediate between these two values (89.7 ± 0.02).

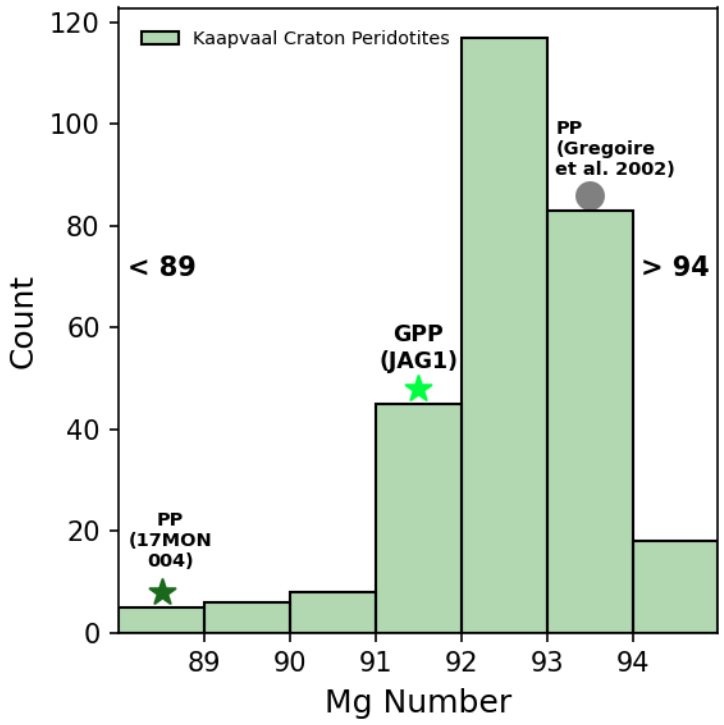

Figure 2.3.5: Mg # in olivines from Kaapvaal craton granular peridotites compared to Kaapvaal-derived metasomatized peridotites from this study. Data for Kaapvaal craton peridotites are from Janney *et al*., (2010) and references therein. A PP lherzolite from Gregoire *et al*., (2002) is also included for comparison.

Figure 2.3.5 compares these values to a literature compilation of olivines in Kaapvaal craton peridotites. The PP xenolith from this study plots at the low end of recorded olivine Mg #. Olivine in a PP xenolith from Gregoire *et al*., (2002) is also plotted for comparison and displays a significantly higher Mg # (93.8). Olivines in the GPP xenolith from this study are within the typical range of Kaapvaal peridotites.

Orthopyroxenes in the metasomatized peridotites analyzed here mirror this trend with decreasing Mg # with an increasing proportion of metasomatic phases (Appendix B.0.1). Orthopyroxenes from GPP and PP lithologies are also Al_2O_3 poor (< 0.70 wt. %) in contrast to the aluminous grains in the spinel lherzolite (3.94 ± 0.27 wt. %) that are typical of spinel facies peridotites (Pearson *et al.,* 2003).

Garnet is found only in the GPP xenolith and are classified as "peridotitic" (Grütter *et al*., 2004). They can be further defined as "lherzolitic" (G9) garnets based on their Cr_2O_3-CaO systematics (Grütter *et al*., 2004; Figure 2.3.6).

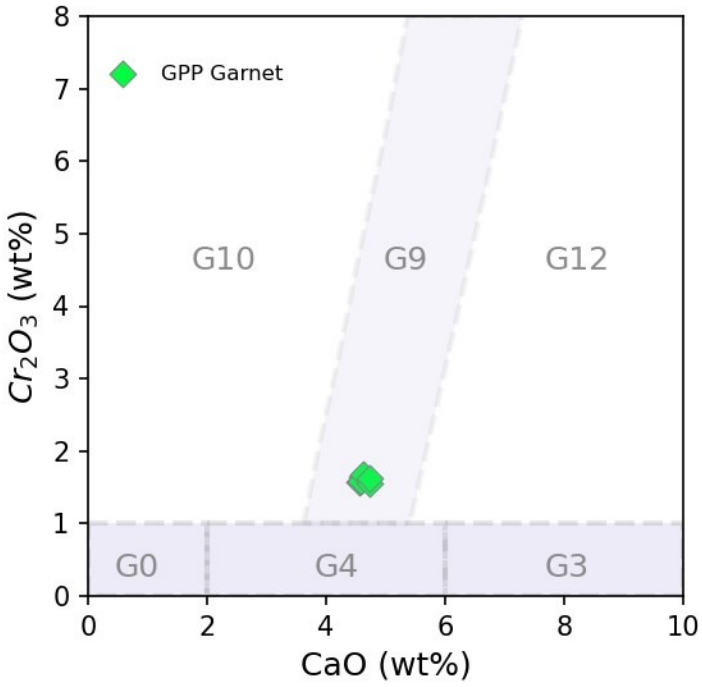

Figure 2.3.6: Garnet classification scheme modified after Grütter *et al*., (2004). GPP garnets in the "G9" field were separated from "G5" garnets (field not shown) due to Mg #'s > 70

Clinopyroxenes in the metasomatized peridotites are diopsides with average Ca #'s (100 * Ca/(Ca + Mg)) of 48.14 ± 0.21, 48.56 ± 0.22, and 51.39 ± 0.14 in the GPP, PP, and spinel lherzolite xenoliths respectively (Figure 2.3.8). PIC clinopyroxene is also diopside (Ca # of 48.14 ± 0.07; Figure 2.3.7) while MARID clinopyroxene (only found in AJE-335) shows considerably more variation (Ca # 44.36 – 50.15). MARID clinopyroxene is primarily augite with two analyses lying in the diopside compositional field (Figure 2.3.7). The CaO-MgO systematics reported here are significantly different than the results obtained from Fitzpayne *et al.,* (2018) which showed more subcalcic PIC clinopyroxenes and a much more limited range in MARID Ca #s. This difference appears to be driven primarily by variability in FeO^T within the MARID clinopyroxenes. FeO^T in MARID clinopyroxene is significantly higher than the other xenoliths in this study while PIC clinopyroxene displays values more typical of peridotites (Figure 2.3.7). PIC clinopyroxenes displays a more refractory-like Mg # (92.0 ± 0.14) than MARID clinopyroxene (83.5 ± 1.7).

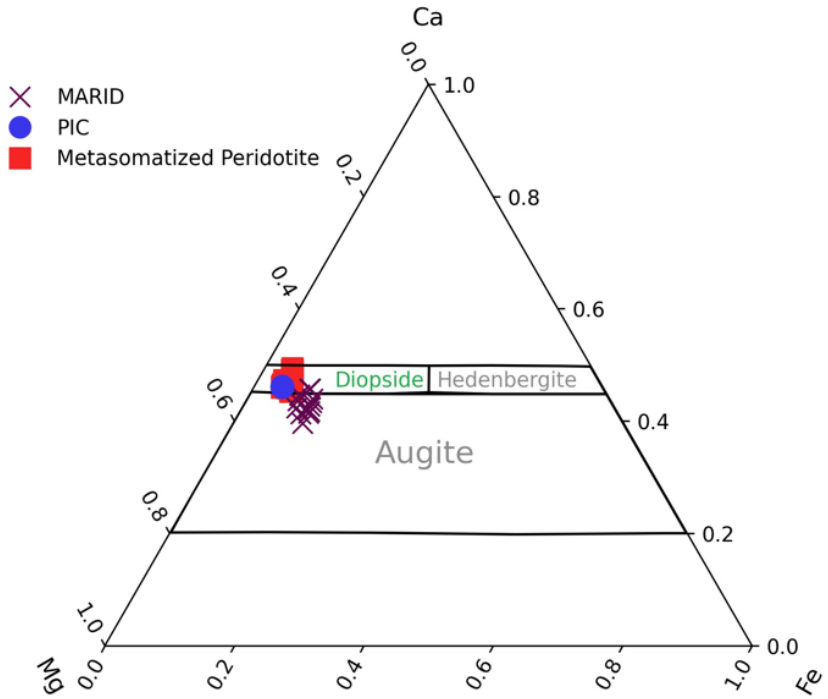

Figure 2.3.7: Clinoyproxene classification based on criteria of Morimoto (1988). Atoms per formula unit (apfu) were calculated on the basis of four cations

GPP and PP clinopyroxenes are Ti-poor (<0.12 wt. %) and have Cr_2O_3 concentrations typical of South African peridotite xenoliths (Figure 2.3.8). Spinel lherzolite clinopyroxenes show elevated Al_2O_3 (7.17 ± 0.25 wt. %) and TiO_2 (0.87 ± 0.06 wt. %).

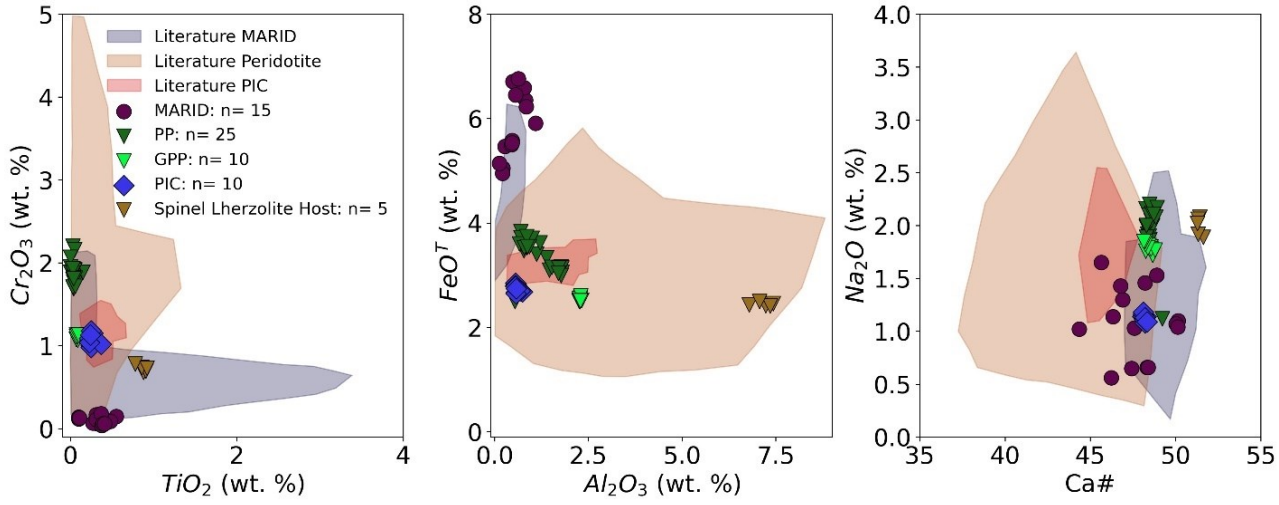

Figure 2.3.8: Major element systematics in clinopyroxenes from metasomatized xenoliths in this study. Compositional fields are from Fitzpayne *et al.,* (2018) and references therein.

Phlogopites in the xenolith suites studied here are clearly distinguished by their MgO-FeO^T systematics. FeO^T in phlogopites increases along a trend of an increasing proportion of metasomatic phases (GPP-PP-MARID; Figure 2.3.9). The exception to this is the PIC xenolith which shows identical MgO-FeO^T systematics to the PP xenolith. PIC phlogopites plot within the range of peridotitic phlogopite and agree well with results from previous studies of PIC xenoliths (Fitzpayne *et al.,* 2018; Gregoire *et al.,* 2002). Phlogopites become Al_2O_3, SiO_2, and Na_2O poor along the same GPP-PP-MARID trend (Figure 2.3.9 Appendix B.0.1). The depletion in Na_2O is well correlated with an increase in K_2O (Pearson correlation coefficient = 0.913; n = 92). The phlogopite grains contained within the Lherz Massif spinel lherzolite vein are high in Al_2O_3, TiO_2, and Na_2O relative to all other phlogopite grains analyzed in this study and plot outside of most compositional fields compiled in Figure 2.3.9.

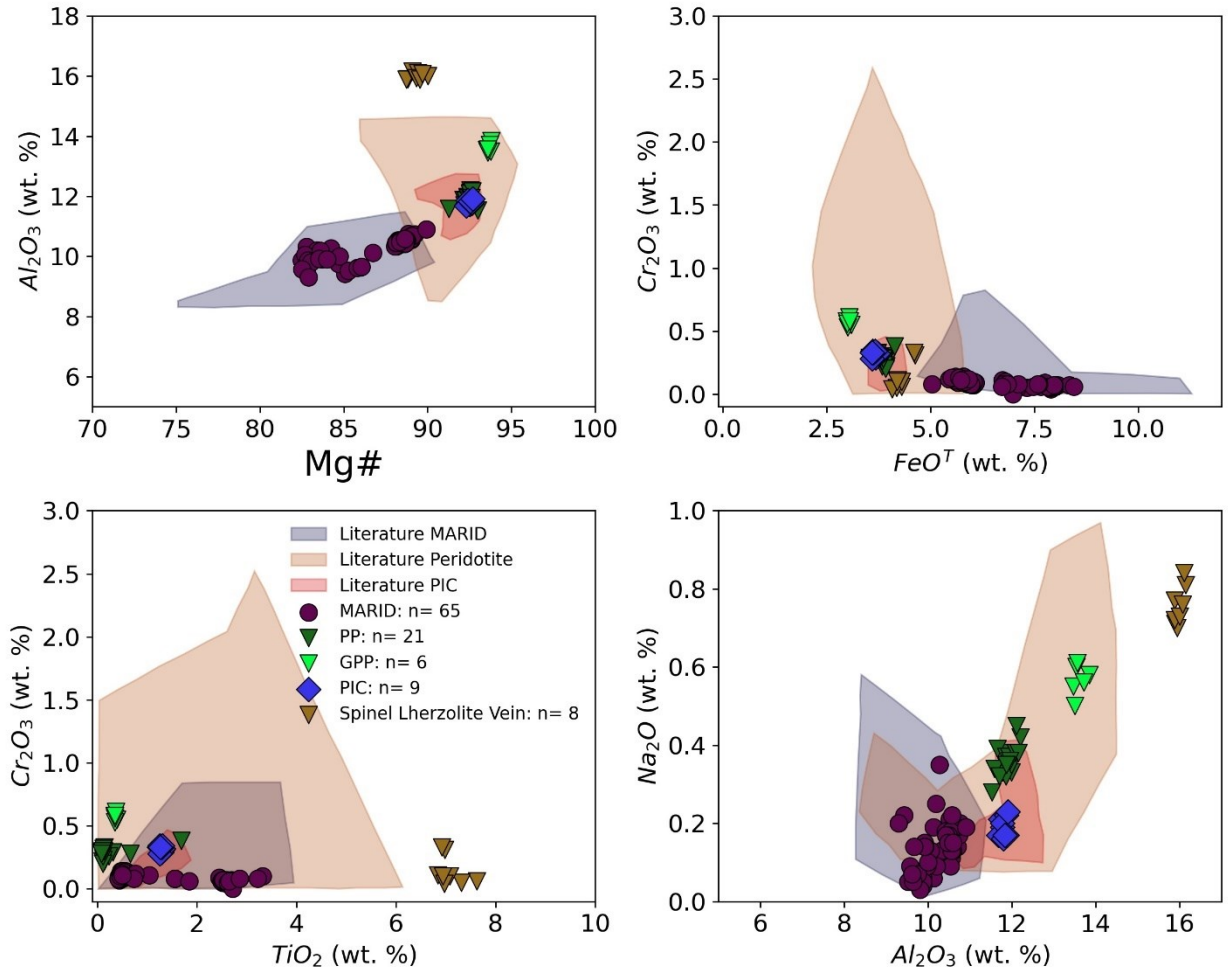

Figure 2.3.9: Major element systematics in phlogopites from metasomatized xenoliths in this study. Compositional fields for cratonic peridotite, MARID, and PIC xenoliths are from Fitzpayne *et al.,* (2018) and references therein.

Amphibole exists in modal quantities as two phases in this study: K-richterite in MARID xenoliths (AJE-326 and AJE-2422) and pargasite in the Lherz Massif spinel lherzolite vein. K-Richterite is defined by its high K_2O and Na_2O contents (4.92 ± 0.22 and 3.49 ± 0.21 respectively in this study) relative to CaO and Al_2O_3 (6.81 ± 0.06 and 1.04 ± 0.10 respectively in this study). Pargasitic amphibole has higher CaO and Al_2O_3 and lower K_2O than K-richterite. Pargasite in this study is titanian pargasite (TiO_2 concentrations of 4.1 ± 0.2 wt. % and 4.46 ± 0.08 wt. % in sample LZM-001's host peridotite and vein respectively). In general, there is very little chemical variation between the vein and host titanian pargasite. The host pargasite is slightly richer in Cr_2O_3 (0.69 ± 0.05 wt %) and poorer in TiO_2 (4.1 ± 0.2 wt. %).

Ilmenite and rutile are present in both the MARID and PIC xenolith suites in this study. In general, MARID ilmenite displays higher FeO^T and extends to lower TiO_2 than PIC ilmenite (Figure 2.3.10).

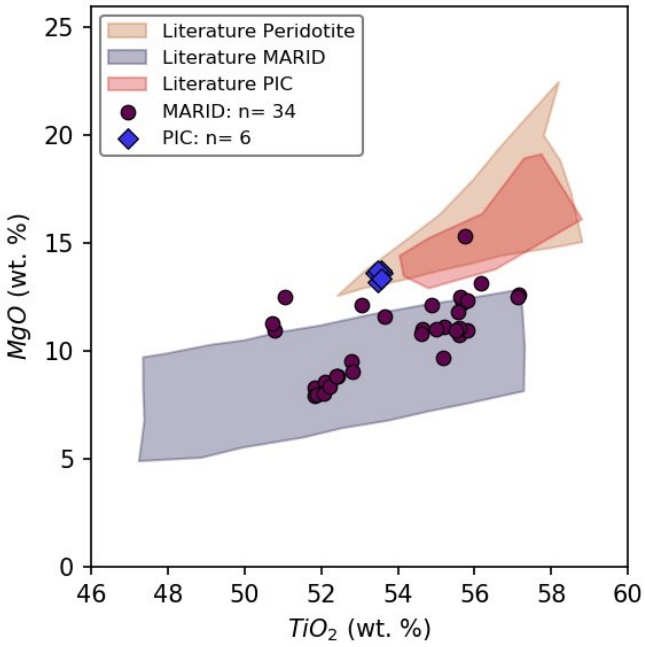

Figure 2.3.10: MgO-TiO_2 systematics in MARID-PIC ilmenite. Compositional fields from Fitzpayne *et al.,* (2018) and references therein

Rutile in both MARID and PIC xenoliths display low total oxide compositions, with PIC rutiles being significantly lower (98.78 ± 1.09 and 94.12 ± 1.01 total wt. % in MARID and PIC rutiles

respectively). It is likely that the low totals are due to high levels of Nb_2O or possibly V_2O_3, neither of which were analyzed by EPMA in this study. Rutile in upper mantle peridotites has been reported to contain up to ~5 wt. % Nb_2O and ~0.5 wt. % V_2O_3 (Fitzpayne *et al.,* 2018; Kalfoun *et* al., 2002; Haggerty 1983). The limited trace element data collected on rutiles in this study confirms that there is wt. % levels of Nb_2O present in the PIC xenolith (Appendix B.1.1). PIC rutile in this study is rich in Cr_2O_3 (3.52 ± 0.39 w.t %) compared to MARID rutile (0.62 ± 0.38 wt. %). The high Cr_2O_3 PIC rutile is similar to values observed in cratonic peridotite (Malkovets *et al*., 2016).

Sulphide Phases

Pentlandite occurs in all xenoliths suites analyzed in this study and is the dominant mantle BMS phase observed. In the GPP and PP xenoliths, pentlandites are Fe-poor (Fe_{at}/Ni_{at} of 0.77 ± 0.03 and 0.82 ± 0.09 in GPP and PP respectively) with consistent Metal/S (($Zn_{at} + Fe_{at} + Co_{at} + Ni_{at} + Cu_{at} + As_{at}$) / S_{at}) ranging from 1.09 to 1.14 wt. %. Cobalt is the most variable element, especially in pentlandite grains that show alteration to heazlewoodite in the GPP xenolith (0.16 – 1.27 wt %). Several of the PP pentlandite data points plot outside the range of typical "mantle xenolith pentlandites" (Figure 2.3.11 B). This is due to the anomalous Co concentration in these grains. Pentlandites in both the lherzolite and vein portion of sample LZM-001 are considerably richer in Fe (Fe_{at}/Ni_{at} of 1.45 ± 0.10 and 1.05 ± 0.10 in the host and vein respectively) with the host grains having consistently higher Fe wt % (37.87 ± 1.06 in the host vs 32.52 ± 1.62 in the vein). Pentlandites from LZM-001 plot within the field of mantle xenolith grains in Figure 2.3.11 (B). Several grains of LZM-001 pentlandite (vein and host) have anomalous Cu concentrations (up to 2.45 wt. %), though no Cu-bearing sulphide phases (e.g., chalcopyrite) were directly observed. Metal/S ratios in the MARID and PIC pentlandites vary from 1.08 to to 1.13 with variable, but generally higher, quantities of Co (1.23 ± 0.76 and 1.03 ± 0.11 wt % in MARID and PIC respectively). MARID and PIC pentlandites are anomalously Ni-rich compared to typical mantle xenoliths Figure (2.3.11 A) leading to low Fe/Ni ratios (0.86 ± 0.26 and 0.71 ± 0.02 in MARID and PIC respectively). Ni-enrichment in pentlandites is commonly attributed to supergene processes and this may be the case for the MARID and PIC xenoliths (e.g., Grèau *et al*., 2013). MARID and PIC pentlandites in close proximity to chalcopyrite commonly show anomalous Cu concentrations (up to 0.98 wt %)

Heazlwoodite in the GPP xenolith primarily occurs replacing pentlandite (Figure 2.3.2 A). GPP heazlewoodite contains wt % levels of Fe (2.29 ± 0.96 wt %; Figure 2.3.11 B) and Ni concentrations ranging from 65.0 to 72.8 wt %. MARID heazlewoodite has generally lower Fe concentrations (1.75 ± 1.04 wt %) and a wider range in Ni (60.8 – 72.8 wt %). The grains of heazlewoodite anaylzed in MARID sample KDB-20 contain anomalous concentrations of arsenic (0.6 wt %).

MARID *pyrrhotite* only occurs in sample AJE-335 and has slightly higher Fe than PIC pyrrhotite (59.48 ± 0.07 vs 57.37 ± 0.56 in MARID and PIC respectively). Both MARID and PIC pyrrhotite have minor concentrations of As (Appendix B.0.2).

Cu-bearing sulphides primarily occur as chalcopyrite in the MARID and PIC xenoliths. Both MARID and PIC chalcopyrite have nearly identical concentrations of Cu (32.9 and 33.6 wt. % respectively) and Fe (30.9 and 30.2 wt. % respectively). One grain of bornite was found intergrown with pentlandite in the PP xenolith (Figure 2.3.11 C). Several small (<10 μm) grains of relatively pure (~ 95 wt %) Cu metal were found in MARID samples AJE-335 and AJE-2422. Their occurrence was associated with heavily weathered grains of chalcopyrite or serpentinized fractures making it unlikely that they are of primary mantle origin.

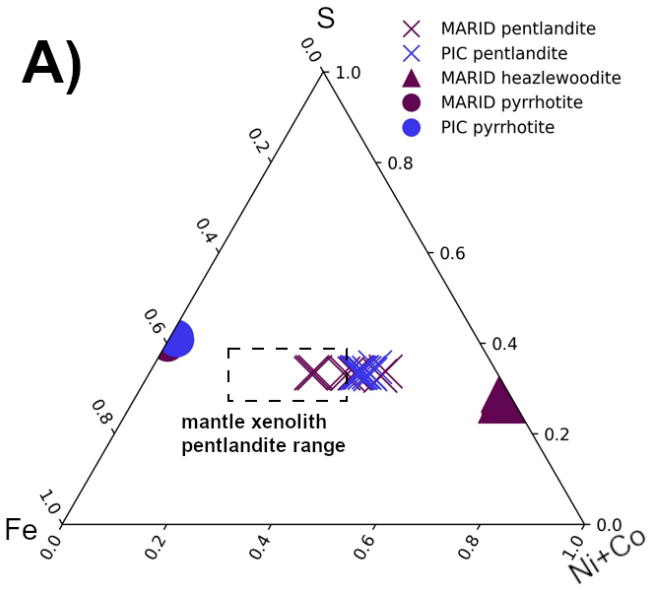
A)
S
Fe
Ni+Co
MARID pentlandite
PIC pentlandite
MARID heazlewoodite
MARID pyrrhotite
PIC pyrrhotite
mantle xenolith
pentlandite range

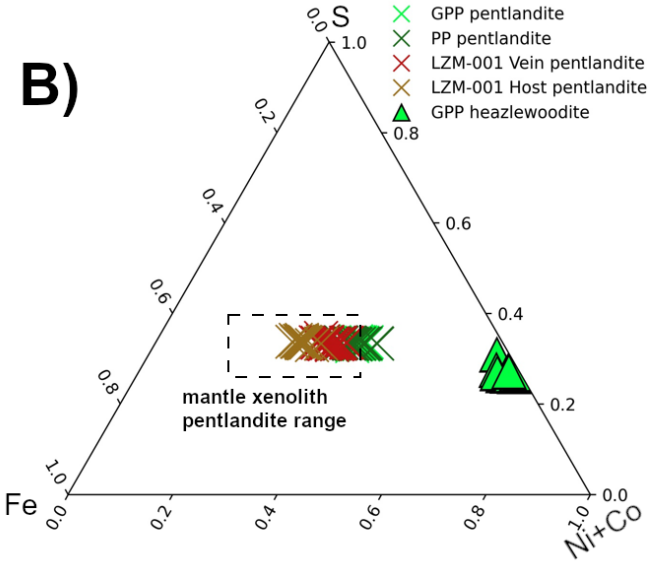
B)
S
Fe
Ni+Co
GPP pentlandite
PP pentlandite
LZM-001 Vein pentlandite
LZM-001 Host pentlandite
GPP heazlewoodite
mantle xenolith
pentlandite range

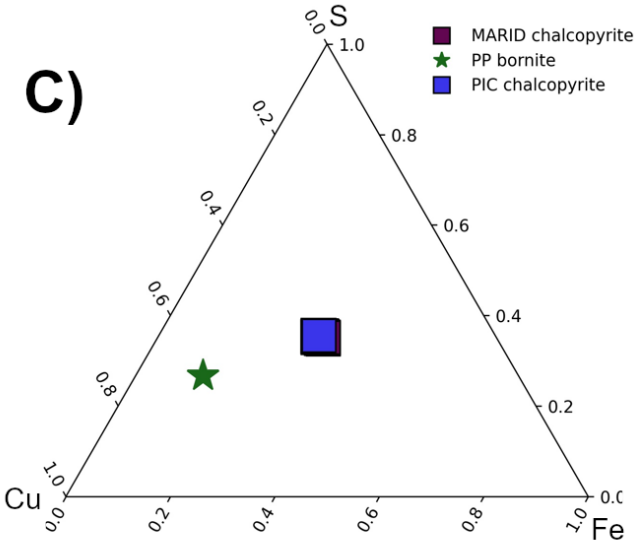
C)
S
Cu
Fe
MARID chalcopyrite
PP bornite
PIC chalcopyrite

Figure 2.3.11: Major element ternary diagrams of primary mantle BMS assemblages observed in this study. A) Fe-Ni BMS in MARID and PIC xenoliths B) Fe-Ni BMS in metasomatized peridotites C) Cu-Fe BMS in MARID, PIC, and metasomatized peridotites. Note that MARID chalcopyrite plots in a nearly identical position to PIC chalcopyrite. "Mantle xenolith pentlandite range" is from Grèau *et al*., (2013) and references therein.

2.3.3 Trace Element and Precious Metal Mineral Chemistry

Tabulated data for lithophile trace element and precious metal mineral chemistry is presented in Appendix B.2.1 and Appendix B.3.1. Due to their trace element poor nature, sulphide mineral phases were analyzed strictly for a suite of precious metals (Ru, Pd, Ag, Re, Ir, Os, Pt, Au) via LA-ICP-MS. Tabulated data for these results are presented in Appendix B.3.2.

Silicate and Oxide Trace Element Mineral Chemistry

Olivine and orthopyroxene in peridotites typically contain extremely low concentrations of most trace elements regardless of the degree of metasomatism experienced (Pearson *et al*., 2003). However, olivine, and to a lesser extent orthopyroxene, host significant (> 500 ppm) quantities of Ni in xenoliths that is negatively correlated to the degree of melt depletion (i.e., Mg #; Pearson *et al.,* 2003). Figure 2.3.12 (A) shows that the GPP xenolith has the highest Ni concentrations in both olivine and orthopyroxene. Several olivines from the PP xenolith have Ni concentrations higher than Lherz massif sample despite lower Mg #. Additionally, olivines from the PP xenolith are consistently enriched in Nb (1.8 ± 0.1 ppm; Figure 2.3.12 C). Orthopyroxenes from the GPP xenolith show variable Nb enrichment.

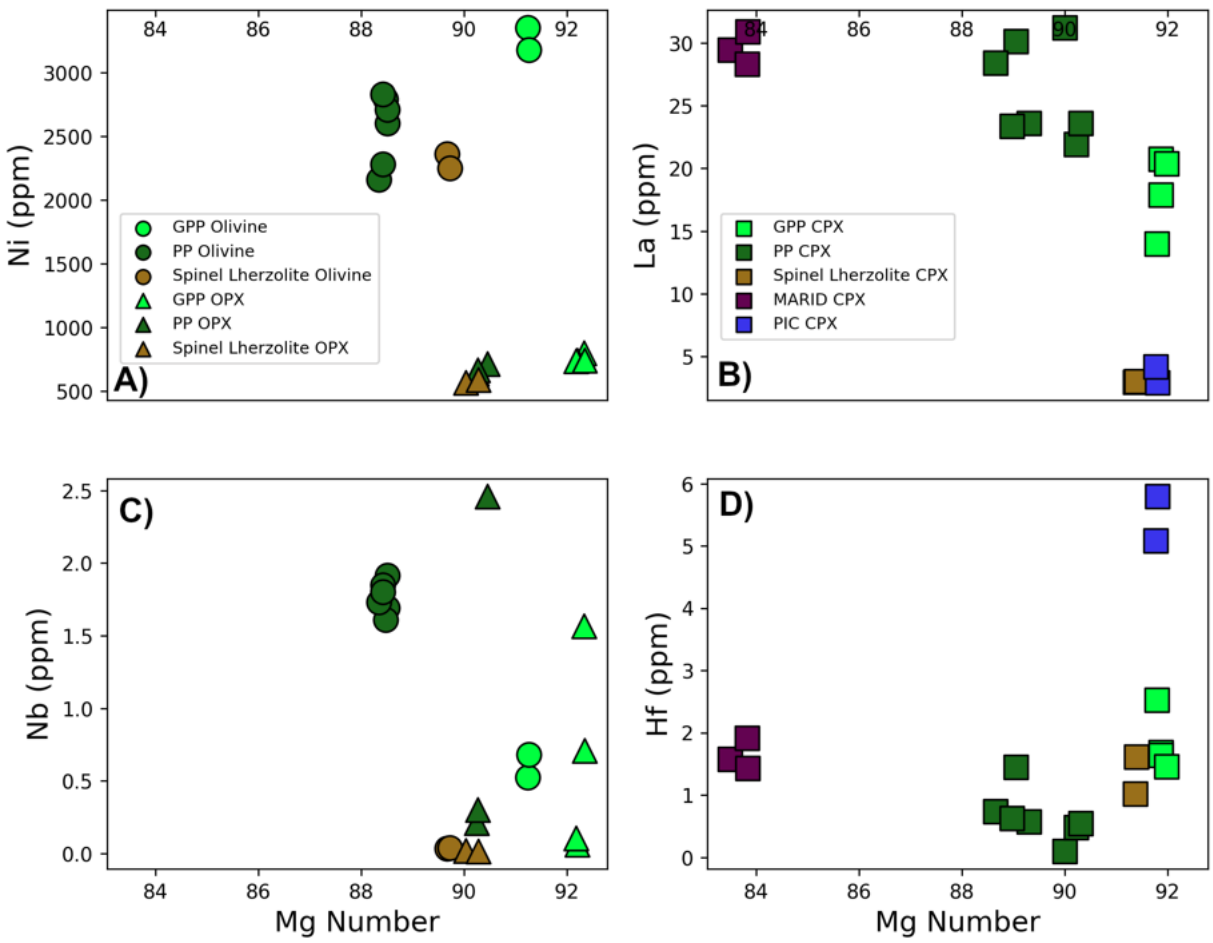

Figure 2.3.12: Bivariate plots highlighting trace element trends in olivine (circles), orthopyroxene (triangles), and clinopyroxene (squares) from xenoliths analyzed in this study. A) Ni vs Mg # in olivine and orthopyroxene. B) La vs Mg # in clinopyroxene. C) Nb vs Mg # in olivine and orthopyroxene. Both minerals in the samples derived from the Kaapvaal craton are variably Nb enriched. D) Hf vs Mg number in clinopyroxene.

Clinopyroxenes in the GPP, PP, and MARID xenoliths show pronounced negative anomalies in HFSE (Nb, Zr, Hf) while PIC clinopyroxenes display positive anomalies in Zr and Hf (Figure 2.3.12; Figure 2.3.13). PIC clinopyroxene is lower in LREE concentration than the GPP-PP-MARID clinopyroxene. Several PP clinopyroxenes display very similar REE geochemistry to that of the MARID cpx (Figure 2.3.13). Clinopyroxenes from the Lherz spinel lherzolite display markedly different geochemistry compared to the Kaapvaal samples. They lack HFSE anomalies and display much higher concentrations of HREE (Appendix B.1.1).

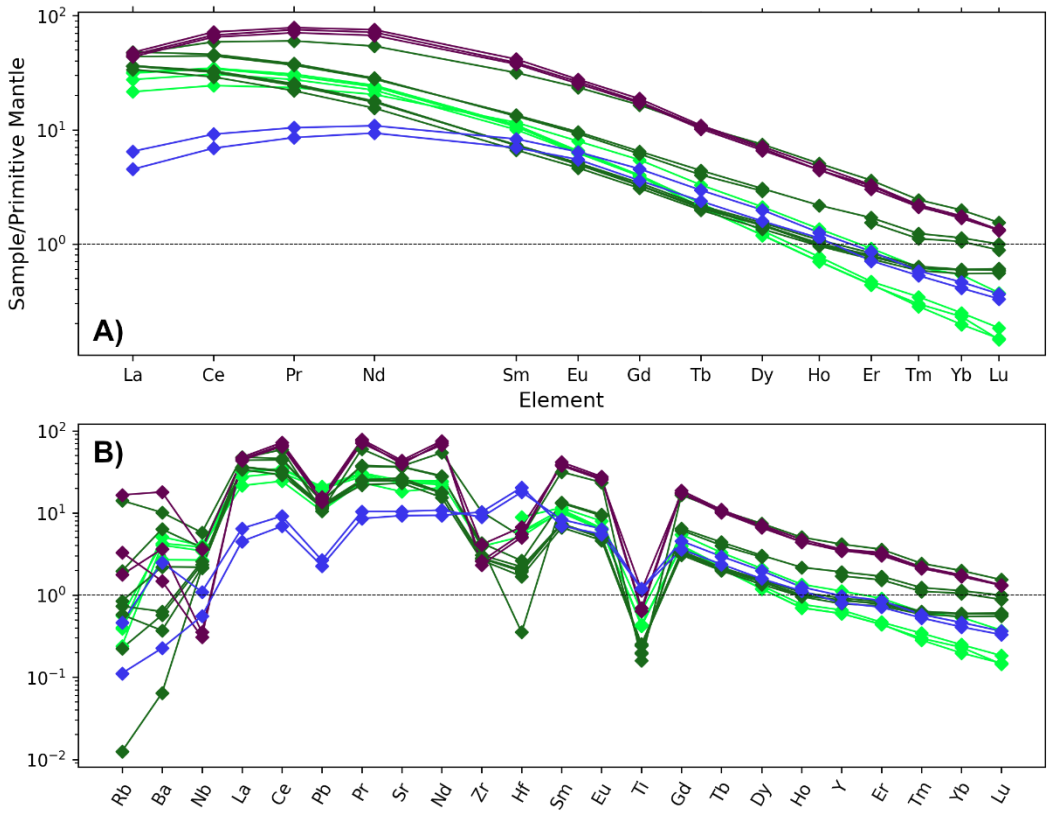

Figure 2.3.13: Trace element geochemistry of clinopyroxenes from the GPP (bright green), PP (dark green), PIC (blue), and MARID (purple) xenoliths. A) REE spider diagram and B) trace element spider diagram.

Garnet anaylses from the GPP xenolith display LREE-depleted, HREE-enriched patterns typical of garnet lherzolites (Appendix B.1.2; O'Reilly and Griffin 2013).

Phlogopites in all xenolith suites are enriched in LILEs and generally poor in REEs (Appendix B.1.1). Phlogopite in the GPP xenolith is extremely high in Ba (4298 ppm) and have positive Pb and Sr anomalies (1.41 and 167 ppm respectively). PP phlogopite is widely variable in composition and lower in total trace element abundances. PP phlogopite displays a similar positive Pb anomaly but at an order of magnitude lower than its GPP counterpart. Phlogopites in the vein of sample LZM-001 have high concentrations of Pb (0.5 ± 0.12 ppm), Sr (180 ± 43 ppm), and Ba (1600 ±142 ppm). MARID and PIC phlogopties are very similar in composition with low REE concentrations and high levels of LILE (Appendix B.1.1).

MARID K-Richterite from this study falls within the range from previous works (Fitzpayne *et al*., 2018; Figure 2.3.14) showing the characteristic depletion in HREEs (La_N/Yb_N = 41-84). MARID K-Richterite has positive anomalies in Rb, Pb, and Sr as well as minor positive HFSE anomalies (Nb, Zr, Hf; Appendix B.1.1). Pargasite amphibole from the host and vein of sample LZM-001 do not display significant geochemical differences and are enriched in REE (especially HREE; Figure 2.3.14) compared to MARID K-richterite.

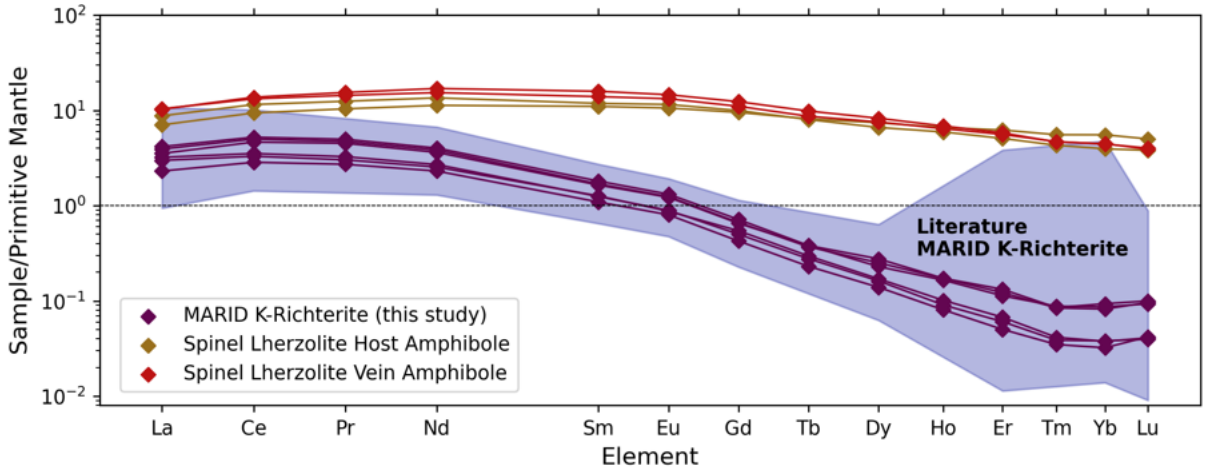

Figure 2.3.14: Primitive mantle normalized REE geochemistry of MARID K-richterite compared to pargasite amphibole from the host and vein of sample LZM-001. Field for literature MARID K-richterite is from Fitzpayne *et al*., (2018).

Both MARID and PIC ilmenites are significant reservoirs for HFSEs. Nb, Zr, and Hf are highly concentrated in MARID ilmenite and show high variability between samples (2100 ±1980 ppm Nb; 340 ± 210 ppm Zr; 9 ± 4.4 ppm Hf; Appendix B). PIC Ilmenite shows similar enrichment in HFSEs (1623 ± 5.7 ppm Nb; 513 ± 7.8 ppm Zr; 13.2 ± 0.12 ppm Hf). Ilmenite also hosts moderate concentrations of transition metals, particularly Co and Ni, with PIC ilmenite containing slightly higher values (172 ± 2.8 ppm Co and 800 ± 150 ppm Ni in MARID; 195 ± 3.2 ppm Co and 1329 ± 2.8 ppm Ni in PIC).

MARID rutile, usually present as fine intergrowths within ilmenite, was not succesfully analyzed. Previous analyses of MARID rutile showed variable but significant enrichment in HFSEs (Gregoire, *et al.,* 2002; Fitzpayne, *et al*., 2018). The sole PIC rutile analyzed in this study contained weight percent levels of Nb (2.99 wt %) and enrichment in Zr and Hf roughly an order of magnitude higher than in MARID and PIC ilmenite (8250 ppm Zr; 226 ppm Hf). Rutile, in contrast to ilmenite, does not host significant concentrations of transition metals analyzed here.

Silicate and Oxide Precious Metal Mineral Chemistry

The vast majority of precious metal (Ag, Pd, Re, Ir, Pt, Au) analyses in silicate and oxide minerals returned values below the limits of quantitation (LOQ) of our method (Appendix B.2.1). This is similar to results from previous research attempting to quantify precious metals (particularly the PGE) in mantle silicate and oxide phases (e.g., Handler and Bennett, 1999; Burton *et al*., 2002; Lorand *et al*., 2008b). Such studies have typically used cleaned mineral separates and solution chemistry to attempt quantification, and we find similar limitations using LA-ICP-MS. Given that the mean LOQ for precious metals in our study are in the ppb to the 10s of ppb range, it is reasonable to conclude that silicate and oxide phases in variably metasomatized mantle xenoliths contain ppb to sub-ppb concentrations of precious metals and are negligible contributors to the whole rock budget.

Re exceeds LOQ in a variety of mineral phases including olivine in the GPP xenolith, chromite in the PP xenolith, phlogopite in the MARID xenoliths, pargasite in the spinel lherzolite vein, and ilmenite and phlogopite in the PIC xenolith. The concentration never exceeds 2.5 ppb and is frequently < 1 ppb reflecting the very low LOQ of Re in these analyses (mean value of 3 ppb across 87 analyses; Table 2.3.3). However, mass balance calculations discussed in Section 2.4.2 indicate that these values are likely to be analytical artifacts or rare Re-rich mineral inclusions.

Analyses that returned values above LOQ for Ag, Pd, Pt, and Au occurred in mineral phases that incorporate high concentrations of HFSE (Zr, Hf, Ta). This is most likely the result of exotic molecular species being created from ionization during the ablation process and creating isobaric overlaps (Butcher *et al*., 1988; Enger *et al., 1995;* Sylvester 2008). These interfering species overlap the mass/charge ratios of many precious metals resulting in artificially inflated time integrated signals. These concentrations are interpreted as analytical artifacts and are not considered further.

Sulphide Precious Metal Mineral Chemistry

All precious metal (Ru, Pd, Ag, Re, Ir, Os, Pt, Au) concentrations reported here are for pentlandites, which was the major BMS phase we observed across all samples that provided the size (33-90 μm) and compositional consistency required for analysis by laser ablation. Some mixed (co-ablation of two phases) phase analyses are also reported and noted in Appendix B.2.2.

IPGE (Os, Ir, Ru) concentrations show two distinct populations between the peridotites and the alakli-rich metasomes (Figure 2.3.15). Pentlandites from the South African peridotite xenoliths are rich in Os, Ir, Ru with supra-chondritic concentrations of all three elements (GPP – 7.49 ± 6.20 ppm Os, 6.16 ± 5.74 ppm Ir, 12.9 ± 8.71 ppm Ru; PP – 0.31 ± 0.02 ppm Os, 0.54 ± 0.04 ppm Ir, 2.0 ± 0.52 ppm Ru) while MARID and PIC pentlandites are extremely IPGE poor (MARID – 0.07 ± 0.05 ppm Os, 0.04 ± 0.01 ppm Ir, 0.32 ± 0.28 ppm Ru; PIC - < LOQ Os, < LOQ Ir, 2.4 ± 0.2 ppm Ru).

IPGE abundances of pentlandites in the Lherz Massif lherzolite host rock are IPGE-rich (8.4 ± 3.4 ppm Os, 3.3 ± 2.6 ppm Ir, 16.5 ± 15.4 ppm Ru) while grains enclosed in the vein are extremely depleted in the same elements (0.05 ± 0.03 ppm Os, 0.03 ± 0.01 ppm Ir, 0.83 ± 0.37 ppm Ru) (Figure 2.3.15). Pentlandites in the peridotite portion of the Lherz spinel lherzolite are especially enriched in Os with a chondrite-normalized Os_N/Ir_N = 2.36 while other xenolith suites are all < 2 (GPP - 1.13 Os_n/Ir_n ; PP – 0.54 Os_N/Ir_N ; Spinel Lherzolite Vein – 1.54 Os_n/Ir_n ; PIC - < LOQ ; MARID – 1.63 Os_n/Ir_n). Outside of the Lherz Massif sample, IPGE elements show good positive correlation, especially Os and Ir (Figure 2.3.16) (r = 0.81 for Os-Ir; n = 34).

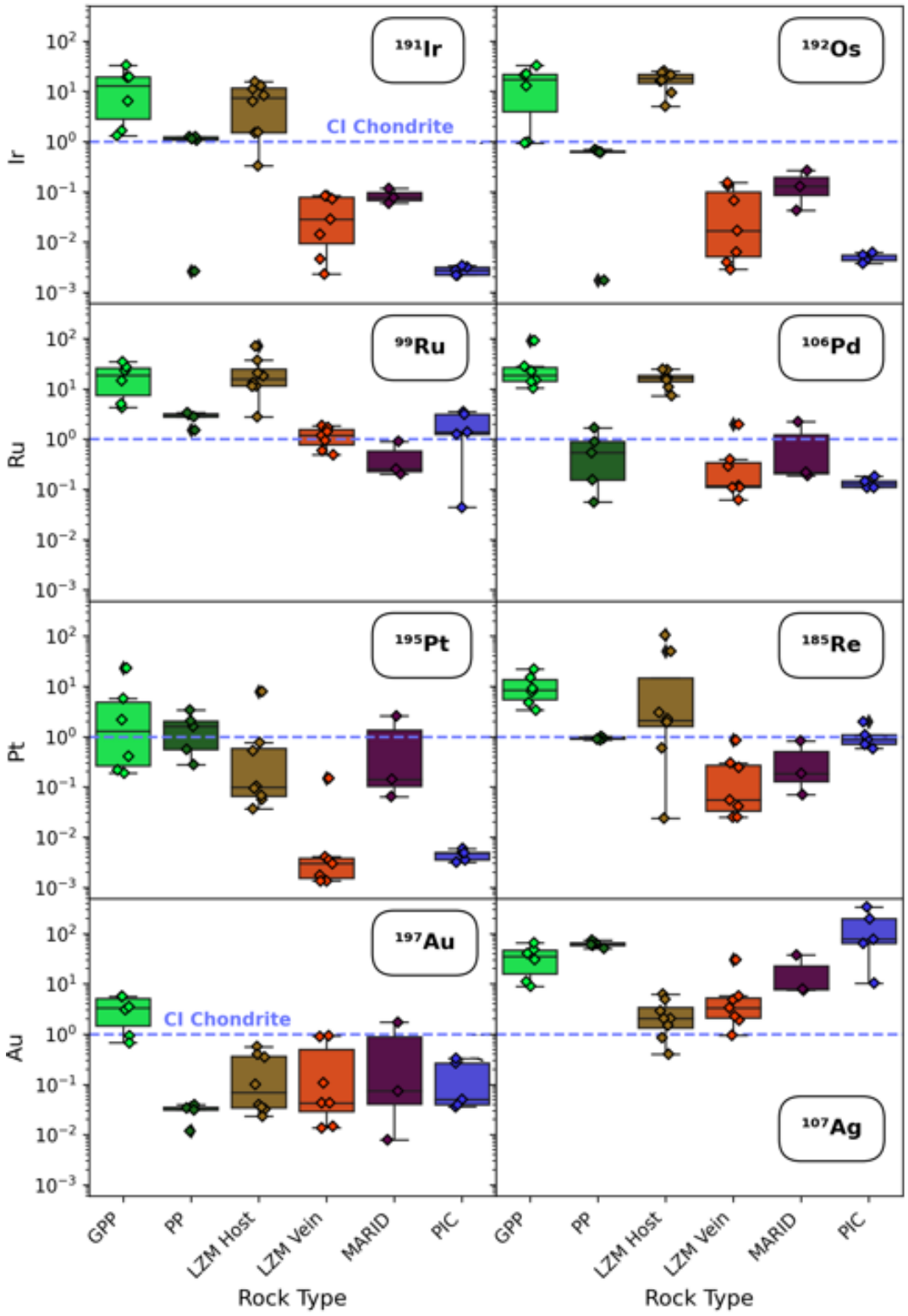

Figure 2.3.15: Box and whisker plots of precious metal concentrations in pentlandites and mixed phases highlighting compositional differences between different xenoliths. All values are normalized to CI chondrite values from McDonough and Sun (1995).

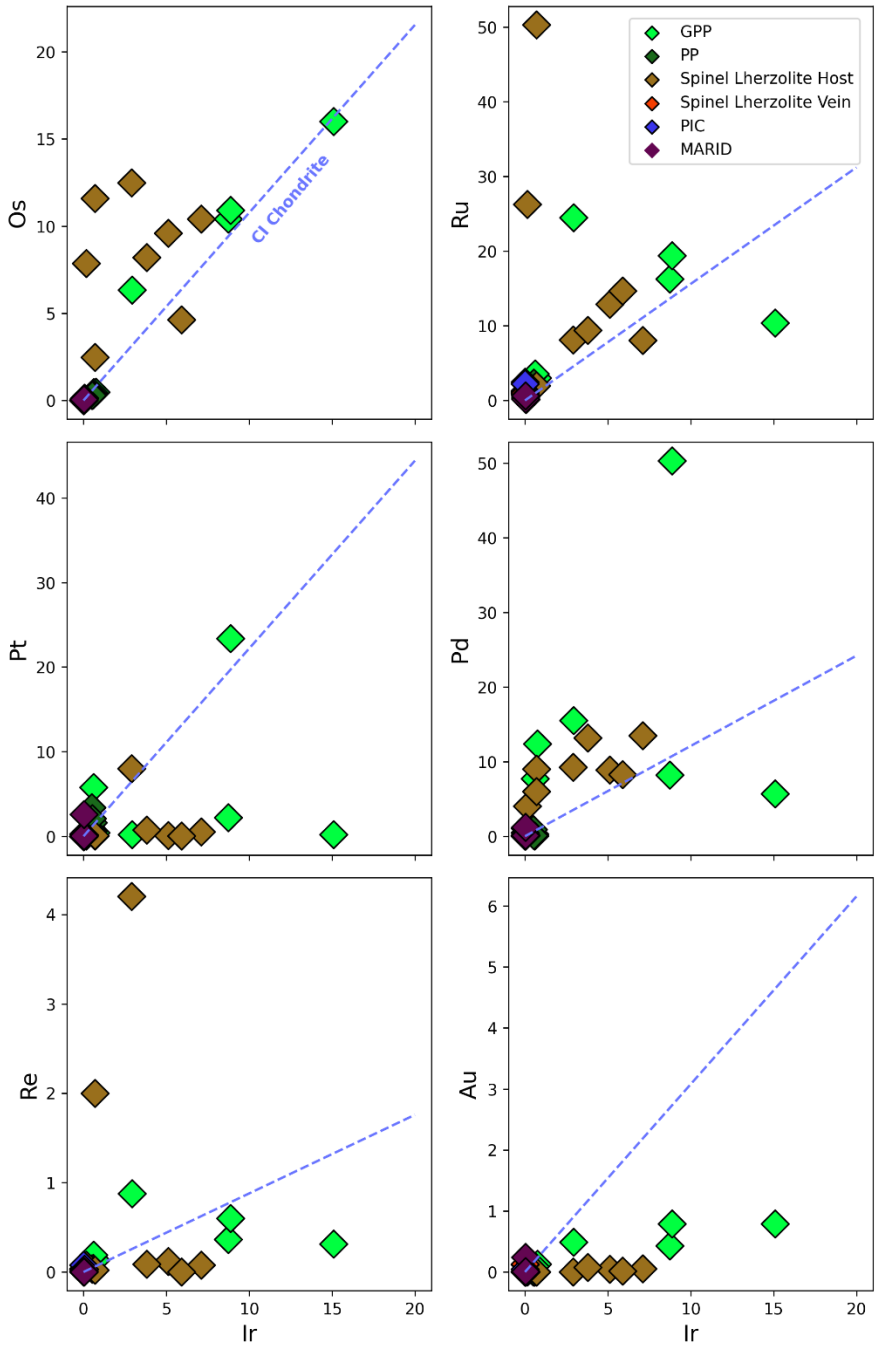

Figure 2.3.16: Covariation of precious metals vs Ir concentration in sulphides across mantle xenolith suites analyzed in this study. Concentrations are in ppm. Data plots above the dotted blue line represent supra-chondritic element ratios. Chondritic ratios are from McDonough and Sun (1995)

Pentlandite typically does not incorporate significant amounts of Pt into its crystal structure (Barnes *et al*., 2008; Lorand and Luget 2016) and this effect is observable as pronounced negative anomalies in chondrite-normalized trace element diagrams (Figure 2.3.17). The

exception to this is pentlandites from the PP xenolith which shows elevated concentrations of Pt relative to other PPGEs (Pt_n/Pd_n = 1.53). Micron scale inclusions of Pt-rich alloy that were directly observed within pentlandites from this xenolith suggests that the elevated Pt concentrations are likely from co-ablating these small inclusions.

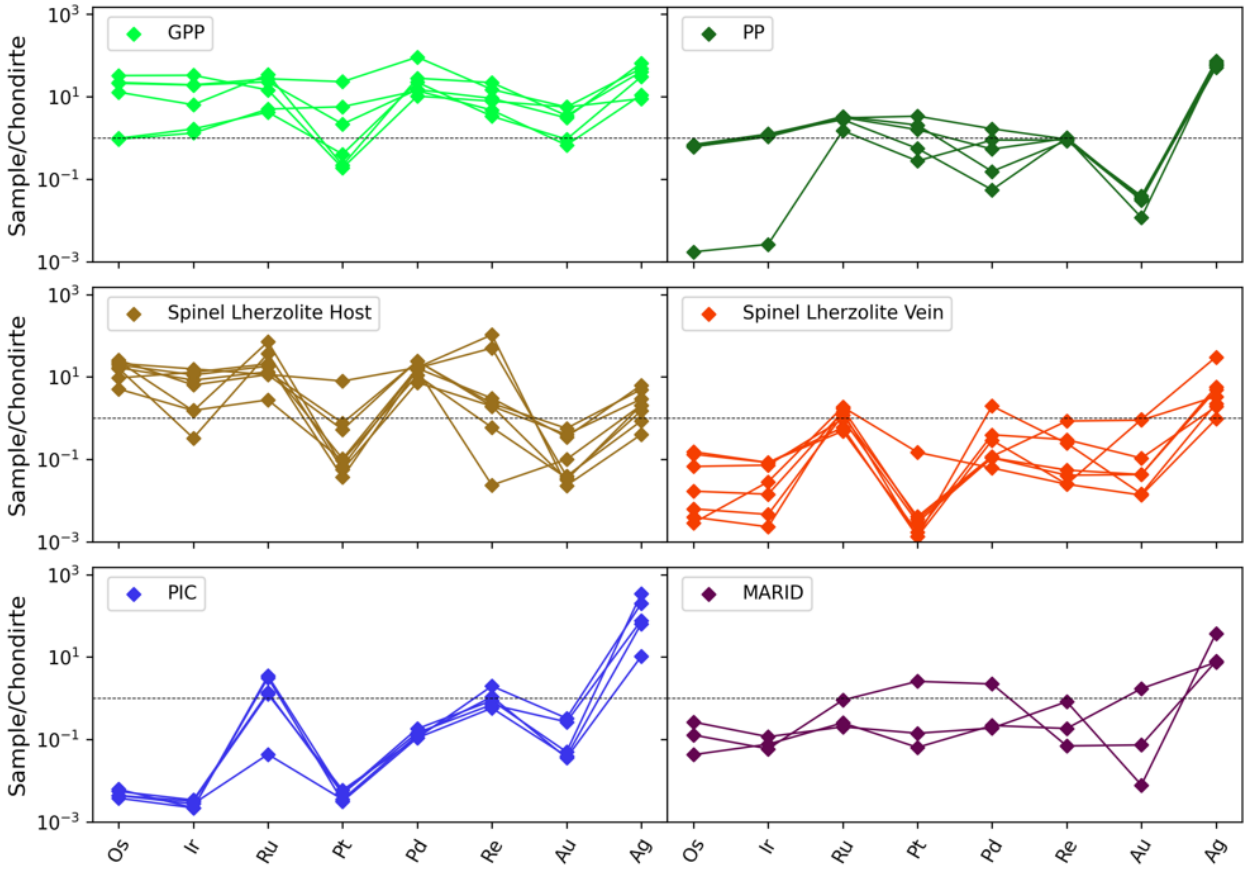

Figure 2.3.17: Chondrite normalized trace element spider diagrams showing variability in sulphide precious metal concentrations analyzed in this study. Normalizing values from Mcdonough and Sun (1995).

Pd_n/Ir_n ratios are generally supra-chondritic with the exception of pentlandites in the PP xenolith which display slightly sub-chondritic values (PP pentlandite Pd_n/Ir_n = 0.87; CI Chondrite = 1.21). Pentlandites from the vein portion of the Lherz spinel lherzolite display highly fractionated Pd_N/Ir_N ratios compared to pentlandites from the peridotitic portion of the xenolith (Pd_n/Ir_n = 13.5 and 2.26 in vein and host pentlandites respectively). MARID sulphides show similarly fractionated ratios to the spinel lherzolite vein (MARID Pd_n/Ir_n = 9.93).

Re concentrations in all sulphide grains are < 1 ppm with the highest values occurring in grains from the GPP and spinel lherzolite xenoliths (GPP – 0.41 ± 0.28 ppm Re ; Spinel Lherzolite –

0.94 ± 1.6 ppm Re). There is no strong correlation between Re and any co-analyzed precious metal. Au concentrations are sub-chondritic in all analyses with the exception of grains in the GPP xenolith (0.45 ± 0.30 ppm Au). Finally, Ag shows no correlation with co-analyzed precious metals and is highest in grains from the PIC xenolith.

2.3.4 Whole Rock Geochemistry

We characterize the whole rock geochemistry of our suite of metasomatized mantle xenoliths using XRF for major/trace elements (SiO_2, TiO_2, Al_2O_3, Cr_2O_3, FeO^T, MnO, MgO, CaO, Na_2O, K_2O, NiO; Rb, Ba, Nb, La, Ce, Pb, Sr, Zr, Y, Sc, Cu, Co) and ID-ICP-MS for precious metals (Os, Ir, Ru, Pt, Pd, Re). Re-Os isotopes were obtained using isotope dilution and N-TIMS. The exception to this is the PIC xenolith (UIB-2) which was only available in thin section. All major and trace element concentrations reported for sample UIB-2 are reconstructed using results from mineral chemistry analyses and modal abundance. Tabulated data for major and trace elements are presented in Appendix B.3.1 and Appendix B.3.2. Tabulated results for precious metals and Re-Os isotopes are presented in Appendix B.3.3. Reconstructed whole rock compositions and their implications are discussed in Section 2.4.2.

Major and Trace Elements

The metasomatized peridotites are mafic in composition (GPP- 45.6 wt. % SiO_2; PP- 49.3 wt. % SiO_2; LZM-001 Host- 45.1 wt. % SiO_2) with Mg # similar to their respective olivines (GPP- 91.6; PP- 90.1; LZM-001 Host- 90.9. Concentrations of Al_2O_3 and CaO (both considered proxies for melt depletion in peridotites; Pearson *et al*., 2003) are depleted relative to primitive mantle in the GPP xenolith (3.37 and 2.45 wt. % respectively), though higher than average depleted cratonic peridotite. The PP xenolith is Al_2O_3 poor (1.02 wt. %) but CaO enriched (6.75 wt. %). The Lherz Massif spinel lherzolite has roughly primitive mantle concentrations of Al_2O_3 and CaO (3.17 and 3.71 wt. % respectively). The GPP composition is TiO_2 poor compared to PP and spinel lherzolite (0.03 vs 0.11 and 0.15 wt. %).

MARID xenoliths are basic-ultrabasic (44.0-48.6 wt. % SiO_2) while the PIC xenolith and spinel lherzolite vein are both ultrabasic (37.2 and 40.9 wt.% SiO_2 respectively). MARID and PIC samples are ultrapotassic (2.4 – 8.0 wt. % K_2O). All of the alkali-rich metasomes are enriched in TiO_2 (MARID- 1.92 to 4.88 wt. %; PIC- 14.5 wt. %; Spinel lherzolite vein- 4.1 wt. %) with the

extreme enrichment in the PIC xenolith caused by the high abundance of ilmenite and rutile in the sample.

GPP and PP xenoliths both display LREE enriched compositions (La_N/Y_N = 2.2 and 6.7 respectively) with the GPP having higher HREE abundances due to the presence of garnet. The spinel lherzolite is weakly LREE enriched (La_N/Y_N = 1.75) and is much lower in LILE than the GPP or PP xenoliths (Appendix B.3.2). Both the GPP and PP xenoliths display negative HFSE anomalies while the spinel lherzolite host has a small positive HFSE anomaly. In all metasomatized peridotites, Co shows roughly primitive mantle values while Cu is highly depleted.

MARID samples are very enriched in LREE (La_N/Y_N ranging from 26.5 to 584) while the PIC xenolith shows LREE enrichment more similar to the metasomatized peridotites (La_N/Y_N = 6.14). The two K-Richterite bearing MARID samples (AJE-326 and AJE-2422) have positive anomalies of Pb, Sr, and the HFSE while sample AJE-335 (low in K-Richterite and ilmenite) has negative anomalies of the same elements. All MARID samples show supra-primitive mantle concentrations of Cu (47-137 ppm) and roughly primitive mantle values of Co (62-82 ppm). The PIC xenolith is depleted in Cu and Co. The spinel lherzolite vein is lower in LILE and does not display the positive HFSE anomalies of most MARID and PIC samples. The vein has supra-primitive mantle values for all REE and does not display the HREE depleted pattern of the MARID and PIC rocks.

Precious Metals

Results from precious metal analyses via ID-ICP-MS show low (ppb-ppt; sub-chondritic) bulk concentrations of the PGE and Re similar to previous studies of mantle xenoliths (e.g., Pearson *et al*., 2004; Lorand *et al*., 2010; Maier *et al*., 2012). The GPP xenolith has the highest total PGE abundance of the South African samples with total IPGE (Os + Ir + Ru) concentrations of 28.5 ppb and total PPGE (Pt + Pd) concentrations of 13.6 ppb. The GPP xenolith is enriched in all

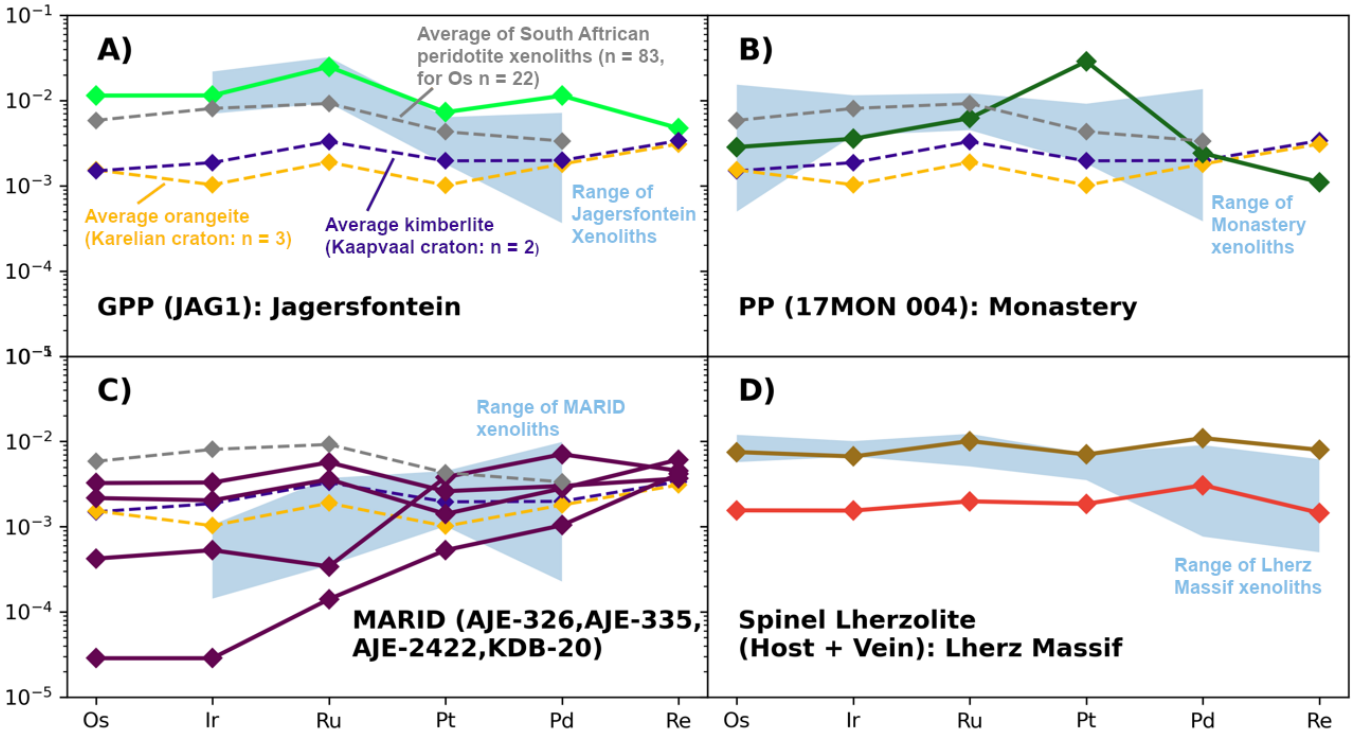

Figure 2.3.18: Chondrite-normalized precious metal concentrations in metasomatized mantle xenoliths from this study. Samples are compared to the average value from a database of South African peridotite xenoliths published in Maier *et al*., (2012), as well as the average value for Kaapvaal craton kimberlites (Premier) from Maier *et al*., (2017). The dashed orange line is the average value for orangeites from the Karelian craton margin published in Maier *et al*., (2017). Ranges for the Jagersfontein and Monastery peridotites, as well as the MARID xenoliths are from Maier *et al*., (2012). The range for Lherz Massif xenoliths is from Becker *et al*., (2006) and Luguet *et al*., (2007).

of the PGE relative to average South African peridotite xenoliths but is within the range of those typically found in the Jagersfontein pipe (Figure 2.3.18 A; Maier *et al.,* 2012). The GPP xenolith displays no PPGE-IPGE fractionation (Pd_N/Ir_N = 0.992) but is slightly depleted in Pt relative to Pd (Pt_N/Pd_N = 0.640). The PP xenolith is low in total IPGE (7.41 ppb) compared to both the GPP xenolith and relative to average South African peridotite xenoliths (Figure 2.3.18). However, it is within the range of peridotite xenoliths measured from the Monastery kimberlite. The PP xenolith is anomalously enriched in Pt (29.1 ppb; Pt_N/Pd_N = 11.96) and shows moderate Pd fractionation (Pd_N/Ir_N = 0.677). Both the GPP and PP xenolith have higher concentrations of the PGE relative to recent values obtained for both orangeites and kimberlites (Figure 2.3.18; Maier *et al*., 2017).

MARID xenoliths display two distinct PGE patterns in Figure 2.3.18 (C). Two samples, AJE-326 and AJE-335, are highly IPGE fractionated (Pd_N/Ir_N = 36.34 and 13.35 respectively) with patterns

that broadly resemble those of basaltic melts (e.g., Barnes *et al*., 2015). The other two MARID samples, AJE-2422, and KDB-20, show little fractionation (Pd_N/Ir_N = 0.91 and 1.38 respectively) and display patterns that are more similar to kimberlites and some unfractionated Kaapvaal craton peridotites (e.g., Pearson *et al.,* 2004; Maier *et al.,* 2012). Of the first group, total IPGE concentrations in AJE-326 are much lower than previous MARID analyses while sample AJE-335 falls within the typical range (Figure 2.3.18 C). Platinum and palladium concentrations in AJE-335 slightly exceed the average values for South African peridotites (3.844 and 3.89 ppb respectively). In the second group, AJE-2422 is higher in total PGE abundance than KDB-20 (11.40 vs 7.51 ppb respectively), but both are depleted in all analyzed elements relative to the average South African peridotite.

The spinel lherzolite from Lherz shows homogeneous PGE concentrations that are typical of samples from the Lherz Massif (Figure 2.3.18 D). The LZM-001 host has supra-chondritic Ru_N/Ir_N (1.52) and Pd_N/Ir_N (1.64) which is a feature ubiquitous in fertile orogenic lherzolites (Lorand *et al*., 2013). PGE concentrations in the LZM-001 amphibole vein are systematically ~1 order of magnitude lower than the host, but display almost identical chondrite normalized patterns (Ru_N/Ir_N = 1.28; Pd_N/Ir_N = 1.99; Figure 2.3.18 D).

Re-Os Isotopes

As discussed above, Os concentrations are sub-chondritic with the peridotite xenoliths showing higher concentrations (1.39-5.6 ppb) than the alkali-rich metasomes (0.014-1.59 ppb). Rhenium concentrations are low compared to primitive mantle (Becker *et al*., 2006) but are comparable to values seen in depleted peridotites from the Lesotho kimberlites (Pearson *et al*., 2004; Appendix B.3.3). The PP xenolith and amphibole vein within the Lherz spinel lherzolite have very low Re concentrations (0.044 and 0.058 ppb respectively) while the spinel lherzolite host displays Re values one order of magnitude higher (0.318 ppb). This variability is reflected in the wide range of Re/Os ratios present in our samples (Figure 2.3.19; Re/Os = 0.032 – 11.86).

The South African GPP and PP xenoliths have unradiogenic Os isotope compositions that indicate time-integrated low $^{187}Re/^{188}Os$ systematics (Figure 2.3.19). Unradiogenic Os isotope compositions are a characteristic feature of Kaapvaal peridotites expressed as negative γOs (a relative unit comparing a sample's $^{187}Os/^{188}Os$ to a chondritic composition as a percent difference) values from a large database of analyzed samples (Figure 2.3.19; Pearson *et al*.

2021). The GPP and PP xenoliths have slightly more radiogenic γOs (-2.92 and -8.05 respectively) than the average value for Kaapvaal peridotites (-9.98), but still plot within the "Kaapvaal" field shown in Figure 2.3.19.

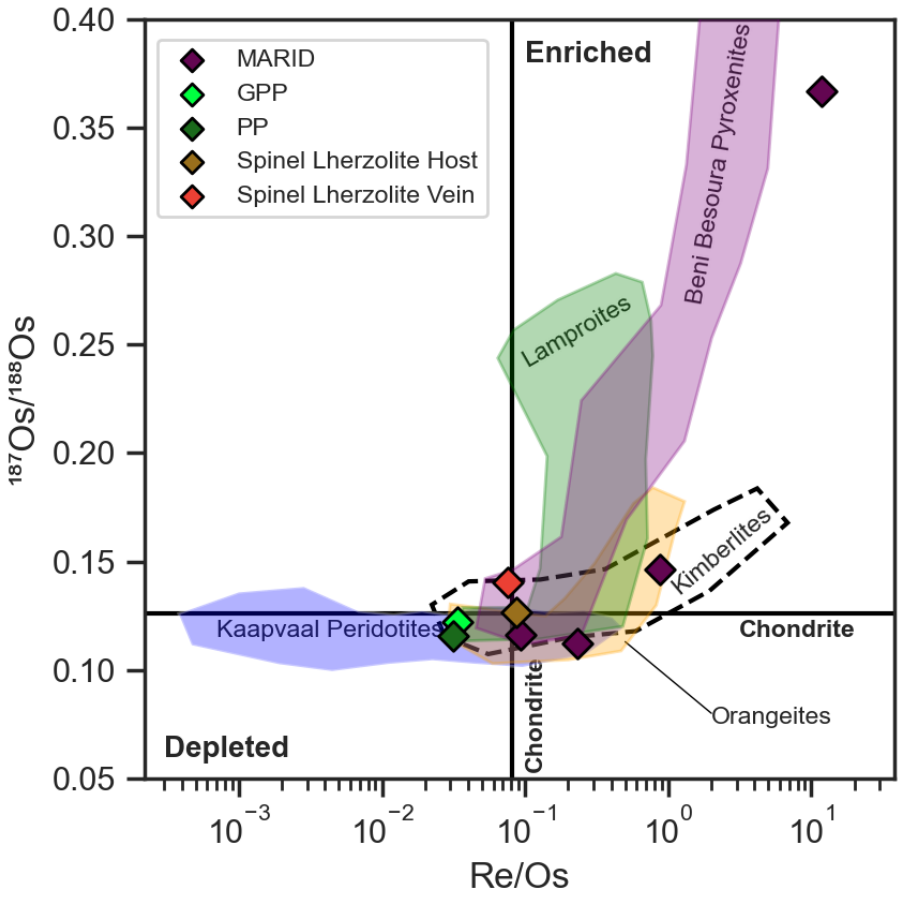

Figure 2.3.19: $^{187}Os/^{188}Os$ vs Re/Os from samples in this study compared to an array of mantle peridotites and mantle-derived melts. Note the log scale on the x-axis. Data points in the lower left quadrant of the diagram are depleted compared to a chondritic composition and require long-term lowered $^{187}Re/^{188}Os$. Data points in the top right quadrant are enriched compared to a chondritic composition and require long-term elevated $^{187}Re/^{188}Os$. Fields for Kaapvaal craton peridotites, lamproites, orangeites, and kimberlites are from Pearson 2019; 2021. Field for lamproites represents both leucite and olivine lamproite samples from North America, Australia, and Southern Africa. Field for orangeites represents samples from Southern Africa. Field for kimberlites represents samples from Southern Africa and Brazil. Field for Beni Bousera pyroxenites from Pearson and Nowell (2004).

The Lherz massif spinel lherzolite displays roughly chondritic values for both Os isotope composition (γOs = 0.282) and Re/Os ratios (0.086) while the cross-cutting amphibole vein is enriched in radiogenic Os (γOs = 11.35) despite a slightly lower Re/Os ratio (0.076), indicating

the inheritance of radiogenic Os from its parental melt. This value also overlaps the range of ocean island basalts (OIB; Figure 2.3.20)

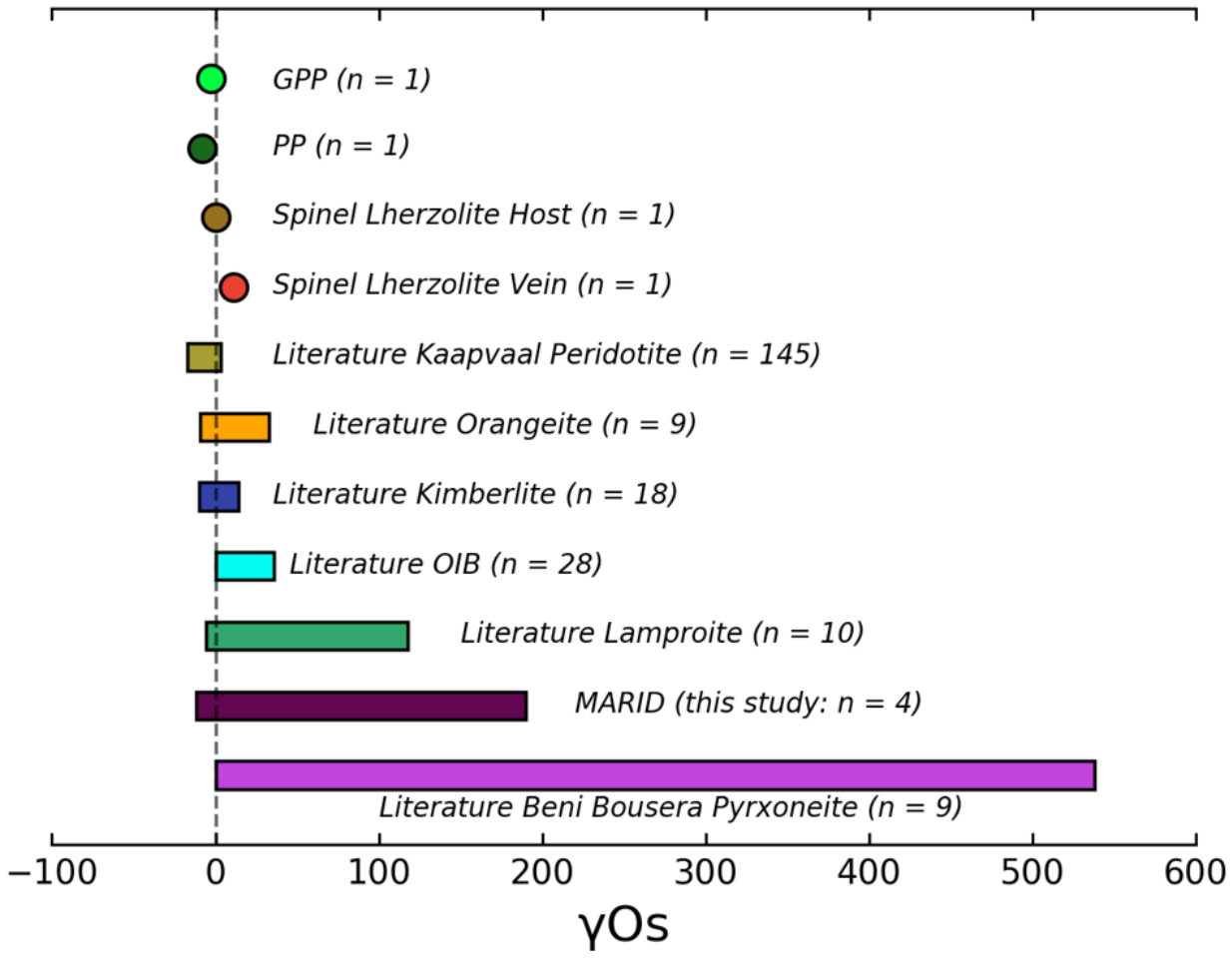

Figure 2.3.20: Comparison of Os isotope compositions in samples from this study vs. an array of mantle peridotites and mantle-derived melts. Os isotope composition is expressed as γOs [($^{187}Os/^{188}Os_{(SampleT)}$ - $^{187}Os/^{188}Os_{(ChondriteT)}$) / $^{187}Os/^{188}Os_{(ChondriteT)}$) * 100]. γOs values were calculated at the time of eruption or massif emplacement and compared to C-chondrite values from Walker *et al*., (2002). Literature γOs values are from the same sources described in Figure 2.3.19 in addition to OIB data from Widom *et al (*1999).

Similar to their IPGE systematics, MARID xenoliths in this study display two distinct sets of Os isotope characteristics (Figure 2.3.19). Two samples (AJE-326 and AJE-335) are enriched in radiogenic Os with γOs values (116 and 11.8 respectively) overlapping the range seen in mantle-derived melts (orangeite/kimberlite/lamproites) or, in the case of AJE-326, an isotopically enriched source such as pyroxenites from the Beni Bousera massif in Morocco (Pearson and Nowell 2004). These two MARID xenoliths are also the samples with highly fractionated

Pd_N/Ir_N described previously. The other two MARID samples analyzed (KDB-20 and AJE-2422) have unradiogenic Os isotopes with γOs values (-12.0 and -7.9 respectively) more typical of Kaapvaal peridotites that have experienced long-term melt depletion. These two MARID samples displayed no Pd_N/Ir_N fractionation. While all four MARID xenoliths contain similar concentrations of Re (0.147 – 0.245 ppb), the two enriched MARID samples with radiogenic Os isotopes have Os concentrations 1-2 orders of magnitude lower than the depleted samples (0.014 and 0.207 pbb vs 1.061 and 1.59 ppb).

2.4 Discussion

The information presented above represents a comprehensive suite of major, trace, and isotopic data at both the mineral and bulk rock scale for a series of modally metasomatized xenoliths. Our data describes the majority of modally altered mantle samples from the Kaapvaal craton associated with metasomatism by intraplate magmatism (excluding the PKP suite) and includes the first published Re-Os isotopic data of MARID xenoliths. In the following sections, we discuss the analytical challenges of quantifying ultra-trace elements, mass balance constraints and major host phases of lithophile trace elements and precious metals in the metasomatized lithospheric mantle and the degree to which mantle-derived melts redistribute these elements. We finish the discussion by examining new geochemical constraints on the source regions and petrogenesis of MARID-veined lithospheric mantle.

2.4.1 Examining Analytical Challenges in Quantifying Precious Metals at the Mineral Scale

Silicate and Oxide Phases

Accurately determining the concentration of precious metals (the PGE, Re, Au, and Ag in the context of this study) in mantle silicate and oxide phases has proven to be extremely difficult due to their ultra-low abundance and potential for contamination by the nugget effect (Lorand *et al*., 2008b). Several previous studies have achieved some success by using chemical digestion of cleaned mineral separates followed by thermal ionization mass spectrometry (e.g., Handler and Bennett 1998; Burton *et al*., 2002). The results of these experiments indicate that silicate and oxide phases in typical fertile lherzolites contain precious metals in the ppt range. Uncertainty in

whether these elements reside within the crystal structure of the minerals in question or are hosted in micro-scale alloy phases further complicates the issue (Burton *et al*., 2002).

In situ analyses of silicates and oxides via LA-ICPMS, while possessing several beneficial attributes, has the drawback of typically less sensitive detection limits when compared with solution digestion methods. Thus, the key analytical limitation faced in our study is the detection sensitivity of our method.

Element	Ag	Re	Pd	Ir	Pt	Au
Mean LOQ (ppb)	20	3.0	6.0	3.0	3.0	8.0

Table 2.4.1: Average limits of quantitation (LOQ) for elements analyzed in silicate and oxide phases via LA-ICPMS. Values originally reported in Section 2.3.3 but are repeated here for ease of access

The limits of quantitation (LOQ) for precious metals analyzed in silicate and oxide phases in our study, while among the lowest reported for studies of this type, are 1-2 orders of magnitude higher than the best estimates for typical mantle concentrations (e.g., Handler and Bennett 1998). Our analyses are unable to precisely constrain precious metal abundances in metasomatized mantle silicates and oxides, however the data enable us to confirm their ultra-trace nature in these phases within a group of rocks not previously characterized.

We also considered a number of precious metal concentrations above the limits of quantitation that were deemed to be analytical artifacts (red values in Appendix B.2.1). This determination was based on readily apparent correlation between precious metal abundance and elements known to form interfering species during laser ablation (Figure 2.4.1; e.g., Sylvester 2007).

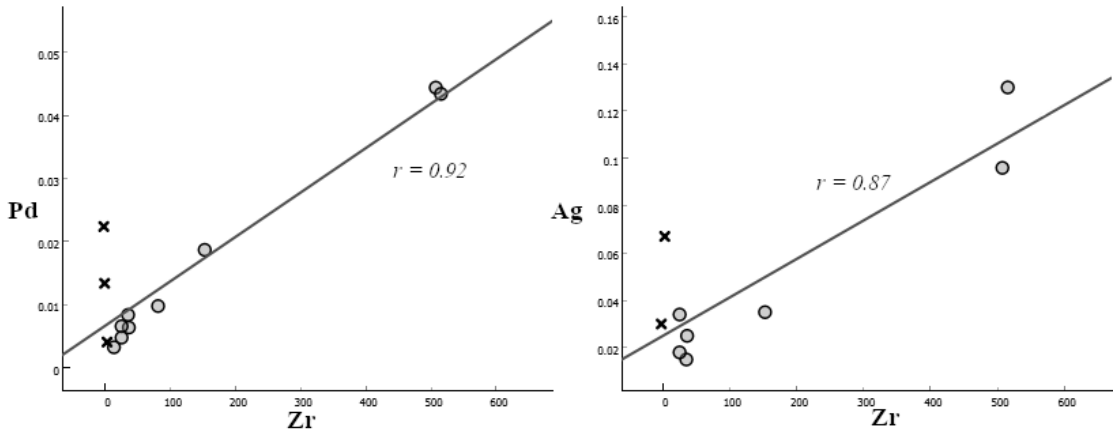

Figure 2.4.1: An example of correlative relationships between precious metal concentration and the presence of elements that typically form isobaric interferences. X symbols represent < 10 ppm Zr

Additionally, rhenium concentrations above detection limits were observed in a variety of phases across all xenolith suites (0.5-3.2 ppb; Appendix B.2.1). These concentrations were not consistent within the observed minerals. For instance, two of the five analyzed phlogopite crystals in sample KDB-20 returned measurable Re concentrations, while three were below detection limits. To test whether these values were likely to be analytical artifacts, we incorporated the observed proportion of Re bearing phases for each sample into mass balance calculations (see Section 2.4.2). The results, even with the most conservative estimates, consistently resulted in a large overestimation of Re compared to whole rock results from ID-ICP-MS (up to 4000% overestimation). Thus we view two possible explanations for Re-bearing silicate/oxide phases: 1) the results are some form of analytical artifact and do not represent real concentrations or 2) silicate minerals in the metasomatized lithospheric mantle contain rare and sporadic Re-bearing inclusions that are not well modelled by mass balance calculations. We choose the most conservative interpretation and treat these values as analytical artifacts going forward. Thus, they are not discussed in mass balance calculations in Section 2.4.2.

We note that better detection limits are possible, using even longer backgrounds than our 60 second counting times, and larger spot sizes, but these conditions might prove prohibitive for routine studies.

Sulphide Phases

Abundances of the PGE in mantle sulphides are typically in the ppm range and are less affected by the sensitivity limitations of LA-ICPMS (Lorand and Luguet 2016). In addition to achieving adequate detection limits, the selection of matrix-matched external calibration standards is a key step in experimental design. For precious metals in sulphides, there is a lack of readily available matrix-matched calibration standards that contain a wide array of elements (Lin *et al*., 2016; Miliszkiewicz *et al.,* 2015). This limitation requires the use of multiple RMs to constrain the different HSE concentrations. Our method used reference material "Po726" (Sylvester *et al*., 2005), a synthetic pyrrhotite ($Fe_{(1-X)}S$) containing verified concentrations of Fe, the PGE, and Au but no Si, Co, Ni, Cu, Ag, or Re. As a result, the elements not present in this matrix-matched standard were calibrated against GSE-1G (a synthetic basalt glass) and may suffer from matrix-dependent elemental fractionation that increases uncertainty in the results (Sylvester 2008). This effect may contribute to the observed difference in Ni concentrations between laser ablation ICP-MS and EPMA analyses (Figure 2.3.3).

In Earth's mantle, sulphide is predominantly stable as Ni-rich, high-T monosulphide solid solution (mss) which breaks down to lower-T, Fe-Ni and Fe-Cu BMS closer to surface (Alard *et al*., 2000; Lorand *et al*., 2010; Lorand and Luget, 2016; Aulbach *et al*., 2021). This has several important implications for analytical work, including that precious metals may redistribute heterogeneously and thus the low-T BMS may not be representative of the original mineral within the mantle unless the entire assemblage is analyzed (unlikely for LA-ICP-MS; Aulbach *et al*., 2021). Additionally, this decomposition of sulphide minerals creates close intermingling of BMS phases that vary at the scale of the laser spot used during ablation (~30-100 µm). This phase heterogeneity, coupled with additional contamination from serpentinization and its by-products (heazlewoodite + magnetite + serpentine), make the large volumes sampled by laser ablation prone to mixed phase analysis (Aulbach *et al.,* 2021; Lawley *et al*., 2020). Due to the scarcity of pristine sulphide phases in the rocks that form this study, we report several mixed phase analyses including pentlandite-magnetite, pentlandite-chalcopyrite, and pentlandite-heazlewoodite (Appendix B.2.2). Internal standard Fe values were adjusted to concentrations intermediate between the mixed phases. A similar strategy was used by Aulbach *et al*., (2021) in their study of mantle sulphides and they found no obvious effects of mixed phase analysis on

precious metal abundances. In our study, an analysis of pure pentlandite in the GPP xenolith showed elevated IPGE/PPGE ratios when compared to the mixed-phase pentlandite-magnetite analyses (Appendix B.2.2). However, this can also be explained by other factors such as multiple populations of metasomatic vs. residual sulphide present in the GPP xenolith (see Section 2.4.3). Analysis of chalcopyrite-pentlandite in the PIC xenolith showed higher Ag, Ru, and Re concentrations than pure pentlandite which could reflect generally higher concentrations of these elements in chalcopyrite (as documented by Richardson *et al*. 2001). Thus the true effects of mixed-phase ablation are non-trivial to unravel using traditional spot analyses. Small-scale (~5 μm) LA-ICPMS element mapping may be better suited to the analysis of complex mantle sulphides (e.g., Lawley *et al*., 2020), though the small spot size severely affects the detection limits of some key elements.

Co-ablation of finely intergrown serpentine during mixed phase analysis often led to elevated concentrations of SiO_2 recorded in our sulphide analyses. We show in this study that silicate phases are not significant repositories for precious metals and so this effect is not likely to effect HSE inter-element ratios but may dilute their overall abundance. To combat this, we required less than 50,000 ppm Si for an analysis to be considered representative of the target mineral. A similar Si cut-off of 40,000 ppm was used in Aulbach *et al*., (2021) which removed most correlative effects between Si and precious metals.

Finally, inclusions of platinum-group minerals (PGM) such as those described in Section 2.3, are now well documented in mantle sulphides (e.g., Luguet *et al*., 2007; Lorand *et al*., 2010). If micro-nuggets of PGM are not directly observed, they are typically identified as spikes in time-resolved LA-ICPMS signals. In the PP xenolith, no spikes were observed in LA-ICPMS signals despite the direct observation of PGM in pentlandite and elevated concentrations of Pt in this sample (Pt_N/Pd_N = 11.96). This may reflect the homogenisation of the signal from these spikes during the ablation and gas mixing process related to LA-ICPMS analysis. Smaller analytical spot sizes would likely resolve better any related signal spikes. Given the incompatibility of Pt in the crystal structure of pentlandite, it is also possible that pentlandites in the PP xenolith are enriched in PGM inclusions to such a degree that they produce consistently elevated time-resolved signals. We reiterate that careful examination of sulphide phases at the micron scale is necessary to properly interpret the results of laser ablation spot analyses.

2.4.2 Comparing Mass Balance Calculations to Whole Rock Analysis: Constraints on Trace Element and Precious Metal Host Phases in the Lithospheric Mantle

Whole rock compositions for metasomatized peridotites and MARID-PIC xenoliths have been reported in several previous studies (Waters, 1987a; Gregoire *et al.,* 2002, 2003) while compositions for some MARID samples in this study (AJE-326, AJE-2422, and AJE-335) were also reported in Fitzpayne *et al*., (2018). Analytical methods for determining bulk rock compositions of mantle rocks derived from kimberlite (XRF; ID-ICP-MS, etc.) do not account for their ubiquitous late-stage modification and thus may not be fully representative of the original whole rock (Fitzpayne *et al*., 2018). To avoid this problem, some studies (including Fitzpayne *et al*., 2018) have concluded that calculated bulk rock reconstructions are more likely to accurately represent the true whole rock. However, this method is sensitive to the accuracy of the modal abundance of primary phases used to calculate the reconstructed composition. In addition, bulk rock reconstructions do not include trace phases that may contribute significant portions of a rock's trace element composition. Metasomatized peridotites and alkali-rich metasomes are sensitive to all of these conditions because: 1) they have experienced late-stage modification from kimberlite entrainment 2) they often show extreme variation in modal abundance of primary phases (especially MARID and PIC xenoliths) and 3) they contain trace phases that are likely to contribute significantly to the trace element budget (e.g., zircon, carbonate, apatite, barite; Fitzpayne *et al*., 2018 & Figure 2.4.2).

In this section, we discuss the reconstructed bulk rock compositions for the metasomatic assemblages analyzed in this study and compare them to whole rock analyses obtained via XRF for major and trace elements and ID-ICP-MS for the PGE and Re. Reconstructed compositions are calculated based on modal abundances of primary phases and mineral chemistry results collected via EPMA and LA-ICP-MS. This includes several elements that were not analyzed via XRF/ID-ICP-MS and we include these in our reconstructed composition in order to discuss the full suite of available trace elements. We estimate a sulphide abundance of 0.1 wt. % in each xenolith (a reasonable proxy based on previous work; e.g., Lorand and Gregoire 2006). Sulphides in the reconstructed models utilize an average composition from each sample and do not represent a particular mineral phase. For instance, both mixed pentlandite-magnetite and pure

pentlandite analyses are present in the GPP xenolith and so we use an average composition from all successful analyses to estimate sulphide contribution to the whole rock budget.

Major and Trace Elements

Mass balance calculations indicate that most major elements can be reliably estimated by modal abundance of primary phases and mineral chemistry results in both peridotites and alkali-rich metasomes (Figure 2.4.2).

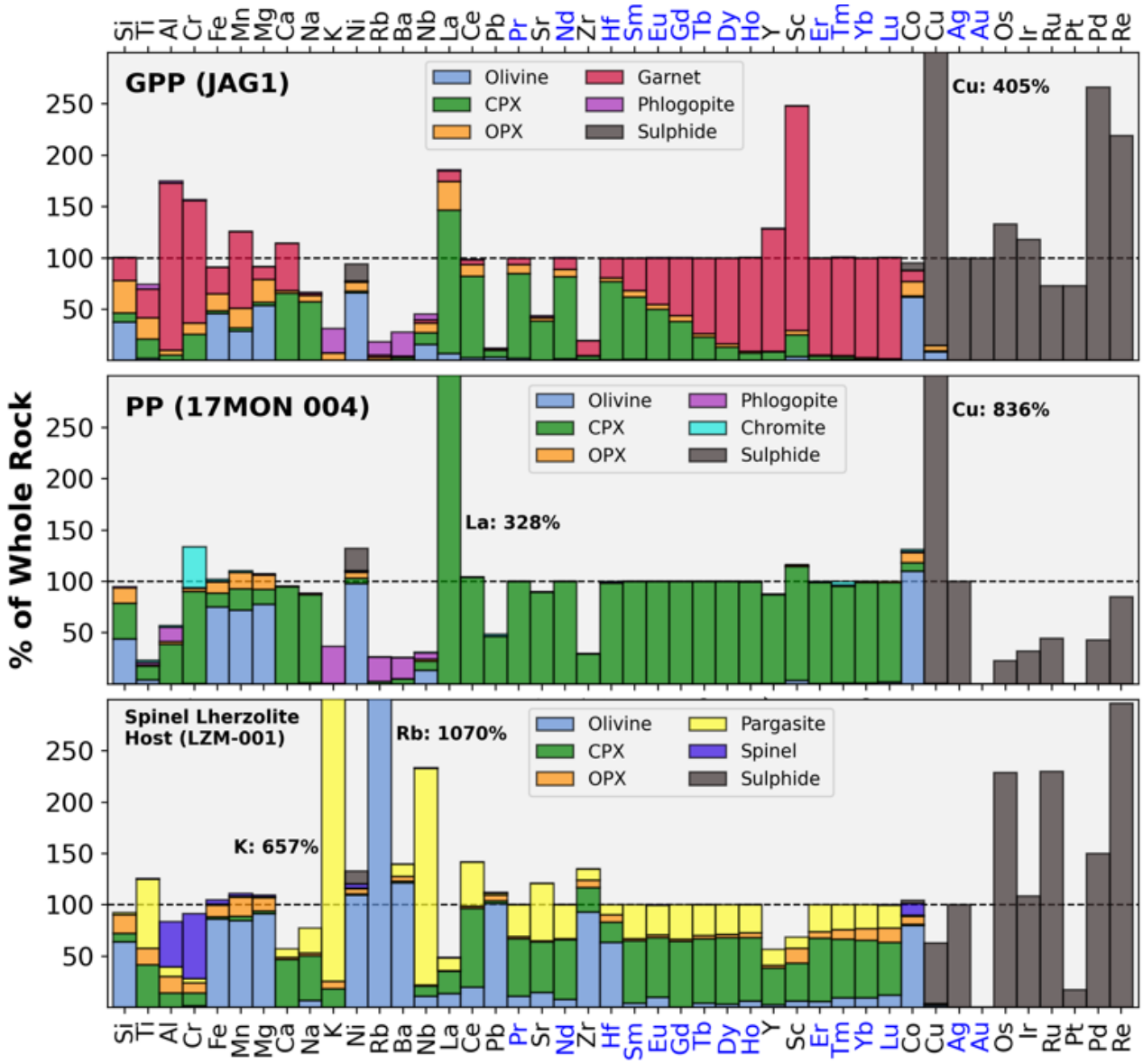

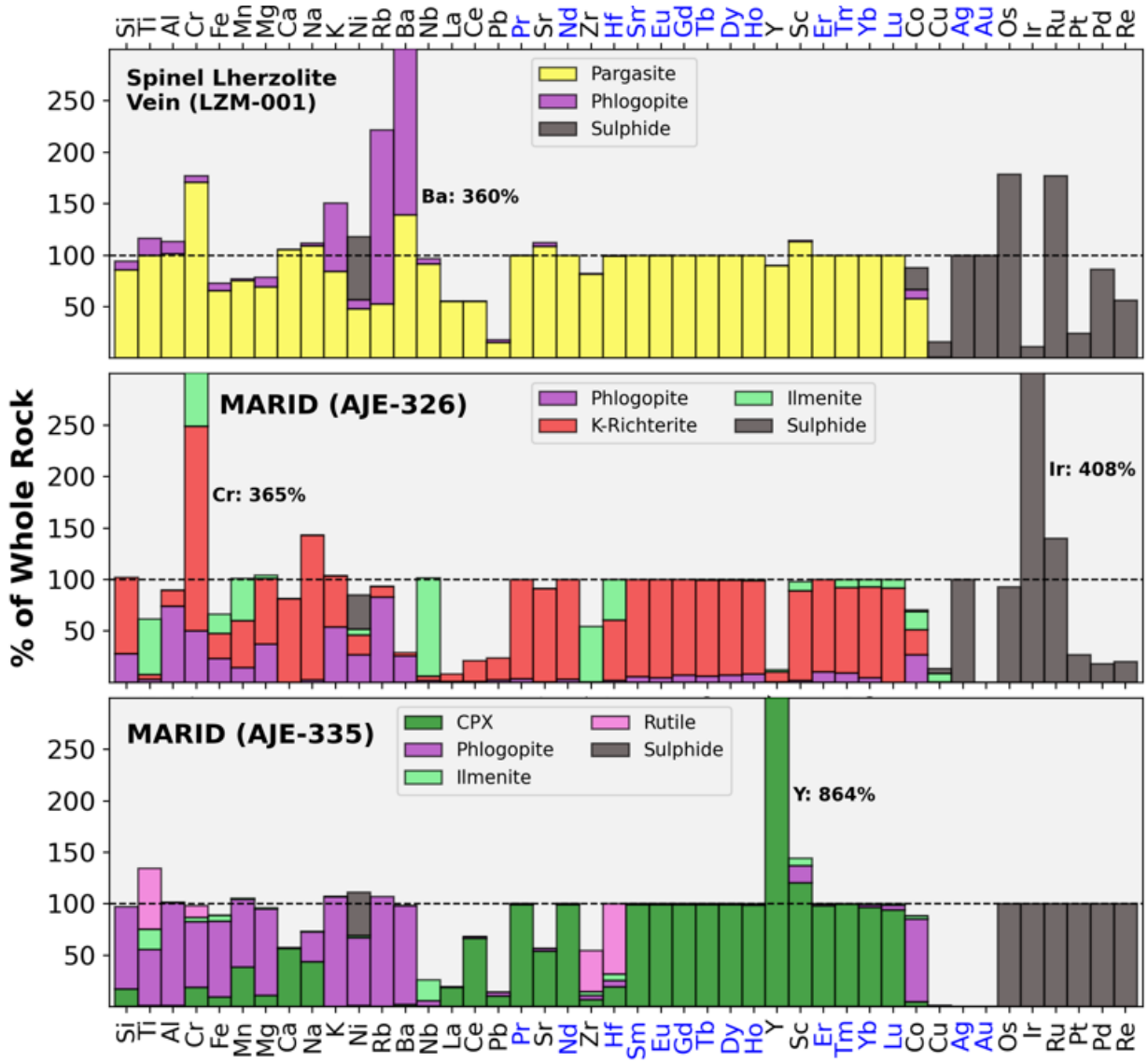
Si Ti Al Cr Fe Mn Mg Ca Na K Ni Rb Ba Nb La Ce Pb Pr Sr Nd Zr Hf Sm Eu Gd Tb Dy Ho Y Sc Er Tm Yb Lu Co Cu Ag Au Os Ir Ru Pt Pd Re
Spinel Lherzolite Vein (LZM-001)
Pargasite
Phlogopite
Sulphide
Ba: 360%
MARID (AJE-326)
Phlogopite
K-Richterite
Ilmenite
Sulphide
Cr: 365%
Ir: 408%
MARID (AJE-335)
CPX
Phlogopite
Ilmenite
Rutile
Sulphide
Y: 864%
% of Whole Rock
50
100
150
200
250

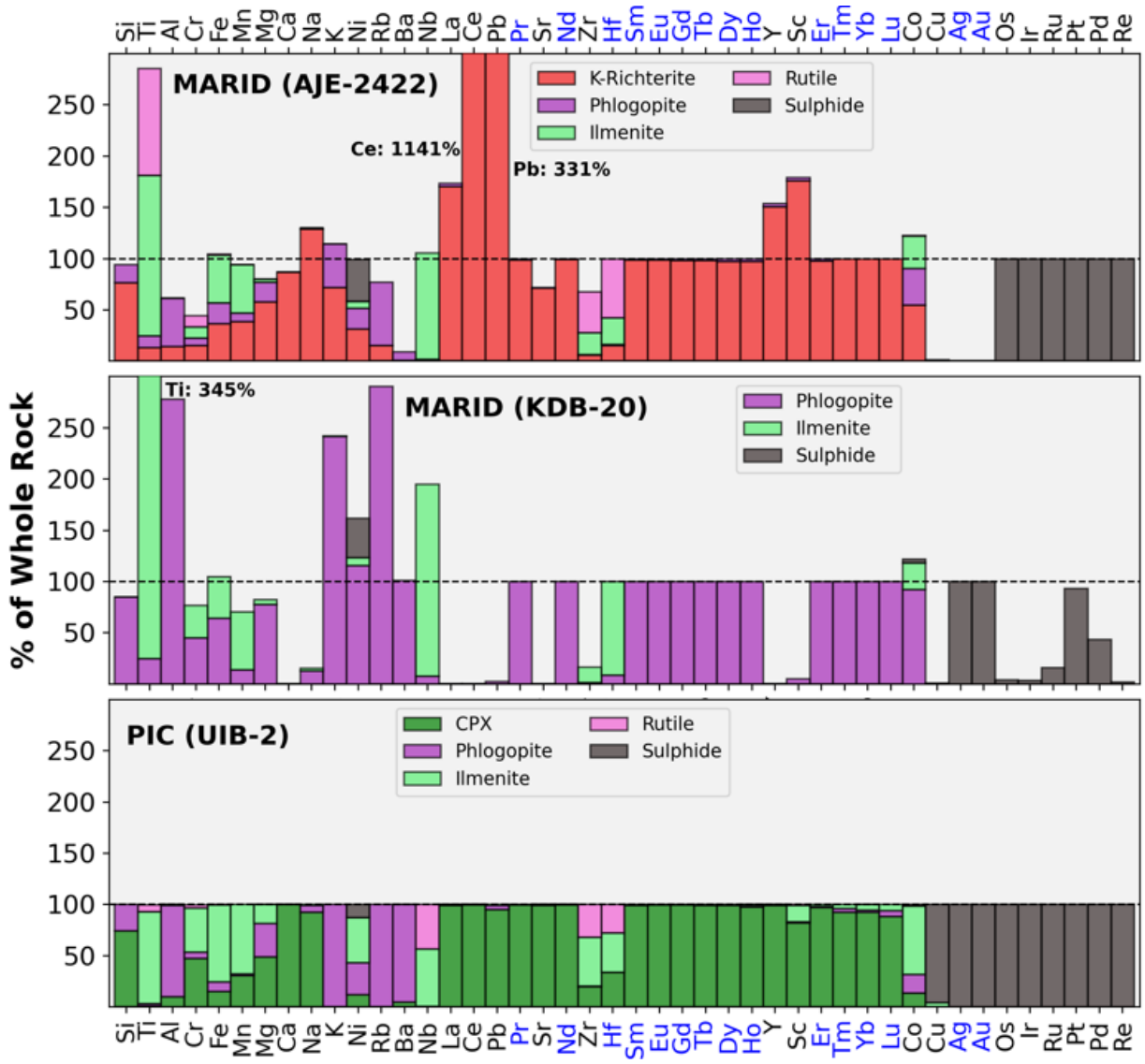

Figure 2.4.2: Primary mineral phases in metasomatized mantle xenoliths from this study and their percent contributions of major and trace elements to the whole rock budget. Elements with black text on the x-axis indicate the reconstructed concentrations are being compared to whole rock analyses obtained via XRF/ID-ICP-MS and can thus be higher or lower than the true value. Elements with blue text on the x-axis were not analyzed via XRF/ID-ICP-MS and are presented as contributions to the calculated whole rock value (i.e., they will always be equal to 100%). Sample UIB-2 is the exception to this and all values represent contributions to a calculated whole rock value. No sulphides were successfully analyzed in samples AJE-335 and AJE-2422 and thus the model assumes 100% of precious metals reside in sulphide phases for these two samples. Values that exceed the y-axis scale are marked as such to preserve visibility of other elements.

Si, Fe, Mn, Mg, and Ni all show good agreement with XRF values across all analyzed xenoliths with a median disagreement of 24.2% and a maximum disagreement of 61.5% (Ni in sample KDB-20). Given that Ni abundance is partially controlled by the presence of Ni-Fe sulphides, the close agreement between calculated and XRF values provides additional confidence in the value

used to estimate sulphide abundance (0.1 wt. %). Calcium and sodium are also well estimated in all samples aside from KDB-20 (median disagreement of 13.9 % and a maximum disagreement of 43.3%) despite these elements being controlled by phases prone to metasomatic heterogeneity (clinopyroxene, k-richterite, phlogopite; Figure 2.4.2).

The metasomatized peridotites from Southern Africa show notable underestimations of Ti, K, Nb, Rb, and Ba while the amphibole vein and host peridotite from the Lherz Massif show large overestimations of the same elements. In the Lherz Massif sample, the anomalously high values appear to be driven primarily by an overestimation of pargasite amphibole in modal abundance calculation. In addition, olivine in LZM-001 showed anomalous concentrations of Rb and Ba that are not reflected in whole rock values.

In the South African peridotites, the message is more complex. Discrepancies in highly incompatible elements (K, Nb, Rb, Ba) are well documented in cratonic peridotites and attributed to a variety of factors including kimberlite melt infiltration or the presence of alkali-rich fluid inclusions in silicate phases (e.g., Rosenbaum *et al*., 1996; Bedini and Bodinier 1999; Pearson *et al*., 2003). In addition, Kalfoun *et al*., (2002) determined that up to 99% of the Nb budget in a suite of Siberian lherzolites was stored in trace disseminated rutile. Given the modal metasomatism shown in our South African peridotites and the underestimation of elements controlled by rutile and phlogopite (Ti and Nb in rutile; K, Rb, Ba in phlogopite), we evaluate the potential effects of trace phases and kimberlite melt infiltration using the GPP xenolith as a reference peridotite (Figure 2.4.3). The addition of 0.4 wt. % primary kimberlite magma (Becker and Le Roex 2006) to the GPP xenolith estimates the concentrations of Ti and Nb reasonably well but does not significantly impact the deficits in LILE (Figure 2.4.3 A). The addition of kimberlite, trace rutile, and phlogopite shown in Figure 2.4.3 (B) has a more pronounced effect. Phlogopite accurately accounts for K and Ba (though not Rb) while even minor amounts of metasomatic rutile (0.01 wt. %) grossly overestimates the Nb budget. This is due in part to the extremely Nb-enriched rutile composition (~1 wt. %; sample UIB-2) used in the model. Addition of 1.5 wt. % phlogopite and 0.4 wt. % kimberlite melt produces the most accurate reconstruction with good estimates of all elements with the exception of Rb. Thus, a combination of trace phases and kimberlite melt likely all contribute to the highly incompatible element budget of metasomatized South African peridotites. If trace metasomatic rutile is present, it will likely be

expressed as Nb values well in excess of mass balance calculations. A variety of other trace phases including ilmenite, barite, apatite, and alkali-rich fluid inclusions are also likely contributors to the trace element budget and are difficult to account for in mass balance calculations. Similar to previous studies, we conclude that highly incompatible LILE and HFSE abundances in peridotites are not coherently explained using mass balance estimations and that heterogeneous distribution of metasomatic phases further complicates the development of accurate models (e.g., Fraser *et al*., 1984; Erlank *et al*., 1987; Gregoire *et al*., 2003).

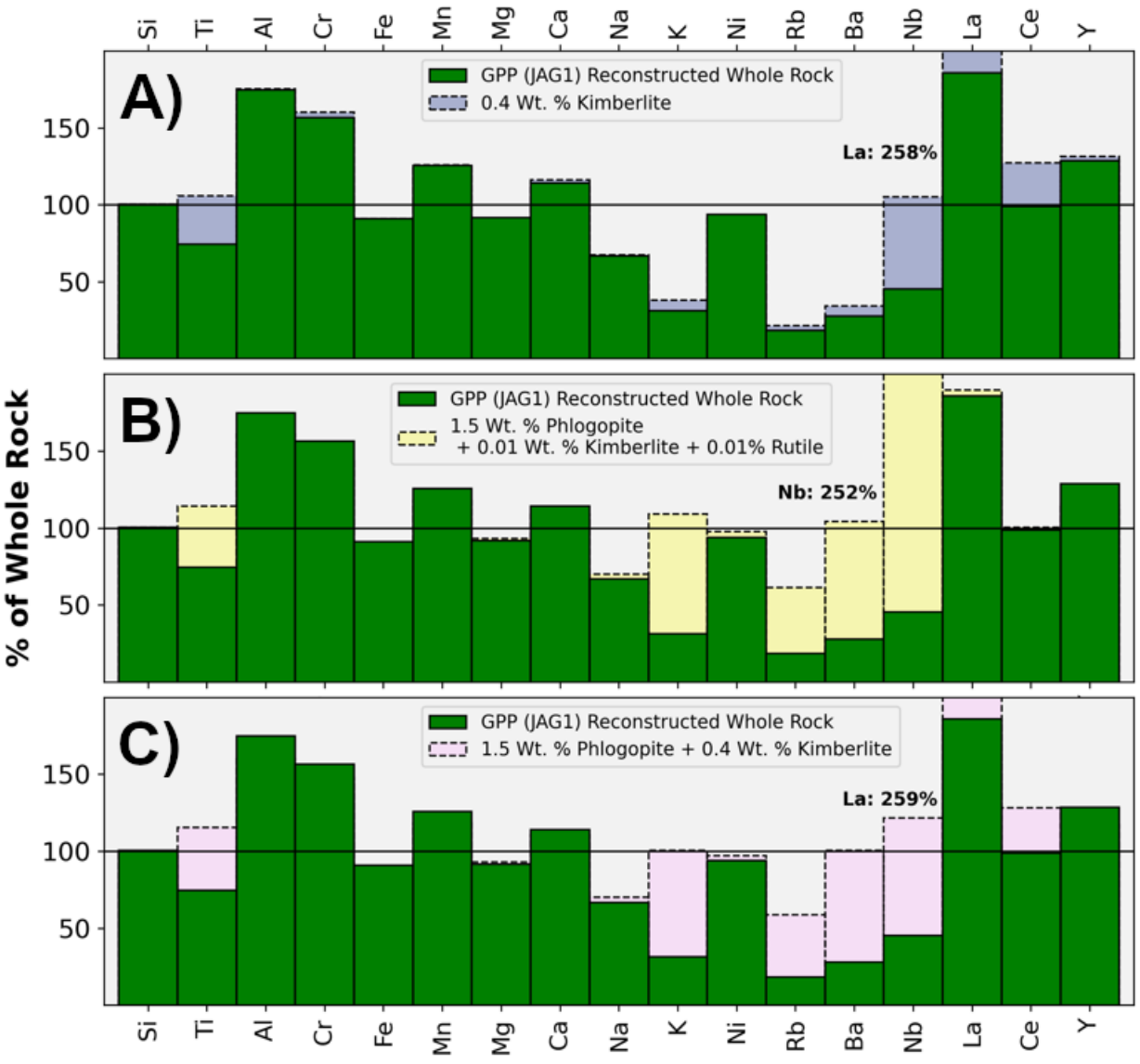

Figure 2.4.3: Reconstructed whole rock composition of selected elements in the GPP xenolith. A) The addition of 0.4 wt. % kimberlite B) The addition of 1.5 wt. % phlogopite, 0.01 wt. % kimberlite, and 0.01% wt. % rutile C) The addition of 1.5 wt. %

phlogopite and 0.4 wt. % kimberlite. Primitive kimberlite composition from Becker and Le Roex (2006). Phlogopite composition from JAG1 mineral chemistry results. Rutile composition from UIB-2 mineral chemistry results.

In the alkali-rich metasomes, LILE abundances are primarily controlled by phlogopite while ilmenite and rutile are the major reservoirs for HFSE. Interestingly, concentrations of these elements in the MARID, PIC, and amphibole vein samples are more appropriately constrained by our model than in the metasomatized peridotites (Figure 2.4.2). This is potentially due to several factors including 1) the overall higher abundance of these elements in alkali-rich metasome samples making them less prone to effects from trace phases or melt infiltration (e.g., Pearson *et al*., 2003) and 2) the coarser grain size of HFSE-LILE bearing phases allows for more accurate estimation of modal abundance and thus mass balance results.

Similar to the LILE and HFSE, REE abundances in mantle peridotites have typically been underestimated by mass balance calculations in previous studies (e.g., Schmidberger and Francis 2001; Pearson and Nowell 2002). This is especially true for the LREE and most models indicate that addition of kimberlite melt explains these deficiencies. In our samples, La and Ce were the LREE analyzed by XRF. Cerium is the most useful proxy to examine LREE deficiencies as La was frequently below detection limits in XRF analyses and is thus more challenging to evaluate (value of 0.5*LOD was used in Figure 2.4.2). Contrary to other studies, Figure 2.4.2 shows that reconstructed compositions almost perfectly replicate Ce concentrations in both the South African and Lherz Massif peridotites. The addition of a kimberlite component shown in Figure 2.4.3 causes a small overestimation of Ce but is still within reasonable bounds of the true value. In all samples, LREE abundance is controlled primarily by clinopyroxene and the whole rock composition reflects the enriched signature of this mineral in each sample. This result reinforces that LREE enrichment accompanies modal metasomatism in a variety of lithospheric mantle settings (cratonic and non-cratonic). This has previously been interpreted as resulting from small-volume, incompatible element-rich silicate melts percolating through depleted mantle lithosphere (e.g., Le Roux *et al*., 2007; O'Reilly and Griffin 2013) and our peridotite samples from both South Africa and the French Pyrenees are consistent with this conclusion. Such a melt may directly crystallize LREE-enriched clinopyroxene or cryptically modify the signature of pre-existing grains (O'Reilly and Griffin 2013). This also implies that modally metasomatized peridotites may not show LREE deficiencies from mass balance calculations described in

previous studies as the enriched composition of their clinopyroxenes buffer them to the effects of kimberlite melt infiltration.

Alkali-rich metasomes have LREE budgets that are controlled primarily by amphibole or clinopyroxene depending on which phase is dominant (Figure 2.4.2). Cerium abundances are significantly underestimated in the majority of samples (AJE-326, AJE-335, KDB-20, LZM-001 vein) with primary phases accounting for an average of ~40% of the whole rock budget. In the South African MARID and PIC samples, a kimberlite component of 1 wt. % accounts for most discrepancies. However, the amphibole vein in sample LZM-001 shows the same LREE discrepancy and cannot be explained by the addition of kimberlite.

HREE abundances in mantle peridotites have been shown to completely reside in primary silicate phases (Pearson *et al*., 2003; Gregoire *et al*., 2003) and our mass balance calculations indicate that this is also the case in modally metasomatized samples. Yttrium (which behaves similarly to the HREE) concentrations are controlled by both garnet (if present) and clinopyroxene in our peridotite samples and mass balance values are within 30% of XRF results for the South African samples. The Lherz Massif sample shows a 52% deficiency in Yttrium concentration, but given the associated deficiencies of Ca and Na this is likely caused by an underestimation of modal clinopyroxene (increasing clinopyroxene abundance by 5% roughly balances the Ca, Na, and Y concentrations). Yttrium concentrations are very low in the South African MARID samples (at or below the XRF detection limits of 0.5 ppm) and are thus prone to error in mass balance calculations. This is reflected in Figure 2.4.2 where mass balance concentrations show poor agreement with XRF values. In contrast, the spinel lherzolite amphibole vein is extremely enriched in Y (24.6 ppm) and mass balance calculations show good agreement with XRF values.

Finally, the concentrations of trace transition metals (Co, Cu) display contrasting trends. Cobalt receives contributions from almost all primary silicate and oxide phases (dominantly olivine if present) and is generally very well accounted for in both peridotite and alkali-rich metasome mass balance calculations. Conversely, copper shows almost no coherence with mass balance calculations. Copper concentrations in cratonic and orogenic peridotites are typically low (< 10 ppm) and mostly reside within BMS phases (Lorand and Luguet 2016). Thus it is extremely sensitive to the composition of sulphides used in mass balance calculations. In our South African

peridotites, Cu concentrations are very low (1 – 3.5 ppm) and so even the small amounts of copper present in our average sulphide compositions severely overestimate abundances in these samples. In contrast, the 12 ppm Cu in the Lherz spinel lherzolite is only 59% accounted for by the average sulphide composition suggesting the presence of Cu-rich BMS that were not analyzed by LA-ICP-MS. Both the GPP xenolith and the Lherz spinel lherzolite receive small Cu contributions from olivine (8.4 % and 2.4 % respectively) and orthopyroxene (4.8 % and 0.66 % respectively) confirming results from experimental studies showing that these two phases preferentially concentrate Cu over other silicates (Liu *et al*., 2014; Bussweiler *et al.* 2019; Veglio *et al.* 2022). The South African MARID samples are anomalously enriched in copper (47-137 ppm) to supra-primitive mantle values. This feature, to the author's knowledge, has not been previously noted in MARID xenoliths and the enrichment is not accounted for by BMS in our mass balance composition. Section 2.3.1 notes the observed occurrences of native Cu metal in MARID samples and this may account for a portion of the Cu enrichment. However, it is unclear whether native Cu is an exotic primary feature of MARID xenoliths or if it is the result of serpentinization in pre-existing BMS (e.g., Aulbach *et al*., 2021).

Precious Metals

Results outlined in Section 2.3 show that silicate and oxide phases are negligible contributors to the whole rock precious metal budget of cratonic metasomes and that sulphides contain these elements in concentrations 2-6 orders of magnitude higher than the bulk rock. Therefore, mineral chemistry results reinforce the conclusions of previous work that most precious metals are indeed stored within BMS phases (Morgan 1986; Lorand *et al*., 2008; Lorand *et al*., 2013; Lorand and Luguet 2016). However, the exact nature of the BMS reservoir is not straightforward. Experimental work by Ballhaus *et al.,* (2006) showed that all of the PGE partition relatively equally into sulphides (sulphide melt – silicate melt partition coefficients of 10^3 to 10^6) and thus any mantle-derived melt formed in equilibrium with residual sulphide should be precious metal poor due to their preference for remaining in the BMS phase (Lorand and Luguet 2016). If the degree of partial melting becomes high enough to completely dissolve residual sulphide (~30%; Lorand *et al*., 2008), then the resulting magma should be PGE rich. Put more simply, these results indicated that all PGE should remain in the sulphide phase until BMS is completely dissolved at high degrees of melting. This posed significant problems as direct

observation of refractory cratonic peridotites (e.g., Pearson *et al*., 2004) display fractionated PGE patterns such as the typical South African peridotite shown in Figure 2.3.18. The main theory proposed to explain this behavior suggests that mantle BMS melts incongruently; first liberating a Cu-Fe rich melt that preferentially partitions the PPGE, Re and Au while the IPGE remain in the residual peridotite via the BMS crystal structure and microscale Os-Ir-Ru alloy phases (Luguet *et al*., 2007; Lorand and Luguet 2016). In addition, partial melting as low as 10% has been shown to form microscale Pt-Ir alloys in BMS through desulphidation that can cause anomalously high concentrations of both elements in residual sulphides (Peregoedova *et al*., 2004). In contrast to the effects of partial melting which unevenly fractionate the PGE, xenoliths that show pervasive evidence of metasomatism have PGE abundances that are reduced by as much as 80% relative to PUM, resulting from the dissolution of intergranular sulphides (Lorand and Alard 2001). Samples that have only interacted with small metasomatic melt fractions show re-enrichment in the PPGE and elevated Pd_N/Ir_N (Pearson *et al*., 2003) due to the precipitation of PPGE-rich metasomatic sulphides. Thus, there are significant complexities in interpreting mass balance calculations from mantle BMS, including that residual vs. metasomatic and Cu vs. Ni rich sulphides will have very different PGE systematics. Microscale alloys of Pt-Ir and Os-Ir-Ru have the potential to further confound calculations.

Figure 2.4.2 shows that there is often poor agreement between reconstructed and whole rock concentrations of the PGE and Re. These elements are prone to both over and underestimation by our model. It is worth reinforcing several limitations in our precious metal mass balance calculations before examining these discrepancies further: 1) We assume that the entire precious metal budget lies within BMS phases 2) No Cu-Fe BMS were successfully analyzed via LA-ICP-MS which likely impacts the abundance of elements that preferentially partition into these phases (Pd, Re, Au; Lorand and Luguet 2016) and 3) Since all BMS analyzed were Fe-Ni phases, we use an average of all successful sulphide analysis points within each sample to determine the reconstructed precious metal composition. This method produced the most accurate reconstruction but considers anomalously high or low concentrations equally to more common values.

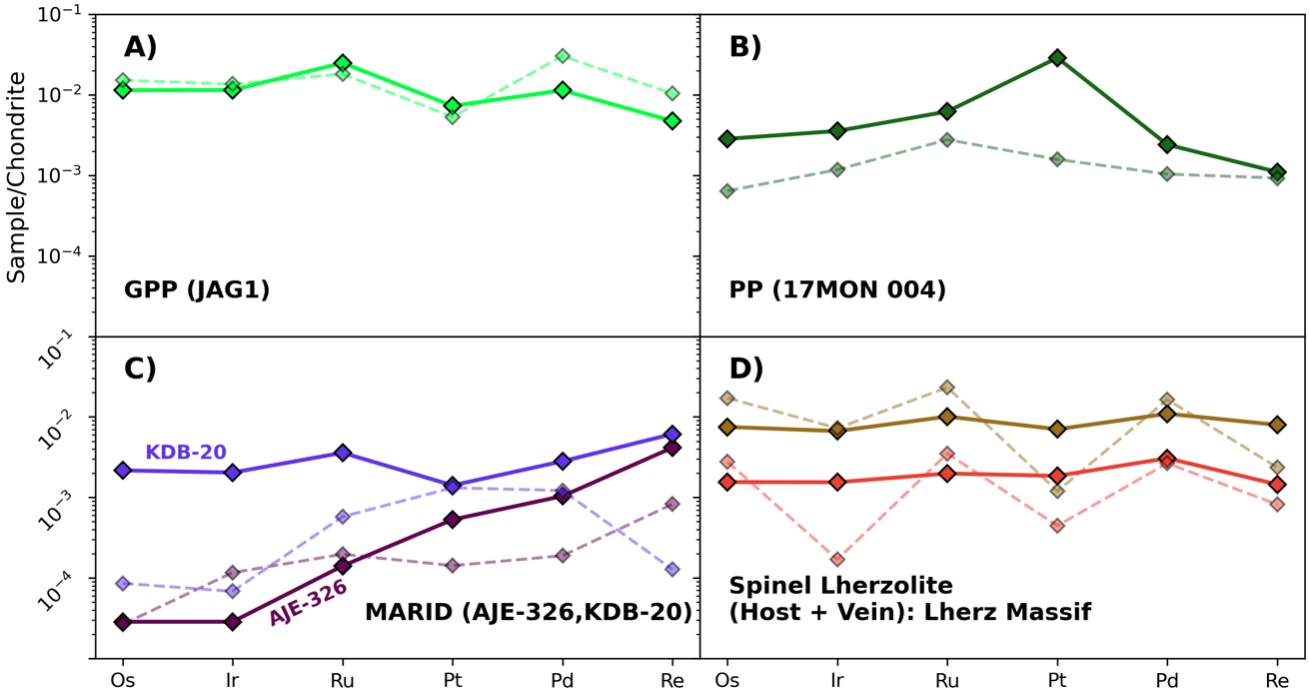

Figure 2.4.4: Chondrite normalized precious metal concentrations from whole rock analysis (solid line) and mass balance reconstruction (dashed line) using 0.1 wt% average sulphide composition from samples where BMS were successfully analyzed. Note that two MARID xenoliths (AJE-2442 and AJE-335) and the PIC xenolith (UIB-2) are not included due to limited data.

The GPP xenolith shows the closest agreement between mass balance calculations and whole rock analysis (Figure 2.4.2; Figure 2.4.4). Osmium and Iridium are entirely accounted for in the reconstruction with slight excesses of 32% and 18% respectively while ruthenium concentrations also show good agreement (72% accounted for by BMS). This reinforces that, in refractory peridotites, IPGE behavior is well explained by BMS and that small degrees of modal metasomatism does not substantially alter their abundance. Surprisingly, the PPGE are also well explained by mass balance calculations. Platinum is 73% accounted for by BMS despite the well-known incompatibility of Pt in Fe-Ni sulphides (Lorand and Luguet 2016) while palladium and rhenium are overestimated by the reconstructed composition (266% and 219% of the whole rock budget respectively). The simplest explanation for the overestimation of the PPGE would be an unintentional bias towards analyzing PPGE-enriched metasomatic sulphides. However, this explanation is seemingly contradicted by the good agreement in IPGE abundances that would indicate a balanced sampling of both residual and metasomatic populations. Possible mechanisms for this enrichment are discussed in Section 2.4.3, but we note here that the broadly

chondritic PPGE/IPGE ratios observed in GPP sulphides and thus the reconstructed composition are not easily explained.

In contrast, the PP xenolith shows poor coherence between mass balance calculations and whole rock analysis. While Figure 2.4.4 shows that both the reconstruction and whole rock display broadly similar chondrite normalized PGE patterns, BMS accounts for only 22 to 44% of IPGE concentrations and 43% of palladium. The anomalously high Pt concentrations observed in whole rock analysis are essentially absent in the reconstructed composition (0.5% of the whole rock Pt budget) reinforcing the role of microscale alloy phases as an important contributor (~99% in this case) to the platinum budget in some samples. Given the textural evidence of melt infiltration in this sample and the low total PGE abundances, it is possible that interaction between the PP xenolith and a melt at high melt/rock ratios dissolved a large portion of intergranular sulphides. Desulphidation of the remaining BMS phases may have resulted in heterogenous PGE distribution and a high proportion of Pt-rich alloy (Lorand and Luguet 2016).

BMS accounts for all osmium, palladium, and ruthenium in the Lherz Massif lherzolite and amphibole vein. Unlike the two South African peridotites, reconstructed chondrite normalized PGE patterns of the Lherz lherzolite and vein show a deficiency in Pt (83% and 76% deficit respectively) due to Pt-pentlandite incompatibility. One peculiar feature of the Lherz sample is the elevated osmium concentrations of the sulphides used in our reconstruction. This manifests as unusually high reconstructed Os_n/Ir_n in both the lherzolite ($Os_n/Ir_n = 2.37$) and amphibole vein ($Os_n/Ir_n = 16.4$) that are not mirrored in whole rock analysis ($Os_n/Ir_n = 1.13$ and 1.01 respectively). Luguet *et al*., 2007 noted the occurrence of Ru-Os alloys in residual harzburgites of the Lherz Massif. An unknown bias towards analyzing sulphides with Ru-Os inclusions could result in the observed Os_n/Ir_n of our reconstructions. This is supported by the co-existing elevated Ru_n/Ir_n in the reconstructed Lherz amphibole vein ($Ru_n/Ir_n = 20.7$) compared to whole rock analysis ($Ru_n/Ir_n = 1.29$).

Of the MARID samples, only AJE-326 and KDB-20 had adequate data to produce reconstructed compositions and both samples show variable coherence with whole rock analysis. In sample KDB-20, the IPGE are significantly underestimated by analyzed BMS (3.96%, 3.35%, and 16.1% of the whole rock budget for Os, Ir, Ru respectively). This discrepancy can be accounted for by the incorporation of an IPGE-rich “residual peridotite” component which is discussed

further in Section 2.4.3, but indicates that sulphides directly precipitated in MARID-type melts are very IPGE-poor. Similarly, the reconstructed composition for AJE-326 is IPGE-poor and shows elevated Re relative to the PPGE in Figure 2.4.4.

In summary, mass balance calculations from our samples reinforce the major role of BMS and microscale PGM as the major repository for precious metals in the lithospheric mantle. The most refractory and least metasomatized samples (GPP xenolith and the Lherz Massif lherzolite) show the most agreement between BMS mass balance and whole rock analysis (especially the IPGE) indicating that small melt volumes do not heterogeneously redistribute the PGE and Re. In contrast, samples that have been pervasively metasomatized by high melt fractions (PP xenolith) and samples derived from mantle melts (MARID xenoliths) show poor coherence between BMS reconstruction and whole rock analysis. The dissolution of intergranular sulphide, precipitation of PGE-poor metasomatic BMS, and the formation of PGM alloys via desulphidation reactions likely all contribute to this heterogeneity.

2.4.3 Precious Metal Systematics in the Metasomatized Lithospheric Mantle: Evaluating a Potential Source Rock for Magmatic Ore Deposits

Given the well-established models linking metasomatized upper mantle to basalt-hosted PGE deposits (Bushveld Complex- Barnes *et al*., 2010; Norilsk Intrusions- Begg *et al*., 2013), we examine new evidence from our study as well as previous work to re-evaluate the lithospheric mantle's potential role as a precious metal-bearing source rock.

Precious Metal Systematics of Mantle Derived Melts

Cratonic peridotites have consistently shown low total PGE content and depleted PPGE patterns from ancient high degree melting events (Pearson *et al*., 2004; Maier *et al*., 2012). Thus, the percolation of mantle derived, small-degree silicate melts is thought to re-enrich the lithospheric mantle in PPGE and other ore forming elements in both cratonic and non-cratonic settings. (Pearson *et al*., 2003; Griffin *et al*., 2013; Lorand and Luguet 2016).

Kimberlites, orangeites, and lamproites of the Kaapvaal Craton represent examples of such melts that derive from geochemically enriched source regions within the mantle, while MARID and

PIC xenoliths likely crystallize directly from interaction between these melts and lithospheric peridotite (Chapter 3 of this study; Gregoire *et al*., 2002). Despite this, little direct observation of precious metal systematics in alkali-rich metasomes and volatile-rich mantle magmas has been recorded. Limited data on Kaapvaal Craton kimberlites and Karelia craton orangeites from Maier *et al*. (2017) show that they contain lower PGE contents (even of the incompatible PPGE) than an average South African cratonic peridotite (Figure 2.3.18) and thus mixing between these two components should decrease total PGE abundance.

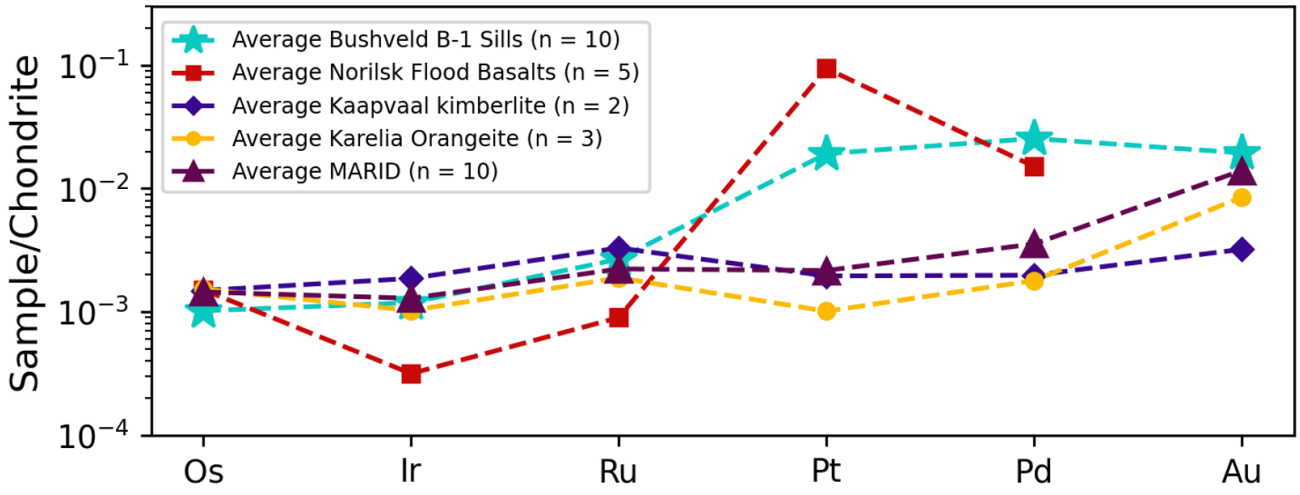

Figure 2.4.5: Chondrite normalized precious metal plots for magmas associated with Ni-Cu-PGE deposits and intraplate mantle derived melts. Data for the Bushveld B-1 sills from Barnes *et al*. (2010). Data for the Norilsk Region flood basalts from Izokh *et al*. (2016). Kimberlite and orangeite data from Maier *et al*. (2017). MARID is an average from this study combined with Maier *et al*. (2012). Note similar Au anomalies between orangeites and MARID xenoliths.

Additionally, unevolved magmas associated with the formation of Ni-Cu-PGE deposits show strong PPGE enrichment while kimberlites, orangeites, and MARIDs are all ~1 order of magnitude lower in PGE concentrations on chondrite normalized plots (Figure 2.4.5). Therefore, based on the available data, it appears unlikely that small volume, alkali-rich silicate melts are capable of enriching the lithospheric mantle in the PGE. Similar conclusions were reached by Maier *et al*. (2017) in which they determined that the metasomatized lithospheric mantle was unlikely to contribute to the formation of the Bushveld Complex based on the PGE poor nature of most xenoliths. They further showed that the unfractionated patterns observed in kimberlites and orangeites could be derived from the mixing of a melt that is PGE poor with high PPGE/IPGE ratios and Kaapvaal Craton SCLM.

A similar explanation can be used to account for most of the variable PGE systematics observed in MARID xenoliths from this study. Given that the majority of the mantle PGE budget is stored in BMS and that small volume silicate melts have been shown to readily dissolve these phases when percolating through mantle peridotite (Lorand and Alard 2001), MARID xenoliths crystallizing from an alkali-rich magma could acquire a peridotitic signature through progressive dissolution of wall rock sulphide.

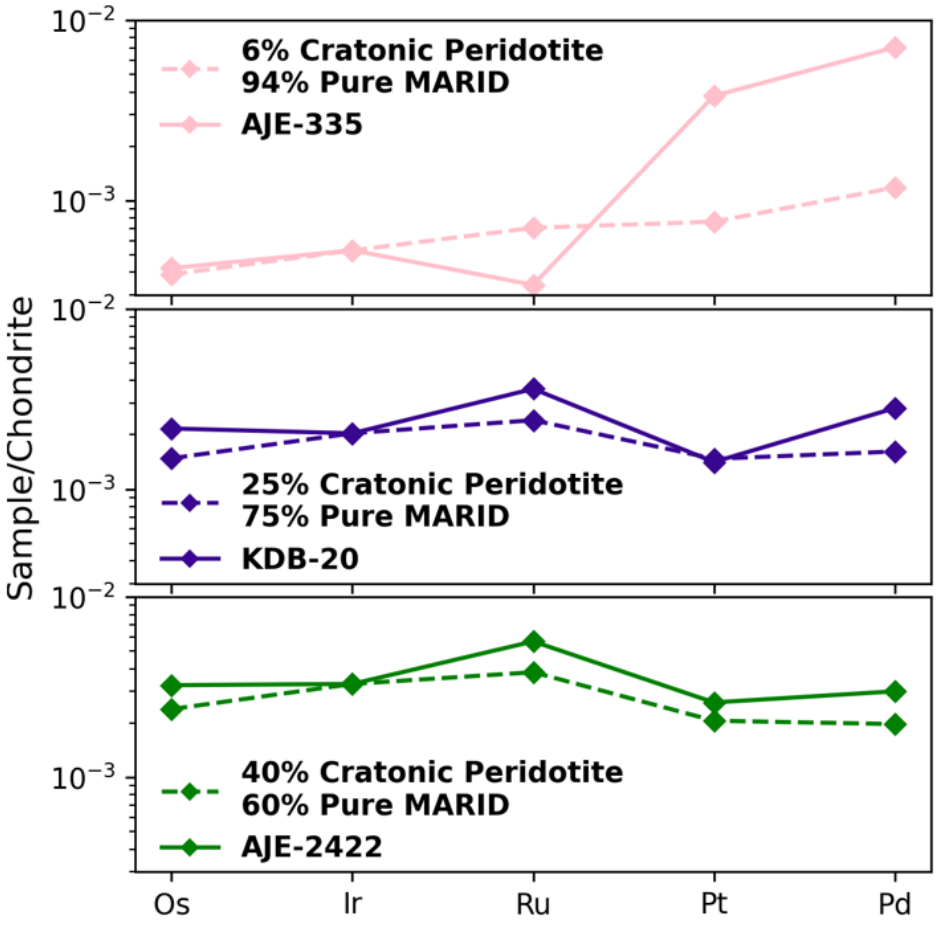

Figure 2.4.6: PGE abundances in MARID xenoliths from this study vs. two component mixing between average South African peridotite and a "pure" MARID composition. Pure MARID is based on sample AJE-326 which showed the most highly fractionated PPGE/IPGE ratios and is PGE-poor. Average South African peridotite from Maier *et al*. (2017). Component fractions in the mixing model are based on iridium contents of each end member.

Simple two component mixing between a "pure" MARID endmember (i.e., sample AJE-326 which showed the highest PPGE/IPGE ratios) and South African cratonic peridotite (Maier *et al*. 2017) shows that a peridotite component between 5-60% broadly reproduces the variable patterns observed in MARID samples (Figure 2.4.6). The exceptions to this are the relatively

high values of platinum and palladium in sample AJE-335. While a 6% peridotite component is sufficient at explaining IPGE abundance, the PGE-poor nature of the chosen MARID endmember composition results in a significant underestimation of Pt and Pd for sample AJE-335 (Figure 2.4.6). It is possible that the AJE-335 MARID xenolith derived from a magma richer in PPGE than our chosen endmember composition. Another explanation is simply that heterogeneous distribution of the PGE in the lithospheric mantle may result in some MARID samples incorporating PGE micro-alloys during wall rock dissolution leading to elevated concentrations of these elements.

Thus, we conclude that kimberlites, orangeites and similar magmas are not effective agents of PGE enrichment in the lithospheric mantle, in the context of providing sources for PGE-fertile magmas at Earth's surface. In fact, the incorporation of lithospheric mantle material during the reaction of parental metasomatic melt with mantle wall rocks is likely the source of the majority of the PGE present in these magmas and some MARID xenoliths.

Precious Metal Enrichment in Metasomatized Lithospheric Peridotite

Despite the above discussion showing the PGE-poor nature of volatile-rich mantle melts and associated MARIDs, metasomatized peridotite xenoliths in our study have minimal PPGE/IPGE fractionation compared to studies focusing on samples lacking hydrous metasomatic phases (Pearson *et al*., 2004; Luguet *et al*. 2007; Maier *et al*., 2012). The elevated Pd_n/Ir_n of the GPP xenolith ($Pd_n/Ir_n = 0.992$) and Pt enrichment in the PP xenolith (Pt = 29.1 ppb; $Pt_n/Pd_n = 11.96$) can traditionally be interpreted as metasomatic overprinting on a previously depleted protolith. However, we show that the HSE-depleted nature of volatile-rich magmas and alkali-rich metasomes are likely to lower PGE concentrations upon interaction with mantle peridotite. Several recent studies have reached similar conclusions regarding interaction between kimberlite-like melts and lithospheric mantle material. For instance, in their examination of BMS in heavily metasomatized mantle xenoliths, Aulbach *et al*. (2021) determined that progressive kimberlite metasomatism of the Kaapvaal Craton caused a net influx of sulphur, but that the BMS phases crystallized were HSE-poor and diluted the overall abundance of precious metals in mantle lithosphere.

Thus, a separate, pre-kimberlite metasomatic event in the Kaapvaal craton lithosphere is required to explain the re-enrichment observed in the GPP and PP xenoliths. In-depth petrogenetic

modeling has shown that mixing of depleted spinel-facies peridotite residue with basaltic melts and sulphides segregated from such melts systematically increases Pd_n/Ir_n of the residue, often to suprachondritic ratios (Rehkämper *et al*., 1999). However, the > 200km thick Kaapvaal lithosphere prohibits the generation of melts with basaltic composition (e.g., Niu 2021) and instead favours the production of small-degree melts such as carbonatite/kimberlite/lamprophyre/lamproite. Despite this, the eruption of the Karoo flood basalts and associated large igneous province (LIP) at ~ 180 Ma may be a candidate for SCLM enrichment. These magmas are argued to have originated in the asthenosphere or deep lithosphere as small-degree enriched melts (assisted by mantle plume activity) before gaining a basaltic composition at shallower depths and extensively modifying the lithospheric mantle during ascent (e.g., Ellam *et al*. 1992; Jourdan *et al*., 2007). Modification of the Kaapvaal lithosphere by precursor small-degree melts linked with the generation of Karoo basalts beneath thinner lithosphere has been linked to phlogopite metasomatism (e.g., Giuliani *et al*., 2014), MARID petrogenesis (though we debate this assertion in Chapter 3 of this study), and pervasive resulphidation (Aulbach *et al*., 2021). A recent study from Burness *et al*. (2020) studied two suites of eclogites residing at different depths in the Kaapvaal craton SCLM. The eclogites determined to be from the base of the SCLM were shown to have interacted with a kimberlite-like melt that precipitated HSE-poor BMS (reinforcing conclusions in our study). The second suite, which resided at mid-lithospheric depths (140-180 km), showed evidence for resulphidation and crystallization of comparatively PGE-enriched BMS. These authors suggested that pervasive crystallization of enriched sulphides may be associated with the passage of Karoo flood basalts based on similarities in PGE systematics between the eclogite sulphides and Karoo magmas (Burness *et al*., 2020; Figure 2.4.7). However, even at the shallower lithospheric depths proposed by Burness *et al*. (2020), the formation of basaltic melts is unlikely based on available experimental petrology data (Niu 2021 and references therein). Therefore, it may be more likely that small-degree, PGE-enriched melts that formed as precursors to the main Karoo flood basalts (and carried the same enriched signature) are a potential source for PGE-rich metasomatic sulphides observed here. Figure 2.4.7 shows that the PPGE, Re, and Au abundances of several of the GPP BMS are similar to Karoo-related sulphides from Burness *et al.* (2020).

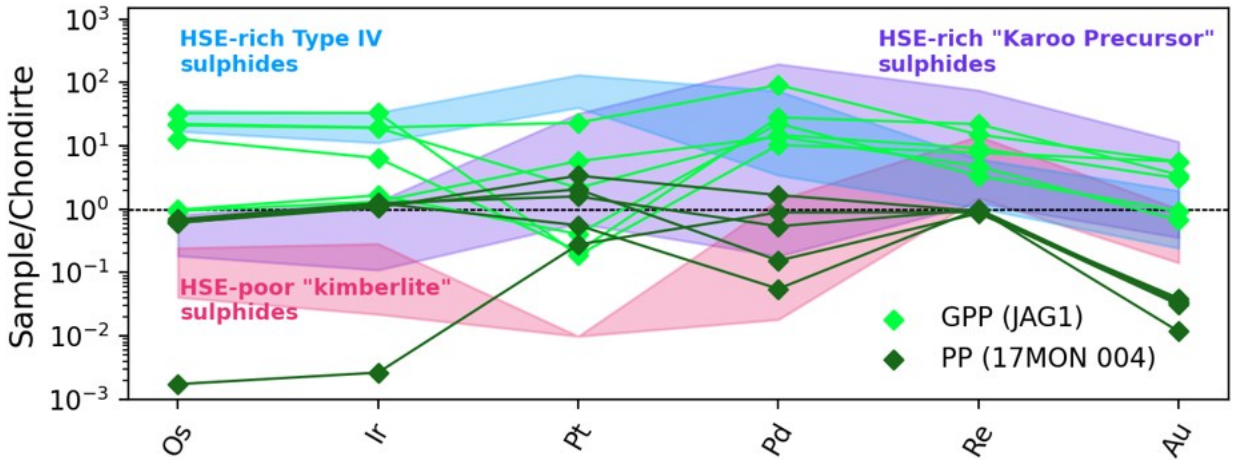

Figure 2.4.7: PGE systematics in sulphides from our Kaapvaal craton samples compared to eclogite sulphides adapted from Burness *et al*. 2020 and Hughes *et al*. (2021).

Several GPP BMS also display elevated IPGE concentrations resulting in a wide range of Pd_n/Ir_n (Pd_n/Ir_n = 0.31 – 13.6) and this observation is difficult to reconcile with a purely metasomatic origin for the GPP sulphide assemblage. IPGE-enriched GPP BMS analyzed here are strikingly similar to "Type-IV" BMS grains described in a recent study of eclogite xenoliths from the Roberts Victor kimberlite (Hughes *et al.* 2021; Figure 2.4.7). Type IV BMS were noted to have extremely high concentrations of the PGE (up to 223 ppm total) with a distinctive IPGE-enriched signature and flat chondrite-normalized patterns (Average Pd_N/Ir_N = 1.3 in Type-IV BMS from Hughes *et al*. 2021; n = 9). This unusual composition was interpreted by the authors as largely being inherited from the original eclogite protolith (i.e., directly from subducted oceanic crust). Therefore, a melt derived from this type of subducted eclogite, upon sulphur saturation and interaction with lithospheric peridotite, could reprecipitate BMS with high total PGE and unfractionated chondrite normalized patterns (Hughes *et al*. 2021). However, the Os isotope data described in Section 2.3.4 contradicts an ancient crustal (i.e., eclogitic) origin for the high-IPGE GPP sulphides. Given that Figure 2.4.4 shows that almost 100% of the IPGE budget of the GPP xenolith is stored within BMS phases, the presence of sulphides derived from melting of ancient, subducted crust would be expected to result in a highly radiogenic osmium isotope signature (e.g., Aulbach *et al*., 2009) and the GPP xenolith does not possess this feature (γOs_i = -2.9).

In the PP xenolith, the generally PGE-poor nature suggests that enrichment from secondary, Karoo-like metasomatic BMS is unlikely. Instead, platinum enrichment (Pt_n/Pd_n = 5.73) in this sample may result from a residual process where desulphidation of mss during melt extraction

stabilized Pt-rich alloys (e.g., Peregoedova *et al*. 2004; Lorand *et al*. 2007). This process is attributed to some Pt-enriched harzburgites that showed similarly elevated Pt_n/Pd_n to the PP xenolith (Lorand *et al*. 2007).

The broadly chondritic interelement PGE ratios in the Lherz Massif spinel lherzoliteis are nearly identical to results collected in previous studies of the region. They are generally interpreted as a result of a large-scale refertilization event (30-60% basaltic melt; Le Roux *et al*. 2007) associated with the Variscan orogeny in the Late Paleozoic (e.g. Lorand *et al*. 2008; Alard *et al*. 2000). The cross-cutting amphibole vein hosted within the lherzolite, while not associated with Paleozoic melt infiltration, provides an additional window into the PGE-carrying capability of more sodic mantle melts invading lithosphere that is shallower than most cratonic mantle. Amphibole veins in Lherz peridotites formed relatively recently (~100 Ma; Henrey *et al*. 1998) and represent late-stage segregates of primary basanite magma that crystallized in pre-existing fractures at relatively low pressure (< 1.3 GPa; Fabriès *et al*. 2001). The absolute abundance of the PGE in the amphibole vein suggest that this type of melt cannot be a source of PGE enrichment in the host lherzolite (~1 order of magnitude lower than the lherzolite host in all elements; Figure 2.3.18) which is similar to results from other studies of basanitic lavas (e.g., Mitchell and Keays 1981). We also note that the roughly chondritic PGE ratios in the Lherz amphibole vein are atypical for basanitic/basaltic magmas (e.g., Day *et al*. 2010; Medvedev *et al*. 2021). Similar to kimberlites and MARID xenoliths, this pattern can be explained by the incorporation of a depleted harzburgite component, but this model may be less suitable to a melt that crystallized at much lower pressures in pre-existing fracture conduits.

In summary, the signatures of melt-related precious metal refertilization are certainly observed in the modally metasomatized lithospheric mantle in both cratonic and noncratonic settings. However, it is also clear that a straight line cannot be drawn between metasomatism and precious metal refertilization. In our cratonic peridotite xenoliths, the origins of the most PGE-enriched BMS are uncertain. The unfractionated, IPGE-rich signatures in some GPP BMS are similar to Type-IV eclogite sulphides from Hughes *et al*. (2021), but the unradiogenic whole rock osmium isotope signature argues against an eclogitic source component. Small-degree melts formed as precursors to Karoo magmatism are a potential source for these PGE-rich sulphides and Re-Os isotope analysis of the individual BMS grains would assist in further characterization. Platinum

enrichment observed in the PP xenolith is most likely a result of residual desulphidation processes.

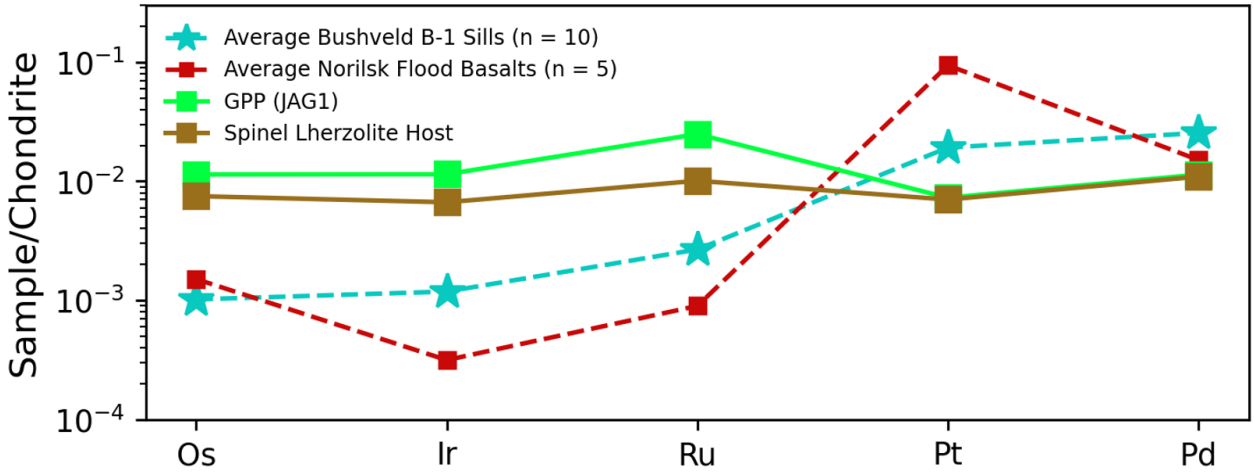

Figure 2.4.8: Chondrite normalized precious metal plots for magmas associated with Ni-Cu-PGE deposits and the most heavily PPGE refertilized samples from our study. Data sources are the same as Figure 2.4.5

In addition, certain cratonic mantle melts (i.e., kimberlite-like magmas) are PGE-poor and will dilute precious metal concentrations in lithospheric peridotite during infiltration. The majority of PGE abundance in kimberlite-like melts likely derives from reaction with peridotite wall rock.

The spinel lherzolite from the Lherz massif affirms the presence of PPGE re-enrichment in non-cratonic mantle, similar to the results of previous studies in the area (e.g., Le Roux *et al*. 2007). This refertilization is not associated with sodic basanites that crystallized amphibole veins in the Mesozoic as they possess PGE concentrations systematically ~1 order of magnitude lower than the host lherzolite.

The generation of crustal PGE deposits from metals partially sourced from the metasomatized lithospheric mantle remains an intriguing possibility. The most PGE-enriched peridotites analyzed in our study (GPP, Lherz Massif spinel lherzolite) have similar, though slightly lower, absolute PPGE abundances to those of primary magmas from Ni-PGE deposits such as the Bushveld Complex and Norilsk (Figure 2.4.8). Thus, we cannot rule out a lithospheric mantle component in the generation of these deposits. Combined with the recent study by Hughes *et al*. (2021), we confirm that zones of PGE-enriched lithospheric mantle are present within the Kaapvaal craton. However, it is uncertain whether these enriched zones make up a sufficiently high proportion of the lithospheric mantle to facilitate magma enrichment.

2.4.4 New PGE and Re-Os Isotope Constraints on MARID Petrogenesis

Using Osmium Isotopes to Trace Peridotite Interaction in MARID Petrogenesis

In Chapter 3, we reinforce the link between the MARID xenolith suite and Cretaceous intraplate magmas using Lu-Hf and U-Pb isotope systematics in MARID zircons. The zircon Lu-Hf isotope system in particular proved to be robust at preserving the original isotopic signature of the source region for MARID magmas. In contrast, Section 2.4.3 shows that the IPGE systematics of MARID magmas are very sensitive to the incorporation of residual peridotite. Using sample AJE-326 (the sample with the highest PPGE/IPGE ratio) as a proxy for a "pure MARID" composition, we demonstrated that even a small portion of peridotite incorporation substantially alters the IPGE systematics of MARID rocks (Figure 2.4.6).

In addition to high IPGE abundances, cratonic peridotites are characterized by unradiogenic $^{187}Os/^{188}Os$ ratios (e.g., Pearson *et al*. 2003) and correspondingly negative γOs values (Figure 2.3.19; Figure 2.3.20; average Kaapvaal peridotite γOs = -11.40 ± 4.2). These values reflect ancient melt depletion events that lowered $^{187}Re/^{188}Os$ and slowed radiogenic ingrowth of ^{187}Os. Our new osmium isotope data for MARID xenoliths show a range of $\gamma Os_{eruption}$ extending from similarly unradiogenic values in samples AJE-2422 and KDB-20 (-7.9 and -12 respectively) to extremely radiogenic compositions in samples AJE-335 and AJE-326 (11.8 and 116 respectively). Again, using AJE-326 as a proxy for a "pure MARID" composition, the effects of interaction with cratonic peridotite on MARID osmium isotope systematics can be roughly modelled using simple two-component mixing (Figure 2.4.9). The mixing line in Figure 2.4.9 indicates that this model is most sensitive at low peridotite fractions and becomes less sensitive at high peridotite fractions where changes to MARID osmium isotopes are negligible as they become dominated by the host peridotite signature. Mixing between MARID and ~3% peridotite produces the osmium isotope composition of sample AJE-335 and this value is very similar to the ~6% used to reproduce Pd/Ir ratios in this sample. Thirty percent peridotite interaction reproduces the Os isotope composition of sample AJE-2422 which is broadly similar to the ~40% constraint obtained from Pd/Ir modelling. The $^{187}Os/^{188}Os$ ratio in sample KDB-20 is slightly more unradiogenic than the average composition of Kaapvaal peridotite, meaning that no amount of mixing will reproduce its osmium isotope values. It is likely that sample KDB-20

simply interacted with cratonic peridotite with less radiogenic Os than our average composition. Regardless, the change in isotopic ratios becomes negligible beyond ~40% peridotite and so sample KDB-20 can qualitatively be described as having significant peridotite contamination.

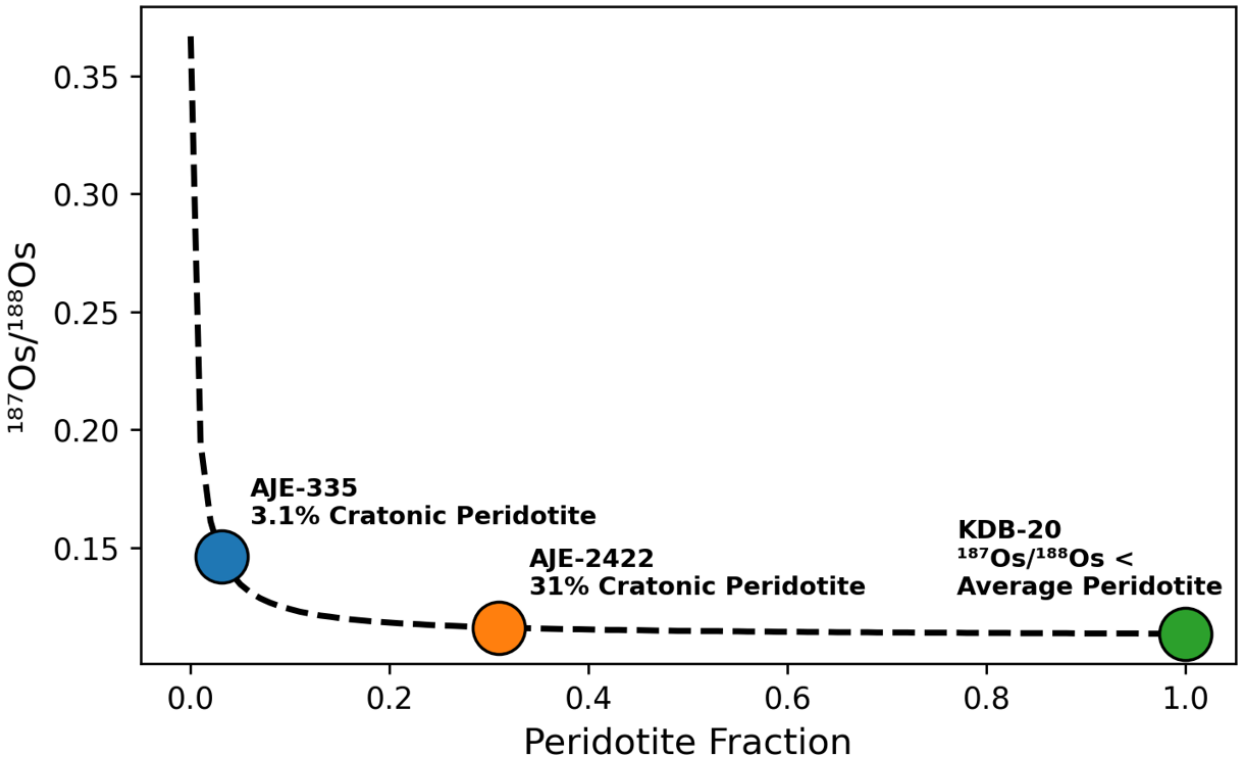

Figure 2.4.9: Two component mixing model between a pure MARID composition (sample AJE-326) and average Kaapvaal craton peridotite. Average Kaapvaal peridotite osmium isotope composition = 0.1136 (Pearson *et al*. 2021).

The good agreement between the Pd/Ir and $^{187}Os/^{188}Os$ modelling is strong evidence that MARID rocks extensively interact with cratonic peridotite during their formation and that IPGE systematics are a robust tracer of this process. Peridotite contamination "flattens" MARID PGE patterns and produces more unradiogenic osmium isotope composition. Our results reinforce models suggesting that MARID crystallization is "open-system" (Fitzpayne *et al*. 2018; Sweeney *et al*., 1993; Chapter 3 of this study) and involves variable degrees of wall rock assimilation as well as other processes such as melt-mixing and crystal fractionation that obscure their original geochemical signatures.

PGE and Osmium Isotope Constraints on the Source Region of MARID magmas

Chapter 3 proposes a simplified geological model for the formation of MARID rocks in the lithospheric mantle from the crystallization of stalled orangeite pipes during the major pulse of

Cretaceous intraplate magmatism. We suggest that MARID (and thus orangeite) magmas may form from the selective melting of eclogitized, subducted slabs or pyroxenite-like metasomes crystallized at the base of the SCLM from subduction-related metasomatism associated with the Kibaran/ Namaqua-Natal Orogeny (~1.1 Ga). This model is similar to one used by Coe *et al*. (2008) to explain the petrogenesis of the Swartsruggens orangeites. The link between MARID magmas and an ancient subduction source was primarily based on the enriched εHf values observed in MARID zircons which are similar to values found in some massif pyroxenites (e.g., Pearson and Nowell 2004). The geochemistry of these pyroxenites were interpreted as being inherited from subduction related metasomatism that had Sm/Nd and Lu/Hf isotopic composition similar to ancient sediments (Coe *et al.* 2008). Our model for orangeite-MARID formation argues against an origin from the melting of refractory lithospheric mantle peridotite suggested by studies such as Becker and Le Roex (2006).

Combining results from Chapter 3 of this study with Re-Os data from our least peridotite-contaminated MARID samples (AJE-335 and AJE-326), we show that MARID magmas must originate from a source rock that is:

1) Depleted in radiogenic hafnium (average εHf_i of -17 in MARID zircon)

2) HSE poor (total PGE [Os+Ir+Ru+Pd+Pt] < 10 ppb in uncontaminated MARID)

3) fractionated in terms of PPGE/IPGE ratios (Pd/Ir > 10 in uncontaminated MARID)

4) variably enriched in radiogenic osmium ($\gamma Os_{eruption}$ from 11.8 – 116 in uncontaminated MARID)

The precisely defined unradiogenic osmium isotope signature of cratonic peridotite precludes direct formation of MARID magmas from the melting of lithospheric peridotite as suggested by Becker and Le Roex (2006) (Figure 2.3.19; Figure 2.3.20). Instead, the radiogenic signature of pyroxenites from the Beni Bousera Massif shows good agreement with our uncontaminated MARID samples (Figure 2.3.19; Figure 2.3.20). In addition, pyroxenites from the Bohemian Massif showed similarly radiogenic γOs values (11.1 – 86.3; Ackerman *et al.* 2013). The Bohemian Massif pyroxenites were also characterized for total PGE systematics by Ackerman *et al*. 2013 and they displayed low total PGE abundances similar to our uncontaminated MARID samples (Os + Ir + Ru + Pt + Pd ranging from 0.44 to 17.8 ppb). Chondrite normalized PGE

patterns of the Bohemian Massif pyroxenites strongly resemble uncontaminated MARID samples and display similar Pd/Ir fractionation (Pd/Ir ranging from 3.0 to 42.2 in Bohemian Massif pyroxenites; Ackerman *et al.* 2013; Figure 2.4.10).

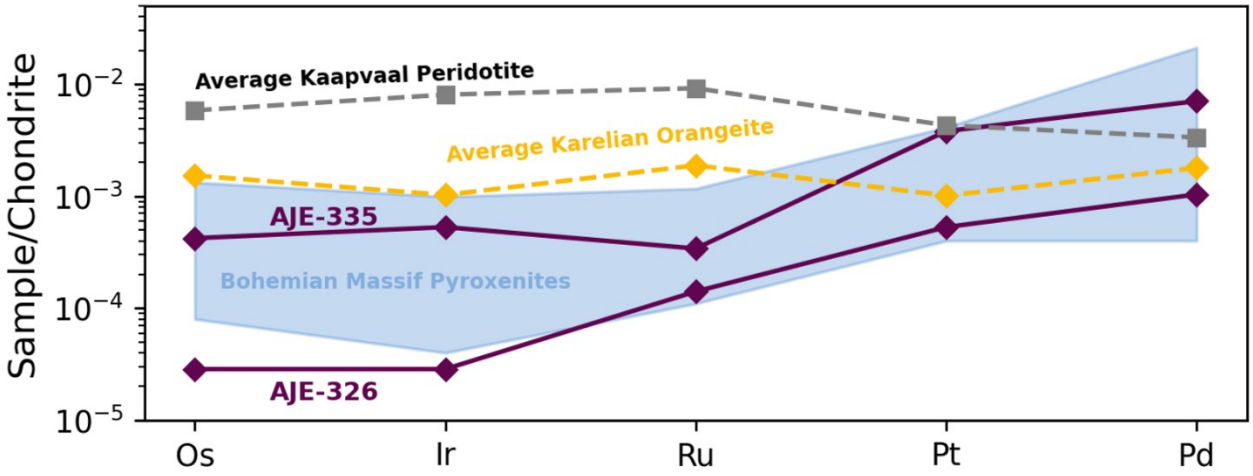

Figure 2.4.10: Comparison of uncontaminated MARID chondrite normalized PGE patterns to Bohemian Massif Pyroxenites and an average Kaapvaal craton peridotite. Field for Bohemian Massif pyroxenites from Ackerman *et al*. (2013). Kaapvaal peridotite from Maier *et al.* (2012)

Thus, MARID xenoliths display similarities to mantle pyroxenites in all four of the major features described above. While one of these features in isolation may not be indicative of a particular mantle source region, all four together provide strong evidence for a subduction-sourced pyroxenite or eclogite component in the MARID parental magmas (e.g., Carlson *et al*. 1996; Carlson and Nowell 2001; Pearson and Nowell 2004; Ackerman *et al*. 2013).

Finally, unlike Lu-Hf isotopes discussed in Chapter 3, the HSE and Re-Os isotope similarities between mantle pyroxenites and MARID rocks do not extend as consistently to orangeite magmas (Figure 2.3.19; Figure 2.4.10). We interpret this as being a result of the hybrid nature of orangeite magmas. The Lu-Hf system in orangeites is likely buffered to the effects of peridotite assimilation due to the trace element enriched nature of the subduction-related source and the low Hf content of the host peridotite. In contrast, orangeite magmas are PGE-poor and thus interaction with high Os lithospheric peridotite wall rock during ascent and crystallization obscures the original HSE signature of the source rock. Uncontaminated MARID samples provide a clearer picture of the source region of these alkali-rich melts and reinforce the

petrogenetic links between MARID xenoliths and parental melts generated from subduction enriched sources.

2.5 Conclusions

The results described here present new major + trace element and isotopic data for modally metasomatized xenoliths from both cratonic and non-cratonic settings. Mass balance calculations show key host phases for major, trace, and highly siderophile elements within metasomatic components of the lithospheric mantle. Precious metal data in these xenoliths describes the degree of enrichment in the SCLM and mantle-derived melts that metasomatized this reservoir. We also provide the first published set of Re-Os isotopic data in MARID xenoliths which further constrains their petrogenesis. This study has reached the following major conclusions:

1. Silicate and oxide phases, even in highly metasomatized mantle lithologies, are negligible contributors to the whole rock precious metal budget of metasomatized lithospheric peridotite and related metasomes (i.e., MARID and PIC xenoliths). LA-ICP-MS analysis of precious metals in these phases is challenging, prone to analytical issues such as detection limits and isobaric interferences and must be approached with caution.
2. Mass balance calculations assuming all precious metals reside within sulphide phases fail to account for the whole rock precious metal budget. This is likely due to a combination of factors including sensitivity to modelling parameters, multiple populations of residual and metasomatic sulphides, and a strong nugget effect from micro-scale PGE alloys. Thus, a combination of BMS and PGE alloy phases are the major repositories for precious metals in metasomatized lithospheric mantle.
3. HFSE and LILE concentrations show significant discrepancies between mass balance calculations and whole rock analysis. These discrepancies are likely caused by kimberlite metasomatism and trace phases not included in modal calculations.
4. Potassic intraplate magmas such as kimberlites and orangeites are PGE-poor and likely dilute the overall abundance of HSE in the mantle upon interaction with lithospheric peridotite. PGE-poor metasomatic sulphides in modally metasomatized xenoliths may have precipitated from these melts when they reached sulphur saturation. MARID xenoliths, interpreted as the crystallization products of these melts, are correspondingly PGE-poor with elevated PPGE/IPGE ratios.

5. Metasomatized peridotites show PPGE enrichment relative to “dry” melt-depleted peridotites in both cratonic and non-cratonic settings. Kimberlite-like melts are unlikely to account for this enrichment. Instead, small-degree melts associated with the Karoo LIP may precipitate PPGE-rich BMS. IPGE-rich, unfractionated BMS in the GPP xenolith resemble “Type IV” eclogite sulphides (Hughes *et al.* 2021) and warrant future study. Residual alloys can potentially result in significant Pt anomalies not associated with metasomatism.
6. Variations in MARID IPGE systematics and Re-Os isotope signatures are well explained by two component mixing between a “pure MARID” composition (representing the parental melt) and lithospheric peridotite. The PGE-poor nature of MARID xenoliths makes them especially prone to contamination via host rock mixing. These results reinforce that MARID formation is a complex, open-system process that involves assimilation of and reaction with lithospheric peridotite at varied melt-rock ratios.
7. Re-Os isotope signatures of uncontaminated MARID samples show strong similarities to pyroxenites from the Beni Bousera and Bohemian Massifs. This, combined with Lu-Hf isotope data in Chapter 3 of this study, suggests a parental melt with similar time-integrated isotopic histories.

Chapter 3: *In situ* Zircon Lu-Hf, U-Pb Isotope Constraints on the Timing and Genesis of MARID-type Metasomatism in the Kaapvaal Craton Lithosphere

3.1 Introduction

3.1.1 Background and Objectives

The suite of mantle xenoliths variably composed of mica, amphibole, rutile, ilmenite, and diopside, collectively known as the MARID suite (Dawson and Smith 1977), that derive from archetypal kimberlites and orangeites in Southern Africa have been the subject of significant research over the previous 50 years. MARID rocks are an extreme example of metasomatic processes occurring in the sub-continental lithospheric mantle (SCLM), and thus provide an opportunity to study the processes that drive chemical heterogeneity in the mantle. The characteristics of MARID rocks can elucidate details of the metasomatic sources that formed them and strengthen our knowledge of functionally inaccessible geochemical reservoirs within the Earth. In addition, the exotic mineralogy of MARID assemblages provides the opportunity to place temporal constraints on mantle metasomatic processes.

The genetic mechanisms that form MARIDs and the related suite of PIC xenoliths are uncertain. Early work by Erlank *et al*., (1987) described a metasomatic "continuum" from unaltered garnet peridotite to garnet phlogopite peridotite (GPP), to phlogopite peridotite (PP), then to phlogopite potassic (K) richterite peridotite (PKP). These authors suggested that MARID rocks may be the final result of peridotites that had been extensively modified by alkali-rich melts at high melt-rock ratios. Erlank *et al*., (1987) proposed that MARID rocks were likely the result of the most extensive metasomatism but did not suggest a firm genetic link for the series due to differences in mineral chemistry. Other early studies interpreted the "cumulate-like" textures in most MARIDs to represent a magmatic origin whereby the rocks formed through crystallization of a silicate melt of bulk MARID composition (Dawson and Smith 1977; Jones *et al*., 1982; Waters

et al., 1989). In later studies, purely cumulate processes were called into question. For instance, Sweeney *et al*., (1993) argued that the temperatures required to sustain such a melt were improbable in relatively cold mantle lithosphere. They proposed two counter-theories to explain MARID genesis: 1) MARID xenoliths could be the result of precipitation from a high-density hydrous fluid percolating through the mantle lithosphere. 2) MARID xenoliths may be the crystallized residues of "failed" (or blind) orangeite intrusions that had undergone olivine fractionation and the exsolution of a carbonatitic component. Since then, there has been a growing consensus in the link between orangeite magmatism and MARID genesis (Konzett *et al.,*1995; Konzett *et al*., 1998; Hamilton *et al*., 1998; Gregoire *et al*., 2002; Giuliani *et al*., 2015; Fitzpayne *et al*., 2019). However, significant complexities in the geochemistry of MARID rocks exist that are not completely explained by the model of Sweeney *et al*., (1993) (e.g., Fitzpayne *et al.,* 2018; Konzett *et al*., 2000; Hoare *et al*., 2021).

Previous attempts to constrain the timing and source of MARID genesis in the Kimberley region using U-Pb isotope analysis of zircon are limited. Hamilton *et al*., (1998) found tightly constrained ages of 120 ± 2 Ma in their ion probe analysis of MARID zircon from Kampfersdam. Two studies by Konzett *et al*. (1998, 2000) reported ages ranging from 80 Ma to 142 Ma in samples from the Kimberley region while studies by Giuliani *et al*. (2015) and Hoare *et al*. (2021) reported similar age ranges (86.6 Ma - 129.8 Ma and 80 – 120 Ma respectively). With the exception of Hamilton *et al*. (1998), all of these studies show large variation of $^{238}U/^{206}Pb$ ages within single zircon grains that span the temporal range of kimberlite and orangeite magmatism in the Kimberley area. Thus, U-Pb isotopes alone are not sufficient to fully constrain the source of MARID genesis.

Several studies have used additional isotopic systems to attempt to constrain the nature of the MARID parent magma. Whole Rock Sr-Nd-Pb isotope systematics reported by Kramers *et al*. (1983) and Erlank *et al.,* (1987) showed that radiogenic isotope characteristics of MARID rocks overlapped that of both kimberlites and orangeites. Unfortunately, this led to the early conclusion that radiogenic isotope studies of MARID rocks would not be effective at clearly resolving the parent magma (Sweeney *et al.,* 1993). However, Gregoire *et al*. (2002) showed that several xenoliths in the early studies were improperly identified. Their re-assignment of rock suites revealed clear isotopic similarities between orangeites and MARID as well as kimberlites and

PIC xenoliths. A study of Sr-Nd-Hf-Pb isotopes of MARID and PIC minerals by Fitzpayne *et al*. (2019) further strengthen the PIC-kimberlite and MARID-orangeite connection. In contrast, Hf isotopes of MARID rutiles spanned a large range of -50 to +110 εHf in a study by Choukroun *et al.* (2005) and are significantly different than results from any other study. Giuliani *et al*. (2015) is the only published study measuring the Hf isotope characteristics of MARID zircon in which they found an average εHf value of -13.8 pointing to an enriched source magma.

Coupled U-Pb and Lu-Hf analyses are robust tools for constraining the timing and source components of magmatic rocks. Until relatively recently, Lu-Hf studies of mantle xenoliths were rare due to analytical challenges in measuring Hf using thermal ionization mass spectrometers (Pearson *et al*., 2003). Multi-collector ICPMS techniques have proven to be a successful solution to this problem, and the data we present here provides a valuable addition to the burgeoning use of the Lu-Hf system as a mantle source region tracer.

Here we conduct U-Pb, Lu-Hf *in situ* laser ablation split stream (LASS) analyses of MARID zircons to study 1) the temporal span of MARID formation in the lithospheric mantle of the Kimberley region in Southern Africa 2) the geochemistry of the source component leading to MARID crystallization 3) the relationship of MARID formation to Mesozoic intraplate magmatism in the Kaapvaal craton.

3.1.2 Samples

One sample from a suite of four MARID xenoliths, AJE-2422, was found to contain numerous zircon grains. AJE-2422 is a coarse-grained MARID xenolith from the Bultfontein kimberlite. It is composed of 69.1 % K-richterite, 22.6% phlogopite, 5.7% ilmenite and 2.6% rutile. Zircons occur as μm-scale grains in textural equilibrium with other primary MARID phases. The petrographic characteristics of AJE-2422 are described in greater detail in Chapter 2.3.1. Sample imagery is viewable in Appendix C.1. BSE images of each zircon grain are viewable in Appendix C.2.

Sample AJE-2422 was also analyzed in a series of studies by Fitzpayne *et al*. (2018, 2019, 2020). We consider the results from radiogenic isotope analysis of AJE-2422 in Fitzpayne *et al*. (2019) and compare them to results obtained from this study.

3.2 Analytical Methods

3.2.1 Cathodoluminescence

Cathodoluminescence (CL) imagery was obtained *in situ* from thick sections of sample AJE-2422 using a Zeiss Sigma Field Emission Scanning Electron Microscope (SEM) at the University of Alberta's SEM Laboratory. Conductive coating was applied using a Leica EM SCD005 evaporative carbon coater and dried using a Bal-Tec CPD 030 critical point dryer. Imagery was collected over one analytical session.

3.2.2 Laser Ablation ICP-MS

Zircon from AJE-2422 were analyzed for a suite of 27 trace elements (^{45}Sc, ^{47}Ti, ^{57}Fe, ^{59}Co, ^{60}Ni, ^{85}Rb, ^{88}Sr, ^{89}Y, ^{90}Zr, ^{93}Nb, ^{137}Ba, ^{139}La, ^{140}Ce, ^{141}Pr, ^{146}Nd, ^{147}Sm, ^{153}Eu, ^{157}Gd, ^{159}Tb, ^{163}Dy, ^{165}Ho, ^{166}Er, ^{169}Tm, ^{172}Yb, ^{175}Lu, ^{178}Hf, ^{208}Pb) via *in situ* laser ablation inductively coupled plasma mass spectrometry (LA-ICP-MS) at the University of Alberta's Arctic Resources Laboratory.

The data was collected concurrently with trace element data described in Chapter 2. Data collection, calibration, and reduction was performed identically to the method described in Chapter 2.2.3.

3.2.3 Laser Ablation Split Stream ICP-MS

Zircon U-Th-Pb Isotope Geochemistry

U-Pb isotopes in zircon grains were measured *in situ* via LASS-ICP-MS at the University of Alberta's Arctic Resources Laboratory. Data was collected concurrently with Lu-Hf isotopes. Ablations were performed with a Resonetics M-50 193 nm laser on thin sections loaded into a 2-volume Laurin-Technic S-155 ablation cell. The ablated material was analyzed simultaneously by a Thermo Scientific Element2 XR-SF-ICPMS (U-Pb) and a Thermo Fisher Scientific Neptune Plus MC-ICP-MS (Lu-Hf). Laser conditions included a repetition rate of 8 Hz, 44% attenuator value, a laser energy of 120 mJ, and a fluence of 6 J/cm^2. Spot sizes for all analytical points were 50 μm. Each analysis consisted of 60 seconds of background and washout time followed by 50 seconds of ablation time.

Seven masses, corresponding to ^{202}Hg, ^{204}Pb, ^{206}Pb, ^{207}Pb, ^{208}Pb, ^{232}Th, and ^{238}U were measured and calibrated using natural zircon reference material Plešovice (Sláma *et al*., 2008) as the primary standard. Natural zircon reference material 91500 (Wiedenbeck *et al*., 1995; Wiedenbeck *et al*., 2004) was used as the secondary standard to monitor measurement accuracy. Reference materials were analyzed at the beginning and end of the analytical session and after each block of eight unknown analyses. Weighted means of $^{206}Pb/^{238}U$ ages for primary and secondary reference materials were calculated using IsoplotR software (Vermeesch 2018) and are summarized in Table 3.2.1. All analyses are reported in Appendix A.2.1. Weighted mean and kernel density estimator (KDE) plots for both reference materials were created in KDX software (Spencer *et al*., 2017) and are viewable in Appendix A.2.1.

Reference Material	Accepted Reference Age (Ma)	$^{206}Pb/^{238}U$ Weighted Mean Age (Ma) (2SE)	MSWD; p(χ^2)	Number of analyses (accepted/reject)
Plešovice (primary)	337.13 ± 0.37	337.19 ± 1.29	0.26; 1.00	14/17
91500 (secondary)	1062.4 ± 0.8	1060.75 ± 3.84	2.11; 0.011	14/14

Table 3.2.1: Summary of reference material results for the calibration of U-Pb isotopes in unknown zircons. Reference ages from Sláma *et al*., (2008) and Wiedenbeck *et al*., (1995). Outliers were rejected by IsoplotR using a modified 2-sigma criterion.

The results from primary zircon standard Plešovice agree with the established reference age within uncertainty. Three analyses were rejected as outliers by IsoplotR. Outliers were not used in the calibration of unknown data points. Results for secondary standard 91500 agree with the established reference age within uncertainty. Uncertainty is higher in 91500 leading to an elevated MSWD, but with no analysis points rejected as outliers.

Signal integration of the time-resolved LA-ICPMS spectra was conducted using the Iolite 3 software package (Paton *et al.,* 2011). Two data reduction schemes (DRS), "X_U_Pb_Geochron" and "Hf_Alberta", were run to process U-Pb and Lu-Hf isotope data simultaneously (see Fisher *et al.,* 2017 for details on this LASS DRS). ^{235}U was calculated based on ^{238}U concentrations and the $^{238}U/^{235}U$ ratio from Jaffey *et al*. (1971). Decay constants for ^{235}U and ^{238}U were taken from Jaffey *et al*. (1971).

Due to the large uncertainties in $^{207}Pb/^{235}U$ ratios inherent to younger zircons, the likelihood of obtaining concordant ages in Cretaceous aged samples (i.e., this study) is lowered. In addition, zircons analyzed here are extremely low in U meaning more accurate results are obtained from using the more abundant ^{238}U decay chain. All ages reported here are $^{206}Pb/^{238}U$ ages with 2σ uncertainty. Common Pb was corrected using the appropriate values from Stacey and Kramers (1975). This correction had a negligible effect on the calculated $^{206}Pb/^{238}U$ ages (age change << 2σ uncertainty).

Zircon Lu-Hf Isotope Geochemistry

Lu-Hf isotopes in zircon grains were measured *in situ* by MC-LA-ICP-MS in the Arctic Resources Laboratory at the University of Alberta. Data was collected concurrently with U-Pb isotopes (discussed above). Laser conditions included a repetition rate of 8 Hz, 28% attenuator value, a laser energy of 120 mJ, and a fluence of 4.5 J/cm^2. Spot sizes for all analytical points were 50 μm. Each analysis consisted of 60 seconds of background and washout time followed by 50 seconds of ablation time.

Nine masses corresponding to ^{172}Yb, ^{173}Yb, ^{175}Lu, ^{176}Hf, ^{177}Hf, ^{178}Hf, ^{179}Hf, ^{180}Hf, ^{181}Ta and their isobaric interferences were measured and calibrated using natural zircon reference material Plešovice (Sláma *et al*., 2008) as the primary standard. Due to the large corrections necessary for the isobaric interference of ^{176}Yb (and ^{176}Lu) on the ^{176}Hf mass each run includes a variety of secondary standards of known age and Hf isotope composition interspersed with unknowns in order to evaluate the accuracy of the interference correction. In this study we monitored the Yb and Lu interference corrections by analysis of a variety of natural and synthetic zircons, with a wide range of Yb/Hf (Yb being the dominant interference). Synthetic HREE-doped zircons (MUN1 and MUN3 – Fisher et al., 2011) were evaluated, along with zircon 91500 (Wiedenbeck *et al*., 1995; Wiedenbeck *et al*., 2004; Blichert-Toft, 2008). The ^{176}Yb interference was calculated as outlined in Vezinet *et al*. (2018) and briefly summarized here. The Yb mass bias factor (β^{Yb}) was determined via the peak-stripping method by analyzing two interference-free isotopes of Yb (^{172}Yb and ^{173}Yb) (Woodhead *et al*., 2004; Fisher *et al.,* 2011). The value of β^{Yb} was then calculated following the exponential law (Russel *et al.,* 1978). Interference of ^{176}Lu on ^{176}Hf was calculated in the same way assuming that ^{176}Lu behaves identically to ^{176}Yb.

The accuracy of the correction was evaluated by comparison to reference materials run as secondary standards, including the MUN zircons, for which MUN-3 has a higher Yb/Hf than any unknown zircon analysed in this study. Table 3.2.2 summarizes results for primary and secondary reference material analyses and compares them to accepted values. All analyses are reported in Appendix A.2.2. The range of Yb/Hf values in our standard reference materials are also presented in Appendix A.2.2. All analyzed MUN3 Yb/Hf ratios were higher than the maximum Yb/Hf ratio in our unknowns (0.00583).

Reference Material	Mean Measured $^{176}Hf/^{177}Hf$ (2σ)	Mean Measured εHf (2σ)	Accepted Reference $^{176}Hf/^{177}Hf$ (2σ)	Accepted Reference εHf (2σ)	Calculated Difference (ε units)
Plešovice (primary) n = 17	0.282483 ± 0.000015	-10.7 ± 0.6	0.282482 ± 0.000013	-10.7 ± 0.5	0
91500 (secondary) n = 14	0.282317 ± 0.000012	-16.5 ± 0.7	0.282308 ± 0.000006	-16.2 ± 0.3	+ 0.3
MUN1 (secondary) n = 6	0.282152 ± 0.000011	-22.4 ± 0.8	0.282135 ±0.000007	-23.0	+ 0.6
MUN3 (secondary) n = 15	0.282181 ± 0.000038	-21.4 ± 2.9	0.282135 ± 0.000007	-23.0	+1.6

Table 3.2.2: Summary of reference material results for the calibration of $^{176}Hf/^{177}Hf$ in unknown zircons

Primary standard Plešovice agrees well with reference values, (0.282482 ± 0.000013; Sláma *et al*., 2008) falling within two standard deviations of the accepted ratio. All three secondary zircon standards show minor deviations from the literature, with mean values slightly higher than published results. Secondary standard 91500 agrees within 2σ of the accepted value (0.282308 ± 0.000006; Blichert-Toft, 2008). Secondary standard MUN1 and MUN3 both fall within 2σ of reference values (0.282135 ± 0.000007; Fisher *et al*., 2011).

$^{176}Hf/^{177}Hf$ values were converted to εHf (a relative unit comparing the $^{176}Hf/^{177}Hf$ at the time of crystallization to the Chondritic Uniform Reservoir [CHUR]) using Equation 2.4.1.

$$\varepsilon Hf_{(t)} = \left(\frac{{}^{176}Hf \Big/ {}^{177}Hf_{sample(t)}}{{}^{176}Hf \Big/ {}^{177}Hf_{CHUR(t)}} - 1 \right) X\ 10000$$

Equation 2.4.1: Formula for εHf where:

t = the $^{206}Pb/^{238}U$ age of the analytical spot,

$$^{176}Hf/^{177}Hf_{sample(t)} = {}^{176}Hf/^{177}Hf_{measured} - {}^{176}Lu/^{177}Hf_{measured} * e^{\lambda Lu * t-1}$$

$$^{176}Hf/^{177}Hf_{CHUR(T)} = {}^{176}Hf/^{177}Hf_{CHUR(present)} - {}^{176}Lu/^{177}Hf_{CHUR(present)} * e^{\lambda Lu * (t * 10000) -1}$$

λLu = 1.87E-11 (Bouvier *et al*., 2008); $^{176}Hf/^{177}Hf_{CHUR(present)} = 0.282785$ (Bouvier *et al*., 2008); $^{176}Lu/^{177}Hf_{CHUR(Present)} = 0.0336$ (Bouvier *et al.,* 2008)

εHf uncertainties were propagated using the methods of Vezinet *et al*. (2018). Using this method, uncertainties in the measured U-Pb age, measured $^{176}Hf/^{177}Hf$ values, and CHUR parameters from Bouvier *et al* (2008) were propagated into εHf uncertainties. All εHf values from unknown zircon analyses in this study returned uncertainties below 1.5 εHf units.

3.3 Results

3.3.1 Cathodoluminescence Imagery

The five zircon grains of MARID sample AJE-2422 display several textures across the two thick sections analyzed. The two grains in Thick Section 1 (Figure 3.5.2 A and B) have faint CL intensity with small zones of very light CL intensity. Occasional "stringers" of these very light zones crosscut the grains following pre-existing fracture patterns. The boundaries between zones of differing intensity are diffuse.

The three grains in Thick Section 2 have sharper boundaries between zones of differing CL intensity (Figure 3.5.2 C, D, E). Off-center cores are visible, particularly in grains 2 and 3, and are surrounded alternating zones of light and dark CL intensity (Figure 3.5.2 D and E).

3.3.2 Trace Element Geochemistry

U and Th concentrations in AJE-2422 zircons vary from 10-159 ppm and 5-93 ppm respectively (Figure 3.3.1; Appendix B.4.1). Th/U ratios are almost all below 1, ranging from 0.3-1.53 (Figure 3.3.2; Appendix B.4.1). Th/U ratios exceeding 0.6 exclusively occur in AJE-2422-01 grain 1 due to very low U concentrations. There is no apparent correlation between CL zonation and variation in U-Th concentration. U-Th concentrations observed here are low compared to zircons crystallizing from basaltic magmas (e.g., Dockman *et al*., 2018), but are typical of previous analyses of MARID zircons (Figure 3.3.1; Hamilton *et al*., 1998; Konzett *et al*., 1998; Konzett *et al*., 2000). MARID zircons commonly overlap the composition of kimberlite

megacrystic zircon in U-Th space but extend to higher concentrations of both elements (Figure 3.3.1). Two analysis points from AJE-2422-01 grain 1 plot outside the field of previously measured MARID zircons in Figure 3.3.1.

Limited trace element data collected here shows a composition intermediate between typical lamproitic zircon and kimberlitic zircon (Figure 3.4.3). Hafnium in zircon from AJE-2422 occurs at weight percent levels (~1.1 wt %; typical of lamproitic and kimberlitic zircon) while other REE values are higher than those typically found in kimberlite megacryst zircons (Belousova *et al*., 2002; Figure 3.4.3). Yttrium values (120 ± 30 ppm) are more similar to typical lamproitic zircon. Zircons from sample AJE-2422 contain anomalous concentrations of Ti (4500 ± 430 ppm) which may be indicative of equilibration between zircon and nearby titanian phases rutile and ilmenite. Trace element patterns show negative anomalies of Ba (0.46 ± 0.02 ppm), La (0.8 ± 0.27 ppm), and Sr (4 ± 1.8 ppm) (Figure 3.4.3).

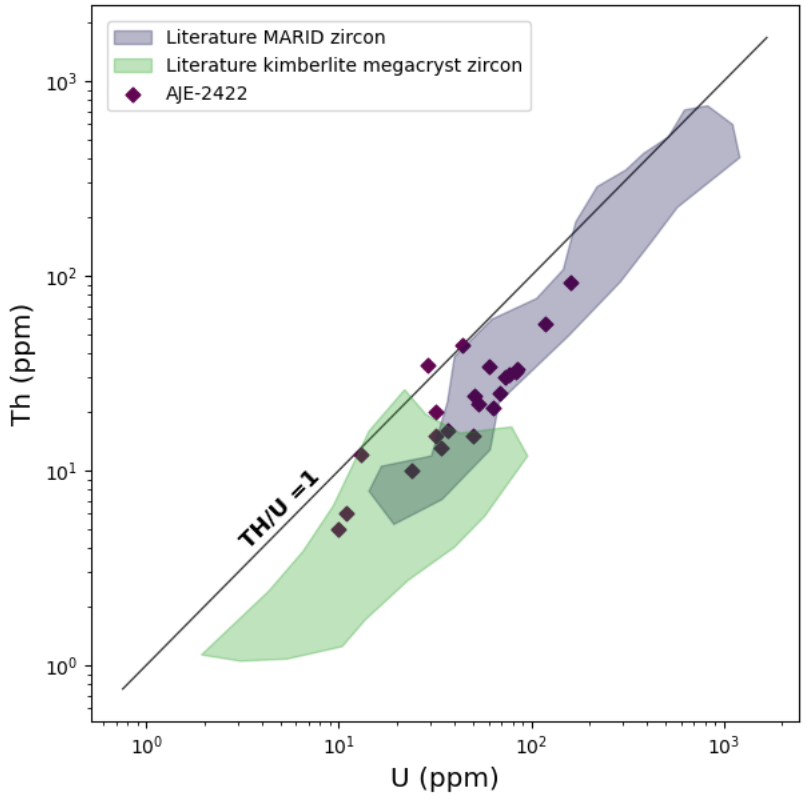

Figure 3.3.1: Bivariate plot of Th-U concentrations in MARID zircons compared to kimberlite megacrysts. Literature compositional fields are from Konzett *et al*., (2000) and references therein.

3.3.3 U-Pb Isotope Geochronology

U-Pb isotope data is listed in Appendix B.4.1. Measured $^{207}Pb/^{206}Pb$ and $^{238}U/^{206}Pb$ ratios of MARID zircons from sample AJE-2422 are plotted on a Terra-Wasserburg concordia diagram (Figure 3.3.3).

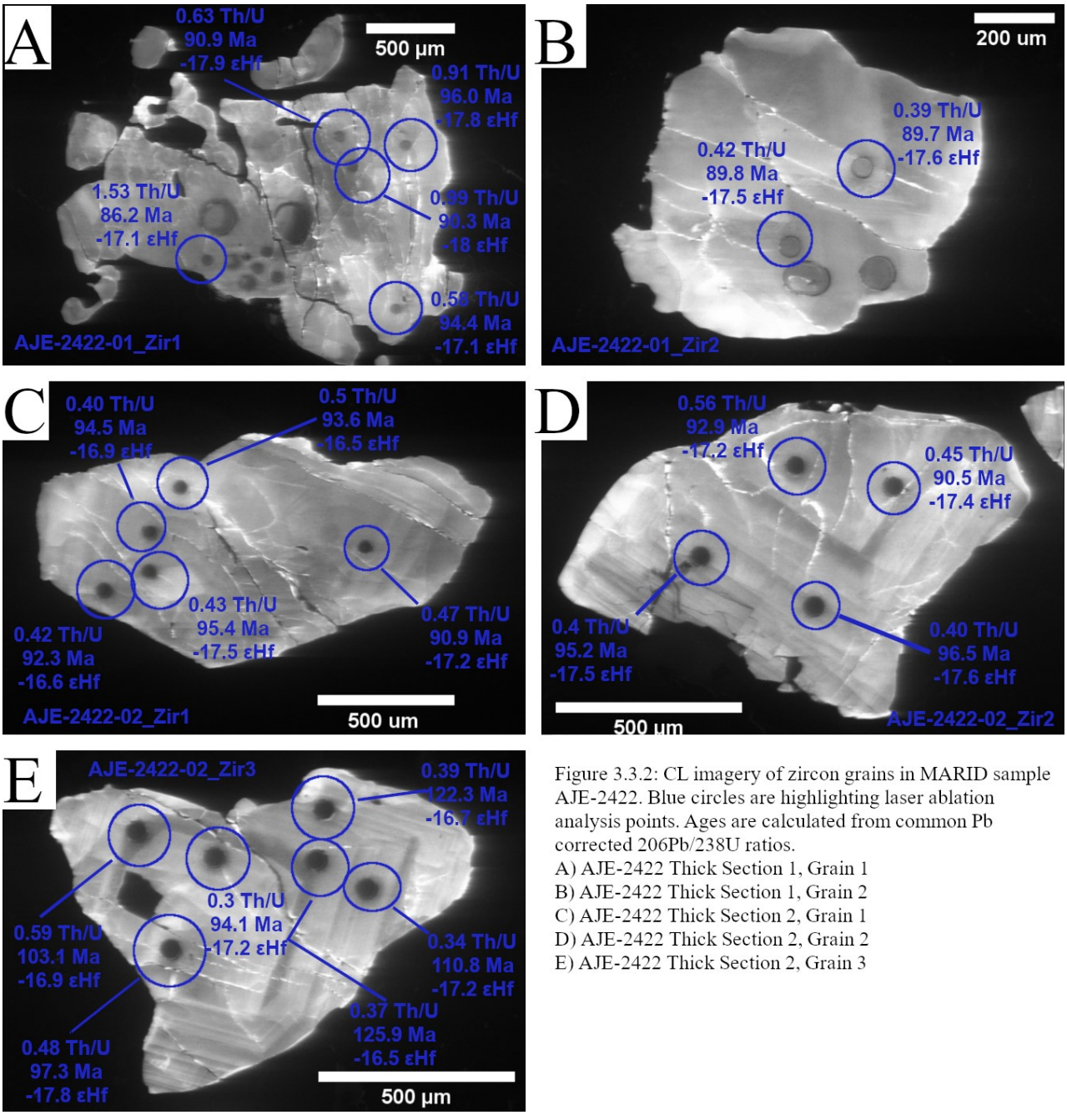

Figure 3.3.2: CL imagery of zircon grains in MARID sample AJE-2422. Blue circles are highlighting laser ablation analysis points. Ages are calculated from common Pb corrected 206Pb/238U ratios.
A) AJE-2422 Thick Section 1, Grain 1
B) AJE-2422 Thick Section 1, Grain 2
C) AJE-2422 Thick Section 2, Grain 1
D) AJE-2422 Thick Section 2, Grain 2
E) AJE-2422 Thick Section 2, Grain 3

Most points plot above concordia along a mixing line between the composition of initial common Pb at ~ 90 Ma (Stacey and Kramers 1975) and the radiogenic Pb composition (Figure

3.3.3). This is likely caused by the incorporation of common Pb which ranges in concentration from 0.53%-4.75% of the total measured ^{206}Pb. A common Pb correction was applied prior to calculating $^{206}Pb/^{238}U$ ages (Appendix B.4.1).

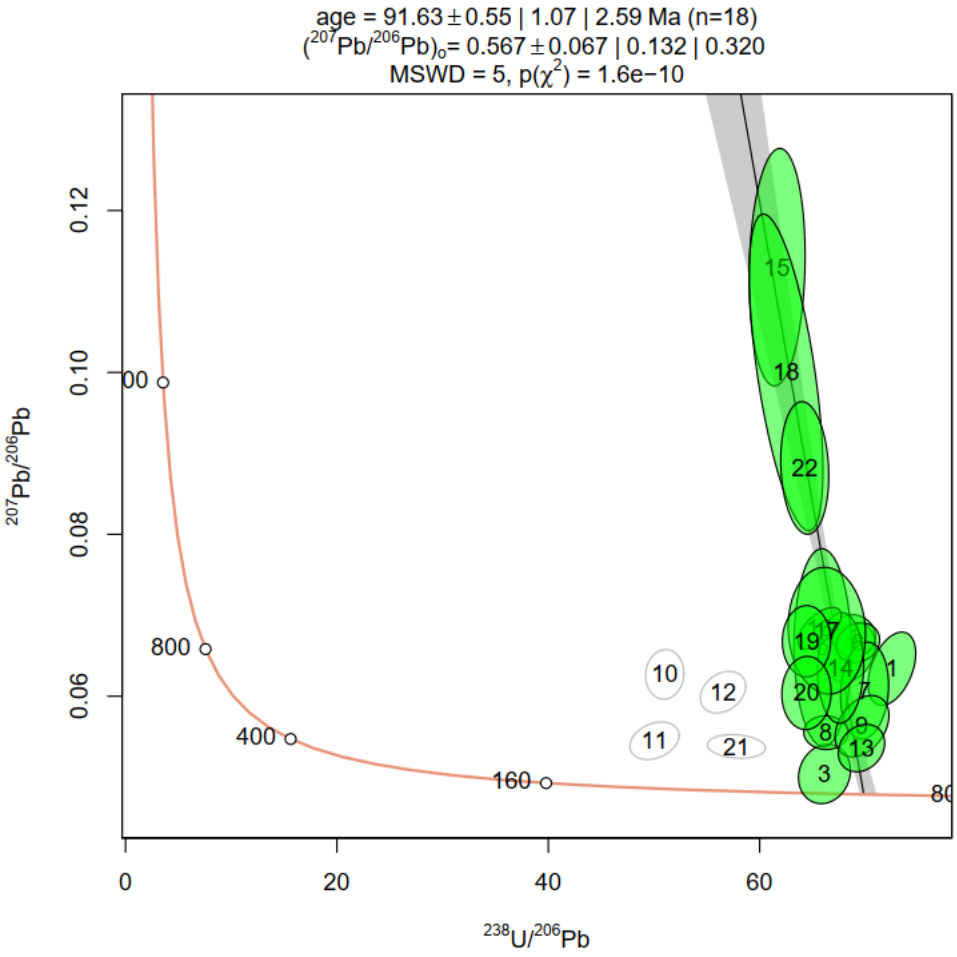

Figure 3.3.3: U-Pb concordia diagram of LASS-ICPMS analysis from AJE-2422 MARID zircons following Terra and Wasserburg (1972). The data is uncorrected for common Pb. The grey line represents a mixing line between initial common Pb from Stacey and Kramers (1975) and the radiogenic composition.

All corrections for common Pb had a very small effect on the calculated $^{206}Pb/^{238}U$ ages (less than uncertainty).

The spatial distribution of $^{206}Pb/^{238}U$ ages calculated in AJE-2422 are illustrated in Figure 3.3.2 and plotted as probability density curves in Figure 3.3.4 below. This figure also compares MARID zircon ages from this study to a compilation of literature $^{206}Pb/^{238}U$ ages from the

handful of published works on U-Pb dating in MARID zircons (Hamilton *et al*., 1998; Konzett *et al*., 1998; Konzett *et al*., 2000; Giuliani *et al*., 2015; Hoare *et al*., 2021).

Zircon ages in this study show significant spread, ranging from 86.2 Ma to 125.9 Ma (Figure 3.3.4 A). No correlation was observed between CL patterns and $^{206}Pb/^{238}U$ ages. Intragrain variability is significant, with single zircon grains displaying minimum and maximum ages separated by as much as 30 million years (Figure 3.3.3 E). No straightforward core-to-rim age pattern was observed in any of the zircons analyzed here, with many of the older ages occurring along the grain margins. This age distribution is very similar to the compilation of values obtained from previous studies (Figure 3.3.4 A and B). Literature ages from MARID zircons in the Kimberley region range from 79.4 to 142 Ma. This range is not solely a function of contrasting values from different studies. Intragrain variability is observed consistently in studies of MARID zircons, with some grains displaying similarly wide gaps between minimum and maximum ages (e.g., Konzett *et al*., 1998 sample 483). The exception to this is the results found in Hamilton *et al.* (1998) which are tightly clustered. This spread in U-Pb ages does not support a single-age crystallization event and suggests a more complex, protracted history for the growth of MARID zircons.

Major modes in the $^{206}Pb/^{238}U$ ages for zircons from AJE-2422 occur at 90.6, 94.6, and 125.8 Ma (Figure 3.3.4 B), spanning the common peaks in kimberlite and orangeite emplacement across southern Africa (e.g., Griffin *et al*., 2014) The youngest zircon ages from AJE-2422 briefly predate the emplacement of the Bultfontein kimberlite (from which AJE-2422 was derived). The largest age mode displayed from the literature compilation (~89 Ma) is also close to Bultfontein emplacement ages estimated from U-Pb in perovskite and suggests a major surge of zircon growth coincident with this event (Figure 3.3.4 B).

Roughly 38% of calculated ages from sample AJE-2422 fall within the major pulse of kimberlite activity in the Kimberley region at ~90 Ma while approximately 15% are coincident with the major pulse of orangeite volcanism at ~120 Ma (Figure 3.5.4 C), overlapping with ages determined by Hamilton *et al.,* (1998). The majority of ages for the AJE-2422 zircon (47%) are intermediate between these age modes. The majority of all ages in the literature compilation (45%) lie within the “kimberlite” field, while 15% lie in the orangeite field (identical to results from this study). 40% of values are intermediate between the two pulses.

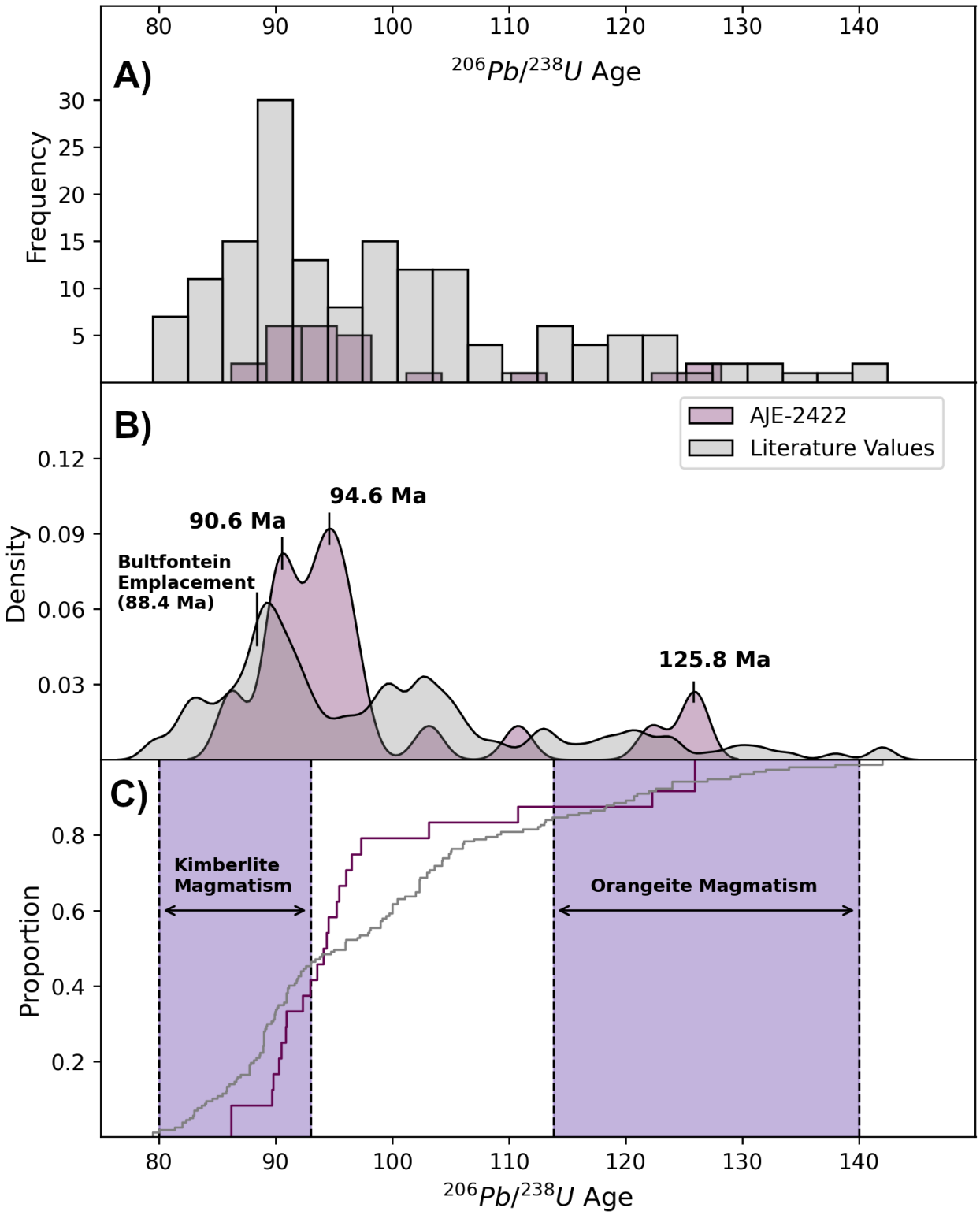
A)
B)
C)
$^{206}Pb/^{238}U$ Age
Frequency
Density
Proportion
AJE-2422
Literature Values
90.6 Ma
94.6 Ma
125.8 Ma
Bultfontein
Emplacement
(88.4 Ma)
Kimberlite
Magmatism
Orangeite Magmatism

Figure 3.3.4: Distribution of $^{206}Pb/^{238}U$ ages in MARID zirons from this study (purple) and previous work (grey; Hamilton *et al*., 1998; Konzett *et al*., 1998; Konzett *et al*., 2000; Giuliani *et al*., 2015; Hoare *et al*., 2021). A) Histogram of age distribution highlighting frequency of age occurrences B) KDE plot highlighting major age modes from this study. Note the correspondence of the major literature age mode with the emplacement of the Bultfontein kimberlite (Davis 1977). C) ECDF plot comparing $^{206}Pb/^{238}U$ age distributions to occurrences of nearby intraplate magmatism. Fields for kimberlite and orangeite magmatism represent age ranges for the major magmatic pulses near the Kimberley region (from Kjarsgaard *et al.,* in press)

3.3.4 Lu-Hf Isotope Geochemistry

Lu-Hf isotope data of MARID zircons from sample AJE-2422 are listed in Appendix B.4.1. Concentrations of Lu are low (typical of zircons) leading to $^{176}Lu/^{177}Hf$ ratios ranging from 0.000014 to 0.00016.

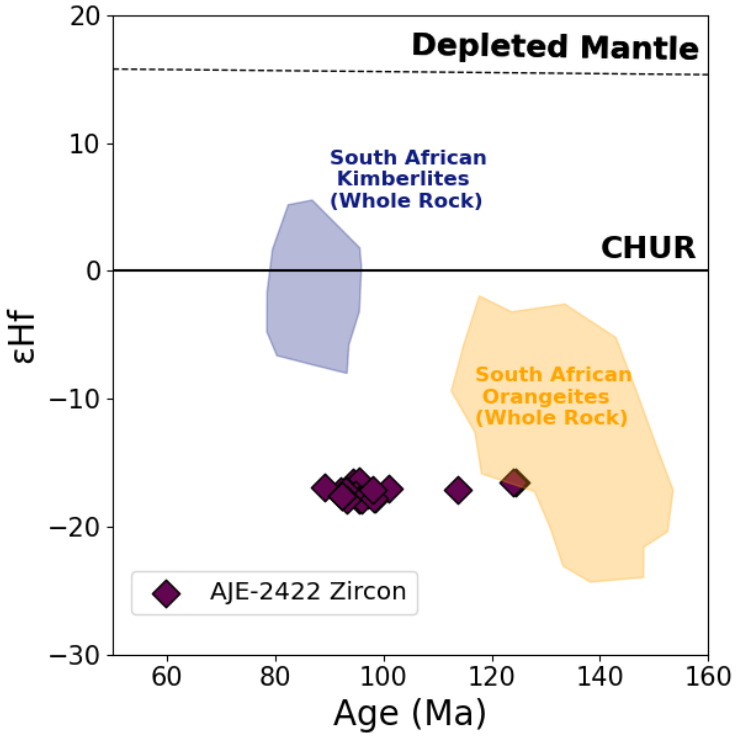

Figure 3.3.5: εHf values vs crystallization age of zircons from MARID xenolith AJE-2422. Fields for South African kimberlites and orangeites represent pipes in the Kimberley region that erupted during the main pulses of Cretaceous intraplate magmatism (Nowell *et al*., 2004; Coe *et al*., 2008; Davies *et al*., 2006). Depleted mantle evolution line from Fisher and Vervoort (2018).

$^{176}Hf/^{177}$ratios are unradiogenic and tightly clustered (Figure 3.3.5), with values from 0.2822 to 0.28226 (εHf values from -17.9 to -16.4). Calculated εHf_i values plotted vs. their $^{206}Pb/^{238}U$ crystallization age (Figure 3.3.5) show uniformity across the temporal spread described in the

previous section (avg. εHf_i of -17.3 ± 1.0). These values show good agreement with previous results obtained from MARID zircons in the Kimberley area (Giuliani *et al*., 2015; avg. εHf_i = -15.9 ± 2.6; Figure 3.3.6 A). In their study of MARID silicate phases, Fitzpayne *et al*., 2019 analyzed a clinopyroxene grain from sample AJE-2422 and found a nearly identical εHf_i value of -17.0. Across all MARID samples from the Kimberley region, Fitzpayne *et al*., (2019) reported similarly unradiogenic εHf values (avg. εHf_i = -13.7 ± 4.9). No correlation between εHf_i and $^{206}Pb^{238}U$ age was observed, despite the wide temporal range of crystallization ages and the contrasting Hf isotope signatures of the major magmatic events occurring in the Kimberley region during that time span.

The initial εHf signatures of MARID zircons and Mesozoic South African kimberlite related magmas are illustrated in Figure 3.3.6. Lamproites from the Aldan Shield (Siberian Craton) are also plotted for comparison (Davies *et al*., 2006). South African orangeites display two major modes at -16 and -5 εHf_i which partially overlap the field for South African kimberlites. Kimberlites are consistently less enriched, with the major modes having supra-chondritic εHf_i values. MARID zircons are consistently enriched in their Hf isotope composition and span a very narrow range of – εHf_i values. This range corresponds well with the major mode of South African orangeites at ~ -16 εHf_i, with Siberian lamproites also overlapping this range but extending to much lower εHf_i values.

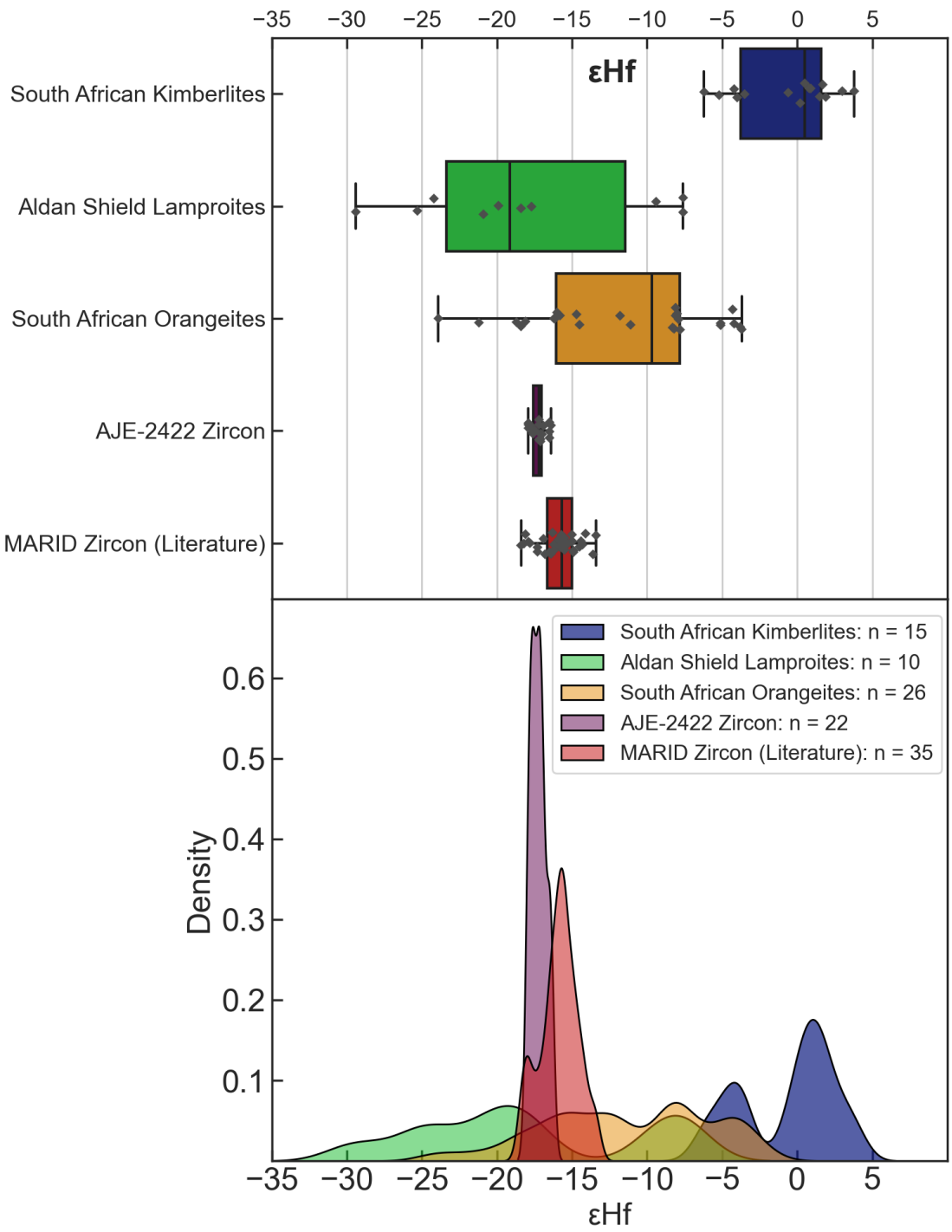

Figure 3.3.6: Hf isotope signatures in MARID zircons compared to South African intraplate magmatism. εHf values for Aldan Shield lamproites are included for comparison. Literature values for MARID zircons from Giuliani *et al*., 2015. Fields for kimberlites, orangeites, and lamproites are compiled from Nowell *et al*. (2004), Davies *et* al. (2006), Coe *et al*. (2008), and Tappe *et al*. (2021).

3.4 Discussion

The data presented here is only the second published study of joint U-Pb and Lu-Hf isotope systematics of MARID zircons (Giuliani *et al*., 2015) and significantly expands the available radiogenic isotope dataset for these rocks. In the following sections, we discuss the temporal span of $^{206}Pb/^{238}U$ ages and the geochemical characteristics of a potential source for the petrogenesis of MARID rocks in the lithospheric mantle.

3.4.1 Assessing the Contribution of Pb Loss to Age Variability in MARID Zircons

For any radiogenic isotope system to provide meaningful age interpretations, the behavior of the parent and daughter isotopes during different geochemical processes must be well understood. For example, the Lu-Hf system is a useful geochemical tracer in part because of the differences in parent-daughter fractionation during partial melting events (Kinny and Maas 2003). It is also critical to understand the "closure" conditions of a given isotopic system. If the crystal system remains open to disequilibrating processes (e.g., diffusion), then the accumulation of radiogenic daughter isotopes will not occur in a predictable fashion. Such conditions affecting the closure of a given system can include temperatures exceeding the "blocking temperature" of a mineral or secondary events such as metamorphism/metasomatism (Kinny and Maas 2003). In the context of the zircon U-Th-Pb system, open system conditions will primarily lead to loss of radiogenic Pb as it is the least compatible in the zircon crystal lattice, sitting in "damaged" sites (Mezger and Krogstad 1997). Despite being extremely robust, zircon may still undergo Pb loss under extreme conditions which commonly manifests as discordance between calculated $^{206}Pb/^{238}U$ and $^{207}Pb/^{235}U$ ages or as overdispersion in ages between grains deemed to be from the same population.

In a recent publication from Hoare *et al*. (2021), the authors argue that Pb loss is unlikely to occur in zircons crystallized from MARID-type metasomatic processes (e.g., PKP, PIC, MARID xenoliths) due to low U contents and their relatively shallow depths in the mantle. In contrast, previous studies have largely considered Pb loss to be a significant contributor to age heterogeneity (Konzett *et al.,* 1998, 2000). The distribution of $^{206}Pb/^{238}U$ ages reported here must

therefore be assessed for the possible contribution of Pb loss and we examine evidence of both viewpoints.

Pb loss in zircon occurs in four primary ways according to Mezger and Krogstad (1997): 1) diffusion in metamict (radiation damaged) zircon 2) diffusion in pristine zircon 3) leaching from metamict zircon and 4) recrystallization of metamict zircon. Metamictization occurs when alpha particles from the decay of U and Th damage the crystal lattice. Zircons in the metamict state lose density and have an internal structure similar to glass (Murakami *et al*., 1991). This makes metamict zircon extremely prone to alteration, especially in the presence of a liquid phase (e.g., kimberlite entrainment; Mezger and Krogstad 1997). Thus, any critical examination of Pb loss should attempt to determine the degree of metamictization in the studied zircon grains.

Metamictization can be quantified using the equation:

$$\boldsymbol{D = 8N_1[e^{a_1 t} - 1] + 7N_2[e^{a_2 t} - 1] + 6N_3[e^{a_3 t} - 1]}$$

Equation 3.4.1 from Holland and Gottfried (1955) and Murakami *et al.* (1991) where:

D = the total dose of α-decay events/mg

N_1, N_2, N_3 = isotopic abundance of ^{238}U, ^{235}U, ^{232}Th respectively (N_2 is calculated based on the natural ratio of $^{238}U/^{235}U$)

a_1, a_2, a_3 = decay constants of ^{238}U, ^{235}U, ^{232}Th respectively

t = age of the zircon

Zircons with total α-dose greater than $3x10^{15}$ α-decay events/mg indicate stage II damage may have occurred to the crystal structure (Murakami *et al*., 1991). Stage II damage marks the threshold where fluid mobile elements (i.e., Pb) are extremely susceptible to removal from the zircon.

Figure 3.4.1 plots the degree of α-dose damage versus the concentration of U in zircons analyzed in this study. Unsurprisingly, U concentration has the largest effect on α-dose damage while the age of the zircon has a smaller secondary effect due to their relatively young ages. While U concentrations reported here are comparable to other studies of MARID zircons, they are extremely low when juxtaposed with typical metamorphic and igneous zircons (10's-100's and 100's-1000's of ppm U respectively; Mezger and Krogstad 1997). In addition, zircons in AJE-2422 are very young which means there has been less time for α-decay events to occur. Both these factors lead to the low levels of α-dose damage/mg observed in this study (Figure 3.4.1).

All data points plot orders of magnitude below the zones where metamictization would begin to present Pb loss concerns.

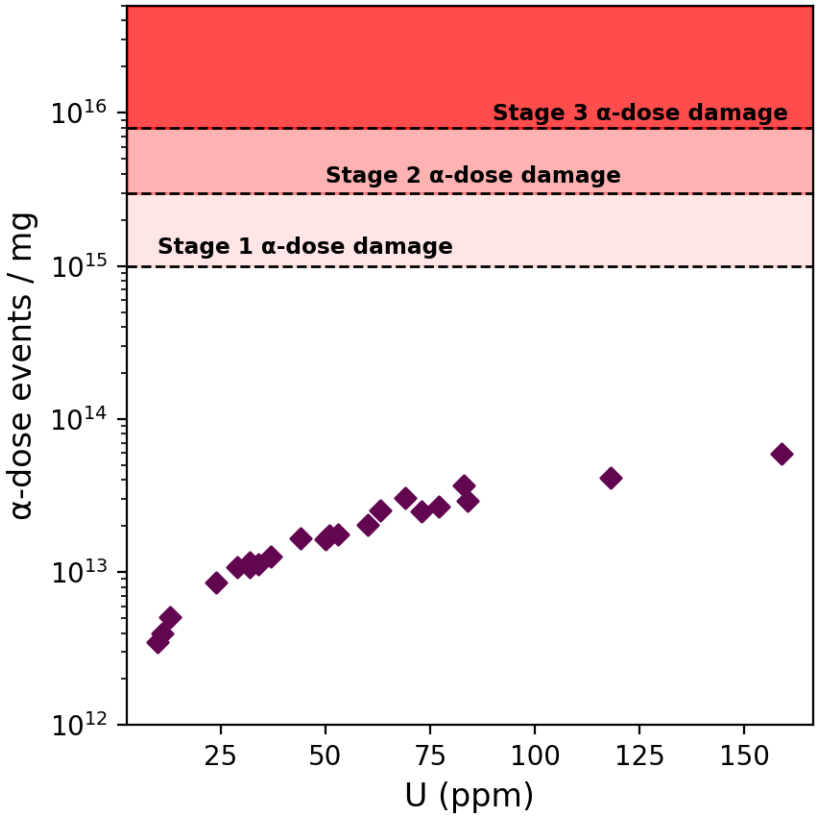

Figure 3.4.1: α-dose events/mg vs U concentration in zircons from MARID xenolith AJE-2442 (purple diamonds). Fields defining stepwise zones of α-dose damage from Murakami *et al*., (1991)

It has been demonstrated that zircons are able to self-anneal any α-decay fission damage at temperatures exceeding 600-650°C (e.g., Yamada *et al*., 1995; Zhang *et al*., 2000). While no precise depth constraints exist for sample AJE-2422, Waters and Erlank (1988) suggest that heavily metasomatized peridotites (PKP,MARID) in the Kimberley area reside at temperatures ranging between 745-885°C which is well above the annealing temperature of zircon. For α-dose damage to accumulate, MARID xenoliths would need to reside slightly shallower in the lithospheric mantle than the current best estimates. Therefore, these estimates for lattice damage, despite being very low, are maximum possible values.

The evidence here suggests that metamictization is extremely unlikely to have occurred in zircons from sample AJE-2422 due to their low U-Th concentrations, young ages, and residence

in the mantle above the zircon annealing temperature. The elimination of significant α-damage means it is not necessary to consider leaching, diffusion or recrystallization of a metamict zircon as viable sources of Pb loss and that the zircons in AJE-2422 are pristine.

Pb loss may still occur in pristine zircon under certain conditions. Above temperatures of ~ 1000 °C, zircon may lose Pb slowly as a result of diffusion in the pristine lattice (Mezger and Krogstad 1997). This estimate is well above the highest temperature estimates of Waters and Erlank (1988) described above, but does restrict MARIDs to a fairly narrow temperature range where Pb diffusion is insignificant. These zircons were probably only subjected to temperatures in excess of 1000 °C during entrainment in the kimberlite magma which can erupt at temperatures as high as 1350 °C (Kavanagh and Sparks 2009). Konzett *et al*., (1998) suggested that Pb loss due to interaction with the host kimberlite was at least partially responsible for the intragrain age variability observed in their study. However, diffusion in pristine zircon is extremely slow and requires millions of years to produce a significant effect on the Pb budget (Mezger and Krogstad 1997). This is incompatible with the extremely rapid ascent that has been modelled for kimberlitic eruptions (e.g., Kelley and Wartho 2000; Wilson and Head III 2007). Therefore diffusion in pristine zircon can also be eliminated as a potential mechanism for Pb loss in MARID zircons.

Several studies note that kimberlitic zircons sampled as "megacrysts" show evidence for remelting and recrystallization from kimberlite magma during entrainment (e.g., Belousova *et al*., 1998; Belousova *et al*., 2002; Hoare *et al*., 2021). If resorption and recrystallization of zircon were to occur during ascent, then the recorded $^{206}Pb/^{238}U$ age would represent the age of kimberlite eruption and not necessarily the age of original crystal growth. While it is impossible to completely eliminate this explanation for several of the observed ages, Hf isotopic evidence discussed in the next section suggests that it is unlikely.

Similar arguments to those presented here were made by Hoare *et al*. (2021) where they determined that recrystallization and growth of new zircon material were more likely to be responsible for the intragrain variability in $^{206}Pb/^{238}U$ ages. Based on the available evidence, we agree with this interpretation and consider the $^{206}Pb/^{238}U$ ages reported for sample AJE-2422 to represent the time of zircon crystallization for the different domains sampled.

One way to further constrain the temperatures at which MARID xenoliths reside in the mantle, and thus their potential for Pb loss, would be to use the joint Ti-in-zircon and Zr-in-rutile thermometers of Ferry and Watson (2007). Though their accuracy may not be perfectly suited to mantle rocks (e.g., Fu *et al*., 2008), there is potential for this method to further constrain MARID genesis. Attempts to utilize these thermometers in this study were thwarted by extremely anomalous concentrations of Ti in zircons of AJE-2422 (~4500 ppm Ti; Appendix B.1) leading to temperatures well in excess of what could reasonably be expected from consideration of cratonic mantle geotherms. Whether this was due to diffusion from nearby ilmenite/rutile or some other geochemical factor is unknown, but this observation indicates that such trace element based thermometers are not well suited to MARID assemblages.

3.4.2 Zircon Lu-Hf systematics as a mantle source tracer

Terminology in mantle Lu-Hf isotope geochemistry

In mantle isotope geochemistry (and in the context of this paper), "enriched" and "depleted" source regions typically describe the degree in which the area in question has interacted with a geochemically enriching agent such as a metasomatic fluid or melt. In the Re-Os isotope system, metasomatically altered zones of the lithospheric mantle are enriched in the radiogenic parent isotope (^{187}Re) due to its preference for mobilization in the liquid phase. Thus, metasomatically altered mantle will often show positive γOs values from elevated time-integrated $^{187}Re/^{188}Os$ ratios (and vice versa for melt depleted lithospheric mantle). However, this terminology is not as well suited to the Lu-Hf isotope system. The radiogenic parent isotope (^{176}Lu) behaves more compatibly (i.e. it will remain the solid phase during interaction with a liquid) than the daughter element (Hf) and so a negative εHf value simultaneously describes a metasomatic enrichment event as well as a depletion in radiogenic hafnium relative to CHUR. Thus it is important to understand that the enriched signature indicated by negative εHf values is describing a general geochemical history of the source region, and not elevated levels of the isotope itself.

Assessing the stability of the zircon Lu-Hf system

In pristine zircon, the Lu-Hf radiogenic isotope system is extremely robust. During crystallization with any co-precipitating phases, zircon incorporates weight percent levels of Hf (1.06 wt % in this study; Appendix B.1) resulting in extreme fractionation of Lu-Hf and $^{176}Lu/^{177}Hf$ ratios typically around 0.0005 (Kinny and Maas 2003; 0.00008 ± 0.00004 in this

study; Appendix B.4.2). Such low levels of radioactive parent means that changes to the $^{176}Hf/^{177}Hf$ ratio from radiogenic ingrowth are virtually negligible over extremely long time periods and zircons preserve the Hf isotopic composition of the source environment at the time of crystallization. Studies have also shown that, once incorporated, Hf isotopic ratios remain extremely consistent during events that would disturb other radiogenic isotopes such as U-Pb, nor are they susceptible to slow-scale diffusion (Hoskin and Black 2000; Cherniak and Watson 2003). Thus, zircons that show multiple stages of growth in the form of crystal zonation will preserve the Hf isotope characteristics during each growth stage across extremely fine scales without being perturbed by the homogenizing effects of diffusion (Cherniak and Watson 2003). This is illustrated in igneous zircon studies such as Bolhar *et al*. (2008) where large variations in εHf values were recorded between micron-scale growth zones. Given the apparent stability and sensitivity of the Lu-Hf isotope system, the zircons analyzed here are of significant interest for several reasons: 1) they are pristine and show minimal damage from metamictization (Chapter 3.4.1) 2) they are crystallized within a MARID mineral assemblage that has remained fairly mysterious in terms of petrogenesis 3) some grains display clear "oscillatory" growth patterns and a significant spread in U-Pb ages suggesting an episodic period of crystal growth 4) the Hf isotopic signature is remarkably consistent despite this apparent temporal heterogeneity. Section 3.1.1 describes the now well-established link between Mesozoic intraplate magmatism and the formation of highly metasomatized peridotites such as the PKP, MARID, and PIC xenoliths. However, there is still considerable disagreement on the timing, source, and mechanisms of MARID petrogenesis. To apply new constraints on the source of the parent MARID magma, we examine the current literature describing likely sources regions for the alkali-rich magmas most frequently attributed to MARID petrogenesis.

Source reservoirs of South African Mesozoic kimberlites, orangeites, and lamproites

A wide variety of source regions have been proposed to explain the complex geochemistry shown in Mesozoic kimberlites of South Africa (see Figure 1.3.3 in Chapter 1.3.2). Becker and Le Roex (2006) modelled the composition of primary South African kimberlite magmas and found that they displayed both refractory (Mg # = 0.82-0.87; 650-1400 ppm Ni) and metasomatically enriched (elevated LREE concentrations) characteristics with trace element patterns similar to ocean-island basalts (OIB). These factors were used to argue for a refractory

SCLM source that had been metasomatically enriched by the percolation of OIB-like magmas associated with upwelling of Mesozoic mantle plumes. Most commonly, however, the kimberlitic source region is placed below the lithosphere, indicated in part by moderately depleted to slightly enriched εHf values. A Hf-Nd study by Nowell *et al*. (2004) showed that South African kimberlites and their megacrysts plot below the mantle array defined by Vervoort *et al.* (1999) and have distinctly more radiogenic εHf values than orangeites. This displacement from the mantle array may have resulted from an OIB-like mechanism whereby subducted oceanic lithosphere is remelted in the asthenosphere or potentially the transition zone (Bizzarro *et al.* 2002; Nowell *et al.* 2004; Tappe *et al*. 2013). A large-scale model for all kimberlites by Torsvik *et al*. (2010) suggests that kimberlites arise from the core-mantle boundary and can be tracked by seismic velocity anomalies in the deepest portions of the mantle. While their exact source region remains mysterious, the major literature consensus places the kimberlite source below the SCLM (Nowell *et al*., 2004; Pearson *et al*., 2019; Tappe *et al*. 2013, 2020, 2021).

In contrast to kimberlites, South African orangeites display a more extreme geochemical signature that broadly overlaps that of lamproites. The Hf isotope systematics of orangeites are characterized by extremely unradiogenic $^{176}Hf/^{177}Hf$ ratios markedly distinct from the broadly chondritic compositions of kimberlites (Figure 3.3.6). A source region depleted in Hf that then experienced long-term isolation from the convecting mantle would be required to produce such time integrated Hf characteristics. Becker and Le Roex (2006) noted that Sr-Nd and trace element characteristics of modelled primary orangeite magmas were compatible wifth an SCLM source modified by calc-alkaline magmas associated with an ancient subduction signature. This model is consistent with an isolated source region that has been frequently modified by subduction metasomatism (Pearson *et al*., 2019). Coe *et al.* (2008) described a similar model for the petrogenesis of the Swartruggens and Star South African orangeites. They proposed that the Kaapvaal SCLM was enriched in subduction inputs from the 1.1 Ga Namaqua Orogeny and these inputs carried a calc-alkaline signature that crystallized clinopyroxene and phlogopite at the expense of garnet at the base of the SCLM. These pyroxene-rich zones evolved to low εHf-εNd compositions over time and were preferentially melted during a Mesozoic thermal event (e.g., mantle plume activity). Some pyroxenites analyzed by Pearson and Nowell (2004) showed suitably enriched εHf and εNd values to be a potential source rock for South African orangeites (-8.5 for both εHf and εNd). The trace element-enriched nature of a pyroxenite component would

dominate the radiogenic isotope signature of the primary magma, regardless of refractory peridotite input which would supply negligible Hf and Nd (Coe *et al*., 2008). Tappe *et al*., (2021) ascribe this model to the generation of the Impala and Sibanye South African orangeites. Fitzpayne *et al*., (2019) note that the original source for orangeite magmas would need to be more enriched than the "enriched-mantle II" (EM-II) endmember composition described by Zindler and Hart (1986).

Lamproites display very similar geochemistry to orangeites, to the point where some have suggested that orangeites are simply lamproites of the Kaapvaal craton (Mitchell 2006) or that the orangeite moniker should be discarded in favor of a CO_2-rich subtype of lamproite (Pearson *et al*., 2019). While we opt to refer to the South African varieties discussed here as orangeites due to the prevalence of the term in the current literature, we note that the overlapping Sr-Nd-Hf and trace element geochemistry suggests that lamproites are derived from a similar source region in the lithospheric mantle which has experienced a similar evolutionary history.

3.4.3 Radiogenic Isotope Constraints on MARID Petrogenesis and South African Intraplate Magmatism

The new data presented here combined with information from previous studies reveals new insights about the formation of MARID xenoliths and the nature of Mesozoic intraplate magmatism in the Kaapvaal craton.

The case for orangeite as the MARID parent magma

The expanding set of Hf isotope data for MARID minerals is beginning to paint a clearer picture of the parent magma. The two data sets available for MARID zircons (this study and that of Giuliani *et al*., 2015) display a very narrow range of εHf values from -13.4 to -18.4 (Figure 3.3.6; Figure 3.4.2). This extremely enriched signature is isotopically distinct from that of kimberlite magmas and shows good agreement with compositional fields for orangeites and lamproites (Figure 3.3.6; Figure 3.4.2; Giuliani *et al*., 2015). In addition to zircon, the Nd-Hf isotope systematics of other MARID silicate phases (clinopyroxene and K-richterite) has shown a similarly close association to South African orangeites (Fitzpayne *et al.,* 2019; Figure 3.4.2).

Despite the isotopic data seemingly precluding kimberlite involvement in the crystallization of a MARID assemblage, there are lines of evidence suggesting the opposite. In their study of a

MARID xenolith, Hoare *et al*. (2021) used a large number of data points to discern several distinct populations of zircon grains within a single sample. One population of zircons displayed trace element characteristics similar to kimberlitic megacrysts and had U-Pb ages matching Kimberley kimberlite magmatism. The growth of this population of zircons was thus attributed to kimberlite magmas and MARID crystallization attributed to a combination of parent magmas. Limited trace element data from our study show a composition intermediate between kimberlitic and lamproitic (a reasonable proxy for orangeite composition) zircons (Figure 3.4.3). However, the trace element compositions of kimberlitic and lamproitic zircon partially overlap, indicating they may not be the most robust indicator of parent magma composition (Figure 3.4.3). A kimberlitic signature is perhaps more clearly illustrated in the model of Fitzpayne *et al*. (2019) which is summarized in Figure 3.4.2.

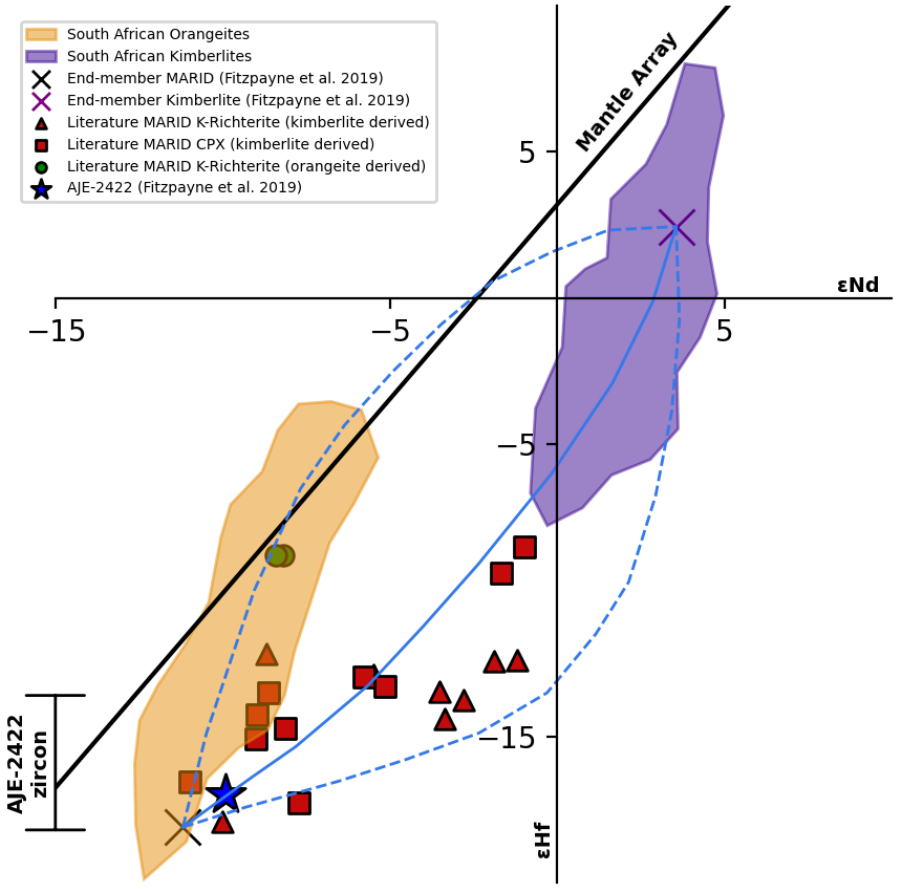

Figure 3.4.2: Nd-Hf isotope systematics of MARID minerals in relation to South African Mesozoic intraplate magmatism. Dotted and solid blue lines represent the range and average (respectively) of model trajectories from Fitzpayne *et al*. (2019) for mixing between an endmember MARID composition and that of a kimberlite melt. The range of εHf from zircon in this study is also shown. Literature values for MARID K-richterite and clinopyroxene from Fitzpayne *et al*. (2019). The blue star represents an AJE-2422 clinopyroxene analysis from Fitzpayne *et al*. (2019). Compositional fields for orangeites and kimberlites from Giuliani *et al*. (2015) and references therein. Mantle array line from Vervoort *et al*. (1999) and is defined as $\varepsilon Hf = 1.33\ \varepsilon Nd + 3.19$

MARID minerals from kimberlite-derived xenoliths plotted on Figure 3.4.2 show displacement below the mantle array (a trendline defining the coherence of Nd-Hf isotope systematics in terrestrial rocks; Vervoort *et al*. 1999) which is a feature ubiquitous in South African kimberlites. Fitzpayne *et al*. (2019) showed that isotope mixing of an original "end-member" MARID composition with that of a kimberlite melt will reproduce the increased displacement from the mantle array and push MARID minerals towards a more kimberlitic composition in Nd-Hf space. Thus, a kimberlite component is clearly visible in both trace elements and radiogenic isotopes, but it is difficult to conclusively determine whether this is a result of metasomatism during xenolith entrainment or from the crystallization of a kimberlitic or hybrid parent magma. Fitzpayne *et al*. (2019) suggest that MARID assemblages originally formed from a source broadly overlapping the composition of South African orangeites which was subsequently modified by kimberlite during eruption. A strong line of evidence for this model is indicated by the two MARID minerals derived from orangeite pipes which display less displacement from the mantle array and plot directly in the orangeite compositional field. Since the effects of metasomatism in MARID rocks attributed to orangeite melt infiltration are generally less pronounced than kimberlites (Fitzpayne *et al*., 2018b), it is more likely that they preserve the original isotopic signature.

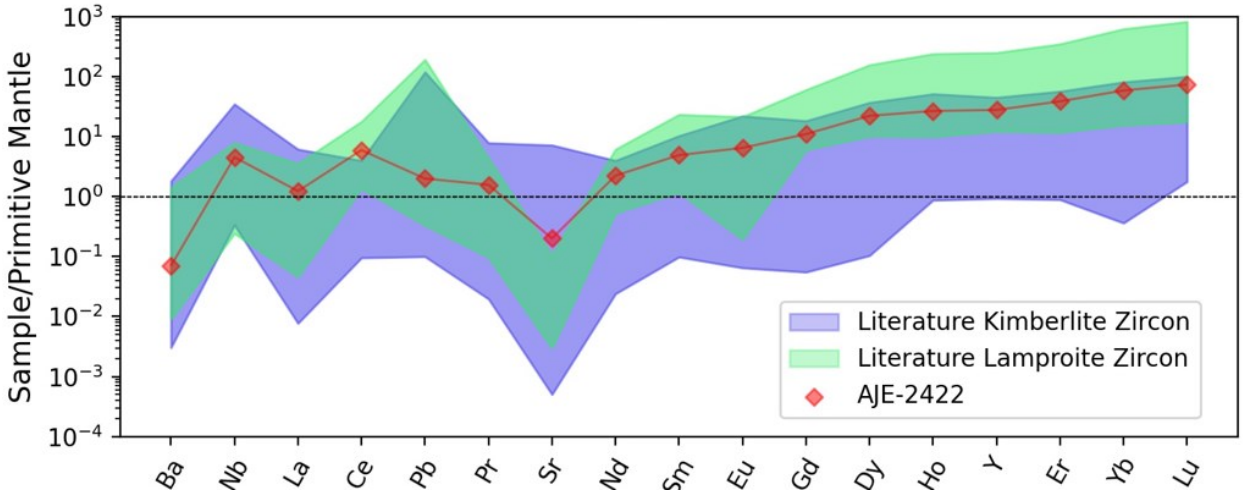

Figure 3.4.3: Primitive mantle normalized trace element patterns of zircons from kimberlites and lamproites. Ranges for kimberlitic and lamproitic zircons from Belousova *et al*. (2002). Values of AJE-2422 from this study are an average of n = 2 data points. Normalizing values from Mcdonough and Sun (1995).

In addition, Hf isotopes appear to be more resistant to the effects of a kimberlite component, with most MARID minerals plotting along the lower trajectory of the mixing model which is characterized by less change in εHf than εNd (Figure 3.4.2; Fitzpayne *et al*. 2019). Given the strong agreement of εHf values in AJE-2422 and previous studies of MARID zircon with that of South African orangeites, we concur that the kimberlitic signature visible in trace elements and radiogenic isotopes is more likely a result of kimberlite melt infiltration and that MARID assemblages originally crystallized from an orangeite (or very similar) source magma that was subsequently modified. This conclusion is consistent with other petrogenetic models linking MARID formation to orangeite magmatism (e.g., Sweeney *et al*., 1993; Gregoire *et al*., 2002; Giuliani *et al*., 2015).

Several complexities in MARID petrogenesis remain unanswered despite strengthening their link with orangeites. It has previously been proposed that a hydrous fluid phase (or in the case of some MARIDs, a highly carbonated fluid phase; e.g., Fitzpayne *et al*., 2018b) exsolved from a magma through decompression could either directly precipitate a MARID assemblage at high pressure or progressively metasomatize mantle peridotite until the original assemblage has been entirely replaced (Sweeney *et al*., 1993; Fitzpayne *et al*., 2018). Metasomatism from such a fluid could eventually produce peridotites altered to PKP or MARID rocks, and data from studies such as Gregoire *et al*., 2002 and Fitzpayne *et al*., 2018 show definite geochemical similarities in PKP and MARID rocks. The results presented here and in Chapter 2 of this study do not preclude this

possibility. We suggest that future research should focus on coupled U-Pb and Lu-Hf isotope analysis of PKP zircons (of which no data exists to the author's knowledge) to further constrain the genetic relationship between PKP and MARID xenoliths.

Additionally, there are distinct differences in MARID major and trace element geochemistry to that of orangeite magmas. Sweeney *et al*., (1993) attempted to explain these discrepancies by proposing that the orangeite magma had fractionated an olivine and carbonate component during ascent. New data from highly evolved orangeites in Southern Africa support this conclusion as their bulk geochemistry is closer to that of most MARID samples (Tappe *et al*., 2021; Chapter 2 of this study). However, the large MARID dataset from Fitzpayne *et al*., (2018) showed that trace element ratios that would certainly be affected by magmatic differentiation are not correlated to Mg # indicating that this process alone cannot be responsible for geochemical discrepancies. If MARID minerals are indeed a result of a magma crystallizing in veins, then a combination of fractionation and peridotite wall rock assimilation/reaction/equilibration would be sufficient to produce the compositional variation observed in MARID xenoliths (Fitzpayne *et al*. 2018). Bulk rock Re-Os modelling from Chapter 2 of this study support this conclusion as the incorporation of varying degrees of a peridotitic component reproduces variability in the MARID isotopic signatures.

Finally, the reverse relationship, that melting of MARID veined lithospheric mantle produces orangeite magma (Giuliani *et al*., 2015) must also be considered. The Lu-Hf isotope and trace element data examined here highlight the MARID-orangeite relationship but does not specify an order in which this relationship may have occurred. Therefore, the primary argument for MARID-veined lithosphere being the source rock for orangeite magmas is drawn from several MARID xenolith ages that predate known occurrences of orangeite magmatism in the Kimberley area (170 ± 30 Ma, Pearson *et al.,* 1995; 142 Ma, Konzett *et al*., 1998; 130 Ma, Giuliani *et al*., 2015). However, the vast majority of U-Pb ages from MARID xenoliths occur well past this period of orangeite magmatism (Figure 3.3.5) and this relationship is examined more closely in the following section.

U-Pb zircon age constraints on Mesozoic orangeite magmatism in the Kimberley region and a genetic relationship between MARID xenoliths and Karoo flood basalts

While the consistent εHf values observed in sample AJE-2422 reinforce the MARID-orangeite connection, the wide range of U-Pb crystallization ages do not support a single-event origin for MARID xenoliths. This temporal range is mirrored in the compilation of literature U-Pb ages shown in Figure 3.3.5 (80-142 Ma). Typically, this range of ages has been interpreted as older ages representing the true age of formation with the younger ages resulting from either Pb loss or zircon recrystallization from kimberlite eruption (Konzett *et al*., 1998; Giuliani *et al*., 2015). As previously discussed, there does not appear to be a viable mechanism for Pb loss to occur in MARID zircons (Section 3.4.1). Recrystallization of portions of the zircon grains from kimberlite entrainment is a possible explanation for the large age mode concurrent with the Bultfontein kimberlite emplacement (where the majority of MARID xenoliths are sourced from), but there are several pieces of evidence suggesting this may not the case: Firstly, recrystallization of minerals via kimberlite primarily occurs as small rims around preexisting phases (e.g., Drury and Van Roermund 1989; Arndt *et al*., 2010). Thus in a recrystallized zircon the younger ages resulting from recrystallization would occur along the rims of the grain, but no such core-to-rim age pattern is observed in sample AJE-2422 (Figure 3.3.3). Secondly, recrystallized portions of mineral grains will have distinct geochemistry that reflects the host kimberlite magma. However, the strongly enriched εHf values observed across all analytical spots, are isotopically distinct from kimberlite and suggest the same orangeite-like source magma is responsible for crystallization across a wide time span. Thirdly, we observed no obvious recrystallization textures in AJE-2422 through the various imaging methods used in this study (EDS, CL, optical microscopy). Given the evidence presented, we interpret this range of ages to reflect a complex period of zircon growth that significantly extends the period of orangeite magmatism in the mantle lithosphere of the Kimberley region.

The record of orangeite magmatism in the Kaapvaal Craton is concentrated in a roughly 80-million-year period from 190-110 Ma with major age modes at ~130 Ma and ~120 Ma (Figure 3.4.4). Several ages younger than this range have also been documented (95 Ma from Driekoppies, Griffin *et al.,* 2014; 79 Ma from Silvery Home, Woodhead *et al*., 2017). One older age (200 Ma; Allsopp and Roddick 1984) from Doklowayo, Eswatini is also noted.

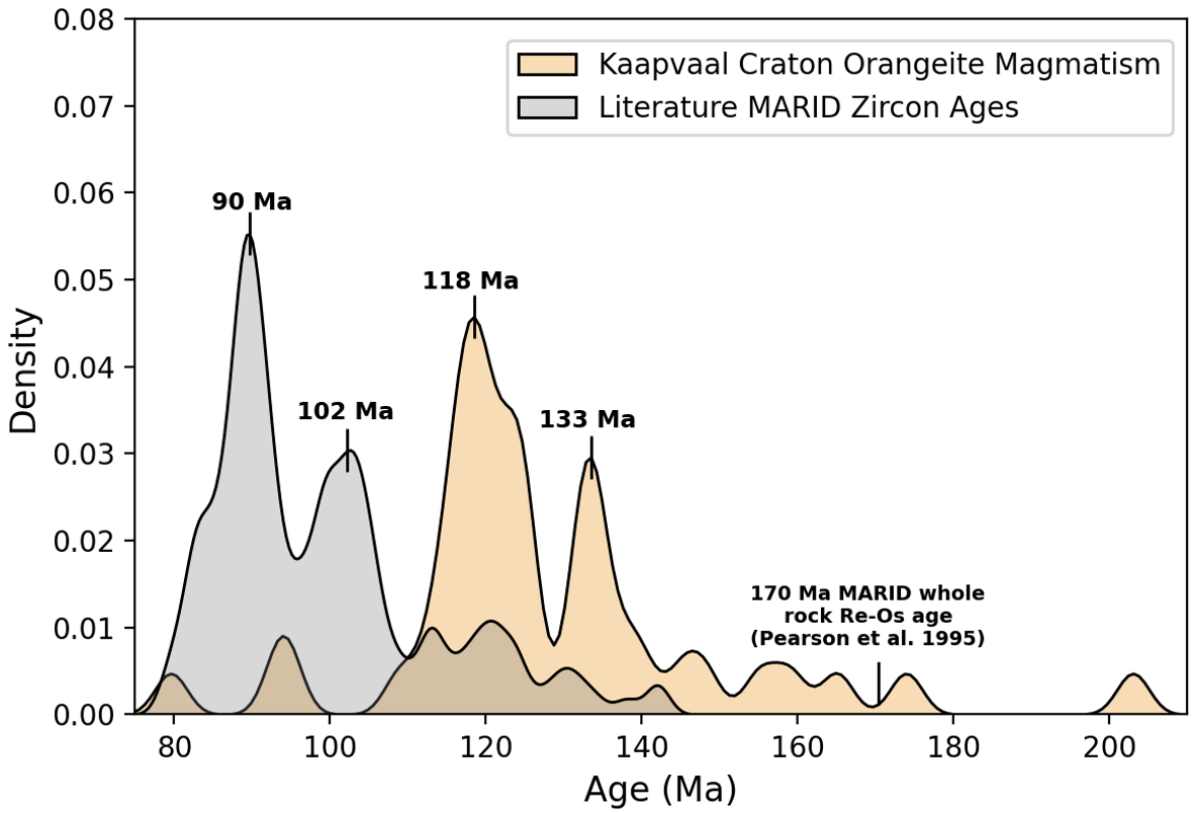

Figure 3.4.4: KDE plot of ages for recorded orangeite magmatism occurrences in the Kaapvaal Craton (orange) and South African MARID zircons (grey). Compilation of South African orangeite ages from Kjarsgaard *et al*., in press. MARID zircon ages from the same sources as Figure 3.3.5

In the direct vicinity of Kimberley-Barkly West, the major pulse occurred between 110-130 Ma with the nearby Swartruggens orangeite erupting at 140 Ma (Kjarsgaard *et al.,* in press; Coe *et al*., 2008). These ages are, of course, gleaned from studies based on the surficial expression of orangeite magmatism (i.e., diatremes). The results presented here suggest that magmas with an orangeite-like composition continued to percolate through the Kaapvaal mantle lithosphere long after the cessation of surface-breaching eruptions- a phenomenon also noted from U-Pb ages of zircon megacrysts from some kimberlites (e.g., Shu *et al*., 2018).

To explain this, we propose a scenario where the major pulse of orangeite magmatism in the Kimberley-Barkly West region occurred between 110-130 Ma. This pulse likely had the highest volume of melt or followed pre-existing fractures in the SCLM leading to frequent surface-breaching eruptions. This was followed by a second phase, where orangeite-like melt percolation continued in the Kaapvaal SCLM but did not reach the surface and instead crystallized in veins at high pressures. This crystallization was likely "open-system" (Fitzpayne *et al*., 2018) leading

to varying degrees of peridotite wall-rock assimilation, crystal fractionation, and melt-mixing. This period is shown by the major MARID zircon age mode at 102 Ma (Figure 3.3.5; Figure 3.4.4). A final pulse of orangeite-like melt percolation is recorded by the major MARID zircon age mode at ~90 Ma coincident with the emplacement of the Bultfontein kimberlite (again, it is worth noting that the majority of MARID samples thus reported are sourced from Bultfontein). This final occurrence may be associated with the same thermal event that caused the major pulse of kimberlite magmatism in the Kimberley region (Figure 3.3.5). A large thermal disturbance (e.g., a mantle plume; Becker and Le Roex 2006)) around this time may have led to new occurrences of both kimberlite and orangeite magmatism in the Kaapvaal SCLM. If this were the case, it is unclear why the kimberlite magmas tended to breach the surface while the orangeite magmas stalled and crystallized in the lithosphere to form MARID veins. Another possibility is that this thermal disturbance at 90 Ma caused selective remelting of pre-existing MARID veins from the ~100 Ma pulse described above. This remelting would reset the U-Pb crystallization age but retain the orangeite-like εHf signatures observed in MARID zircons. The remelted veins produced small volumes of melt that then re-crystallized before being entrained by passing kimberlite melts that eventually breached the surface. Kimberlite entrainment proceeded to subtly modify the trace element geochemistry of MARID rocks as described above. A similar, multi-stage model for Kaapvaal Mesozoic intraplate magmatism was proposed by Hoare *et al*., (2021). However, we suggest that the ~90 Ma age mode in MARID zircons is more likely recording the same thermal event that caused the generation of kimberlite magmas rather than the direct involvement of kimberlite magmas in the formation of MARID xenoliths. This is supported by the orangeite-like εHf values in the ~90 Ma MARID zircon and pyroxene assemblages (Figure 3.4.2).

A close association between ~90 Ma kimberlite eruptions and a preceding orangeite-like signature has been noted in previous studies. Zircons from the Orapa kimberlite in Botswana (~95 Ma; Griffin *et al*., 2014) showed two distinct populations of εHf values: one with a range from -12 to -14 and one with a range of 1.1 to 2.3 (Griffin *et al*., 2000; Nowell *et al*., 2004). Griffin *et al*., (2000) attributed the low εHf values of some Orapa zircons to mixing between a parent magma from the convecting mantle and the SCLM. This was mainly based on a prediction that SCLM should possess unradiogenic εHf values which is still a debated topic (Simon *et al*., 2002; Pearson *et al*., 2003; Nowell *et al*., 2004). An alternative explanation is that these two

populations are recording two distinct generations of crystallization: one associated with a kimberlite megacryst magma and one associated with an older, orangeite magma. This interpretation was favored by Nowell *et al*., (2004), who described two distinct generations of "megacryst magma". It is possible that zircons with low εHf values from Orapa are actually sourced from disaggregated MARID xenoliths rather than being megacrystic. However there are no recorded occurrences of MARID rocks from this pipe. Regardless, this association provides additional evidence that metasomatic minerals with orangeite-like Hf isotope signatures can occur in close temporal proximity to the emplacement of an archetypal kimberlite pipe.

The geochronological timeline we propose is difficult to reconcile with models suggesting orangeite magmas are sourced from MARID-veined lithosphere (Giuliani *et al*., 2015). Figure 3.4.4 illustrates that several occurrences of orangeite magmatism predate any recorded MARID xenolith age. The most prominent age modes for orangeite magmatism predate the age modes obtained from MARID zircons providing strong evidence that orangeite magmas occur prior to the formation of MARID rocks. The exception to this is the Re-Os model age of 170 ± 30 Ma (Pearson *et al*., 1995). While this is significantly different than other published MARID ages, it is also the only Re-Os age and the large error bars mean it could feasibly be associated with the small number of ~140 Ma ages from Konzett *et al*., (2000).

Finally, MARID metasomatism has also been linked to the eruption of the Karoo flood basalts roughly 180 Ma (Erlank *et al.,* 1987; Konzett *et al*., 1998; Jourdan *et al*., 2005; Giuliani *et al.,* 2014; Giuliani *et al*., 2015). The three major pieces of evidence for this are 1) U-Pb dating of LIMA (lindsleyite-mathiasite) minerals in metasomatized periodites showing that metasomatic phases (including phlogopite) were introduced coeval to Karoo magmatism (Giuliani *et al.,* 2014) 2) Major element and radiogenic isotope similarities between high-K Karoo picrites and MARID rocks (Erlank 1984) and 3) Older MARID ages broadly overlapping with that of Karoo magmatism (Konzett *et al*., 1998; Giuliani *et al*., 2015). Directly comparing the geochemistry of Karoo magmas with that of MARID rocks is outside the scope of this paper, but the U-Pb ages of MARID xenoliths do not support a genetic link between Karoo flood basalts and MARID rocks. Only the 170 ± 30 Ma Re-Os age from Pearson *et al*., (1995) is coeval with Karoo magmatism while all other ages significantly postdate this event. Instead, the U-Pb ages of MARID zircons

as well as the Hf isotope systematics are much more coherently linked to Mesozoic orangeite magmatism in the Kaapvaal craton.

A proposed model for the generation of orangeite magmas and subsequent MARID veining in the Kaapvaal craton lithospheric mantle

In this section, we take the evidence described above and attempt to place it within a simplified geological model. The goal of this model is to provide geological context to the results and explain the most important characteristics observed in this study and previous work.

Phase #1 (~1.1 Ga)

The Kaapvaal craton lithospheric mantle was modified by the subduction of ancient crust (formed during craton stabilization in the Archean) associated with the accretion of the Namaqua-Natal belt during the Kibaran orogeny roughly 1.1 Ga (Becker and Le Roex 2006; Coe *et al*., 2008). The subducted, eclogitized crust carried a calc-alkaline geochemical signature and an Hf-Nd isotopic composition similar to ancient sediments which evolved to increasingly negative εNd and εHf during long-term isolation from the convecting mantle (Figure 3.4.5). A zircon diamond inclusion in an eclogite xenolith (derived from ancient, subducted crust) from the Lace kimberlite provides a suitable estimate for this enriched mantle component (εHf_i = -27.8, Karaevangelou *et al*. 2021; Figure 3.4.5) Another possibility is that fluids/melts created during the subduction process metasomatized the refractory base of the Kaapvaal craton SCLM and crystallized clinopyroxene and phlogopite at the expense of garnet (Coe *et al*., 2008). These pyroxenite-like metasomes possessed very low Sm/Nd and Lu/Hf and evolved to negative εNd and εHf relatively quickly (Figure 3.4.5; Figure 3.4.6). The Lu/Hf ratios of some garnet-poor pyroxenites from the Beni Bousera Massif provide a reasonable estimate for this potential component (Pearson and Nowell 2004).

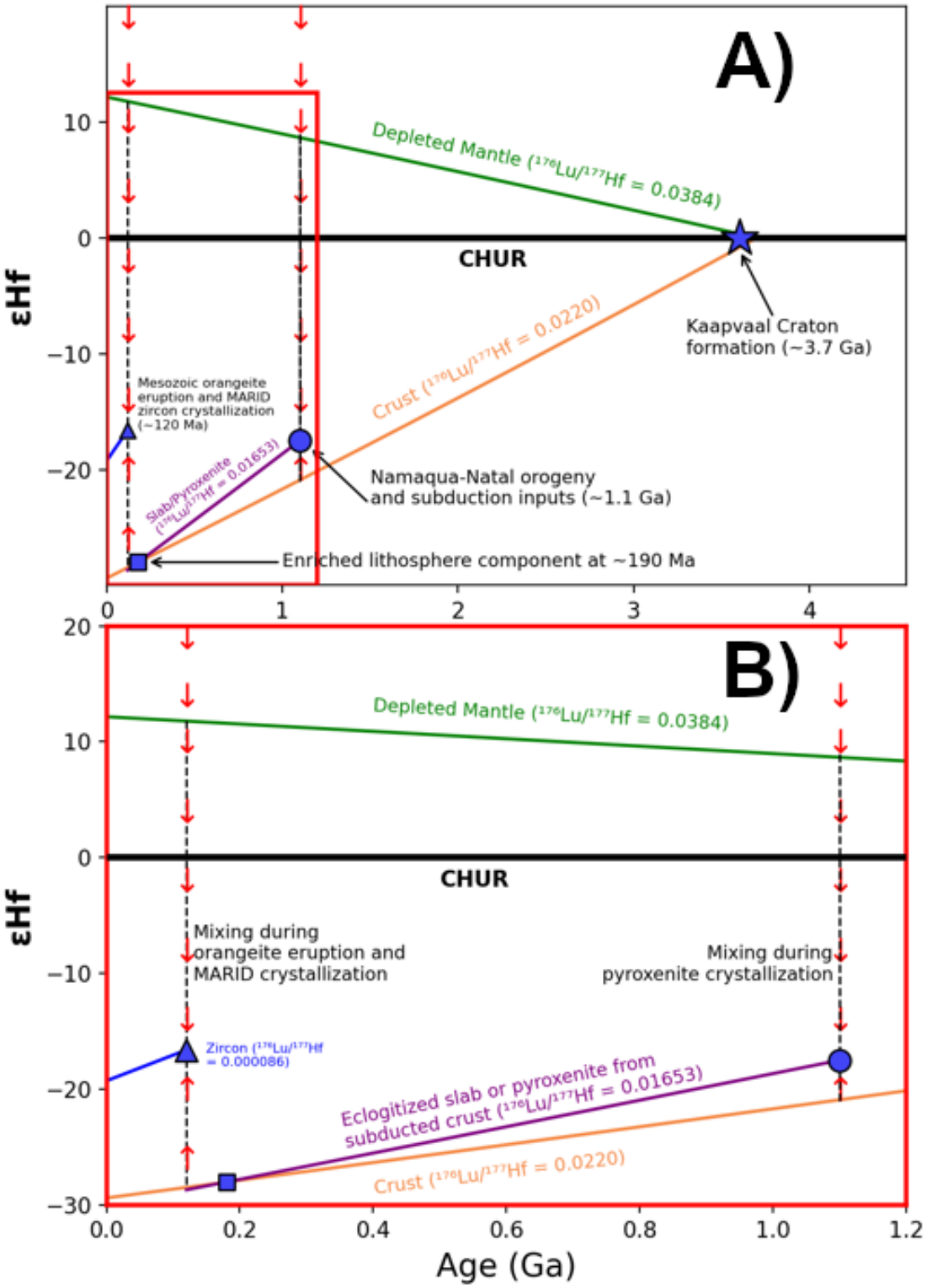
A)
Depleted Mantle ($^{176}Lu/^{177}Hf$ = 0.0384)
CHUR
Kaapvaal Craton formation (~3.7 Ga)
Crust ($^{176}Lu/^{177}Hf$ = 0.0220)
Mesozoic orangeite eruption and MARID zircon crystallization (~120 Ma)
Slab/Pyroxenite ($^{176}Lu/^{177}Hf$ = 0.01653)
Namaqua-Natal orogeny and subduction inputs (~1.1 Ga)
Enriched lithosphere component at ~190 Ma
εHf
B)
Depleted Mantle ($^{176}Lu/^{177}Hf$ = 0.0384)
CHUR
Mixing during orangeite eruption and MARID crystallization
Mixing during pyroxenite crystallization
Zircon ($^{176}Lu/^{177}Hf$ = 0.000086)
Eclogitized slab or pyroxenite from subducted crust ($^{176}Lu/^{177}Hf$ = 0.01653)
Crust ($^{176}Lu/^{177}Hf$ = 0.0220)
εHf
Age (Ga)

Figure 3.4.5: $^{176}Hf/^{177}Hf$ isotope evolution diagram of the Kaapvaal SCLM (based on a CHUR composition) evolving to the enriched composition from Karaevangelou *et al*. (2021) (blue square). After craton formation (~3.7 Ga), ancient crust is subducted at 1.1 Ga and mixes with depleted lithosphere, potentially crystallizing a hydrous pyroxenite-like assemblage. This component (purple line) has very low Lu/Hf and evolves relatively quickly to the enriched composition observed in the eclogite diamond inclusion. The depleted lithosphere component would likely have an εHf value greater than that of the Depleted Mantle evolution line and this is indicated by red arrows. Mesozoic (~120 Ma) orangeite magmas generated from selective melting of this enriched component variably stall in the mantle and mix with depleted lithospheric peridotite during MARID crystallization (black dotted line at 120 Ma). This process results in the εHf values observed in zircons from MARID sample AJE-2422. Figure 3.4.4 B shows a magnified view of the red square in Figure 3.4.4 A. CHUR parameters are from Bouvier *et al*. 2008. Lu/Hf of subducted crust from Amelin *et al*. (2011). Lu/Hf of mantle pyroxenite from garnet-poor wehrlites described in Pearson and Nowell (2004). Lu/Hf of depleted mantle from Griffin *et al*. (2000). Lu/Hf of MARID zircon is an average of all data points from this study (n = 18).

Phase #2 (~200-110 Ma)

Selective melting of the eclogitized crust or pyroxenite-like metasomes occurred during Mesozoic plume activity associated with the breakup of Gondwana (Becker and Le Roex 2006; Coe *et al*., 2008). Higher volumes of melts and/or a structurally assisted passage to the surface led to the major period of surface-breaching orangeite eruptions (Figure 3.4.5; Figure 3.4.6).

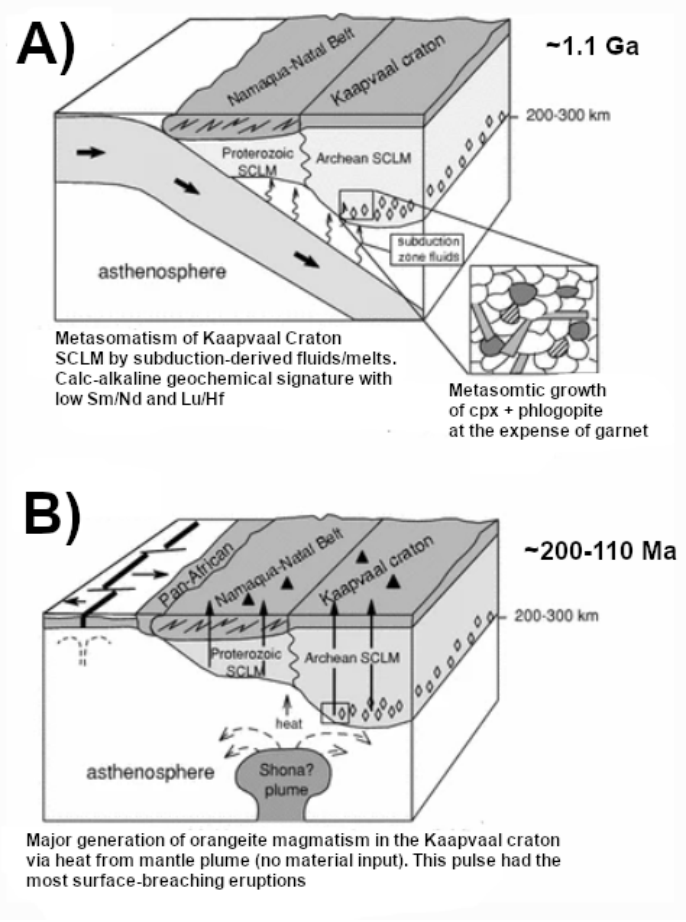

Figure 3.4.6: Summary schematic sketch for the first two phases of orangeite magma generation modified from Coe *et al*., (2008). A) Metasomatism of the Kaapvaal craton SCLM by subduction inputs during the Kibaran orogeny. B) Selective melting of eclogitized crust or pyroxenite-like metasomes at the base of the Kaapvaal SCLM. Melting is facilitated by mantle plume activity but no material input from the plume is assumed.

Phase #3 (110-90 Ma)

The exhaustion of the subduction-derived component at the base of the SCLM led to lower volume orangeite magmas. These magmas, after undergoing crystal fractionation and wall rock assimilation, stalled in the lithospheric mantle and crystallized a MARID assemblage under open system conditions (Sweeney *et al*., 1993; Fitzpayne *et al.,* 2018). MARID rocks were melt-buffered due to the Hf-poor nature of the wall rock (i.e., they retain strongly enriched εNd and εHf values). Some degree of peridotite incorporation into the crystallizing MARID assemblage is reinforced by their variable Re-Os isotope systematics (high Os in wall rock relative to the incoming melt; Chapter 2 of this study). This event is represented by the major MARID zircon age mode at ~100 Ma. Subsequently, a major pulse of convecting mantle derived kimberlite melts (also associated with Mesozoic mantle plumes?) and possible associated lithospheric mantle erosion occurred at ~90 Ma (Bell *et al.,* 2003; Mather *et al*., 2010). This thermal event either led to the final generation of stalled orangeite veining or selectively remelted pre-existing MARID veins leading to the major zircon age mode at ~90 Ma. The Bulftontein kimberlite erupted through veined lithospheric mantle and entrained a significant number of MARID xenoliths. Finally, the entrained MARID xenoliths were modified by kimberlite producing lower REE concentrations and increased Nd-Hf displacement from the mantle array (Figure 3.4.2; Figure 3.4.3). The Hf isotopic signature was more resistant to this effect and mostly retained the enriched signature of the original source.

3.5 Conclusions

The results described in this paper combined with a review of previously published data shed new light on major magmatic events in the lithospheric mantle of the Kaapvaal craton. We report an average εHf of -17.3 in zircons from MARID sample AJE-2422 and show that Hf isotopic evidence strongly reinforces the orangeite-MARID genetic link. Zircon U-Pb ages from sample AJE-2422 ranged from 86.2 to 125.9 Ma and displayed prominent modes at 90.6 Ma, 94.6 Ma, and 125.8 Ma. Our data suggests that MARID zircon growth in the Kaapvaal craton lithospheric

mantle occurred over a temporally extended period. This study has reached the following major conclusions:

1) The extremely enriched Hf isotope signature of MARID zircons is distinct from archetypal kimberlites and shows good agreement with previously published results for South African orangeites and lamproites. We interpret this as strong evidence for an orangeite magma source for MARID xenoliths. These magmas may have been derived from an enriched component of the lithospheric mantle such as subducted ancient crust or hydrous pyroxenite-like metasomes.
2) A kimberlitic signature is visible in MARID trace element systematics and previously published Nd-Hf isotope data for MARID silicate phases (Giuliani *et al*., 2015; Fitzpayne *et al*., 2019). This signature is likely the result of minor melt infiltration during kimberlite entrainment and not an indicator that MARID melts are crystallized from a hybrid magma (e.g., Hoare *et al*., 2021). Hf isotopes appear to be the most resistant to this effect and preserve the original magmatic signature.
3) The spread in U-Pb ages found in MARID zircons is unlikely to be caused by Pb loss or recrystallization during kimberlite entrainment. Instead, we suggest that a protracted period of orangeite magmatism in the Kaapvaal craton lithosphere is responsible for crystal growth over an extended time span. This is reinforced by the consistent orangeite-like εHf values regardless of the U-Pb age of the analytical spot. Major MARID zircon age modes at ~100 Ma may represent a phase of orangeite magmatism that failed to reach the surface and instead crystallized in the SCLM at high pressure. The major MARID zircon age mode at ~90 Ma coincident with the emplacement of the Bultfontein kimberlite may represent a final stage of stalled orangeite pipes or re-melting of pre-existing MARID veins in the lithospheric mantle.
4) U-Pb data from this study and a compilation of literature values indicate that MARID-veined lithosphere is unlikely to be the source rock for orangeite-like magmatism. Age discrepancies also provide evidence that MARID metasomatism is not likely to be genetically related to the Karoo igneous event at ~180 Ma

Chapter 4: Conclusion

4.1 Summary of Findings

Key Findings from Chapter 2

1. Silicate and oxide phases, even in highly metasomatized mantle lithologies, are negligible contributors to the whole rock precious metal budget of metasomatized lithospheric peridotite and related metasomes (i.e., MARID and PIC xenoliths).
2. Mass balance calculations assuming all precious metals reside within sulphide phases fail to account for the whole rock precious metal budget. This is likely due to a combination of factors including sensitivity to modelling parameters, multiple populations of residual and metasomatic sulphides, and a strong nugget effect from micro-scale PGE alloys. Thus, a combination of BMS and PGE alloy phases are the major repositories for precious metals in metasomatized lithospheric mantle.
3. HFSE and LILE concentrations show significant discrepancies between mass balance calculations and whole rock analysis. These discrepancies are likely caused by kimberlite metasomatism and trace phases not included in modal calculations.
4. Potassic intraplate magmas such as kimberlites and orangeites are PGE-poor and likely dilute the overall abundance of HSE in the mantle upon interaction with lithospheric peridotite. PGE-poor metasomatic sulphides in modally metasomatized xenoliths may have precipitated from these melts when they reached sulphur saturation. MARID xenoliths, interpreted as the crystallization products of these melts, are correspondingly PGE-poor with elevated PPGE/IPGE ratios.
5. Metasomatized peridotites show PPGE enrichment relative to “dry” melt-depleted peridotites in both cratonic and non-cratonic settings. Kimberlite-like melts are unlikely to account for this enrichment. Instead, small-degree melts associated with the Karoo LIP may precipitate PPGE-rich BM. IPGE-rich, unfractionated BMS in the GPP xenolith resemble “Type IV” eclogite sulphides (Hughes *et al.* 2021) and warrant future study. Residual alloys can potentially result in significant Pt anomalies not associated with metasomatism.

6. Variations in MARID IPGE systematics and Re-Os isotope signatures are well explained by two component mixing between a "pure MARID" composition (representing the parental melt) and lithospheric peridotite. The PGE-poor nature of MARID xenoliths makes them especially prone to contamination via host rock mixing. These results reinforce that MARID formation is a complex, open-system process that involves assimilation of and reaction with lithospheric peridotite at varied melt-rock ratios.
7. Re-Os isotope signatures of uncontaminated MARID samples show strong similarities to pyroxenites from the Beni Bousera and Bohemian Massifs. This, combined with Lu-Hf isotope data in Chapter 3 of this study, suggests a parental melt with similar time-integrated isotopic histories.

Key Findings from Chapter 3

1) The extremely enriched Hf isotope signature of MARID zircons is distinct from archetypal kimberlites and shows good agreement with previously published results for South African orangeites and lamproites. We interpret this as strong evidence for an orangeite magma source for MARID xenoliths. These magmas may have been derived from an enriched component of the lithospheric mantle such as subducted ancient crust or hydrous pyroxenite-like metasomes.
2) A kimberlitic signature is visible in MARID trace element systematics and previously published Nd-Hf isotope data for MARID silicate phases (Giuliani *et al*., 2015; Fitzpayne *et al*., 2019). This signature is likely the result of minor melt infiltration during kimberlite entrainment and not an indicator that MARID melts are crystallized from a hybrid magma (e.g., Hoare *et al*., 2021). Hf isotopes appear to be the most resistant to this effect and preserve the original magmatic signature.
3) The spread in U-Pb ages found in MARID zircons is unlikely to be caused by Pb loss or recrystallization during kimberlite entrainment. Instead, we suggest that a protracted period of orangeite magmatism in the Kaapvaal craton lithosphere is responsible for crystal growth over an extended time span. This is reinforced by the consistent orangeite-like εHf values regardless of the U-Pb age of the analytical spot. Major MARID zircon age modes at ~100 Ma may represent a phase of orangeite magmatism that failed to reach the surface and instead crystallized in the SCLM at high pressure. The major MARID

zircon age mode at ~90 Ma coincident with the emplacement of the Bultfontein kimberlite may represent a final stage of stalled orangeite pipes or re-melting of pre-existing MARID veins in the lithospheric mantle.

4) U-Pb data from this study and a compilation of literature values indicate that MARID-veined lithosphere is unlikely to be the source rock for orangeite-like magmatism. Age discrepancies also provide evidence that MARID metasomatism is not likely to be genetically related to the Karoo igneous event at ~180 Ma

4.2 Future Work

Results presented in Chapter 2 of this thesis provide new data that constrains the abundance and distribution of precious metals in the metasomatized lithospheric mantle. However, many questions remain about how precious metal enrichment occurs and their phase distributions. Mass balance calculations indicate that BMS phases fail to completely account for the precious metal abundances observed in heavily metasomatized xenoliths. This may have been, in part, due to the difficulty of locating suitable sulphide grains for LA-ICP-MS analysis. Future research, ideally with an increased focus on MARID and PIC xenoliths, should focus on locating additional well-crystallized BMS phases of different types (i.e., more analyses of chalcopyrite, pyrrhotite, etc.). Additionally, LA-ICP-MS mapping similar to the work of Lawley *et al*. (2020) may highlight micro-scale PGM phases that will further constrain key host phases in these rocks. The PGE enrichment observed in the GPP xenolith also warrants further attention. Specifically, the IPGE-rich, unfractionated pentlandite grains display distinct similarities to "Type-IV" eclogite sulphides described in Hughes *et al*. (2021). Re-Os isotope analysis of the individual grains may be able to constrain the source magma leading to their crystallization.

Chapter 3 of this study provides new temporal and petrogenetic constraints on Mesozoic orangeite magmatism and the formation of MARID xenoliths. Future research should focus on more accurately determining the depths at which MARID xenoliths reside in the SCLM coupled with more accurately defining trace element partition coefficients between MARID silicate phases and kimberlitic melts. Such efforts would allow the production of more accurate models assessing the inputs of kimberlite magmas into the formation of MARID rocks. Additionally, there are still geochemical inconsistencies between orangeite magmas and MARID rocks. New

modelling may be able to further constrain this relationship. Finally, we suggest that the precise relationship between PKP and MARID xenoliths may be elucidated by combined U-Pb and Lu-Hf isotope analysis of PKP zircons. Such a study would quickly determine whether PKP xenoliths possess the same enriched εHf values found in MARID rocks.

Bibliography

Abbey, S. (1983) ‘Studies in “standard samples” of silicate rocks and minerals 1969-1982’, *Can. Geol. Surv. Paper*, 114, pp. 83–15.

Ackerman, L. *et al.* (2013) ‘Highly siderophile element geochemistry of peridotites and pyroxenites from Horní Bory, Bohemian Massif: Implications for HSE behaviour in subduction-related upper mantle’, *Geochimica et Cosmochimica Acta*, 100, pp. 158–175. doi:10.1016/j.gca.2012.09.050.

Alard, O. *et al.* (2000) ‘Non-chondritic distribution of the highly siderophile elements in mantle sulphides’, *Nature*, 407(6806), pp. 891–894. doi:10.1038/35038049.

Alard, O. *et al.* (2011) ‘Volatile-rich Metasomatism in Montferrier Xenoliths (Southern France): Implications for the Abundances of Chalcophile and Highly Siderophile Elements in the Subcontinental Mantle’, *Journal of Petrology*, 52(10), pp. 2009–2045. doi:10.1093/petrology/egr038.

Allsop, H.L. and Roddick, J.C. (1984) ‘Rb-Sr 40Ar-39Ar age determinations of phlogopite micas from the Pre-Lebombo Group Dokolwayo kimberlite pipe’, *Special Publications of the Geological Society of South Africa*, (13), pp. 267–271.

Armstrong, R.A. *et al.* (1991) ‘Zircon ion microprobe studies bearing on the age and evolution of the Witwatersrand triad’, *Precambrian Research*, 53(3), pp. 243–266. doi:10.1016/0301-9268(91)90074-K.

Arndt, N. (2013) ‘The Lithospheric Mantle Plays No Active Role in the Formation of Orthomagmatic Ore Deposits’, *Economic Geology*, 108(8), pp. 1953–1970. doi:10.2113/econgeo.108.8.1953.

Arndt, N.T. *et al.* (2010) ‘Olivine, and the Origin of Kimberlite’, *Journal of Petrology*, 51(3), pp. 573–602. doi:10.1093/petrology/egp080.

Aulbach, S. *et al.* (2009) ‘Sulfide and whole rock Re–Os systematics of eclogite and pyroxenite xenoliths from the Slave Craton, Canada’, *Earth and Planetary Science Letters*, 283(1), pp. 48–58. doi:10.1016/j.epsl.2009.03.023.

Aulbach, S. *et al.* (2021) ‘Siderophile and chalcophile elements in spinels, sulphides and native Ni in strongly metasomatised xenoliths from the Bultfontein kimberlite (South Africa)’, *Lithos*, 380–381, p. 105880. doi:10.1016/j.lithos.2020.105880.

Ballhaus, C. *et al.* (2006) ‘Fractionation of the noble metals by physical processes’, *Contributions to Mineralogy and Petrology*, 152(6), pp. 667–684. doi:10.1007/s00410-006-0126-z.

Barnes, S.-J. *et al.* (2008) ‘The location of the chalcophile and siderophile elements in platinum-group element ore deposits (a textural, microbeam and whole rock geochemical study): Implications for the formation of the deposits’, *Chemical Geology*, 248(3), pp. 295–317. doi:10.1016/j.chemgeo.2007.08.004.

Barnes, S.-J., Maier, W.D. and Curl, E.A. (2010) ‘Composition of the Marginal Rocks and Sills of the Rustenburg Layered Suite, Bushveld Complex, South Africa: Implications for the

Formation of the Platinum-Group Element Deposits', *Economic Geology*, 105(8), pp. 1491–1511. doi:10.2113/econgeo.105.8.1491.

Becker, H. *et al.* (2006) 'Highly siderophile element composition of the Earth's primitive upper mantle: Constraints from new data on peridotite massifs and xenoliths', *Geochimica et Cosmochimica Acta*, 70(17), pp. 4528–4550. doi:10.1016/j.gca.2006.06.004.

Becker, M. and Le Roex, A. (2006) 'Geochemistry of South African On- and Off-craton, Group I and Group II Kimberlites: Petrogenesis and Source Region Evolution', *Journal of Petrology*, 47(4), pp. 673–703. doi:10.1093/petrology/egi089.

Bedini, R.M. and Bodinier, J.-L. (1999) 'Distribution of incompatible trace elements between the constituents of spinel peridotite xenoliths: ICP-MS data from the East African rift', *Geochimica et Cosmochimica Acta*, 63(22), pp. 3883–3900. doi:10.1016/S0016-7037(99)00154-4.

Begg, G.C. *et al.* (2010) 'Lithospheric, Cratonic, and Geodynamic Setting of Ni-Cu-PGE Sulfide Deposits', *Economic Geology*, 105(6), pp. 1057–1070. doi:10.2113/econgeo.105.6.1057.

Bell, D.R. *et al.* (2005) 'Silica and volatile-element metasomatism of Archean mantle: a xenolith-scale example from the Kaapvaal Craton', *Contributions to Mineralogy and Petrology*, 150(3), p. 251. doi:10.1007/s00410-005-0673-8.

Belousova, E.A. *et al.* (2002) 'Igneous zircon: trace element composition as an indicator of source rock type', *Contributions to Mineralogy and Petrology*, 143, pp. 602–622. doi:10.1007/s00410-002-0364-7.

Belousova, E.A., Griffin, W.L. and Pearson, N.J. (1998) 'Trace element composition and cathodoluminescence properties of southern African kimberlitic zircons', *Mineralogical Magazine*, 62(3), pp. 355–366. doi:10.1180/002646198547747.

Birck, J.L., Barman, M.R. and Capmas, F. (1997) 'Re-Os Isotopic Measurements at the Femtomole Level in Natural Samples', *Geostandards Newsletter*, 21(1), pp. 19–27. doi:10.1111/j.1751-908X.1997.tb00528.x.

Bizzarro, M. *et al.* (2002) 'Hf isotope evidence for a hidden mantle reservoir', *Geology*, 30(9), pp. 771–774. doi:10.1130/0091-7613(2002)030<0771:HIEFAH>2.0.CO;2.

Blichert-Toft, J. (2008) 'The Hf isotopic composition of zircon reference material 91500', *Chemical Geology*, 253(3), pp. 252–257. doi:10.1016/j.chemgeo.2008.05.014.

Bodinier, J.L. *et al.* (1990) 'Mechanisms of Mantle Metasomatism: Geochemical Evidence from the Lherz Orogenic Peridotite', *Journal of Petrology*, 31(3), pp. 597–628. doi:10.1093/petrology/31.3.597.

Bodinier, J.L. *et al.* (2004) 'Silicate, Hydrous and Carbonate Metasomatism at Lherz, France: Contemporaneous Derivatives of Silicate Melt–Harzburgite Reaction', *Journal of Petrology*, 45(2), pp. 299–320. doi:10.1093/petrology/egg107.

Bodinier, J.-L. and Godard, M. (2003) 'Orogenic, Ophiolitic, and Abyssal Peridotites', *Treatise on Geochemistry*, 2, p. 568. doi:10.1016/B0-08-043751-6/02004-1.

Bolhar, R. *et al.* (2008) 'Systematics of zircon crystallisation in the Cretaceous Separation Point Suite, New Zealand, using U/Pb isotopes, REE and Ti geothermometry', *Contributions to Mineralogy and Petrology*, 156(2), pp. 133–160. doi:10.1007/s00410-007-0278-5.

Bouvier, A., Vervoort, J.D. and Patchett, P.J. (2008) 'The Lu–Hf and Sm–Nd isotopic composition of CHUR: Constraints from unequilibrated chondrites and implications for the bulk composition of terrestrial planets', *Earth and Planetary Science Letters*, 273(1), pp. 48–57. doi:10.1016/j.epsl.2008.06.010.

Boyd, F.R. and Nixon, P.H. (1978) 'Ultramafic nodules from the Kimberley pipes, South Africa', *Geochimica et Cosmochimica Acta*, 42(9), pp. 1367–1382. doi:10.1016/0016-7037(78)90042-X.

Buick, I.S., Maas, R. and Gibson, R. (2001) 'Precise U–Pb titanite age constraints on the emplacement of the Bushveld Complex, South Africa', *Journal of the Geological Society*, 158(1), pp. 3–6. doi:10.1144/jgs.158.1.3.

Burnham, O.M. *et al.* (1998) 'The petrogenesis of the eastern Pyrenean peridotites: an integrated study of their whole-rock geochemistry and Re-Os isotope composition', *Geochimica et Cosmochimica Acta*, 62(13), pp. 2293–2310. doi:10.1016/S0016-7037(98)00092-1.

Burton, K.W. *et al.* (2002) 'The compatibility of rhenium and osmium in natural olivine and their behaviour during mantle melting and basalt genesis', *Earth and Planetary Science Letters*, 198(1), pp. 63–76. doi:10.1016/S0012-821X(02)00518-6.

Bussweiler, Y. *et al.* (2019) 'Trace element analysis of high-Mg olivine by LA-ICP-MS – Characterization of natural olivine standards for matrix-matched calibration and application to mantle peridotites', *Chemical Geology*, 524, pp. 136–157. doi:10.1016/j.chemgeo.2019.06.019.

Butcher, D.J. *et al.* (1988) 'Laser-excited Atomic Fluorescence Spectrometry in Flames, Plasmas and Electrothermal Atomisers: A Review', *Journal of Analytical Atomic Spectrometry*, 3, pp. 1059–1077.

Carlson, R.W., Esperança, S. and Svisero, D.P. (1996) 'Chemical and Os isotopic study of Cretaceous potassic rocks from Southern Brazil', *Contributions to Mineralogy and Petrology*, 125(4), pp. 393–405. doi:10.1007/s004100050230.

Carlson, R.W. and Nowell, G.M. (2001) 'Olivine-poor sources for mantle-derived magmas: Os and Hf isotopic evidence from potassic magmas of the Colorado Plateau', *Geochemistry, Geophysics, Geosystems*, 2(6). doi:10.1029/2000GC000128.

Carpenter, R.L., Edgar, A.D. and Thibault, Y. (2002) 'Origin of spongy textures in clinopyroxene and spinel from mantle xenoliths, Hessian Depression, Germany', *Mineralogy and Petrology*, 74(2), pp. 149–162. doi:10.1007/s007100200002.

Cherniak, D.J. and Watson, E.B. (2003) 'Diffusion in Zircon', *Reviews in Mineralogy and Geochemistry*, 53(1), pp. 113–143. doi:10.2113/0530113.

Choukroun, M. *et al.* (2005) 'Hf isotopes of MARID (mica-amphibole-rutile-ilmenite-diopside) rutile trace metasomatic processes in the lithospheric mantle', *Geology*, 33(1), pp. 45–48. doi:10.1130/G21084.1.

Coe, N. *et al.* (2008) 'Petrogenesis of the Swartruggens and Star Group II kimberlite dyke swarms, South Africa: constraints from whole rock geochemistry', *Contributions to Mineralogy and Petrology*, 156(5), p. 627. doi:10.1007/s00410-008-0305-1.

Cohen, A.S. and Waters, F.G. (1996) 'Separation of osmium from geological materials by solvent extraction for analysis by thermal ionisation mass spectrometry', *Analytica Chimica*

Acta, 332(2), pp. 269–275. doi:10.1016/0003-2670(96)00226-7.

Currie, L. (1968) 'Limits for qualitative detection and quantitative determination. Application to radiochemistry', *Analytical Chemistry*, 40(3), pp. 586–593.

Davies, G.R. *et al.* (2006) 'Trace Element and Sr–Pb–Nd–Hf Isotope Evidence for Ancient, Fluid-Dominated Enrichment of the Source of Aldan Shield Lamproites', *Journal of Petrology*, 47(6), pp. 1119–1146. doi:10.1093/petrology/egl005.

Davies, J.H. *et al.* (2002) 'The continental lithospheric mantle: characteristics and significance as a mantle reservoir', *Philosophical Transactions of the Royal Society of London. Series A: Mathematical, Physical and Engineering Sciences*, 360(1800), pp. 2383–2410. doi:10.1098/rsta.2002.1074.

Dawson, J.B. and Smith, J.V. (1977) 'The MARID (mica-amphibole-rutile-ilmenite-diopside) suite of xenoliths in kimberlite', *Geochimica et Cosmochimica Acta*, 41(2), pp. 309–323. doi:10.1016/0016-7037(77)90239-3.

Dockman, D.M. *et al.* (2018) 'Timing and origin of magmatism in the Sverdrup Basin, Northern Canada—Implications for lithospheric evolution in the High Arctic Large Igneous Province (HALIP)', *Tectonophysics*, 742–743, pp. 50–65. doi:10.1016/j.tecto.2018.05.010.

Donovan, J. *et al.* (2012) *Probe for EPMA: acquisition, automation, and analysis*. Eugene, Oregon: Probe Software Inc.

Drury, M.R. and Van Roermund, H.L.M. (1989) 'Fluid Assisted Recrystallization in Upper Mantle Peridotite Xenoliths from Kimberlites', *Journal of Petrology*, 30(1), pp. 133–152. doi:10.1093/petrology/30.1.133.

Duncan, R.A. *et al.* (1997) 'The timing and duration of the Karoo igneous event, southern Gondwana', *Journal of Geophysical Research: Solid Earth*, 102(B8), pp. 18127–18138. doi:10.1029/97JB00972.

Economou-Eliopoulos, M. and Mungall, J. (2005) 'Chapter 10: Platinum group element potential of porphyry deposits', in *Mineralogical Association of Canada Short Course*, pp. 203–246.

Enger, J. *et al.* (1995) 'Laser-induced fluorescence in a graphite furnace as a sensitive technique for assessment of traces in North Arctic atmospheric aerosol samples', *Analyst*, 120(3), pp. 635–641. doi:10.1039/AN9952000635.

Erlank, A.J. (1984) 'Petrogenesis of the volcanic rocks on the Karoo Province.', *Special Publications of the Geological Society of South Africa*, (13), p. p.

Erlank, A.J. *et al.* (1987) 'Evidence for mantle metasomatism in peridotite nodules from the Kimberley pipes, South Africa', *Mantle Metasomatism*, pp. 221–311.

Fabries, J. *et al.* (1991) 'Evolution of the Upper Mantle beneath the Pyrenees: Evidence from Orogenic Spinel Lherzolite Massifs', *Journal of Petrology*, Special_Volume(2), pp. 55–76. doi:10.1093/petrology/Special_Volume.2.55.

Fabriès, J., Lorand, J.-P. and Guiraud, M. (2001) 'Petrogenesis of the amphibole-rich veins from the Lherz orogenic lherzolite massif (Eastern Pyrenees, France): a case study for the origin of orthopyroxene-bearing amphibole pyroxenites in the lithospheric mantle', *Contributions to Mineralogy and Petrology*, 140(4), pp. 383–403. doi:10.1007/s004100000132.

Ferry, J.M. and Watson, E.B. (2007) 'New thermodynamic models and revised calibrations for the Ti-in-zircon and Zr-in-rutile thermometers', *Contributions to Mineralogy and Petrology*, 154, pp. 429–437. doi:10.1007/s00410-007-0201-0.

Fisher, C.M. *et al.* (2011) 'Synthetic zircon doped with hafnium and rare earth elements: A reference material for in situ hafnium isotope analysis', *Chemical Geology*, 286(1), pp. 32–47. doi:10.1016/j.chemgeo.2011.04.013.

Fisher, C.M. *et al.* (2017) 'Data Reduction of Laser Ablation Split-Stream (LASS) Analyses Using Newly Developed Features Within Iolite: With Applications to Lu-Hf + U-Pb in Detrital Zircon and Sm-Nd +U-Pb in Igneous Monazite', *Geochemistry, Geophysics, Geosystems*, 18(12), pp. 4604–4622. doi:10.1002/2017GC007187.

Fisher, C.M. and Vervoort, J.D. (2018) 'Using the magmatic record to constrain the growth of continental crust—The Eoarchean zircon Hf record of Greenland', *Earth and Planetary Science Letters*, 488, pp. 79–91. doi:10.1016/j.epsl.2018.01.031.

Fitzpayne, A., Giuliani, A., Phillips, D., *et al.* (2018) 'Kimberlite-related metasomatism recorded in MARID and PIC mantle xenoliths', *Mineralogy and Petrology*, 112. doi:10.1007/s00710-018-0573-z.

Fitzpayne, A., Giuliani, A., Hergt, J., *et al.* (2018) 'New geochemical constraints on the origins of MARID and PIC rocks: Implications for mantle metasomatism and mantle-derived potassic magmatism', *Lithos*, 318–319, pp. 478–493. doi:10.1016/j.lithos.2018.08.036.

Fitzpayne, A. *et al.* (2019) 'Progressive metasomatism of the mantle by kimberlite melts: Sr–Nd–Hf–Pb isotope compositions of MARID and PIC minerals', *Earth and Planetary Science Letters*, 509, pp. 15–26. doi:10.1016/j.epsl.2018.12.013.

Fitzpayne, A. *et al.* (2020) 'Isotopic analyses of clinopyroxenes demonstrate the effects of kimberlite melt metasomatism upon the lithospheric mantle', *Lithos*, 370–371, p. 105595. doi:10.1016/j.lithos.2020.105595.

Fraser, D.G. *et al.* (1984) 'Direct determination of strontium enrichment on grain boundaries in a garnet lherzolite xenolith by proton microprobe analysis', *Nature*, 312(5992), pp. 352–354. doi:10.1038/312352a0.

Fu, B. *et al.* (2008) 'Ti-in-zircon thermometry: applications and limitations', *Contributions to Mineralogy and Petrology*, 156(2), pp. 197–215. doi:10.1007/s00410-008-0281-5.

Giuliani, A. *et al.* (2014) 'LIMA U–Pb ages link lithospheric mantle metasomatism to Karoo magmatism beneath the Kimberley region, South Africa', *Earth and Planetary Science Letters*, 401, pp. 132–147. doi:10.1016/j.epsl.2014.05.044.

Giuliani, A. *et al.* (2015) 'Did diamond-bearing orangeites originate from MARID-veined peridotites in the lithospheric mantle?', *Nature Communications*, 6(1), p. 6837. doi:10.1038/ncomms7837.

Giuliani, A. and Pearson, G. (2019) 'Kimberlites: From Deep Earth to Diamond Mines', *Elements*, 15, pp. 377–380. doi:10.2138/gselements.15.6.377.

Govindaraju, K. (1994) '1994 Compilation of Working Values and Sample Description for 383 Geostandards', *Geostandards Newsletter*, 18(S1), pp. 1–158. doi:10.1046/j.1365-2494.1998.53202081.x-i1.

Gréau, Y. *et al.* (2013) 'Sulfides and chalcophile elements in Roberts Victor eclogites: Unravelling a sulfide-rich metasomatic event', *Chemical Geology*, 354, pp. 73–92. doi:10.1016/j.chemgeo.2013.06.015.

Grégoire, M., Bell, D. and Le Roex, A. (2002) 'Trace element geochemistry of phlogopite-rich mafic mantle xenoliths: their classification and their relationship to phlogopite-bearing peridotites and kimberlites revisited', *Contributions to Mineralogy and Petrology*, 142(5), pp. 603–625. doi:10.1007/s00410-001-0315-8.

Gregoire, M., Bell, D.R. and Le Roex, A.P. (2003) 'Garnet Lherzolites from the Kaapvaal Craton (South Africa): Trace Element Evidence for a Metasomatic History', *Journal of Petrology*, 44(4), pp. 629–657. doi:10.1093/petrology/44.4.629.

Griffin, W.L. *et al.* (1996) 'Trace-element zoning in mantle minerals; metasomatism and thermal events in the upper mantle', *The Canadian Mineralogist*, 34(6), pp. 1179–1193.

Griffin, W.L. *et al.* (1999) 'Harzburgite to lherzolite and back again: metasomatic processes in ultramafic xenoliths from the Wesselton kimberlite, Kimberley, South Africa', *Contributions to Mineralogy and Petrology*, 2–3(134), pp. 232–250. doi:10.1007/s004100050481.

Griffin, W.L. *et al.* (2003) 'The evolution of lithospheric mantle beneath the Kalahari Craton and its margins', *Lithos*, 71(2), pp. 215–241. doi:10.1016/j.lithos.2003.07.006.

Griffin, W.L. *et al.* (2014) 'Emplacement ages and sources of kimberlites and related rocks in southern Africa: U–Pb ages and Sr–Nd isotopes of groundmass perovskite', *Contributions to Mineralogy and Petrology*, 168(1), pp. 1–13. doi:10.1007/s00410-014-1032-4.

Griffin, W.L., Begg, G.C. and O'Reilly, S.Y. (2013) 'Continental-root control on the genesis of magmatic ore deposits', *Nature Geoscience*, 6(11), pp. 905–910. doi:10.1038/ngeo1954.

Griffin, W.L. and O'Reilly, S.Y. (2007) 'Cratonic lithospheric mantle: Is anything subducted?', *Episodes: journal of international geoscience*, 30(1), pp. 43–53.

Grütter, H.S. *et al.* (2004) 'An updated classification scheme for mantle-derived garnet, for use by diamond explorers', *Lithos*, 77(1), pp. 841–857. doi:10.1016/j.lithos.2004.04.012.

Haggerty, S.E. (1983) 'The mineral chemistry of new titanates from the jagersfontein kimberlite, South Africa: Implications for metasomatism in the upper mantle', *Geochimica et Cosmochimica Acta*, 47(11), pp. 1833–1854. doi:10.1016/0016-7037(83)90201-6.

Hamilton, M.A. *et al.* (1998) 'Constraints on MARID petrogenesis: SHRIMP II U-Pb zircon evidence for pre-eruption metasomatism at Kampfersdam', *International Kimberlite Conference: Extended Abstracts*, 7, pp. 296–298. doi:10.29173/ikc2714.

Handler, M.R. and Bennett, V.C. (1999) 'Behaviour of Platinum-group elements in the subcontinental mantle of eastern Australia during variable metasomatism and melt depletion', *Geochimica et Cosmochimica Acta*, 63(21), pp. 3597–3618. doi:10.1016/S0016-7037(99)00143-X.

Harte, B. (1983) 'Mantle peridotites and process--the kimberlite sample', in *Continental basalts and their mantle xenoliths*. Shiva Publishing Limited.

Harvey, J., König, S. and Luguet, A. (2015) 'The effects of melt depletion and metasomatism on highly siderophile and strongly chalcophile elements: S–Se–Te–Re–PGE systematics of

peridotite xenoliths from Kilbourne Hole, New Mexico', *Geochimica et Cosmochimica Acta*, 166, pp. 210–233. doi:10.1016/j.gca.2015.06.028.

Hatton, C.J. (1995) 'Mantle plume origin for the Bushveld and Ventersdorp magmatic provinces', *Journal of African Earth Sciences*, 21(4), pp. 571–577. doi:10.1016/0899-5362(95)00106-9.

Henry, P. *et al.* (1998) 'Late mantle evolution of the Pyrenean sub-continental lithospheric mantle in the light of new 40Ar–39Ar and Sm–Nd ages on pyroxenites and peridotites (Pyrenees, France)', *Tectonophysics*, 296(1), pp. 103–123. doi:10.1016/S0040-1951(98)00139-5.

Hoare, B.C., O'Sullivan, G. and Tomlinson, E.L. (2021) 'Metasomatism of the Kaapvaal Craton during Cretaceous intraplate magmatism revealed by combined zircon U-Pb isotope and trace element analysis', *Chemical Geology*, 578, p. 120302. doi:10.1016/j.chemgeo.2021.120302.

Holland, H.D. and Gottfried, D. (1955) 'The effect of nuclear radiation on the structure of zircon', *Acta Crystallographica*, 8(6), pp. 291–300. doi:10.1107/S0365110X55000947.

Holwell, D.A. *et al.* (2019) 'A metasomatized lithospheric mantle control on the metallogenic signature of post-subduction magmatism', *Nature Communications*, 10(1), p. 3511. doi:10.1038/s41467-019-11065-4.

Hoskin, P. w. o. and Black, L. p. (2000) 'Metamorphic zircon formation by solid-state recrystallization of protolith igneous zircon', *Journal of Metamorphic Geology*, 18(4), pp. 423–439. doi:10.1046/j.1525-1314.2000.00266.x.

Hughes, H.S.R. *et al.* (2021) 'Base metal sulphide geochemistry of southern African mantle eclogites (Roberts Victor): Implications for cratonic mafic magmatism and metallogenesis', *Lithos*, 382–383, p. 105918. doi:10.1016/j.lithos.2020.105918.

Jacobs, J. *et al.* (2008) 'The Kalahari Craton during the assembly and dispersal of Rodinia', *Precambrian Research*, 160(1), pp. 142–158. doi:10.1016/j.precamres.2007.04.022.

Jaffey, A.H. *et al.* (1971) 'Precision Measurement of Half-Lives and Specific Activities of 235U and 238U', *Physical Review C*, 4(5), pp. 1889–1906. doi:10.1103/PhysRevC.4.1889.

James, D.E. *et al.* (2001) 'Tectospheric structure beneath southern Africa', *Geophysical Research Letters*, 28(13), pp. 2485–2488. doi:10.1029/2000GL012578.

Janney, P.E. *et al.* (2010) 'Age, Composition and Thermal Characteristics of South African Off-Craton Mantle Lithosphere: Evidence for a Multi-Stage History', *Journal of Petrology*, 51(9), pp. 1849–1890. doi:10.1093/petrology/egq041.

Jochum, K.P. *et al.* (2005) 'GeoReM: A New Geochemical Database for Reference Materials and Isotopic Standards', *Geostandards and Geoanalytical Research*, 29(3), pp. 333–338. doi:10.1111/j.1751-908X.2005.tb00904.x.

Jochum, K.P. *et al.* (2011) 'Determination of Reference Values for NIST SRM 610–617 Glasses Following ISO Guidelines', *Geostandards and Geoanalytical Research*, 35(4), pp. 397–429. doi:10.1111/j.1751-908X.2011.00120.x.

Jones, A.P., Smith, J.V. and Dawson, J.B. (1982) 'Mantle Metasomatism in 14 Veined Peridotites from Bultfontein Mine, South Africa', *The Journal of Geology*, 90(4), pp. 435–453. doi:10.1086/628695.

Jourdan, F. *et al.* (2005) 'Karoo large igneous province: Brevity, origin, and relation to mass extinction questioned by new 40Ar/39Ar age data', *Geology*, 33(9), pp. 745–748. doi:10.1130/G21632.1.

Kalfoun, F., Ionov, D. and Merlet, C. (2002) 'HFSE residence and Nb/Ta ratios in metasomatised, rutile-bearing mantle peridotites', *Earth and Planetary Science Letters*, 199(1), pp. 49–65. doi:10.1016/S0012-821X(02)00555-1.

Kavanagh, J.L. and Sparks, R.S.J. (2009) 'Temperature changes in ascending kimberlite magma', *Earth and Planetary Science Letters*, 286(3), pp. 404–413. doi:10.1016/j.epsl.2009.07.011.

Kelley, S.P. and Wartho, J.-A. (2000) 'Rapid Kimberlite Ascent and the Significance of Ar-Ar Ages in Xenolith Phlogopites', *Science*, 289(5479), pp. 609–611. doi:10.1126/science.289.5479.609.

Kinny, P.D. and Maas, R. (2003) 'Lu–Hf and Sm–Nd isotope systems in zircon', *Reviews in Mineralogy and Geochemistry*, 53(1), pp. 327–341. doi:10.2113/0530327.

König, S. *et al.* (2015) 'Mineralogical control of selenium, tellurium and highly siderophile elements in the Earth's mantle: Evidence from mineral separates of ultra-depleted mantle residues', *Chemical Geology*, 396, pp. 16–24. doi:10.1016/j.chemgeo.2014.12.015.

Konzett, J. *et al.* (1998) 'The timing of MARID metasomatism in the Kaapvaal mantle: An ion probe study of zircons from MARID xenoliths', *Earth and Planetary Science Letters*, 160(1), pp. 133–145. doi:10.1016/S0012-821X(98)00073-9.

Konzett, J., Armstrong, R.A. and Günther, D. (2000) 'Modal metasomatism in the Kaapvaal craton lithosphere: constraints on timing and genesis from U–Pb zircon dating of metasomatized peridotites and MARID-type xenoliths', *Contributions to Mineralogy and Petrology*, 139(6), pp. 704–719. doi:10.1007/s004100000160.

Konzett, J., Sweeney, R.J. and Compston, W. (1995) 'The correlation of kimberlite activity with mantle metasomatism', *International Kimberlite Conference: Extended Abstracts*, 6, pp. 285–286. doi:10.29173/ikc1864.

Kramers, J.D., Roddick, J.C.M. and Dawson, J.B. (1983) 'Trace element and isotope studies on veined, metasomatic and "MARID" xenoliths from Bultfontein, South Africa.', *Earth and Planetary Science Letters*, 65(1), pp. 90–106. doi:10.1016/0012-821X(83)90192-9.

Larrea, M.L., Castro, S.M. and Bjerg, E.A. (2014) 'A software solution for point counting. Petrographic thin section analysis as a case study', *Arabian Journal of Geosciences*, 7(8), pp. 2981–2989. doi:10.1007/s12517-013-1032-0.

Lawley, C.J.M. *et al.* (2020) 'Element and isotopic signature of re-fertilized mantle peridotite as determined by nanopowder and olivine LA-ICPMS analyses', *Chemical Geology*, 536, p. 119464. doi:10.1016/j.chemgeo.2020.119464.

Le Roux, V. *et al.* (2007) 'The Lherz spinel lherzolite: Refertilized rather than pristine mantle', *Earth and Planetary Science Letters*, 259(3), pp. 599–612. doi:10.1016/j.epsl.2007.05.026.

Le Roux, V., Tommasi, A. and Vauchez, A. (2008) 'Feedback between melt percolation and deformation in an exhumed lithosphere–asthenosphere boundary', *Earth and Planetary Science Letters*, 274(3), pp. 401–413. doi:10.1016/j.epsl.2008.07.053.

Lin, J. *et al.* (2016) 'Calibration and correction of LA-ICP-MS and LA-MC-ICP-MS analyses for element contents and isotopic ratios', *Solid Earth Sciences*, 1(1), pp. 5–27. doi:10.1016/j.sesci.2016.04.002.

Locock, A.J. (2014) 'An Excel spreadsheet to classify chemical analyses of amphiboles following the IMA 2012 recommendations', *Computers & Geosciences*, 62, pp. 1–11. doi:10.1016/j.cageo.2013.09.011.

Longerich, H., Jackson, S. and Günther, D. (1996) 'Inter-laboratory note. Laser ablation inductively coupled plasma mass spectrometric transient signal data acquisition and analyte concentration calculation', *Journal of Analytical Atomic Spectrometry*, 11(9), pp. 899–904. doi:10.1039/JA9961100899.

Lorand, J.P. (1989) 'Abundance and distribution of CuFeNi sulfides, sulfur, copper and platinum-group elements in orogenic-type spinel lherzolite massifs of Ariège (northeastern Pyrenees, France)', *Earth and Planetary Science Letters*, 93(1), pp. 50–64. doi:10.1016/0012-821X(89)90183-0.

Lorand, J.-P. *et al.* (2008) 'Abundance and distribution of platinum-group elements in orogenic lherzolites; a case study in a Fontete Rouge lherzolite (French Pyrénées)', *Chemical Geology*, 248(3), pp. 174–194. doi:10.1016/j.chemgeo.2007.06.030.

Lorand, J.-P. and Alard, O. (2001) 'Platinum-group element abundances in the upper mantle: new constraints from in situ and whole-rock analyses of Massif Central xenoliths (France)', *Geochimica et Cosmochimica Acta*, 65(16), pp. 2789–2806. doi:10.1016/S0016-7037(01)00627-5.

Lorand, J.-P., Alard, O. and Luguet, A. (2010) 'Platinum-group element micronuggets and refertilization process in Lherz orogenic peridotite (northeastern Pyrenees, France)', *Earth and Planetary Science Letters*, 289(1), pp. 298–310. doi:10.1016/j.epsl.2009.11.017.

Lorand, J.-P. and Grégoire, M. (2006) 'Petrogenesis of base metal sulphide assemblages of some peridotites from the Kaapvaal craton (South Africa)', *Contributions to Mineralogy and Petrology*, 151(5), p. 521. doi:10.1007/s00410-006-0074-7.

Lorand, J.-P. and Luguet, A. (2016) 'Chalcophile and Siderophile Elements in Mantle Rocks: Trace Elements Controlled By Trace Minerals', *Reviews in Mineralogy and Geochemistry*, 81(1), pp. 441–488. doi:10.2138/rmg.2016.81.08.

Lorand, J.-P., Luguet, A. and Alard, O. (2013) 'Platinum-group element systematics and petrogenetic processing of the continental upper mantle: A review', *Lithos*, 164–167, pp. 2–21. doi:10.1016/j.lithos.2012.08.017.

Lorand, J.-P., Luguet, A. and Alard, O. (August 1, 2008b) 'Platinum-Group Elements: A New Set of Key Tracers for the Earth's Interior', *Elements*, 4(4), pp. 247–252. doi:10.2113/GSELEMENTS.4.4.247.

Luguet, A. *et al.* (2007) 'Residual platinum-group minerals from highly depleted harzburgites of the Lherz massif (France) and their role in HSE fractionation of the mantle', *Geochimica et Cosmochimica Acta*, 71(12), pp. 3082–3097. doi:10.1016/j.gca.2007.04.011.

Luguet, A., Nowell, G.M. and Pearson, D.G. (2008) '184Os/188Os and 186Os/188Os measurements by Negative Thermal Ionisation Mass Spectrometry (N-TIMS): Effects of

interfering element and mass fractionation corrections on data accuracy and precision', *Chemical Geology*, 248(3), pp. 342–362. doi:10.1016/j.chemgeo.2007.10.013.

Maier, W.D. *et al.* (2012) 'The concentration of platinum-group elements and gold in southern African and Karelian kimberlite-hosted mantle xenoliths: Implications for the noble metal content of the Earth's mantle', *Chemical Geology*, 302–303, pp. 119–135. doi:10.1016/j.chemgeo.2011.06.014.

Maier, W.D. *et al.* (2017) 'Platinum-group element contents of Karelian kimberlites: Implications for the PGE budget of the sub-continental lithospheric mantle', *Geochimica et Cosmochimica Acta*, 216, pp. 358–371. doi:10.1016/j.gca.2017.07.002.

Maier, W.D., Arndt, N.T. and Curl, E.A. (2000) 'Progressive crustal contamination of the Bushveld Complex: evidence from Nd isotopic analyses of the cumulate rocks', *Contributions to Mineralogy and Petrology*, 140(3), pp. 316–327. doi:10.1007/s004100000186.

Malkovets, V.G. *et al.* (2016) 'Cr-rich rutile: A powerful tool for diamond exploration', *Lithos*, 265, pp. 304–311. doi:10.1016/j.lithos.2016.08.017.

McDonald, I. *et al.* (1995) 'The geochemistry of the platinum-group elements in Brazilian and southern African kimberlites', *Geochimica et Cosmochimica Acta*, 59(14), pp. 2883–2903. doi:10.1016/0016-7037(95)00183-2.

McDonough, W.F. and Sun, S. -s. (1995) 'The composition of the Earth', *Chemical Geology*, 120(3), pp. 223–253. doi:10.1016/0009-2541(94)00140-4.

Menzies, M. and Hawkesworth, C. (1986) 'Mantle metasomatism'. Available at: https://www.osti.gov/biblio/5870369 (Accessed: 7 December 2021).

Menzies, Martin Adrian and Bodinier, J.L. (1993) 'Growth of the European lithospheric mantle—dependence of upper-mantle peridotite facies and chemical heterogeneity on tectonics and age', *Physics of the Earth and Planetary Interiors*, 79(1), pp. 219–240. doi:10.1016/0031-9201(93)90149-4.

Mertzman, S.A. (2015) 'Franklin and Marshall College XRF Laboratory Methods'. Franklin and Marshall College. Available at: https://www.fandm.edu/earth-environment/laboratory-facilities/xrf-and-xrd-lab (Accessed: 21 February 2022).

Mezger, K. and Krogstad, E.J. (1997) 'Interpretation of discordant U-Pb zircon ages: An evaluation', *Journal of Metamorphic Geology*, 15(1), pp. 127–140. doi:10.1111/j.1525-1314.1997.00008.x.

Miliszkiewicz, N., Walas, S. and Tobiasz, A. (2015) 'Current approaches to calibration of LA-ICP-MS analysis', *Journal of Analytical Atomic Spectrometry*, 30(2), pp. 327–338. doi:10.1039/C4JA00325J.

Mitchell, R.H. (1995) 'Kimberlites and Orangeites', in Mitchell, R.H. (ed.) *Kimberlites, Orangeites, and Related Rocks*. Boston, MA: Springer US, pp. 1–90. doi:10.1007/978-1-4615-1993-5_1.

Mitchell, R.H. (2008) 'Petrology of hypabyssal kimberlites: Relevance to primary magma compositions', *Journal of Volcanology and Geothermal Research*, 174(1), pp. 1–8. doi:10.1016/j.jvolgeores.2007.12.024.

Mitchell, R.H. and Keays, R.R. (1981) ‘Abundance and distribution of gold, palladium and iridium in some spinel and garnet lherzolites: implications for the nature and origin of precious metal-rich intergranular components in the upper mantle’, *Geochimica et Cosmochimica Acta*, 45(12), pp. 2425–2442. doi:10.1016/0016-7037(81)90096-X.

Morgan, J.W. (1986) ‘Ultramafic xenoliths: Clues to Earth’s late accretionary history’, *Journal of Geophysical Research: Solid Earth*, 91(B12), pp. 12375–12387. doi:10.1029/JB091iB12p12375.

Morimoto, N. (1988) ‘Nomenclature of Pyroxenes’, *Mineralogy and Petrology*, 39(1), pp. 55–76. doi:10.1007/BF01226262.

Murakami, T. *et al.* (1991) ‘Alpha-decay event damage in zircon’, *American Mineralogist*, 76(9–10), pp. 1510–1532.

Naldrett, A. *et al.* (2011) ‘Genesis of the PGE-Enriched Merensky Reef and Chromitite Seams of the Bushveld Complex’. doi:10.5382/Rev.17.

Nowell, G.M. *et al.* (2004) ‘Hf Isotope Systematics of Kimberlites and their Megacrysts: New Constraints on their Source Regions’, *Journal of Petrology*, 45(8), pp. 1583–1612. doi:10.1093/petrology/egh024.

O’Reilly, S.Y. and Griffin, W.L. (2013) ‘Mantle Metasomatism’, in Harlov, D.E. and Austrheim, H. (eds) *Metasomatism and the Chemical Transformation of Rock: The Role of Fluids in Terrestrial and Extraterrestrial Processes*. Berlin, Heidelberg: Springer (Lecture Notes in Earth System Sciences), pp. 471–533. doi:10.1007/978-3-642-28394-9_12.

Page, F.Z. *et al.* (2007) ‘Zircons from kimberlite: New insights from oxygen isotopes, trace elements, and Ti in zircon thermometry’, *Geochimica et Cosmochimica Acta*, 71(15), pp. 3887–3903. doi:10.1016/j.gca.2007.04.031.

Paton, C. *et al.* (2011) ‘Iolite: Freeware for the visualisation and processing of mass spectrometric data’, *Journal of Analytical Atomic Spectrometry*, 26(12), pp. 2508–2518. doi:10.1039/C1JA10172B.

Pearson, D.G., Shirey, S.B., *et al.* (1995) ‘Re□Os, Sm□Nd, and Rb□Sr isotope evidence for thick Archaean lithospheric mantle beneath the Siberian craton modified by multistage metasomatism’, *Geochimica et Cosmochimica Acta*, 59(5), pp. 959–977. doi:10.1016/0016-7037(95)00014-3.

Pearson, D.G., Rogers, N.W., *et al.* (1995) ‘Source regions of kimberlites and lamproites: constraints from Re-Os isotopes’, *International Kimberlite Conference: Extended Abstracts*, 6, pp. 430–432. doi:10.29173/ikc1919.

Pearson, D.G. *et al.* (1998) ‘Sulphide inclusions in diamonds from the Koffiefontein kimberlite, S Africa: constraints on diamond ages and mantle Re–Os systematics’, *Earth and Planetary Science Letters*, 160(3), pp. 311–326. doi:10.1016/S0012-821X(98)00092-2.

Pearson, D.G. (1999) ‘The age of continental roots’, *Lithos*, 48(1), pp. 171–194. doi:10.1016/S0024-4937(99)00026-2.

Pearson, D.G. *et al.* (2004) ‘Re–Os isotope systematics and platinum group element fractionation during mantle melt extraction: a study of massif and xenolith peridotite suites’, *Chemical Geology*, 208(1), pp. 29–59. doi:10.1016/j.chemgeo.2004.04.005.

Pearson, D.G. *et al.* (2021) 'Deep continental roots and cratons', *Nature*, 596(7871), pp. 199–210. doi:10.1038/s41586-021-03600-5.

Pearson, D.G. (2021) 'Kimberlite Geochronolgical Database (Unpublished)'. Unpublished.

Pearson, D.G., Canil, D. and Shirey, S.B. (2003) 'Mantle Samples Included in Volcanic Rocks: Xenoliths and Diamonds', *Treatise on Geochemistry*, 2, p. 568. doi:10.1016/B0-08-043751-6/02005-3.

Pearson, D.G. and Nowell, G.M. (2004) 'Re–Os and Lu–Hf Isotope Constraints on the Origin and Age of Pyroxenites from the Beni Bousera Peridotite Massif: Implications for Mixed Peridotite–Pyroxenite Mantle Sources', *Journal of Petrology*, 45(2), pp. 439–455. doi:10.1093/petrology/egg102.

Pearson, D.G. and Nowell, G.M. (no date) *The continental lithospheric mantle: characteristics and significance as a mantle reservoir*. doi:10.1098/rsta.2002.1074.

Pearson, D.G., Woodhead, J. and Janney, P.E. (2019) 'Kimberlites as Geochemical Probes of Earth's Mantle', *Elements*, 15(6), pp. 387–392. doi:10.2138/gselements.15.6.387.

Pearson, D.G. and Woodland, S.J. (2000) 'Solvent extraction/anion exchange separation and determination of PGEs (Os, Ir, Pt, Pd, Ru) and Re–Os isotopes in geological samples by isotope dilution ICP-MS', *Chemical Geology*, 165(1), pp. 87–107. doi:10.1016/S0009-2541(99)00161-8.

Pearson, G. and Wittig, N. (2014) 'The Formation and Evolution of Cratonic Mantle Lithosphere – Evidence from Mantle Xenoliths', in *Treatise on geochemistry (Second Edition), Volume 3: The mantle and core*, pp. 255–292. doi:10.1016/B978-0-08-095975-7.00205-9.

Peregoedova, A., Barnes, S.-J. and Baker, D.R. (2004) 'The formation of Pt–Ir alloys and Cu–Pd-rich sulfide melts by partial desulfurization of Fe–Ni–Cu sulfides: results of experiments and implications for natural systems', *Chemical Geology*, 208(1), pp. 247–264. doi:10.1016/j.chemgeo.2004.04.015.

Richards, J.P. (2011) 'Magmatic to hydrothermal metal fluxes in convergent and collided margins', *Ore Geology Reviews*, 40(1), pp. 1–26. doi:10.1016/j.oregeorev.2011.05.006.

Richardson, S.H. *et al.* (2001) 'Archean subduction recorded by Re–Os isotopes in eclogitic sulfide inclusions in Kimberley diamonds', *Earth and Planetary Science Letters*, 191(3), pp. 257–266. doi:10.1016/S0012-821X(01)00419-8.

Richardson, S.H. and Shirey, S.B. (2008) 'Continental mantle signature of Bushveld magmas and coeval diamonds', *Nature*, 453(7197), pp. 910–913. doi:10.1038/nature07073.

Richardson, S.H., Shirey, S.B. and Harris, J.W. (2004) 'Episodic diamond genesis at Jwaneng, Botswana, and implications for Kaapvaal craton evolution', *Lithos*, 77(1), pp. 143–154. doi:10.1016/j.lithos.2004.04.027.

Roering, C. *et al.* (1992) 'Tectonic model for the evolution of the Limpopo Belt', *Precambrian Research*, 55(1), pp. 539–552. doi:10.1016/0301-9268(92)90044-O.

Rosenbaum, J.M., Zindler, A. and Rubenstone, J.L. (1996) 'Mantle fluids: Evidence from fluid inclusions', *Geochimica et Cosmochimica Acta*, 60(17), pp. 3229–3252. doi:10.1016/0016-7037(96)00167-6.

Russell, W.A., Papanastassiou, D.A. and Tombrello, T.A. (1978) 'Ca isotope fractionation on the

Earth and other solar system materials', *Geochimica et Cosmochimica Acta*, 42(8), pp. 1075–1090. doi:10.1016/0016-7037(78)90105-9.

Schiano, P. and Clocchiatti, R. (1994) 'Worldwide occurrence of silica-rich melts in sub-continental and sub-oceanic mantle minerals', *Nature*, 368(6472), pp. 621–624. doi:10.1038/368621a0.

Schmidberger, S.S. and Francis, D. (2001) 'Constraints on the Trace Element Composition of the Archean Mantle Root beneath Somerset Island, Arctic Canada', *Journal of Petrology*, 42(6), pp. 1095–1117. doi:10.1093/petrology/42.6.1095.

Schmitz, M.D. *et al.* (2004) 'Subduction and terrane collision stabilize the western Kaapvaal craton tectosphere 2.9 billion years ago', *Earth and Planetary Science Letters*, 222(2), pp. 363–376. doi:10.1016/j.epsl.2004.03.036.

Shirey, S.B. *et al.* (2002) 'Diamond Genesis, Seismic Structure, and Evolution of the Kaapvaal-Zimbabwe Craton', *Science*, 297(5587), pp. 1683–1686. doi:10.1126/science.1072384.

Shirey, S.B. *et al.* (2013) 'Diamonds and the Geology of Mantle Carbon', *Reviews in Mineralogy and Geochemistry*, 75(1), pp. 355–421. doi:10.2138/rmg.2013.75.12.

Simon, N.S.C. *et al.* (2002) 'The Lu-Hf isotope composition of cratonic lithosphere: disequilibrium between garnet and clinopyroxene in kimberlite xenoliths', *Geochimica et Cosmochimica Acta*, 15A. Available at: https://research.vu.nl/en/publications/22754086-4895-4285-ae5a-9798998954ad (Accessed: 29 December 2021).

Simon, N.S.C. *et al.* (2007) 'The Origin and Evolution of the Kaapvaal Cratonic Lithospheric Mantle', *Journal of Petrology*, 48(3), pp. 589–625. doi:10.1093/petrology/egl074.

Sláma, J. *et al.* (2008) 'Plešovice zircon — A new natural reference material for U–Pb and Hf isotopic microanalysis', *Chemical Geology*, 249(1), pp. 1–35. doi:10.1016/j.chemgeo.2007.11.005.

Smith, C.B. *et al.* (1985) 'Geochemical character of Southern African Kimberlites: a new approach based on isotopic constraints', *Transactions of the Geological Society of South Africa*, 88(2), pp. 267–280.

Spencer, C.J., Yakymchuk, C. and Ghaznavi, M. (2017) 'Visualising data distributions with kernel density estimation and reduced chi-squared statistic', *Geoscience Frontiers*, 8(6), pp. 1247–1252. doi:10.1016/j.gsf.2017.05.002.

Stacey, J.S. and Kramers, J.D. (1975) 'Approximation of terrestrial lead isotope evolution by a two-stage model', *Earth and Planetary Science Letters*, 26(2), pp. 207–221. doi:10.1016/0012-821X(75)90088-6.

Sullivan, N. *et al.* (2021) 'The solubility of gold and palladium in magmatic brines: Implications for PGE enrichment in mafic-ultramafic and porphyry environments', *Geochimica et Cosmochimica Acta*, 316. doi:10.1016/j.gca.2021.09.010.

Sweeney, R.J., Thompson, A.B. and Ulmer, P. (1993) 'Phase relations of a natural MARID composition and implications for MARID genesis, lithospheric melting and mantle metasomatism', *Contributions to Mineralogy and Petrology*, 115(2), pp. 225–241. doi:10.1007/BF00321222.

Sylvester, P.J. (2008) 'LA-(MC)-ICP-MS Trends in 2006 and 2007 with Particular Emphasis on Measurement Uncertainties', *Geostandards and Geoanalytical Research*, 32(4), pp. 469–488. doi:10.1111/j.1751-908X.2008.00924.x.

Tappe, S. *et al.* (2013) 'Mantle transition zone input to kimberlite magmatism near a subduction zone: Origin of anomalous Nd–Hf isotope systematics at Lac de Gras, Canada', *Earth and Planetary Science Letters*, 371–372, pp. 235–251. doi:10.1016/j.epsl.2013.03.039.

Tappe, S. *et al.* (2020) 'The tungsten-182 record of kimberlites above the African superplume: Exploring links to the core-mantle boundary', *Earth and Planetary Science Letters*, 547, p. 116473. doi:10.1016/j.epsl.2020.116473.

Tappe, S. *et al.* (2021) 'Evolution of ultrapotassic volcanism on the Kaapvaal craton: deepening the orangeite versus lamproite debate', *Geological Society, London, Special Publications*, 513. doi:10.1144/SP513-2021-84.

Torsvik, T.H. *et al.* (2010) 'Diamonds sampled by plumes from the core–mantle boundary', *Nature*, 466(7304), pp. 352–355. doi:10.1038/nature09216.

Veglio, C. *et al.* (2022) 'Olivine xenocrysts reveal carbonated mid-lithosphere in the northern Slave craton', *Lithos*, 414–415, p. 106633. doi:10.1016/j.lithos.2022.106633.

Vermeesch, P. (2018) 'IsoplotR: A free and open toolbox for geochronology', *Geoscience Frontiers*, 9(5), pp. 1479–1493. doi:10.1016/j.gsf.2018.04.001.

Vervoort, J.D. *et al.* (1999) 'Relationships between Lu–Hf and Sm–Nd isotopic systems in the global sedimentary system', *Earth and Planetary Science Letters*, 168(1), pp. 79–99. doi:10.1016/S0012-821X(99)00047-3.

Vervoort, J.D. and Blichert-Toft, J. (1999) 'Evolution of the depleted mantle: Hf isotope evidence from juvenile rocks through time', *Geochimica et Cosmochimica Acta*, 63(3), pp. 533–556. doi:10.1016/S0016-7037(98)00274-9.

Vezinet, A. *et al.* (2018) 'Hydrothermally-altered mafic crust as source for early Earth TTG: Pb/Hf/O isotope and trace element evidence in zircon from TTG of the Eoarchean Saglek Block, N. Labrador', *Earth and Planetary Science Letters*, 503, pp. 95–107. doi:10.1016/j.epsl.2018.09.015.

Wagner, P.A. (1914) *The Diamond Fields of Southern Africa*. Transvaal leader.

Walker, R.J. *et al.* (2002) 'Comparative 187Re-187Os systematics of chondrites: Implications regarding early solar system processes', *Geochimica et Cosmochimica Acta*, 66(23), pp. 4187–4201. doi:10.1016/S0016-7037(02)01003-7.

Waters, F.G. (1987) 'A suggested origin of MARID xenoliths in kimberlites by high pressure crystallization of an ultrapotassic rock such as lamproite', *Contributions to Mineralogy and Petrology*, 95, pp. 523–533. doi:10.1007/BF00402210.

Waters, F.G. and Erlank, A.J. (1988) 'Assessment of the Vertical Extent and Distribution of Mantle Metasomatism below Kimberley, South Africa', *Journal of Petrology*, Special_Volume(1), pp. 185–204. doi:10.1093/petrology/Special_Volume.1.185.

Waters, F.G., Erlank, A.J. and Daniels, L.R.M. (1989) 'Contact relationships between MARID rock and metasomatised peridotite in a kimberlite xenolith', *Geochemical Journal*, 23(1), pp. 11–

17. doi:10.2343/geochemj.23.11.

Waterton, P., Mungall, J. and Pearson, D.G. (2021) 'The komatiite-mantle platinum-group element paradox', *Geochimica et Cosmochimica Acta*, 313, pp. 214–242. doi:10.1016/j.gca.2021.07.037.

Widom, E. *et al.* (1999) 'Os Isotope Systematics in the Canary Islands and Madeira: Lithospheric Contamination and Mantle Plume Signatures', *Journal of Petrology*, 40(2), pp. 279–296. doi:10.1093/petroj/40.2.279.

Wiedenbeck, M. *et al.* (1995) 'Three Natural Zircon Standards for U-Th-Pb, Lu-Hf, Trace Element and Ree Analyses', *Geostandards Newsletter*, 19(1), pp. 1–23. doi:10.1111/j.1751-908X.1995.tb00147.x.

Wiedenbeck, M. *et al.* (2004) 'Further Characterisation of the 91500 Zircon Crystal', *Geostandards and Geoanalytical Research*, 28(1), pp. 9–39. doi:10.1111/j.1751-908X.2004.tb01041.x.

Wilson, L. and Head III, J.W. (2007) 'An integrated model of kimberlite ascent and eruption', *Nature*, 447(7140), pp. 53–57. doi:10.1038/nature05692.

Winterburn, P.A., Harte, B. and Gurney, J.J. (1990) 'Peridotite xenoliths from the Jagersfontein kimberlite pipe: I. Primary and primary-metasomatic mineralogy', *Geochimica et Cosmochimica Acta*, 54(2), pp. 329–341. doi:10.1016/0016-7037(90)90322-C.

de Wit, M.J. *et al.* (1992) 'Formation of an Archaean continent', *Nature*, 357(6379), pp. 553–562. doi:10.1038/357553a0.

Wittig, N. *et al.* (2008) 'Origin of cratonic lithospheric mantle roots: A geochemical study of peridotites from the North Atlantic Craton, West Greenland', *Earth and Planetary Science Letters*, 274(1), pp. 24–33. doi:10.1016/j.epsl.2008.06.034.

Woodhead, J. *et al.* (2004) 'Zircon Hf-isotope analysis with an excimer laser, depth profiling, ablation of complex geometries, and concomitant age estimation', *Chemical Geology*, 209(1), pp. 121–135. doi:10.1016/j.chemgeo.2004.04.026.

Woodhead, J. *et al.* (no date) 'Tracking continent-scale modification of the Earth's mantle using zircon megacrysts'.

Woodhead, J.D. *et al.* (2007) 'Isotopic and Elemental Imaging of Geological Materials by Laser Ablation Inductively Coupled Plasma-Mass Spectrometry', *Geostandards and Geoanalytical Research*, 31(4), pp. 331–343. doi:10.1111/j.1751-908X.2007.00104.x.

Woodland, A.B. *et al.* (1996) 'Metasomatic interactions in the lithospheric mantle: petrologic evidence from the Lherz massif, French Pyrenees', *Chemical Geology*, 134(1), pp. 83–112. doi:10.1016/S0009-2541(96)00082-4.

Yamada, R. *et al.* (1995) 'Annealing kinetics of fission tracks in zircon: an experimental study', *Chemical Geology*, 122(1), pp. 249–258. doi:10.1016/0009-2541(95)00006-8.

Zhang, M. *et al.* (2000) 'Annealing of alpha-decay damage in zircon: a Raman spectroscopic study', *Journal of Physics: Condensed Matter*, 12(13), pp. 3131–3148. doi:10.1088/0953-8984/12/13/321.

Zindler, A. and Hart, S. (1986) ‘Chemical Geodynamics’, *Annual Review of Earth and Planetary Sciences*, 14(1), pp. 493–571. doi:10.1146/annurev.ea.14.050186.002425.

Appendix A: Standard and Calibration Data

A.1 Trace Element Calibration Data

A.1.1 Silicate Trace Element Calibration Data

Reference Material	^{45}Sc	^{47}Ti	^{57}Fe	^{59}Co	^{60}Ni	^{63}Cu	^{85}Rb	^{88}Sr	^{89}Y	^{90}Zr	^{93}Nb	^{106}Pd	^{107}Ag	^{137}Ba	^{139}La	^{140}Ce	^{141}Pr	^{146}Nd
NIST 612 (primary)																		
Average Measured Value ($\bar{x}$)	39.9	44	51	35.5	38.8	-	31.4	78	38	37	38.9	-	-	39	36.0	38.4	37.9	35.5
Measured Uncertainty (2SD)	0.52	1.31	1.90	0.94	0.94	-	0.62	1.8	1.0	1.1	0.71	-	-	1.1	0.83	0.68	0.69	0.8
Reference Value	39.9	44	51	35.5	38.8	-	31.4	78.4	38.3	37.9	38.9	-	-	39.3	36	38.4	37.9	35.5
Reference Uncertainty (2SD)	2.5	2.3	2	1	0.2	-	0.4	0.2	1.4	1.2	2.1	-	-	0.9	0.7	0.7	1	0.7
Percent Error (%)	0	0	0	0	0	-	0	0	0	0	0	-	-	0	0	0	0	0
NIST 610 (primary)																		
Average Measured Value ($\bar{x}$)	-	-	-	-	-	441	-	-	-	-	-	1.21	251	-	-	-	-	-
Measured Uncertainty (2SD)	-	-	-	-	-	5.54	-	-	-	-	-	0.07	3.2	-	-	-	-	-
Reference Value	-	-	-	-	-	441	-	-	-	-	-	1.21	251	-	-	-	-	-
Reference Uncertainty (2SD)	-	-	-	-	-	15	-	-	-	-	-	0.44	9	-	-	-	-	-
Percent Error (%)	-	-	-	-	-	0	-	-	-	-	-	0	0	-	-	-	-	-
BIR-1G (secondary)																		
Average Measured Value ($\bar{x}$)	42.6	5843	79998	54.7	184	-	0.24	102	13.6	13.3	0.50	-	-	6.2	0.58	1.78	0.35	2.2
Measured Uncertainty (2SD)	6.24	532	4314	2.8	9.8	-	0.13	9.8	1.9	2.1	0.07	-	-	0.3	0.06	0.09	0.03	0.24
Reference Value	43	6234	80839	52	178	-	0.197	109	14.3	14.0	0.52	-	-	6.5	0.61	1.89	0.37	2.37
Reference Uncertainty (2SD)	3	420	777	5	18	-	0.007	2	1.4	1.2	0.04	-	-	0.07	0.02	0.04	0.02	0.03
Percent Error (%)	-0.83	-6.29	-1.04	5.15	3.30	-	20.8	-6.19	-4.66	-5.17	-4.54	-	-	-4.23	-4.75	-5.75	-6.84	-6.86
GSE-1G (secondary)																		
Average Measured Value ($\bar{x}$)	-	-	-	-	-	396	-	-	-	-	-	-	220	-	-	-	-	-
Measured Uncertainty (2SD)	-	-	-	-	-	20.1	-	-	-	-	-	-	10.8	-	-	-	-	-
Reference Value	-	-	-	-	-	380	-	-	-	-	-	-	200	-	-	-	-	-
Reference Uncertainty (2SD)	-	-	-	-	-	80	-	-	-	-	-	-	40	-	-	-	-	-
Percent Error (%)	-	-	-	-	-	-4.13	-	-	-	-	-	-	-9.49	-	-	-	-	-
BHVO-2G (secondary)																		
Average Measured Value ($\bar{x}$)	-	-	-	44	-	125	-	-	-	-	-	-	-	-	-	-	-	-
Measured Uncertainty (2SD)	-	-	-	1.9	-	6.0	-	-	-	-	-	-	-	-	-	-	-	-
Reference Value	-	-	-	44	-	127	-	-	-	-	-	-	-	-	-	-	-	-
Reference Uncertainty (2SD)	-	-	-	2	-	22	-	-	-	-	-	-	-	-	-	-	-	-
Percent Error (%)	-	-	-	0	-	-1.57	-	-	-	-	-	-	-	-	-	-	-	-

Reference Material	^{147}Sm	^{153}Eu	^{157}Gd	^{159}Tb	^{163}Dy	^{165}Ho	^{166}Er	^{169}Tm	^{172}Yb	^{175}Lu	^{178}Hf	^{185}Re	^{191}Ir	^{195}Pt	^{197}Au	^{208}Pb	^{238}U
NIST 612 (primary)																	
Average Measured Value ($\bar{x}$)	37.7	35.6	37.3	37.6	35.5	38.3	38	36.8	39.2	37.0	36.7	-	-	-	-	39	37
Measured Uncertainty (2SD)	0.68	0.88	0.85	0.92	0.76	0.85	1.0	0.9	0.8	0.8	0.9	-	-	-	-	1	1.1
Reference Value	37.7	35.6	37.3	37.6	35.5	38.3	38	36.8	39.2	37	36.7	-	-	-	-	38.6	37.38
Reference Uncertainty (2SD)	0.8	0.8	0.9	1.1	0.7	0.8	0.9	0.6	0.9	0.9	1.2	-	-	-	-	0.2	0.08
Percent Error (%)	0	0	0	0	0	0	0	0	0	0	0	-	-	-	-	1.0	-1.0
NIST 610 (primary)																	
Average Measured Value ($\bar{x}$)	-	-	-	-	-	-	-	-	-	-	-	49.9	-	3.14	23.6	-	-
Measured Uncertainty (2SD)	-	-	-	-	-	-	-	-	-	-	-	0.9	-	0.37	1.5	-	-
Reference Value	-	-	-	-	-	-	-	-	-	-	-	49.9	-	3.12	23.6	-	-
Reference Uncertainty (2SD)	-	-	-	-	-	-	-	-	-	-	-	3.7	-	0.08	1.7	-	-
Percent Error (%)	-	-	-	-	-	-	-	-	-	-	-	0	-	0.64	0	-	-
BIR-1G (secondary)																	
Average Measured Value ($\bar{x}$)	1.05	0.50	1.7	0.34	2.4	0.55	1.6	0.23	1.6	0.24	0.7	-	-	-	-	3.5	0.045
Measured Uncertainty (2SD)	0.12	0.06	0.2	0.05	0.4	0.08	0.3	0.04	0.2	0.03	0.4	-	-	-	-	0.1	0.1
Reference Value	1.09	0.517	1.85	0.35	2.55	0.56	1.70	0.240	1.64	0.250	0.57	-	-	-	-	3.7	0.023
Reference Uncertainty (2SD)	0.02	0.005	0.02	0.04	0.02	0.03	0.02	0.030	0.03	0.009	0.03	-	-	-	-	0.3	0.006
Percent Error (%)	-4.01	-3.31	-6.49	-3.21	-5.51	-2.72	-5.81	-2.68	-3.72	-5.10	16.1	-	-	-	-	-6.45	95.3
GSE-1G (secondary)																	
Average Measured Value ($\bar{x}$)	-	-	-	-	-	-	-	-	-	-	-	77	120	64.2	10	-	-
Measured Uncertainty (2SD)	-	-	-	-	-	-	-	-	-	-	-	3.9	0	98.6	1.8	-	-
Reference Value	-	-	-	-	-	-	-	-	-	-	-	78.9	120	30	7	-	-
Reference Uncertainty (2SD)	-	-	-	-	-	-	-	-	-	-	-	7.7	-	-	-	-	-
Percent Error (%)	-	-	-	-	-	-	-	-	-	-	-	-2.41	0	114	42.9	-	-
BHVO-2G (secondary)																	
Average Measured Value ($\bar{x}$)	-	-	-	-	-	-	-	-	-	-	-	0.008	-	0.2	-	-	-
Measured Uncertainty (2SD)	-	-	-	-	-	-	-	-	-	-	-	0.03	-	0.16	-	-	-
Reference Value	-	-	-	-	-	-	-	-	-	-	-	0.0005	-	0.46	-	-	-
Reference Uncertainty (2SD)	-	-	-	-	-	-	-	-	-	-	-	0.0003	-	0.09	-	-	-
Percent Error (%)	-	-	-	-	-	-	-	-	-	-	-	1500	-	-130	-	-	-

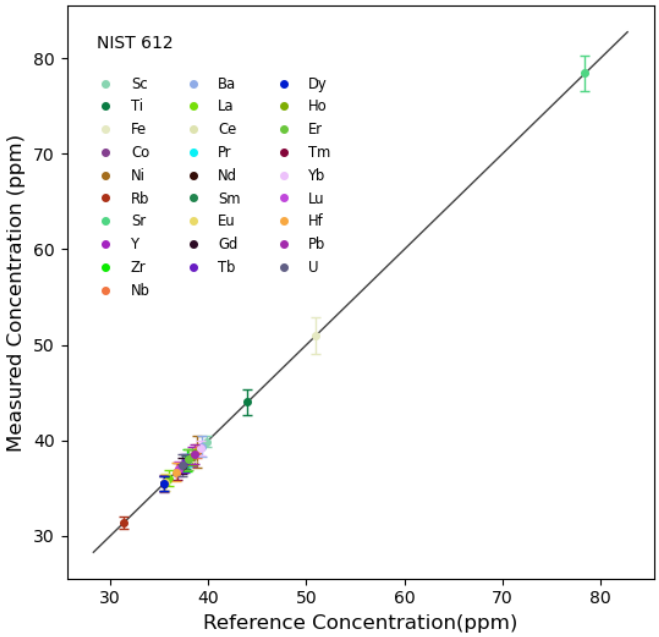

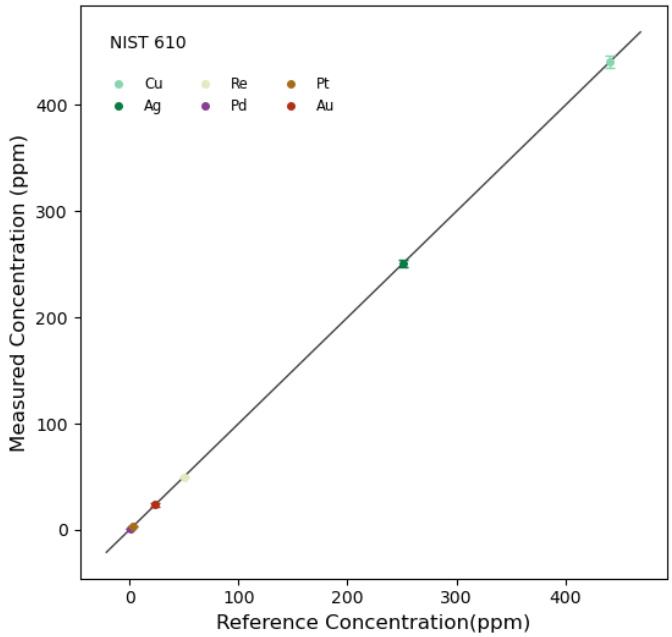
NIST 610
Cu
Ag
Re
Pd
Pt
Au
Measured Concentration (ppm)
Reference Concentration(ppm)
0
100
200
300
400

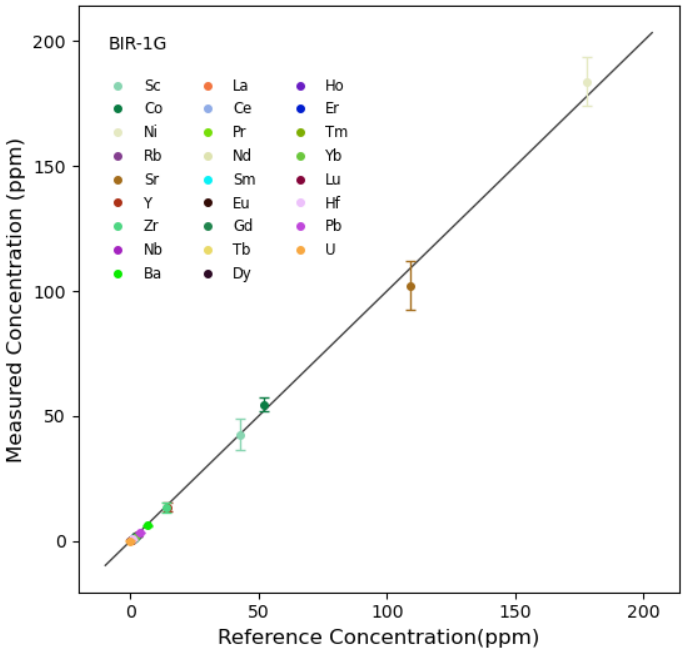
BIR-1G
Sc
Co
Ni
Rb
Sr
Y
Zr
Nb
Ba
La
Ce
Pr
Nd
Sm
Eu
Gd
Tb
Dy
Ho
Er
Tm
Yb
Lu
Hf
Pb
U
Measured Concentration (ppm)
Reference Concentration(ppm)
0
50
100
150
200

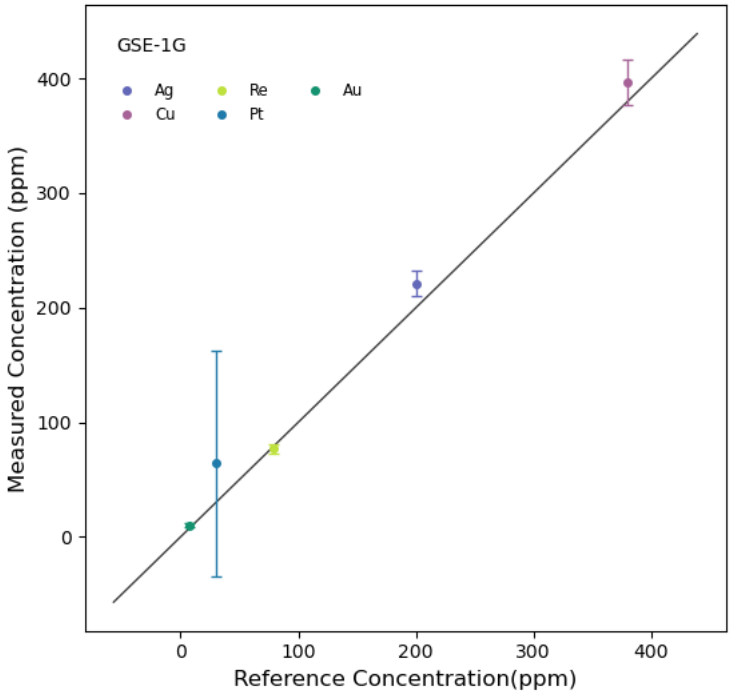
GSE-1G
Ag
Re
Au
Cu
Pt
Measured Concentration (ppm)
Reference Concentration(ppm)
0
100
200
300
400

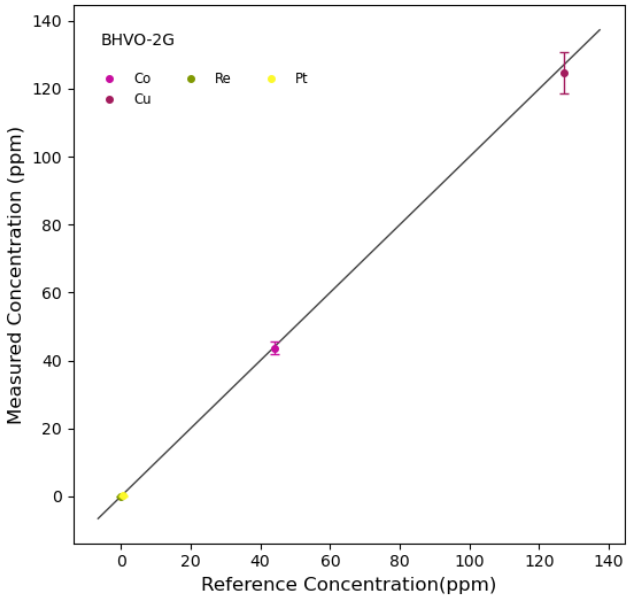
BHVO-2G
Co
Re
Pt
Cu
Measured Concentration (ppm)
Reference Concentration(ppm)
0
20
40
60
80
100
120
140

A.1.2 Oxide Trace Element Calibration Data

Reference Material	^{29}Si	^{45}Sc	^{47}Ti	^{59}Co	^{60}Ni	^{63}Cu	^{85}Rb	^{88}Sr	^{89}Y	^{90}Zr	^{93}Nb	^{106}Pd	^{107}Ag	^{137}Ba	^{139}La	^{140}Ce	^{141}Pr	^{146}Nd
BHVO-2G (primary)																		
Average Measured Value ($\bar{x}$)	230600	33.0	16700	44.0	116	-	9.2	397	26.1	170	18.3	-	-	131	15.2	38	5.35	24.5
Measured Uncertainty (2SD)	3994	0.63	251	0.54	2.0	-	0.28	9	0.74	4.77	0.43	-	-	3.3	0.36	1.1	0.09	0.6
Reference Value	230460	33	16725	44	116	-	9.20	396	26	170	18.3	-	-	131	15.2	37.6	5.35	24.5
Reference Uncertainty (2SD)	468	2	120	2	7	-	0.04	1	2	7	0.8	-	-	2	0.2	0.2	0.22	0.2
Percent Error (%)	0.06	0	-0.15	0	0	-	0	0.14	0.21	0	0	-	-	0	0	1.06	0	0
NIST 610 (primary)																		
Average Measured Value ($\bar{x}$)	-	-	-	-	-	441	-	-	-	-	-	1.211	251	-	-	-	-	-
Measured Uncertainty (2SD)	-	-	-	-	-	4.4	-	-	-	-	-	0.009	3	-	-	-	-	-
Reference Value	-	-	-	-	-	441	-	-	-	-	-	1.21	251	-	-	-	-	-
Reference Uncertainty (2SD)	-	-	-	-	-	15	-	-	-	-	-	0.44	9	-	-	-	-	-
Percent Error (%)	-	-	-	-	-	0	-	-	-	-	-	0	0	-	-	-	-	-
BCR-2G (secondary)																		
Average Measured Value ($\bar{x}$)	247240	34	13674	36.1	11	-	47	337	36	185	12.5	-	-	674	25	52	6.8	29
Measured Uncertainty (2SD)	12848	4.5	583	0.59	1.1	-	1.6	16.7	4.8	25.4	0.7	-	-	24.4	2.5	2.5	0.4	2.6
Reference Value	254300	33	13608	38	13	-	47	342	35	184	12.5	-	-	683	24.7	53.3	6.7	28.9
Reference Uncertainty (2SD)	1869.9	2	239.8	2	2	-	0.5	4	3	15	1	-	-	7	0.3	0.5	0.4	0.3
Percent Error (%)	-2.78	3.86	0.49	-4.88	-14.8	-	0	-1.50	2.16	0.4	0	-	-	-1.29	1.21	-2.27	0.02	0.19
GSE-1G (secondary)																		
Average Measured Value ($\bar{x}$)	-	-	-	-	-	415	-	-	-	-	-	-	225	-	-	-	-	-
Measured Uncertainty (2SD)	-	-	-	-	-	16.1	-	-	-	-	-	-	5.8	-	-	-	-	-
Reference Value	-	-	-	-	-	380	-	-	-	-	-	-	200	-	-	-	-	-
Reference Uncertainty (2SD)	-	-	-	-	-	80	-	-	-	-	-	-	40	-	-	-	-	-
Percent Error (%)	-	-	-	-	-	9.21	-	-	-	-	-	-	12.5	-	-	-	-	-

Reference Material	^{147}Sm	^{153}Eu	^{157}Gd	^{159}Tb	^{163}Dy	^{165}Ho	^{166}Er	^{169}Tm	^{172}Yb	^{175}Lu	^{178}Hf	^{185}Re	^{191}Ir	^{195}Pt	^{197}Au	^{208}Pb	^{238}U
BHVO-2G (primary)																	
Average Measured Value ($\bar{x}$)	6.1	2.07	6.2	0.92	5.3	0.98	2.57	0.34	2.01	0.28	4.3	-	-	-	-	1.70	0.40
Measured Uncertainty (2SD)	0.19	0.06	0.19	0.03	0.2	0.03	0.09	0.02	0.07	0.02	0.16	-	-	-	-	0.08	0.02
Reference Value	6.10	2.07	6.20	0.92	5.28	0.98	2.56	0.34	2.01	0.28	4.32	-	-	-	-	1.7	0.403
Reference Uncertainty (2SD)	0.03	0.01	0.05	0.04	0.05	0.04	0.02	0.02	0.02	0.003	0.18	-	-	-	-	0.2	0.003
Percent Error (%)	0	0	0	0	0.76	0	0.29	0	0	0	0.3	-	-	-	-	0	-0.15
NIST 610 (primary)																	
Average Measured Value ($\bar{x}$)	-	-	-	-	-	-	-	-	-	-	-	49.9	-	3.2	24	-	-
Measured Uncertainty (2SD)	-	-	-	-	-	-	-	-	-	-	-	0.8	-	0.62	2.32	-	-
Reference Value	-	-	-	-	-	-	-	-	-	-	-	49.9	-	3.12	23.6	-	-
Reference Uncertainty (2SD)	-	-	-	-	-	-	-	-	-	-	-	3.7	-	0.08	1.7	-	-
Percent Error (%)	-	-	-	-	-	-	-	-	-	-	-	0	-	2.56	1.69	-	-
BCR-2G (secondary)																	
Average Measured Value ($\bar{x}$)	6.6	2.0	6.7	1.0	6.4	1.3	3.7	0.53	36	0.51	4.8	-	-	-	-	11	1.57
Measured Uncertainty (2SD)	0.57	0.12	0.88	0.15	0.74	0.20	0.5	0.05	4.8	0.07	0.8	-	-	-	-	1.1	0.09
Reference Value	6.59	1.97	6.71	1.02	6.44	1.27	3.70	0.51	35	0.503	4.85	-	-	-	-	11	1.69
Reference Uncertainty (2SD)	0.07	0.02	0.07	0.08	0.06	0.08	0.04	0.04	3	0.005	0.28	-	-	-	-	1	0.12
Percent Error (%)	0.15	0.27	0.66	2.37	-1.30	2.99	0	3.06	2.16	0.95	1.03	-	-	-	-	0	6.92
GSE-1G (secondary)																	
Average Measured Value ($\bar{x}$)	-	-	-	-	-	-	-	-	-	-	-	78	-	71	12	-	-
Measured Uncertainty (2SD)	-	-	-	-	-	-	-	-	-	-	-	6.35	-	138	3.9	-	-
Reference Value	-	-	-	-	-	-	-	-	-	-	-	78.9	-	30	7	-	-
Reference Uncertainty (2SD)	-	-	-	-	-	-	-	-	-	-	-	7.7	-	-		-	-
Percent Error (%)	-	-	-	-	-	-	-	-	-	-	-	1.14	-	137	71.4	-	-

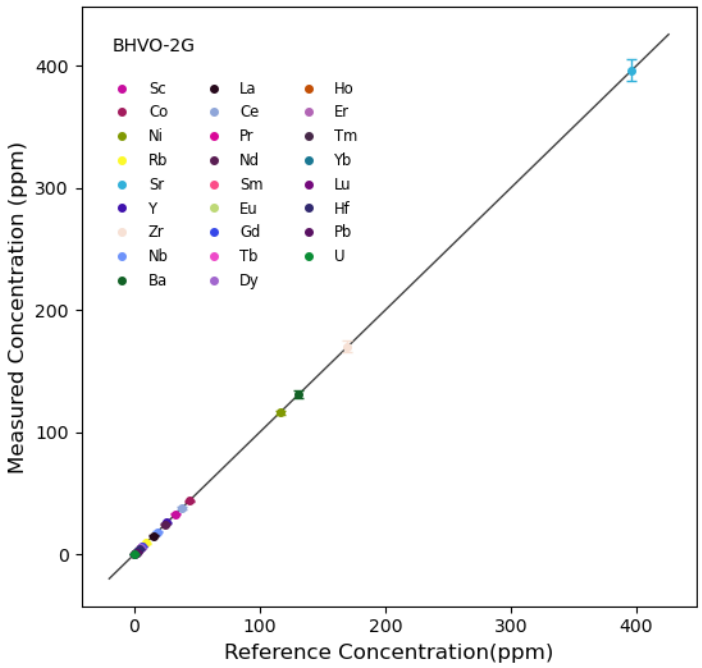
BHVO-2G
Sc
Co
Ni
Rb
Sr
Y
Zr
Nb
Ba
La
Ce
Pr
Nd
Sm
Eu
Gd
Tb
Dy
Ho
Er
Tm
Yb
Lu
Hf
Pb
U
Measured Concentration (ppm)
Reference Concentration(ppm)
0
100
200
300
400

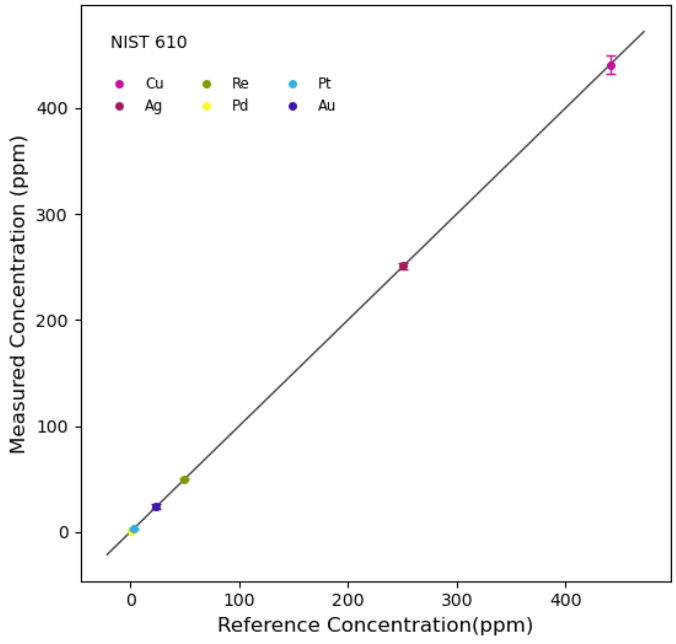
NIST 610
Cu
Ag
Re
Pd
Pt
Au
Measured Concentration (ppm)
Reference Concentration(ppm)
0
100
200
300
400

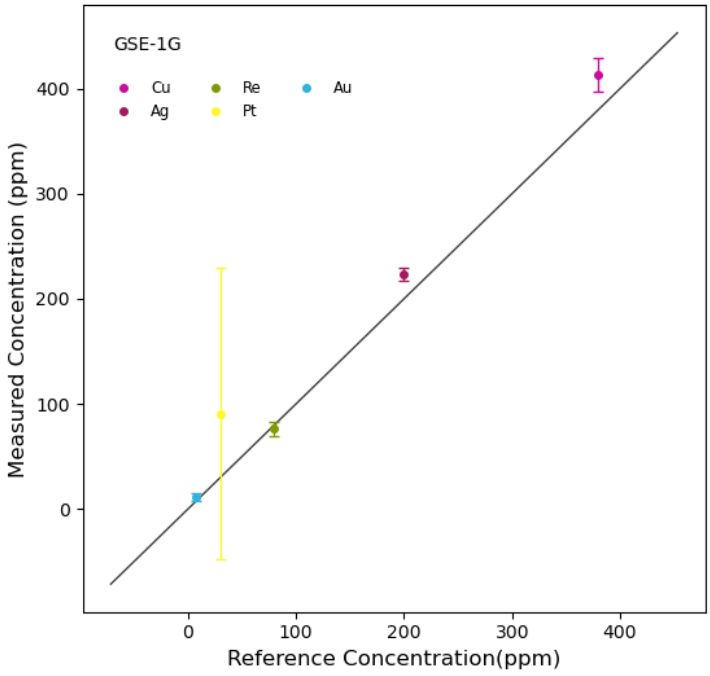
GSE-1G
Cu
Ag
Re
Pt
Au
Measured Concentration (ppm)
Reference Concentration(ppm)
0
100
200
300
400

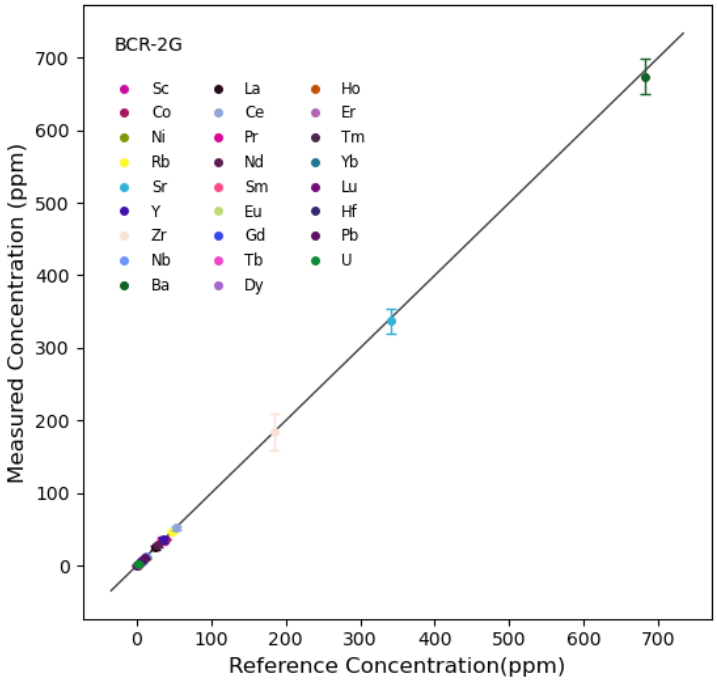
BCR-2G
Sc
Co
Ni
Rb
Sr
Y
Zr
Nb
Ba
La
Ce
Pr
Nd
Sm
Eu
Gd
Tb
Dy
Ho
Er
Tm
Yb
Lu
Hf
Pb
U
Measured Concentration (ppm)
Reference Concentration(ppm)
0
100
200
300
400
500
600
700

A.2 U-Pb and Lu-Hf Isotope Calibration Data

A.2.1 U-Pb Isotope Calibration Data

All ages and uncertainties are reported as Ma

Analysis	Final $^{206}Pb/^{238}U$ Age	$^{206}Pb/^{238}U$ Age Propagated 2SE	Final $^{207}Pb/^{235}U$ Age	$^{207}Pb/^{235}U$ Age Propagated 2SE
Plesovice	337.1	4.9	336.2	91
Plesovice_1	327	5.5	333	82
Plesovice_2	337.1	4.9	338.8	91
Plesovice_3	335.9	5.1	370.9	92
Plesovice_4	313.8	5.5	309.5	82
Plesovice_5	337.5	4.8	333.9	78
Plesovice_6	337.1	4.7	337.7	90
Plesovice_7	336.8	4.7	336.6	88
Plesovice_8	338.1	4.9	337.9	89
Plesovice_9	336.8	4.8	337	89
Plesovice_10	337.3	4.7	337.4	89
Plesovice_11	337	4.8	340.3	88
Plesovice_12	343.2	4.9	347.4	90
Plesovice_13	336.4	4.7	338.9	89
Plesovice_14	338.8	4.9	331.9	89
Plesovice_15	340.2	5.1	389.6	98
Plesovice_16	334.8	4.9	320	85
91500	1083.3	15	903.2	190
91500_1	1054.2	14	855.7	180
91500_2	1065.7	15	833.9	180
91500_3	1074	15	1227.8	220
91500_4	1068.1	14	1252.6	210
91500_5	1054	14	1259.9	220

91500_6	1062.1	14	1073.8	200
91500_7	1070	15	1054.8	200
91500_8	1053.3	14	1041.4	200
91500_9	1065.9	14	1048.8	200
91500_10	1056.1	14	1033.2	200
91500_11	1044.2	14	1030.3	200
91500_12	1052.8	14	1005.3	210
91500_13	1052.1	15	977.6	200

Plešovice Reference Analyses

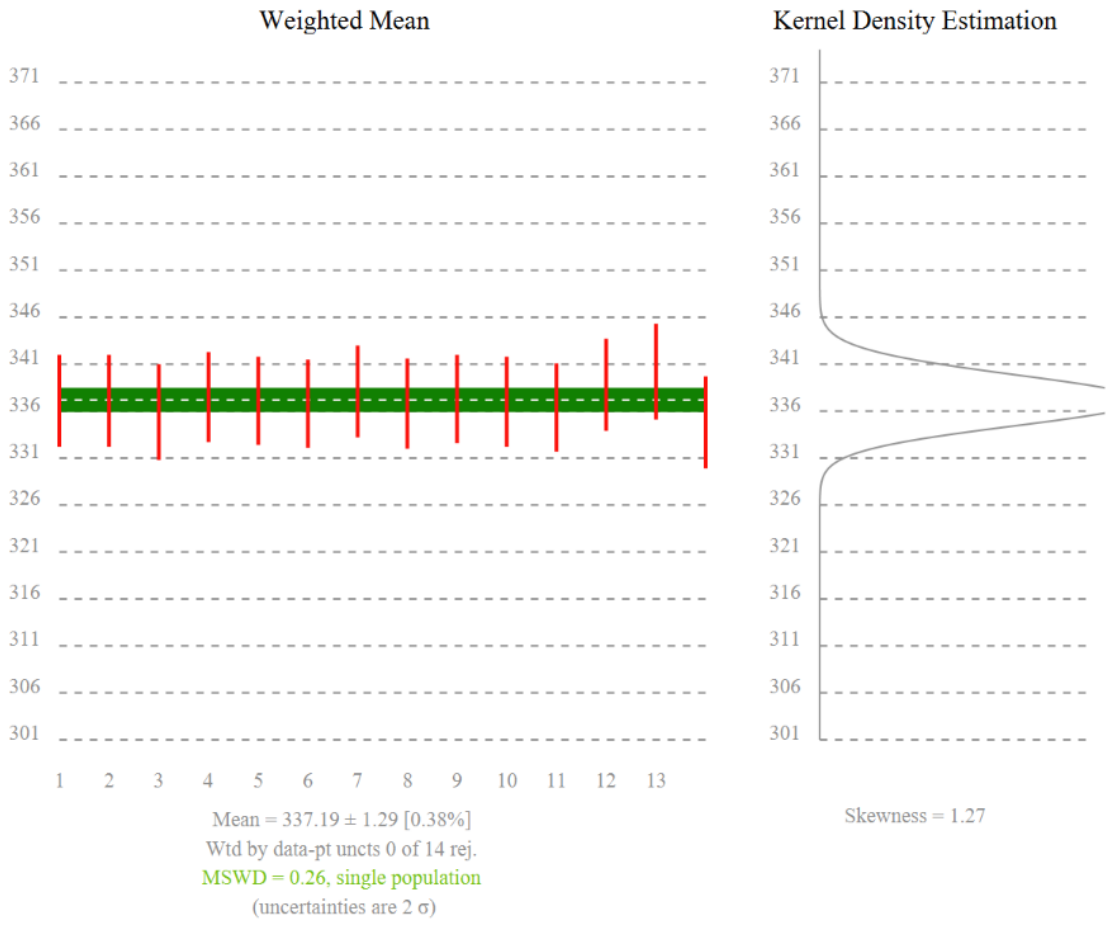

91500 Reference Material Analyses

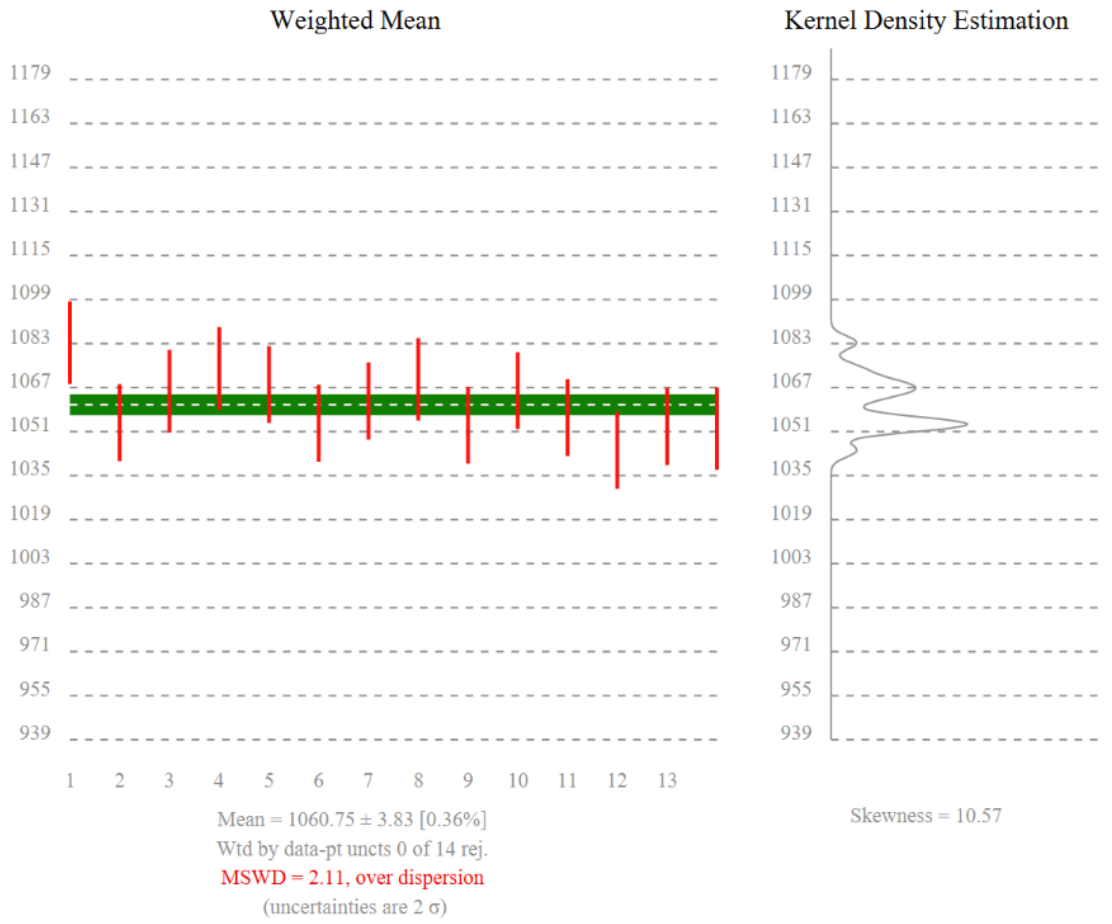

A.2.2 Lu-Hf Isotope Calibration Data

Analysis	$^{176}Hf/^{177}Hf$	$^{176}Hf/^{177}Hf$ 2SE	$^{176}Lu/^{177}Hf$	$^{176}Lu/^{177}Hf$ 2SE	εHf_0	εHf 2SE	Yb/Hf	Yb/Hf 2SE
Plesovice	0.282473	0.000018	0.000204	0.000006	-11.0	0.71	0.0090	0.0002
Plesovice_1	0.282468	0.000017	0.000184	0.000004	-11.2	0.71	0.00785	0.00008
Plesovice_2	0.282498	0.000016	0.000179	0.000004	-10.1	0.71	0.0080	0.0002
Plesovice_3	0.282496	0.000014	0.000202	0.000004	-10.2	0.71	0.0090	0.0001
Plesovice_4	0.282486	0.000013	0.000144	0.000002	-11.2	0.71	0.00665	0.00003
Plesovice_5	0.282485	0.000014	0.000144	0.000003	-10.6	0.71	0.00622	0.00009
Plesovice_6	0.282480	0.000011	0.000141	0.000003	-10.8	0.71	0.00616	0.00008
Plesovice_7	0.282485	0.000013	0.000138	0.000003	-10.6	0.71	0.0060	0.0001
Plesovice_8	0.282482	0.000014	0.000147	0.000003	-10.7	0.71	0.0064	0.0001
Plesovice_9	0.282488	0.000014	0.000138	0.000002	-10.5	0.71	0.00603	0.0001

Plesovice_10	0.282491	0.000013	0.000120	0.000004	-10.4	0.71	0.0050	0.0001
Plesovice_11	0.282477	0.000016	0.000101	0.000006	-10.9	0.71	0.00435	0.00003
Plesovice_12	0.282474	0.000012	0.000091	0.0000003	-11.0	0.71	0.00402	0.00003
Plesovice_13	0.282483	0.000014	0.000090	0.0000005	-10.7	0.71	0.00398	0.00003
Plesovice_14	0.282482	0.000018	0.000075	0.000002	-10.7	0.71	0.0033	0.0001
Plesovice_15	0.282487	0.000012	0.000087	0.0000009	-10.5	0.71	0.00382	0.00002
Plesovice_16	0.282484	0.000012	0.000069	0.000001	-10.6	0.71	0.0030	0.00004
91500	0.282318	0.000018	0.000337	0.0000004	-16.5	0.71	0.01004	0.00006
91500_1	0.282329	0.000018	0.000326	0.0000018	-16.1	0.71	0.00977	0.00003
91500_2	0.282344	0.000021	0.000326	0.0000006	-15.6	0.71	0.00973	0.00007
91500_3	0.282331	0.000017	0.000338	0.0000010	-16.1	0.71	0.01006	0.00008
91500_4	0.282323	0.000018	0.000340	0.0000012	-16.3	0.71	0.01013	0.00004
91500_5	0.282306	0.000021	0.000339	0.0000011	-16.9	0.71	0.01013	0.00009
91500_6	0.282316	0.000020	0.000349	0.0000004	-16.6	0.71	0.01028	0.00006
91500_7	0.282312	0.000016	0.000334	0.0000005	-16.7	0.71	0.00996	0.00005
91500_8	0.282316	0.000016	0.000341	0.0000007	-16.6	0.71	0.01001	0.00005
91500_9	0.282317	0.000021	0.000351	0.000003	-16.6	0.71	0.01038	0.00006
91500_10	0.282292	0.000020	0.000312	0.000002	-17.4	0.71	0.00942	0.00008
91500_11	0.282309	0.000019	0.000341	0.0000004	-16.8	0.71	0.01006	0.00006
91500_12	0.282320	0.000017	0.000334	0.0000004	-16.4	0.71	0.01011	0.00006
91500_13	0.282307	0.000016	0.000332	0.0000004	-16.9	0.71	0.01003	0.00007
MUN1	0.282139	0.000011	0.000333	0.0000078	-22.8	0.4	0.01011	0.00015
MUN1_1	0.282165	0.000016	0.004386	0.000076	-21.9	0.7	0.02875	0.00047
MUN1_2	0.282148	0.000016	0.002960	0.00018	-22.5	0.7	0.0184	0.00140
MUN1_3	0.282157	0.000012	0.000707	0.0000056	-22.2	0.4	0.02326	0.00008
MUN1_4	0.282141	0.000011	0.001460	0.000110	-22.8	0.4	0.00881	0.00078
MUN1_5	0.282164	0.000021	0.003164	0.00004	-22.0	0.7	0.01907	0.00038
MUN3	0.282254	0.000015	0.00308	0.00007	-18.8	0.7	0.0943	0.0012

MUN3_1	0.282157	0.000012	0.00272	0.00011	-22.2	0.4	0.02587	0.00099
MUN3_2	0.282170	0.000017	0.00321	0.00004	-21.7	0.7	0.02906	0.00044
MUN3_3	0.282163	0.000028	0.00636	0.00057	-22.0	1.1	0.210	0.018
MUN3_4	0.282159	0.000014	0.00362	0.00027	-22.1	0.4	0.0364	0.0032

Appendix B: Geochemical Results

B.1 Major Element Mineral Chemistry

B.1.1 Silicate and Oxide Phases

N/A indicates element or data treatment that was not analyzed. All values are in weight percentage (wt. %) and represent the mean of all analyses.

Mineral	SiO_2	TiO_2	ZnO	Al_2O_3	Cr_2O_3	FeO^T	NiO	MnO	MgO	CaO	BaO
GPP (JAG1)											
Olivine (n = 13)	**40.2**	**Bdl**	**Bdl**	**0.002**	**Bdl**	**8.59**	**0.42**	**0.09**	**49.7**	**0.008**	**N/A**
S.D. (1σ)	0.33	-	-	0.004	-	0.06	0.01	0.01	0.11	0.004	-
CPX (n = 10)	**54.2**	**0.08**	**Bdl**	**2.28**	**1.10**	**2.53**	**0.04**	**0.05**	**16.0**	**20.94**	**N/A**
S.D. (1σ)	0.26	0.01	-	0.02	0.02	0.03	0.01	0.01	0.12	0.06	-
OPX (n = 9)	**57.5**	**0.03**	**Bdl**	**0.69**	**0.14**	**5.31**	**0.10**	**0.10**	**35.4**	**0.27**	**N/A**
S.D. (1σ)	0.11	0.01	-	0.03	0.02	0.04	0.01	0.01	0.15	0.02	-
Garnet (n = 9)	**41.5**	**0.04**	**0.004**	**22.50**	**1.61**	**8.33**	**0.01**	**0.40**	**20.3**	**4.63**	**N/A**
S.D. (1σ)	0.18	0.01	0.005	0.09	0.04	0.07	0.01	0.03	0.16	0.07	-
Phlogopite (n = 6)	**41.0**	**0.36**	**Bdl**	**13.6**	**0.57**	**3.03**	**0.23**	**0.02**	**25.1**	**0.01**	**N/A**
S.D. (1σ)	**0.24**	**0.02**	**-**	**0.15**	**0.03**	**0.04**	**0.01**	**0.01**	**0.17**	**0.02**	**-**
PP (17MON 004)											
Olivine (n = 27)	**40.1**	**0.01**	**0.01**	**0.001**	**0.01**	**11.0**	**0.32**	**0.17**	**47.3**	**0.010**	**0.004**
S.D. (1σ)	0.17	0.01	0.01	0.003	0.01	0.13	0.03	0.01	0.27	0.003	0.002
CPX (n = 25)	**54.3**	**0.04**	**0.001**	**1.2**	**1.9**	**3.4**	**0.03**	**0.09**	**15.5**	**20.4**	**Bdl**
S.D. (1σ)	0.27	0.03	0.006	0.45	0.13	0.32	0.02	0.01	0.24	0.37	-
OPX (n = 5)	**57.3**	**0.02**	**Bdl**	**0.3**	**0.17**	**6.6**	**0.08**	**0.17**	**34.5**	**0.23**	**0.003**
S.D. (1σ)	0.48	0.02	-	0.14	0.06	0.11	0.01	0.01	0.19	0.01	0.006
Phlogopite (n = 21)	**41.8**	**0.2**	**Bdl**	**11.9**	**0.28**	**3.8**	**0.17**	**0.02**	**26.1**	**0.001**	**0.3**
S.D. (1σ)	0.27	0.36	-	0.18	0.04	0.12	0.03	0.02	0.45	0.005	0.12
Chromite (n = 29)	**Bdl**	**0.5**	**0.13**	**2.6**	**57.3**	**30.9**	**0.09**	**0.38**	**7.0**	**0.02**	**Bdl**
S.D. (1σ)	-	0.11	0.015	1.1	1.7	1.2	0.02	0.02	0.3	0.05	-
Spinel Lherzolite Host (LZM-001)											
Olivine (n = 4)	**39.93**	**Bdl**	**Bdl**	**Bdl**	**Bdl**	**10.1**	**0.37**	**0.14**	**48.5**	**0.01**	**Bdl**
S.D. (1σ)	0.09	-	-	-	-	0.11	0.01	0.01	0.26	0.01	-

CPX (n = 5)	**50.7**	**0.87**	**Bdl**	**7.2**	**0.73**	**2.44**	**0.03**	**0.07**	**13.9**	**20.4**	**Bdl**
S.D. (1σ)	0.21	0.06	-	0.25	0.04	0.04	0.01	0.01	0.10	0.21	-
OPX (n = 5)	**54.3**	**0.16**	**Bdl**	**3.9**	**0.27**	**6.50**	**0.08**	**0.15**	**32.8**	**0.37**	**Bdl**
S.D. (1σ)	0.26	0.02	-	0.24	0.02	0.07	0.01	0.01	0.23	0.09	-
Pargasite (n = 8)	**41.7**	**4.1**	**Bdl**	**14.2**	**0.69**	**3.86**	**0.09**	**0.05**	**15.9**	**11.21**	**Bdl**
S.D. (1σ)	0.28	0.19	-	0.35	0.06	0.05	0.01	0.01	0.14	0.05	-
Spinel (n = 6)	**Bdl**	**0.04**	**0.17**	**58.0**	**9.3**	**11.9**	**0.33**	**0.10**	**18.8**	**Bdl**	**Bdl**
S.D. (1σ)	-	0.01	0.02	1.3	1.8	0.10	0.03	0.01	0.78	-	-
Mineral	**SiO_2**	**TiO_2**	**ZnO**	**Al_2O_3**	**Cr_2O_3**	**FeO^T**	**NiO**	**MnO**	**MgO**	**CaO**	**BaO**
Spinel Lherzolite Vein (LZM-001)											
Pargasite (n = 3)	**41.3**	**4.46**	**Bdl**	**14.5**	**0.4**	**3.89**	**0.10**	**0.05**	**15.79**	**11.15**	**Bdl**
S.D. (1σ)	0.16	0.08	-	0.11	0.16	0.02	0.01	0.01	0.04	0.07	-
Phlogopite (n = 8)	**37.3**	**7.1**	**Bdl**	**16.0**	**0.1**	**4.3**	**0.17**	**0.01**	**20.3**	**Bdl**	**0.1**
S.D. (1σ)	0.22	0.26	-	0.11	0.12	0.20	0.02	0.01	0.33	-	0.11
PIC (UIB-2)											
Phlogopite (n = 9)	**41.4**	**1.28**	**Bdl**	**11.81**	**0.32**	**3.65**	**0.14**	**0.01**	**25.5**	**Bdl**	**0.01**
S.D. (1σ)	0.25	0.03	-	0.08	0.02	0.05	0.01	0.01	0.19	-	0.03
CPX (n = 10)	**53.8**	**0.26**	**Bdl**	**0.60**	**1.07**	**2.75**	**0.02**	**0.07**	**16.82**	**21.8**	**Bdl**
S.D. (1σ)	0.17	0.04	-	0.06	0.07	0.07	0.01	0.005	0.07	0.10	-
Ilmenite (n = 6)	**Bdl**	**53.52**	**Bdl**	**0.10**	**2.06**	**28.9**	**0.18**	**0.33**	**13.5**	**0.02**	**Bdl**
S.D. (1σ)	-	0.07	-	0.01	0.03	0.26	0.01	0.02	0.23	0.01	-
Rutile (n = 10)	**Bdl**	**89.4**	**Bdl**	**0.04**	**3.5**	**1.0**	**Bdl**	**Bdl**	**0.1**	**Bdl**	**Bdl**
S.D. (1σ)	-	2.0	-	0.03	0.39	0.82	-	-	0.18	-	-
MARID (AJE-326)											
Phlogopite (n = 25)	**41.9**	**0.5**	**Bdl**	**10.5**	**0.09**	**5.9**	**0.11**	**0.02**	**25.4**	**Bdl**	**0.02**
S.D. (1σ)	0.22	0.12	-	0.13	0.02	0.24	0.02	0.01	0.23	-	0.04
K-Richterite (n = 20)	**55.2**	**0.35**	**Bdl**	**1.08**	**0.19**	**3.10**	**0.04**	**0.04**	**21.9**	**6.81**	**Bdl**
S.D. (1σ)	0.36	0.02	-	0.07	0.02	0.06	0.006	0.01	0.17	0.07	-
Ilmenite (n = 7)	**Bdl**	**53.1**	**0.01**	**0.03**	**1.4**	**30.9**	**0.15**	**0.4**	**12.4**	**0.08**	**Bdl**
S.D. (1σ)	-	2.3	0.02	0.03	0.58	3.7	0.05	0.27	1.4	0.12	-
Rutile (n = 2)	**Bdl**	**96.7**	**Bdl**	**0.01**	**2.02**	**0.20**	**Bdl**	**Bdl**	**0.01**	**0.01**	**Bdl**

S.D. (1σ)	-	0.27	-	0.01	0.08	0.02	-	-	0.01	0.01	-

Mineral	SiO_2	TiO_2	ZnO	Al_2O_3	Cr_2O_3	FeO^T	NiO	MnO	MgO	CaO	BaO
MARID (AJE-335)											
Phlogopite (n = 21)	**42.7**	**2.7**	**Bdl**	**9.9**	**0.06**	**7.7**	**0.08**	**0.04**	**21.7**	**0.01**	**Bdl**
S.D. (1σ)	0.86	0.22	-	0.27	0.02	0.42	0.008	0.01	0.57	0.02	-
CPX (n = 15)	**54.0**	**0.3**	**Bdl**	**0.5**	**0.11**	**5.9**	**Bdl**	**0.14**	**16.3**	**20.6**	**Bdl**
S.D. (1σ)	0.23	0.13	-	0.27	0.04	0.63	-	0.02	0.66	1.1	-
Ilmenite (n = 10)	**Bdl**	**55.3**	**Bdl**	**0.04**	**0.22**	**31.2**	**0.07**	**0.41**	**11.2**	**0.2**	**Bdl**
S.D. (1σ)	-	0.45	-	0.02	0.07	1.1	0.01	0.06	0.83	0.21	-
Rutile (n = 2)	**Bdl**	**99.2**	**Bdl**	**0.07**	**0.39**	**0.18**	**Bdl**	**Bdl**	**Bdl**	**Bdl**	**Bdl**
S.D. (1σ)	-	0.35	-	0.05	0.04	0.08	-	-	-	-	-
MARID (AJE-2422)											
Phlogopite (n = 4)	**42.60**	**1.6**	**Bdl**	**9.61**	**0.08**	**6.9**	**0.1**	**0.03**	**23.23**	**Bdl**	**Bdl**
S.D. (1σ)	0.09	0.14	-	0.06	0.01	0.18	0.008	0.006	0.07	-	-
K-Richterite (n = 5)	**54.79**	**0.552**	**Bdl**	**0.88**	**0.04**	**3.65**	**0.046**	**0.034**	**21.30**	**6.81**	**Bdl**
S.D. (1σ)	0.09	0.008	-	0.02	0.03	0.02	0.005	0.005	0.07	0.02	-
Ilmenite (n = 12)	**Bdl**	**52.4**	**Bdl**	**0.03**	**0.25**	**36.7**	**0.080**	**0.33**	**8.8**	**0.01**	**Bdl**
S.D. (1σ)	-	0.53	-	0.01	0.02	1.5	0.009	0.03	1.0	0.02	-
Rutile (n = 16)	**Bdl**	**94.7**	**Bdl**	**0.04**	**0.68**	**2.1**	**Bdl**	**Bdl**	**0.08**	**0.01**	**Bdl**
S.D. (1σ)	-	1.1	-	0.01	0.04	0.87	-	-	0.1	0.04	-
MARID (KDB-20)											
Phlogopite (n = 15)	**42.0**	**0.54**	**Bdl**	**10.6**	**0.12**	**5.7**	**0.13**	**0.02**	**25.3**	**Bdl**	**0.01**
S.D. (1σ)	0.25	0.09	-	0.12	0.02	0.21	0.01	0.01	0.10	-	0.04
Ilmenite (n = 5)	**Bdl**	**56.3**	**0.01**	**Bdl**	**0.7**	**29.0**	**0.07**	**0.7**	**12.1**	**0.11**	**Bdl**
S.D. (1σ)	-	0.8	0.02	-	0.44	1.4	0.008	0.12	0.99	0.04	-

Mineral	Na_2O	K_2O	H_2O	Total	Mg #
GPP (JAG1)					
Olivine (n = 13)	**0.002**	**Bdl**	**N/A**	**99.0**	**91.17**
S.D. (1σ)	0.008	-	-	0.34	0.06
CPX (n = 10)	**1.80**	**Bdl**	**N/A**	**99.1**	**91.9**
S.D. (1σ)	0.04	-	-	0.44	0.10

Mineral	Na_2O	K_2O	H_2O	Total	Mg #
OPX (n = 9)	**0.06**	**Bdl**	**N/A**	**99.0**	**91.17**
S.D. (1σ)	0.02	-	-	0.34	0.06
Garnet (n = 9)	**0.02**	**Bdl**	**N/A**	**99.3**	**N/A**
S.D. (1σ)	0.02	-	-	0.23	-
Phlogopite (n = 6)	**0.57**	**9.6**	**4.20**	**98.3**	**93.7**
S.D. (1σ)	0.04	0.14	-	0.49	0.1
PP (17MON 004)					
Olivine (n = 27)	**0.01**	**Bdl**	**N/A**	**99.0**	**88.4**
S.D. (1σ)	0.01	-	-	0.31	0.1
CPX (n = 25)	**2.0**	**Bdl**	**N/A**	**98.8**	**89.7**
S.D. (1σ)	0.22	-	-	0.25	0.83
OPX (n = 5)	**0.06**	**0.002**	**N/A**	**99.4**	**90.4**
S.D. (1σ)	0.01	0.002	-	0.38	0.10
Chromite (n = 29)	**Bdl**	**Bdl**	**N/A**	**98.8**	**29.5**
S.D. (1σ)	-	-	-	0.22	1.5
Spinel Lherzolite Host (LZM-001)					
Olivine (n = 4)	**0.03**	**Bdl**	**N/A**	**99.1**	**89.69**
S.D. (1σ)	0.02	-	-	0.40	0.02
CPX (n = 5)	**1.99**	**0.01**	**N/A**	**98.3**	**91.43**
S.D. (1σ)	0.08	0.01	-	0.14	0.07
OPX (n = 5)	**0.06**	**Bdl**	**N/A**	**98.7**	**90.13**
S.D. (1σ)	0.01	-	-	0.20	0.09
Pargasite (n = 8)	**3.2**	**1.0**	**2.10**	**98.2**	**88.0**

S.D. (1σ)	0.18	0.23	0.04	0.25	0.19
Spinel (n = 6)	**Bdl**	**Bdl**	**N/A**	**98.7**	**73.8**
S.D. (1σ)	-	-	-	0.67	2.5
Spinel Lherzolite Vein (LZM-001)					
Pargasite (n = 3)	**3.11**	**1.22**	**2.10**	**98.03**	**87.87**
S.D. (1σ)	0.03	0.03	-	0.04	0.09
Mineral	**Na_2O**	**K_2O**	**H_2O**	**Total**	**Mg #**
Phlogopite (n = 8)	**0.76**	**9.3**	**4.22**	**99.7**	**89.3**
S.D. (1σ)	0.05	0.11	0.01	0.16	0.43
PIC (UIB-2)					
Phlogopite (n = 9)	**0.19**	**10.46**	**4.24**	**98.9**	**92.6**
S.D. (1σ)	0.03	0.08	0.03	0.34	0.13
CPX (n = 10)	**1.13**	**0.01**	**N/A**	**98.3**	**92.0**
S.D. (1σ)	0.03	0.005	-	0.13	0.14
Ilmenite (n = 6)	**0.02**	**Bdl**	**N/A**	**98.7**	**N/A**
S.D. (1σ)	0.03	-	-	0.15	-
Rutile (n = 10)	**0.01**	**Bdl**	**N/A**	**94.1**	**N/A**
S.D. (1σ)	0.02	-	-	1.01	-
MARID (AJE-326)					
Phlogopite (n = 25)	**0.14**	**10.5**	**4.20**	**99.3**	**88.4**
S.D. (1σ)	0.04	0.15	0.01	0.28	0.48
K-Richterite (n = 20)	**3.59**	**4.82**	**2.13**	**99.2**	**92.8**
S.D. (1σ)	0.07	0.05	0.01	0.48	0.19
Ilmenite (n = 7)	**0.08**	**Bdl**	**N/A**	**98.6**	**N/A**
S.D. (1σ)	0.09	-	-	0.12	-
Rutile (n = 2)	**Bdl**	**Bdl**	**N/A**	**99.0**	**N/A**
S.D. (1σ)	-	-	-	0.21	-
MARID (AJE-335)					
Phlogopite (n = 21)	**0.12**	**10.4**	**4.18**	**99.6**	**83.3**
S.D. (1σ)	0.08	0.12	0.01	0.41	0.80
CPX (n = 15)	**1.1**	**0.03**	**N/A**	**99.0**	**83.5**

S.D. (1σ)	0.34	0.05	-	0.29	1.7
Ilmenite (n = 10)	**Bdl**	**Bdl**	**N/A**	**98.7**	**N/A**
S.D. (1σ)	-	-	-	0.22	-
Rutile (n = 16)	**Bdl**	**Bdl**	**N/A**	**99.8**	**N/A**
S.D. (1σ)	-	-	-	0.26	-

Mineral	Na_2O	K_2O	H_2O	Total	Mg #
MARID (AJE-2422)					
Phlogopite (n = 4)	**0.08**	**10.52**	**4.19**	**98.91**	**85.8**
S.D. (1σ)	0.04	0.03	0.004	0.08	0.35
K-Richterite (n = 5)	**3.09**	**5.35**	**2.12**	**98.67**	**91.22**
S.D. (1σ)	0.03	0.03	-	0.08	0.03
Ilmenite (n = 12)	**0.01**	**Bdl**	**N/A**	**98.6**	**N/A**
S.D. (1σ)	0.01	-	-	0.11	-
Rutile (n = 16)	**Bdl**	**Bdl**	**N/A**	**97.7**	**N/A**
S.D. (1σ)	-	-	-	0.40	-
MARID (KDB-20)					
Phlogopite (n = 15)	**0.17**	**10.6**	**4.20**	**99.4**	**88.8**
S.D. (1σ)	0.02	0.11	0.01	0.33	0.38
Ilmenite (n = 5)	**0.27**	**0.04**	**N/A**	**99.2**	**N/A**
S.D. (1σ)	0.03	0.04	-	0.14	-

B.1.2 Sulphide Phases

Mineral	**Zn**	**Fe**	**Co**	**Ni**	**Cu**	**S**	**As**	**Total**
GPP (JAG1)								
Pentlandite (n = 25)	**Bdl**	**27.45**	**0.73**	**37.61**	**Bdl**	**33.04**	**Bdl**	**98.83**
Rsd (%)	-	2.73	31.5	1.60	-	0.67	-	0.60
min	-	25.60	0.16	36.25	-	32.14	-	97.95
max	-	28.61	1.27	39.17	-	33.36	-	99.99
Heazlewoodite (n = 13)	**Bdl**	**2.29**	**0.06**	**70.74**	**Bdl**	**26.80**	**Bdl**	**99.88**
Rsd (%)	-	41.92	99.98	2.43	-	3.10	-	3.10
min	-	0.70	0.02	64.99	-	26.04	-	97.64

max	-	4.38	0.24	72.84	-	30.15	-	101.41
PP (17MON 004)								
Pentlandite (n =18)	**Bdl**	**28.54**	**0.63**	**36.69**	**Bdl**	**33.09**	**Bdl**	**98.95**
Rsd (%)	-	6.62	16.5	5.15	-	0.60	-	0.52
min	-	23.81	0.46	34.32	-	32.78	-	98.11
max	-	31.43	0.88	41.06	-	33.45	-	99.95
Bornite (n = 1)	**Bdl**	**12.58**	**0.05**	**1.75**	**58.87**	**25.94**	**Bdl**	**99.19**
Rsd (%)	-	-	-	-	-	-	-	-
min	-	-	-	-	-	-	-	-
max	-	-	-	-	-	-	-	-
Spinel Lherzolite Host (LZM-001)								
Pentlandite (n = 11)	**Bdl**	**37.87**	**0.22**	**27.56**	**0.21**	**33.35**	**0.01**	**99.22**
Rsd (%)	-	2.80	27.27	4.61	233	1.08	4100	0.41
min	-	34.52	0.13	25.43	Bdl	32.73	Bdl	98.59
max	-	39.75	0.36	31.32	1.79	34.17	0.03	100
Spinel Lherzolite Vein (LZM-001)								
Pentlandite (n = 13)	**Bdl**	**32.52**	**0.36**	**32.74**	**0.19**	**33.05**	**0.01**	**98.87**
Rsd (%)	-	4.98	47.2	5.35	294	0.51	154	0.39
min	-	29.34	0.14	29.68	Bdl	32.73	Bdl	97.93
max	-	35.33	0.65	35.72	2.45	33.31	0.04	99.63
PIC (UIB-2)								
Pentlandite (n = 7)	**Bdl**	**26.10**	**1.03**	**38.44**	**Bdl**	**32.97**	**Bdl**	**98.58**
Rsd (%)	-	1.99	10.5	1.25	-	0.39	-	0.15
min	-	25.08	0.89	37.97	-	32.82	-	98.45
max	-	26.64	1.16	39.45	-	33.22	-	98.90
Chalcopyrite (n = 10)	**0.04**	**30.19**	**0.02**	**0.40**	**33.61**	**34.96**	**Bdl**	**99.21**
Rsd (%)	50.0	0.30	150	47.5	0.54	0.40	-	0.27
min	0.02	30.11	Bdl	0.28	33.45	34.87	-	98.92
max	0.06	30.28	0.05	0.62	33.80	35.12	-	99.45
Pyrrhotite (n = 3)	**Bdl**	**57.37**	**Bdl**	**1.22**	**Bdl**	**40.87**	**0.04**	**99.51**
Rsd (%)	-	0.98	-	18.0	-	2.00	50	1.16
min	-	56.73	-	1.07	-	40.00	0.02	98.26
max	-	57.77	-	1.48	-	41.63	0.05	100.6
Mineral	Zn	Fe	Co	Ni	Cu	S	As	Total
MARID (AJE-326)								
Pentlandite (n = 11)	**Bdl**	**29.1**	**1.20**	**35.5**	**Bdl**	**33.1**	**Bdl**	**98.9**
Rsd (%)	-	17.6	61	4.7	-	0.8	-	0.5
min	-	20.8	0.35	29.3	-	32.6	-	98.1
max	-	35.1	2.7	42.0	-	33.5	-	99.5
Heazlewoodite (n = 16)	**Bdl**	**1.3**	**0.2**	**71.1**	**Bdl**	**27.0**	**Bdl**	**99.6**
Rsd (%)	-	70	127	1.5	-	2.7	-	0.6

min	-	0.41	Bdl	69.6	-	26.6	-	98.3
max	-	3.2	0.6	72.8	-	29.6	-	100.6
Chalcopyrite (n = 8)	**Bdl**	**30.9**	**Bdl**	**0.5**	**32.9**	**34.8**	**Bdl**	**99.1**
Rsd (%)	-	0.6	-	26.4	0.7	0.9	-	0.5
min	-	30.8	-	0.3	32.5	34.1	-	98.1
max	-	31.4	-	0.6	33.1	35.2	-	99.6
MARID (AJE-335)								
Heazlewoodite (n = 8)	**Bdl**	**2.6**	**0.3**	**66.7**	**1.4**	**26.8**	**Bdl**	**98.1**
Rsd (%)	-	36.9	221	6.1	177	5.1	-	2.1
min	-	0.9	0.01	60.8	0.1	25.2	-	98.0
max	-	4.2	1.8	71.7	7.3	29.4	-	101.7
Copper Metal (n = 3)	**Bdl**	**1.8**	**Bdl**	**0.6**	**95.9**	**0.08**	**Bdl**	**98.5**
Rsd (%)	-	74.9	-	69.6	2.8	61	-	3.2
min	-	0.5	-	0.3	94.2	0.05	-	95.1
max	-	3.2	-	1.0	98.9	0.2	-	101.3
MARID (AJE-2422)								
Heazlewoodite (n = 11)	**Bdl**	**2.6**	**0.2**	**70.0**	**Bdl**	**27.3**	**Bdl**	**100.1**
Rsd (%)	-	29.6	229	1.7	-	3.0	-	1.2
min	-	1.7	0.01	68.2	-	26.2	-	98.5
max	-	3.9	1.3	71.4	-	28.6	-	101.5
Copper Metal (n = 2)	**Bdl**	**2.5**	**Bdl**	**0.4**	**95.9**	**0.05**	**Bdl**	**99.8**
Rsd (%)	-	0.3	-	35	0.4	77.8	-	0.1
min	-	2.49	-	0.3	95.8	0.02	-	99.8
max	-	2.5	-	0.5	95.9	0.07	-	99.9
MARID (KDB-20)								
Heazlewoodite (n = 2)	**Bdl**	**0.6**	**0.3**	**70.8**	**Bdl**	**25.9**	**0.6**	**98.2**
Rsd (%)	-	99.4	20	0.1	-	1.5	33	0.1
min	-	0.2	0.3	70.3	-	25.6	0.4	98.1
max	-	0.9	0.4	71.3	-	26.1	0.7	98.3

B.2 Trace Element Mineral Chemistry

B.2.1 Silicate and Oxide Phases

N/A indicates no successful analysis or major element in select phase. "-" in S.D. indicates <2 successful analyses. Concentrations and limits of quantitation (LOQ) are mean values. All concentrations are in parts per million (ppm)

Mineral	Rb	Ba	Nb	La	Ce	Pb	Pr	Sr	Nd	Zr	Hf	Sm
GPP (JAG1)												
Olivine (n = 2)	**0.03**	**0.6**	**0.6**	**0.165**	**0.34**	**0.2**	**0.034**	**1.0**	**0.112**	**0.29**	**0.0035**	**0.016**
S.D. (1σ)	0.035	0.68	0.11	0.0077	0.023	0.29	0.0035	0.36	0.0021	0.022	0.0007	0.0023
LOQ	0.03	0.02	0.008	0.0008	0.001	0.002	0.0009	0.01	0.003	0.003	0.0009	0.003
CPX (n = 4)	**0.24**	**27**	**2.3**	**18**	**52**	**2.7**	**7.1**	**440**	**28**	**41.2**	**1.8**	**4.4**
S.D. (1σ)	0.08	6.6	0.39	3.1	7.9	0.72	0.82	57	2.3	-	0.5	0.27
LOQ	0.06	0.04	0.004	0.004	0.004	0.007	0.003	0.03	0.02	0.008	0.01	0.02
OPX (n = 4)	**0.5**	**4**	**0.6**	**1**	**2**	**0.1**	**0.2**	**11**	**0.8**	**2.2**	**0.02**	**0.1**
S.D. (1σ)	0.63	5.6	0.7	1.4	2.9	0.15	0.29	14	0.9	-	0.015	0.12
LOQ	0.04	0.03	0.004	0.003	0.003	0.006	0.002	0.02	0.01	0.003	0.01	0.01
Garnet (n = 3)	**0.4**	**2**	**0.2**	**0.4**	**1**	**0.05**	**0.17**	**3**	**1.2**	**18.3**	**0.10**	**0.7**
S.D. (1σ)	0.31	1.9	0.18	0.48	0.8	0.04	0.08	3.4	0.4	0.26	0.07	0.33
LOQ	0.2	0.09	0.01	0.007	0.009	0.02	0.007	0.4	0.04	0.007	0.04	0.04
Phlogopite (n = 1)	**178**	**4298**	**19.7**	**2.0**	**4.7**	**1.41**	**0.52**	**167**	**1.92**	**7.0**	**0.09**	**0.28**
S.D. (1σ)	-	-	-	-	-	-	-	-	-	-	-	-
LOQ	0.2	0.2	0.01	0.006	0.003	0.01	0.006	0.09	0.03	0.02	0.009	0.04
PP (17MON004)												
Olivine (n = 6)	**<LOQ**	**<LOQ**	**1.8**	**<LOQ**	**<LOQ**	**<LOQ**	**<LOQ**	**<LOQ**	**<LOQ**	**0.10**	**<LOQ**	**<LOQ**
S.D. (1σ)	-	-	0.11	-	-	-	-	-	-	0.03	-	-
LOQ	0.01	0.01	0.12	0.004	0.004	0.002	0.0006	0.01	0.003	0.04	0.1	0.5
CPX (n = 7)	**2**	**19**	**2.0**	**26**	**70**	**1.8**	**8**	**600**	**30**	**40**	**0.7**	**5**
S.D. (1σ)	3.3	25.6	0.89	3.8	18	0.2	3.4	124	17	29	0.4	3.6
LOQ	0.02	0.4	0.1	2.4	6.8	0.2	1.0	0.009	4.3	0.3	0.2	0.9
OPX (n = 3)	**<LOQ**	**0.3**	**1**	**0.025**	**0.07**	**0.006**	**0.010**	**0.5**	**0.048**	**<LOQ**	**<LOQ**	**0.01**
S.D. (1σ)	-	0.19	1.3	0.009	0.02	0.003	0.001	0.19	0.008	-	-	0.001
LOQ	0.02	0.02	0.001	0.0006	0.001	0.001	0.0005	0.01	0.003	0.5	0.001	0.003
Phlogopite (n = 8)	**430**	**2000**	**40**	**0.05**	**0.2**	**<LOQ**	**0.02**	**9**	**0.1**	**6**	**0.2**	**0.03**
S.D. (1σ)	47	1500	16	0.041	0.15	-	0.02	3.9	0.09	6.4	0.28	0.026
LOQ	0.2	283	4	0.01	0.03	0.4	0.006	0.08	0.02	3	0.02	0.01
Chromite (n = 4)	**4**	**40**	**7**	**0.16**	**0.3**	**4.4**	**<LOQ**	**20**	**0.17**	**4**	**0.26**	**<LOQ**
S.D. (1σ)	2.3	66	2.4	0.08	0.18	-	-	29	0.08	4.6	-	-
LOQ	0.3	0.9	4.5	0.06	0.08	0.09	0.02	0.2	0.1	0.5	0.07	0.05

Mineral	Rb	Ba	Nb	La	Ce	Pb	Pr	Sr	Nd	Zr	Hf	Sm
Spinel Lherzolite Host (LZM-001)												
Olivine (n = 2)	**3.5**	**20**	**0.037**	**0.19**	**0.27**	**0.70**	**0.035**	**3.7**	**0.13**	**21**	**0.42**	**0.02**
S.D. (1σ)	0.78	12	0.001	0.02	0.1	0.07	0	0.6	0.02	3.5	0.06	0.010
LOQ	0.09	0.1	0.008	0.005	0.005	0.004	0.005	0.07	0.008	0.07	0.008	0.009
CPX (n = 2)	**0.4**	**3**	**0.35**	**3.01**	**10.6**	**0.18**	**1.8**	**123**	**9**	**50**	**1.3**	**2.9**
S.D. (1σ)	0.23	3.0	0.02	0.02	0.54	0.06	0.27	9.1	1.4	16	0.42	0.7
LOQ	0.1	0.1	0.009	0.006	0.004	0.008	0.006	0.09	0.02	0.07	0.01	0.02
OPX (n = 2)	**0.7**	**4**	**0.018**	**0.051**	**0.13**	**0.195**	**0.025**	**1.2**	**0.10**	**8**	**0.22**	**0.05**
S.D. (1σ)	0.7	2.0	0.002	0.002	0.046	0.007	0.002	0.16	0.01	1.3	0.081	0.017
LOQ	0.08	0.09	0.006	0.003	0.003	0.004	0.004	0.05	0.01	0.1	0.004	0.01
Pargasite (n = 2)	**1.5**	**70**	**20**	**5.1**	**17**	**0.37**	**2.9**	**410**	**15**	**70**	**1.9**	**4.6**
S.D. (1σ)	0.38	31	6.1	0.78	2.5	0.031	0.37	31	2.0	5.9	0.51	0.24
LOQ	0.1	0.2	0.008	0.006	0.005	0.01	0.006	0.1	0.01	0.06	0.008	0.02
Spinel Lherzolite Vein (LZM-001)												
Pargasite (n = 2)	**1.7**	**100**	**35**	**6.68**	**22.5**	**0.34**	**3.8**	**555**	**20**	**86**	**2.8**	**6.0**
S.D. (1σ)	0.59	17	2.1	0.057	0.63	0.033	0.19	8.5	1.4	6.1	0.39	0.55
LOQ	0.05	0.03	0.002	0.0005	0.0008	0.008	0.0009	0.02	0.004	0.06	0.02	0.006
Phlogopite (n = 2)	**52**	**1600**	**19**	**0.023**	**0.03**	**0.5**	**0.008**	**200**	**<LOQ**	**6.04**	**0.18**	**<LOQ**
S.D. (1σ)	9.1	142	1.5	0.0028	0.011	0.12	-	43	-	0.057	0.060	-
LOQ	0.1	0.2	0.01	0.008	0.006	0.01	0.007	0.1	0.03	0.1	0.02	0.04
PIC (UIB-2)												
Phlogopite (n = 3)	**390**	**400**	**12.2**	**0.03**	**0.07**	**0.04**	**0.01**	**3.1**	**0.03**	**2.74**	**0.09**	**0.04**
S.D. (1σ)	10.9	55	0.19	0.045	0.093	0.012	0.019	0.30	0.040	0.046	0.011	-
LOQ	0.04	0.02	0.0007	0.0007	0.0007	0.001	0.0003	0.01	0.002	1.4	0.06	0.01
CPX (n = 2)	**0.2**	**9**	**0.5**	**3.6**	**13**	**0.37**	**2.4**	**200**	**13**	**100**	**5.4**	**3.1**
S.D. (1σ)	0.15	10.6	0.25	0.90	2.7	0.041	0.34	16	1.3	10	0.50	0.39
LOQ	0.05	0.07	0.003	0.003	0.001	0.003	0.002	0.04	0.01	1.3	0.01	0.02
Ilmenite (n = 2)	**<LOQ**	**0.04**	**1623**	**0.02**	**0.02**	**0.006**	**0.006**	**0.135**	**0.01**	**512**	**13.2**	**0.007**
S.D. (1σ)	-	0.015	6	0.028	0.03	0.0017	0.0007	0.0012	-	7.8	0.12	0.0032
LOQ	0.05	0.02	0.007	0.0009	0.0006	0.002	0.0004	0.02	0.006	0.008	0.03	0.005
Rutile (n=1)	**<LOQ**	**<LOQ**	**29880**	**0.006**	**0.01**	**<LOQ**	**<LOQ**	**0.3**	**<LOQ**	**8250**	**226**	**<LOQ**
S.D. (1σ)	-	-	-	-	-	-	-	-	-	-	-	-
LOQ	0.2	0.1	0.05	0.002	0.002	0.01	0.003	0.05	0.01	0.03	0.03	0.01

Mineral	Rb	Ba	Nb	La	Ce	Pb	Pr	Sr	Nd	Zr	Hf	Sm
MARID (AJE-326)												
Phlogopite (n = 3)	**520**	**460**	**10**	**0.36**	**0.5**	**0.3**	**0.05**	**6**	**0.2**	**4**	**0.1**	**0.06**
S.D. (1σ)	23	70	1.3	-	0.64	0.30	0.071	7.0	0.28	3.6	0.10	-
LOQ	0.08	0.05	0.02	0.003	0.004	0.2	0.002	0.04	0.02	0.08	0.007	0.02
K-Richterite (n = 3)	**32.4**	**27**	**9**	**1.8**	**5.4**	**1.3**	**0.76**	**800**	**3.1**	**30**	**1.4**	**0.49**
S.D. (1σ)	0.46	7.8	1.6	0.30	0.58	0.31	0.070	145	0.25	3.5	0.15	0.038
LOQ	0.03	1.3	0.4	0.2	0.4	1.0	0.05	0.01	0.2	0.006	0.2	0.09
Ilmenite (n=2)	**<LOQ**	**<LOQ**	**3840**	**<LOQ**	**<LOQ**	**<LOQ**	**<LOQ**	**0.4**	**<LOQ**	**520**	**12.8**	**<LOQ**
S.D. (1σ)	-	-	8.5	-	-	-	-	0.34	-	11	0.13	-
LOQ	0.1	1.2	950	0.8	1.9	1.7	0.2	0.02	0.7	7	4.8	0.1
MARID (AJE-335)												
CPX (n = 3)	**4**	**50**	**0.9**	**30**	**110**	**2.2**	**19**	**830**	**89**	**30**	**1.6**	**16.0**
S.D. (1σ)	4.9	59	1.2	1.3	6.0	0.15	1.0	41	5.1	10	0.25	0.83
LOQ	0.05	0.05	0.003	0.002	0.002	0.003	0.002	0.04	0.008	0.01	0.0008	0.005
Phlogopite (n = 4)	**540**	**360**	**1.9**	**0.2**	**0.4**	**0.13**	**0.04**	**6**	**0.16**	**3.5**	**0.091**	**0.022**
S.D. (1σ)	18	82	0.40	0.12	0.23	0.020	0.023	4.2	0.057	0.32	0.0094	0.0059
LOQ	0.07	0.06	0.006	0.003	0.003	0.005	0.009	0.05	0.01	0.04	0.005	0.009
Ilmenite (n=2)	**<LOQ**	**0.03**	**420**	**0.005**	**0.02**	**0.005**	**0.004**	**0.16**	**<LOQ**	**157.55**	**5.12**	**0.007**
S.D. (1σ)	-	-	11	0.003	0.011	0.0038	0.0010	0.035	-	0.071	0.092	0.0003
LOQ	0.03	0.02	0.002	0.0005	0.0004	0.0009	0.0003	0.01	0.7	0.004	0.001	0.002
MARID (AJE-2422)												
Phlogopite (n = 3)	**500**	**510**	**5**	**0.2**	**0.4**	**0.18**	**0.04**	**7**	**0.1**	**2.7**	**0.09**	**0.03**
S.D. (1σ)	21	24	1.2	0.13	0.31	0.011	0.035	2.6	0.12	0.6	0.02	0.024
LOQ	0.07	0.06	0.003	0.003	0.002	0.003	0.002	0.05	0.01	0.02	0.008	0.008
K-Richterite (n = 3)	**37.5**	**18.5**	**1.7**	**2.5**	**8.3**	**4.83**	**1.20**	**600**	**4.8**	**7.8**	**0.42**	**0.70**
S.D. (1σ)	0.79	0.79	0.18	0.21	0.49	0.081	0.059	20	0.25	0.25	0.020	0.035
LOQ	0.02	0.02	0.001	0.0007	0.0007	0.001	0.0008	0.01	0.003	0.007	0.001	0.002
Zircon (n = 2)	**<LOQ**	**0.46**	**3**	**0.8**	**10**	**0.3**	**0.4**	**4**	**2.8**	**N/A**	**10600**	**2.0**
S.D. (1σ)	-	0.02	1.9	0.27	1.7	0.22	0.15	1.8	1.0	-	1287	0.7
LOQ	0.07	0.08	0.003	0.003	0.003	0.005	0.003	0.05	0.01	-	0.009	0.02
MARID (KDB-20)												
Phlogopite (n = 5)	**560**	**480**	**7.4**	**0.08**	**0.2**	**0.14**	**0.02**	**3**	**0.07**	**2.9**	**0.07**	**0.014**
S.D. (1σ)	13	72	0.42	0.076	0.11	0.027	0.012	1.9	0.040	0.69	0.022	0.0061
LOQ	0.06	0.03	0.001	0.0008	0.0009	0.002	0.0008	0.02	0.004	1.5	0.006	0.005

Mineral	Eu	Ti	Gd	Tb	Dy	Ho	Y	Er	Tm	Yb	Lu	Sc
GPP (JAG1)												
Olivine (n = 2)	**0.003**	**60**	**0.009**	**0.001**	**0.005**	**0.001**	**0.013**	**0.003**	**0.002**	**0.002**	**<LOQ**	**0.814**
S.D. (1σ)	0	3.4	0	0.0008	0.0004	-	0.004	-	-	0.001	-	0.0021
LOQ	0.0008	0.6	0.005	0.0002	0.002	0.0005	0.001	0.002	0.0003	0.001	0.0006	0.06
CPX (n = 4)	**1.0**	**600**	**2.4**	**0.24**	**1.0**	**0.13**	**3**	**0.2**	**0.03**	**0.13**	**0.014**	**25**
S.D. (1σ)	0.12	120	0.41	0.06	0.30	0.05	1.1	0.10	0.011	0.069	0.0073	1.8
LOQ	0.006	0.6	0.03	0.003	0.01	0.003	0.005	0.009	0.003	0.02	0.005	0.08
OPX (n = 4)	**0.03**	**200**	**0.11**	**0.011**	**0.07**	**0.008**	**0.11**	**0.018**	**0.003**	**<LOQ**	**<LOQ**	**1.5**
S.D. (1σ)	0.030	7.0	0.065	0.0062	-	0.0035	0.097	0.0037	-	-	-	0.21
LOQ	0.005	0.5	0.02	0.003	0.01	0.003	0.004	0.008	0.002	0.008	0.003	0.097
Garnet (n = 3)	**0.3**	**240**	**1.1**	**0.25**	**2.0**	**0.51**	**15**	**1.8**	**0.282**	**2.21**	**0.355**	**81**
S.D. (1σ)	0.13	47	0.52	0.067	0.40	0.051	2.0	0.10	0.0018	0.039	0.0090	7.4
LOQ	0.01	3.3	0.05	0.008	0.02	0.008	0.01	0.02	0.006	0.04	0.01	0.2
Phlogopite (n = 1)	**0.1**	**2068**	**0.2**	**0.03**	**0.2**	**0.04**	**1.1**	**0.13**	**0.02**	**0.14**	**0.02**	**5.7**
S.D. (1σ)	-	-	-	-	-	-	-	-	-	-	-	-
LOQ	0.02	3.7	0.05	0.003	0.01	0.003	0.02	0.002	0.004	0.02	0.002	0.3
PP (17MON 004)												
Olivine (n = 6)	**<LOQ**	**25**	**<LOQ**	**<LOQ**	**<LOQ**	**<LOQ**	**0.007**	**0.001**	**0.0003**	**0.0025**	**<LOQ**	**0.90**
S.D. (1σ)	-	3.3	-	-	-	-	0.0007	0.0002	0	0.0003	-	0.051
LOQ	0.0008	0.3	0.002	0.0003	0.01	0.009	0.001	0.0008	0.0002	0.001	0.003	0.03
CPX (n = 7)	**1**	**270**	**3**	**0.4**	**2**	**0.3**	**7**	**0.6**	**0.07**	**0.4**	**0.06**	**46**
S.D. (1σ)	1.0	43	2.6	0.31	1.5	0.2	5.2	0.5	0.05	0.24	0.024	2
LOQ	0.2	0.3	0.6	0.08	0.4	0.1	0.001	0.1	0.01	0.1	0.009	0.03
OPX (n = 3)	**0.0035**	**130**	**0.009**	**0.001**	**0.009**	**0.002**	**0.05**	**0.006**	**0.001**	**0.008**	**0.0017**	**1.7**
S.D. (1σ)	0.0002	13	0.001	0.0003	0.0026	0.0004	0.017	0.0022	0.0002	0.0004	0.0006	0.30
LOQ	0.001	0.4	0.004	0.0005	0.001	0.0004	0.002	0.002	0.0003	0.002	0.0005	0.03
Phlogopite (n = 8)	**0.024**	**5000**	**<LOQ**	**<LOQ**	**<LOQ**	**<LOQ**	**0.05**	**<LOQ**	**<LOQ**	**<LOQ**	**<LOQ**	**2**
S.D. (1σ)	0.0066	6400	-	-	-	-	0.04	-	-	-	-	1.2
LOQ	0.01	7.0	0.05	0.005	0.01	0.003	0.02	0.01	0.004	0.01	0.004	0.3
Chromite (n = 4)	**0.07**	**3000**	**<LOQ**	**<LOQ**	**<LOQ**	**<LOQ**	**<LOQ**	**0.3**	**0.2**	**<LOQ**	**<LOQ**	**1.2**
S.D. (1σ)	0.031	330	-	-	-	-	-	0.15	0.11	-	-	0.55
LOQ	0.04	8.5	0.1	0.02	0.03	0.008	0.08	0.05	0.03	0.04	0.02	0.6

Mineral	Eu	Ti	Gd	Tb	Dy	Ho	Y	Er	Tm	Yb	Lu	Sc
Spinel Lherzolite Host (LZM-001)												
Olivine (n = 2)	**0.02**	**18.6**	**<LOQ**	**0.004**	**0.02**	**0.007**	**0.15**	**0.0185**	**0.0045**	**0.029**	**0.0053**	**0.84**
S.D. (1σ)	0.0028	0.35	-	0.0007	0.01	0.0006	0.03	0.0007	0.0007	0.008	0.0008	0.03
LOQ	0.007	2.6	0.03	0.002	0.005	0.002	0.009	0.003	0.003	0.008	0.002	0.2
CPX (n = 2)	**1.1**	**4600**	**3.4**	**0.57**	**3.6**	**0.72**	**18.6**	**2.0**	**0.27**	**1.7**	**0.23**	**51**
S.D. (1σ)	0.18	900	0.73	0.062	0.39	0.088	0.71	0.22	0.026	0.11	0.025	3.4
LOQ	0.009	3.1	0.05	0.005	0.01	0.002	0.01	0.01	0.002	0.007	0.001	0.2
OPX (n = 2)	**0.023**	**970**	**0.051**	**0.013**	**0.09**	**0.024**	**0.65**	**0.09**	**0.021**	**0.16**	**0.030**	**9.6**
S.D. (1σ)	0.002	84	-	0	0.011	0.003	0.045	0.011	0.004	0.01	0.006	0.52
LOQ	0.005	2.8	0.03	0.002	0.004	0.001	0.007	0.001	0.001	0.004	0.002	0.19
Pargasite (n = 2)	**1.7**	**23000**	**5.3**	**0.798**	**4.7**	**0.93**	**24**	**2.5**	**0.33**	**2.1**	**0.30**	**44**
S.D. (1σ)	0.10	1100	0.17	0.009	0.38	0.071	2.7	0.35	0.060	0.49	0.058	4.9
LOQ	0.01	3.8	0.07	0.003	0.009	0.003	0.01	0.01	0.003	0.01	0.004	0.4
Spinel Lherzolite Vein (LZM-001)												
Pargasite (n = 2)	**2.1**	**26000**	**6.3**	**0.91**	**5.3**	**0.99**	**24.4**	**2.49**	**0.318**	**1.96**	**0.267**	**38**
S.D. (1σ)	0.15	806	0.50	0.081	0.34	0.045	0.52	0.066	0.0021	0.011	0.0051	6.3
LOQ	0.001	0.82	0.007	0.0005	0.001	0.0005	0.002	0.006	0.0005	0.002	0.003	0.1
Phlogopite (n = 2)	**0.03**		**40000**	**<LOQ**	**<LOQ**	**<LOQ**	**0.02**	**<LOQ**	**<LOQ**	**<LOQ**	**<LOQ**	**3.5**
S.D. (1σ)	0.005		1600	-	-	-	0.006	-	-	-	-	0.33
LOQ	0.01		3.7	0.05	0.005	0.007	0.015	0.008	0.006	0.02	0.006	0.4
PIC (UIB-2)												
Phlogopite (n = 3)	**0.008**	**8000**	**0.011**	**0.003**	**0.008**	**0.004**	**0.01**	**0.009**	**0.003**	**<LOQ**	**0.004**	**1.57**
S.D. (1σ)	0.003	110	0.008	0.003	0.008	0.004	0.013	0.008	0.004	-	0.005	0.038
LOQ	0.001	0.5	0.004	0.0003	0.002	0.0003	0.002	0.001	0.0003	0.002	0.0005	0.08
CPX (n = 2)	**0.9**	**1440**	**2.2**	**0.26**	**1.2**	**0.18**	**3.8**	**0.34**	**0.038**	**0.19**	**0.023**	**80**
S.D. (1σ)	0.10	13	0.36	0.041	0.19	0.013	0.53	0.046	0.003	0.017	0.002	2.8
LOQ	0.003	1.3	0.02	0.001	0.0009	0.002	0.005	0.006	0.0004	0.005	0.002	0.1
Ilmenite (n = 2)	**0.0029**	**N/A**	**0.011**	**0.003**	**0.015**	**0.006**	**0.077**	**0.014**	**0.0034**	**0.025**	**<LOQ**	**34**
S.D. (1σ)	0.0007	-	0.0002	0.002	0.002	0.001	0.009	0.003	0	0	-	2.4
LOQ	0.002	-	0.006	0.0004	0.001	0.0004	0.003	0.003	0.0003	0.002	0.006	0.3
Rutile (n=1)	**<LOQ**	**N/A**	**<LOQ**	**<LOQ**	**<LOQ**	**0.0004**	**0.051**	**<LOQ**	**<LOQ**	**0.0034**	**<LOQ**	**34.5**
S.D. (1σ)	-	-	-	-	-	-	-	-	-	-	-	-
LOQ	0.010	-	0.02	0.002	0.01	0.0002	0.006	0.004	0.002	0.0008	0.01	0.6

Mineral	Eu	Ti	Gd	Tb	Dy	Ho	Y	Er	Tm	Yb	Lu	Sc
MARID (AJE-326)												
Phlogopite (n = 3)	**0.013**	**3200**	**0.04**	**<LOQ**	**0.016**	**0.002**	**0.04**	**<LOQ**	**<LOQ**	**<LOQ**	**<LOQ**	**1.3**
S.D. (1σ)	0.009	630	-	-	-	-	0.043	-	-	-	-	0.54
LOQ	0.005	2.5	0.02	0.004	0.01	0.0003	0.01	0.006	0.004	0.02	0.004	0.1
K-Richterite (n = 3)	**0.132**	**2400**	**0.27**	**0.027**	**0.11**	**0.014**	**0.30**	**0.026**	**0.003**	**0.016**	**0.0028**	**28.9**
S.D. (1σ)	0.007	210	0.032	0.003	0.011	0.002	0.05	0.004	0.0002	0.001	0.0008	0.63
LOQ	0.01	0.2	0.02	0.002	0.01	0.002	0.0009	0.003	0.0005	0.008	0.0003	0.03
Ilmenite (n=2)	**<LOQ**	**N/A**	**<LOQ**	**<LOQ**	**<LOQ**	**<LOQ**	**0.10**	**<LOQ**	**<LOQ**	**0.017**	**0.003**	**37**
S.D. (1σ)	-	-	-	-	-	-	0.07	-	-	0.008	0.001	1.2
LOQ	0.04	-	0.07	0.009	0.04	0.005	0.005	0.07	0.03	0.009	0.002	0.05
MARID (AJE-335)												
CPX (n = 3)	**4.1**	**1000**	**9.7**	**1.05**	**4.6**	**0.68**	**15.2**	**1.39**	**0.146**	**0.76**	**0.0894**	**60.3**
S.D. (1σ)	0.18	330	0.42	0.04	0.2	0.03	0.4	0.056	0.0032	0.018	0.0006	0.48
LOQ	0.003	1.0	0.014	0.001	0.006	0.001	0.004	0.01	0.0008	0.01	0.001	0.1
Phlogopite (n = 4)	**0.007**	**16500**	**<LOQ**	**<LOQ**	**<LOQ**	**<LOQ**	**0.04**	**0.004**	**<LOQ**	**<LOQ**	**<LOQ**	**1.42**
S.D. (1σ)	0.0006	280	-	-	-	-	0.021	0.001	-	-	-	0.07
LOQ	0.006	1.7	0.02	0.002	0.009	0.002	0.005	0.003	0.002	0.01	0.0009	0.2
Ilmenite (n=2)	**0.0027**	**N/A**	**0.009**	**0.0027**	**0.0291**	**0.007**	**0.151**	**0.031**	**0.0070**	**0.0642**	**0.0126**	**33.44**
S.D. (1σ)	0.0003	-	0.002	0.0002	0.0003	-	0.004	0.002	0.0007	0.0001	0.0008	0.03
LOQ	0.001	-	0.003	0.0003	0.007	0.005	0.001	0.03	0.003	0.0008	0.002	0.1
MARID (AJE-2422)												
Phlogopite (n = 3)	**0.008**	**9500**	**<LOQ**	**0.002**	**0.02**	**0.002**	**0.04**	**0.0039**	**<LOQ**	**<LOQ**	**<LOQ**	**2.11**
S.D. (1σ)	0.005	320	-	0.0010	-	-	0.018	0.0005	-	-	-	0.09
LOQ	0.002	1.5	0.02	0.0015	0.008	0.0015	0.005	0.003	0.003	0.004	0.0008	0.2
K-Richterite (n = 3)	**0.194**	**3470**	**0.37**	**0.0373**	**0.17**	**0.0253**	**0.55**	**0.054**	**0.0058**	**0.039**	**0.0065**	**36.3**
S.D. (1σ)	0.0079	56	0.018	0.0007	0.016	0.0006	0.029	0.004	0.0001	0.003	0.0002	0.65
LOQ	0.001	0.5	0.005	0.004	0.0009	0.0005	0.001	0.001	0.0005	0.001	0.0003	0.06
Zircon (n = 2)	**1.0**	**4500**	**6**	**1.5**	**15**	**4**	**120**	**17**	**3.1**	**26**	**5**	**990**
S.D. (1σ)	0.39	430	1.9	0.50	5.0	1.4	33	5.2	0.95	7.6	1.2	12.0
LOQ	0.005	1.9	0.02	0.002	0.004	0.001	0.007	0.002	0.001	0.006	0.001	0.2
MARID (KDB-20)												
Phlogopite (n = 5)	**0.007**	**3400**	**0.012**	**0.002**	**0.006**	**0.002**	**0.03**	**0.004**	**0.004**	**<LOQ**	**0.0020**	**0.9**
S.D. (1σ)	0.003	730	0.004	0.0013	0.0043	0.0010	0.020	0.0018	0.0066	-	0.0004	0.13
LOQ	0.001	0.7	0.006	0.0004	0.003	0.0004	0.002	0.001	0.0004	0.007	0.0008	0.1

Mineral	Co	Ni	Cu
GPP (JAG1)			
Olivine (n = 2)	**147**	**3300**	**0.198**
S.D. (1σ)	3.8	120	0.009
LOQ	0.03	0.1	0.02
CPX (n = 4)	**18.5**	**340**	**0.17**
S.D. (1σ)	0.75	4.5	-
LOQ	0.2	0.9	0.02
OPX (n = 4)	**56**	**760**	**0.19**
S.D. (1σ)	1.3	29	-
LOQ	0.09	0.8	0.03
Garnet (n = 3)	**44.5**	**25.0**	**<LOQ**
S.D. (1σ)	0.84	0.45	-
LOQ	0.3	1.5	0.06
Phlogopite (n = 1)	**56**	**1090**	**<LOQ**
S.D. (1σ)	-	-	-
LOQ	0.2	1.1	0.17
PP (17MON 004)			
Olivine (n = 6)	**157**	**2600**	**<LOQ**
S.D. (1σ)	6.6	280	-
LOQ	0.008	0.2	0.1
CPX (n = 7)	**19**	**310**	**<LOQ**
S.D. (1σ)	1.6	47	-
LOQ	0.008	0.2	0.07
OPX (n = 3)	**60**	**670**	**<LOQ**
S.D. (1σ)	4.7	38	-
LOQ	0.3	0.3	0.1
Phlogopite (n = 8)	**63**	**1600**	**<LOQ**
S.D. (1σ)	1.6	390	-
LOQ	0.008	4.6	0.1
Chromite (n = 4)	**290**	**680**	**1.1**
S.D. (1σ)	19	82	-
LOQ	0.2	8.9	0.08

Mineral	Co	Ni	Cu
Spinel Lherzolite Host (LZM-001)			
Olivine (n = 2)	**110**	**2310**	**0.39**
S.D. (1σ)	3.5	77	0.04
LOQ	0.08	0.9	0.1
CPX (n = 2)	**16.5**	**247**	**0.54**
S.D. (1σ)	0.64	4.9	0.06
LOQ	0.1	1.1	0.2
OPX (n = 2)	**50**	**580**	**0.5**
S.D. (1σ)	1.0	16	0.14
LOQ	0.05	0.6	0.1
Pargasite (n = 2)	**33.7**	**680**	**0.65**
S.D. (1σ)	0.52	46	0.07
LOQ	0.1	1.4	0.2
Spinel Lherzolite Vein (LZM-001)			
Phlogopite (n = 2)	**54**	**1400**	**1.01**
S.D. (1σ)	7.5	220	0.03
LOQ	0.1	1.8	0.2
Pargasite (n = 2)	**37.1**	**748**	**0.7**
S.D. (1σ)	0.7	4.2	0.1
LOQ	0.02	0.4	0.06
OPX (n = 3)			
S.D. (1σ)			
LOQ			
PIC (UIB-2)			
Phlogopite (n = 3)	**55**	**1120**	**0.44**
S.D. (1σ)	1.9	36	0.090
LOQ	0.01	0.2	0.03
CPX (n = 2)	**19.0**	**225**	**0.20**
S.D. (1σ)	0.24	4.2	0.05
LOQ	0.04	0.6	0.08
Ilmenite (n = 2)	**195**	**1329**	**12**
S.D. (1σ)	3.2	2.8	1.1
LOQ	0.02	0.2	0.1
Rutile (n = 1)	**2.1**	**19.5**	**-**
S.D. (1σ)	-	-	-
LOQ	0.06	0.8	-

Mineral	Co	Ni	Cu
MARID (AJE-326)			
Phlogopite (n = 3)	**62.8**	**830**	**0.31**
S.D. (1σ)	0.75	12	0.056
LOQ	0.05	1.7	0.03
K-Richterite (n =3)	**28.6**	**338**	**0.57**
S.D. (1σ)	0.88	9.6	0.07
LOQ	0.007	0.2	0.02
Ilmenite (n = 2)	**171**	**890**	**7.9**
S.D. (1σ)	3.74	53	0.47
LOQ	0.02	1.1	0.2
MARID (AJE-335)			
Phlogopite (n = 4)	**80**	**660**	**1.5**
S.D. (1σ)	2.8	27	0.42
LOQ	0.06	0.7	0.1
CPX (n = 3)	**27**	**141**	**0.9**
S.D. (1σ)	1.9	9.4	0.42
LOQ	0.03	0.4	0.03
Ilmenite (n = 2)	**174**	**634**	**8.0**
S.D. (1σ)	1.0	4.4	0.14
LOQ	0.01	0.1	0.05
MARID (AJE-2422)			
Phlogopite (n = 3)	**72**	**1000**	**0.9**
S.D. (1σ)	3.1	294	0.71
LOQ	0.05	0.6	0.1
K-Richterite (n = 3)	**33.7**	**354**	**0.4**
S.D. (1σ)	0.80	7.0	0.13
LOQ	0.02	0.2	0.03
Zircon (n = 2)	**<LOQ**	**1.1**	**<LOQ**
S.D. (1σ)	-	-	-
LOQ	0.07	0.8	0.1
MARID (KDB-20)			
Phlogopite (n = 5)	**67**	**1090**	**0.15**
S.D. (1σ)	1.2	31	0.09
LOQ	0.03	0.2	0.04

B.3 Precious Metal Mineral Chemistry

B.3.1 Precious Metal Mineral Chemistry in Silicate and Oxide Phases

"-" in S.D. indicates <2 successful analyses. Concentrations and limits of quantitation (LOQ) are mean values. All concentrations are in parts per billion (ppb). Red text indicates results affected by interfering species during ablation. Red values are not considered in any mass balance calculations.

Mineral	Ag	Pd	Re	Ir	Pt	Au
GPP (JAG1)						
Olivine (n = 2)	**< LOQ**	**< LOQ**	**0.3**	**< LOQ**	**< LOQ**	**< LOQ**
S.D. (1σ)	-	-	0.13	-	-	-
LOQ	9	1	0.17	6	3	20
# of analysis > LOQ	0	0	2	0	0	0
CPX (n = 1)	**24**	**6**	**< LOQ**	**< LOQ**	**< LOQ**	**< LOQ**
S.D. (1σ)	-	-	-	-	-	-
LOQ	10	1	0.2	6	4	20
# of analysis > LOQ	1	1	0	0	0	0
OPX (n = 1)	**< LOQ**	**< LOQ**	**< LOQ**	**< LOQ**	**< LOQ**	**< LOQ**
S.D. (1σ)	-	-	-	-	-	-
LOQ	10	1	0.3	7	3	20
# of analysis > LOQ	0	0	0	0	0	0
Garnet (n = 2)	**< LOQ**	**2.87**	**< LOQ**	**< LOQ**	**< LOQ**	**< LOQ**
S.D. (1σ)	-	0.07	0	-	-	-
LOQ	2	2.5	0.3	14	6.7	27
# of analysis > LOQ	0	2	0	0	0	0
Phlogopite (n = 1)	**< LOQ**	**< LOQ**	**< LOQ**	**< LOQ**	**< LOQ**	**< LOQ**
S.D. (1σ)	-	-	-	-	-	-
LOQ	63	7	3	11	17	70
# of analysis > LOQ	0	0	0	0	0	0
PP (17MON 004)						
Olivine (n = 7)	**< LOQ**	**< LOQ**	**< LOQ**	**< LOQ**	**< LOQ**	**< LOQ**
S.D. (1σ)	-	-	-	-	-	-
LOQ	9	2	0.2	0.4	0.7	1
# of analysis > LOQ	0	0	0	0	0	0
CPX (n = 8)	**14**	**8**	**< LOQ**	**< LOQ**	**< LOQ**	**< LOQ**
S.D. (1σ)	4	4.4	-	-	-	-
LOQ	9.9	2	0.3	0.5	0.8	1
# of analysis > LOQ	7	8	0	0	0	0
OPX (n = 1)	**< LOQ**	**< LOQ**	**< LOQ**	**< LOQ**	**< LOQ**	**< LOQ**
S.D. (1σ)	-	-	-	-	-	-
LOQ	1	3	0.5	0.4	1	2

# of analysis > LOQ	0	0	0	0	0	0
Phlogopite (n = 4)	**< LOQ**	**< LOQ**	**< LOQ**	**< LOQ**	**< LOQ**	**3**
S.D. (1σ)	-	-	-	-	-	3.6
LOQ	14	3	0.3	0.8	0.9	1
# of analysis > LOQ	0	0	0	0	0	3
Chromite (n = 1)	**< LOQ**	**13**	**2**	**< LOQ**	**< LOQ**	**< LOQ**
S.D. (1σ)	-	-	-	-	-	-
LOQ	3	6	1.4	3	2	3
# of analysis > LOQ	0	1	1	0	0	0
Mineral	Ag	Pd	Re	Ir	Pt	Au
Spinel Lherzolite Host (LZM-001)						
Olivine (n = 2)	**< LOQ**	**< LOQ**	**< LOQ**	**< LOQ**	**< LOQ**	**< LOQ**
S.D. (1σ)	-	-	-	-	-	-
LOQ	42	9	1	2	4	4
# of analysis > LOQ	0	0	0	0	0	0
CPX (n = 2)	**< LOQ**	**< LOQ**	**< LOQ**	**< LOQ**	**< LOQ**	**< LOQ**
S.D. (1σ)	-	-	-	-	-	-
LOQ	63	15	2	4	5	5
# of analysis > LOQ	0	0	0	0	0	0
OPX (n = 2)	**< LOQ**	**< LOQ**	**< LOQ**	**< LOQ**	**< LOQ**	**< LOQ**
S.D. (1σ)	-	-	-	-	-	-
LOQ	42	9	0.8	2	3	3
# of analysis > LOQ	0	0	0	0	0	0
Pargasite (n = 2)	**< LOQ**	**< LOQ**	**< LOQ**	**< LOQ**	**< LOQ**	**< LOQ**
S.D. (1σ)	-	-	-	-	-	-
LOQ	70	18	3	4	5	6
# of analysis > LOQ	0	0	0	0	0	0
Spinel Lherzolite Vein (LZM-001)						
Pargasite (n = 2)	**< LOQ**	**9.4**	**< LOQ**	**< LOQ**	**< LOQ**	**3.2**
S.D. (1σ)	-	1.1	-	-	-	-
LOQ	25	7	0.6	1.7	1.6	2.0
# of analysis > LOQ	0	2	0	0	0	1
Phlogopite (n = 2)	**< LOQ**	**< LOQ**	**< LOQ**	**< LOQ**	**< LOQ**	**< LOQ**
S.D. (1σ)	-	-	-	-	-	-
LOQ	100	26	2	6	7	6
# of analysis > LOQ	0	0	0	0	0	0
PIC (UIB-2)						
CPX (n = 2)	**< LOQ**	**< LOQ**	**< LOQ**	**< LOQ**	**< LOQ**	**< LOQ**
S.D. (1σ)	-	-	-	-	-	-
LOQ	71	29	1	5	1	3

# of analysis > LOQ	0	0	0	0	0	0
Phlogopite (n = 3)	**< LOQ**	**< LOQ**	**0.5**	**< LOQ**	**< LOQ**	**< LOQ**
S.D. (1σ)	-	-	-	-	-	-
LOQ	38	10	0.3	1	1	1
# of analysis > LOQ	0	0	1	0	0	0
Ilmenite (n = 2)	**95**	**44**	**0.7**	**1.4**	**3.5**	**106**
S.D. (1σ)	10	0.3	-	-	0.4	0.6
LOQ	20	43	0.6	0.8	0.97	2.6
# of analysis > LOQ	2	2	1	1	2	2
Mineral	Ag	Pd	Re	Ir	Pt	Au
MARID (AJE-326)						
Phlogopite (n = 3)	**< LOQ**	**< LOQ**	**< LOQ**	**< LOQ**	**< LOQ**	**< LOQ**
S.D. (1σ)	-	-	-	-	-	-
LOQ	11	3	0.3	0.8	0.8	1
# of analysis > LOQ	0	0	0	0	0	0
K-Richterite (n = 3)	**33**	**6.2**	**< LOQ**	**< LOQ**	**< LOQ**	**< LOQ**
S.D. (1σ)	2.8	1.4	-	0.4	-	-
LOQ	7.6	1.9	0.2	0.4	0.6	0.8
# of analysis > LOQ	3	3	0	0	0	0
Ilmenite (n = 3)	**129**	**43**	**< LOQ**	**2.4**	**3.6**	**9.4**
S.D. (1σ)	27	11	-	-	0.3	5.7
LOQ	22	6.4	6.2	2.2	1.9	2.3
# of analysis > LOQ	3	3	0	1	3	3
MARID (AJE-335)						
CPX (n = 2)	**17**	**4.4**	**< LOQ**	**< LOQ**	**< LOQ**	**< LOQ**
S.D. (1σ)	0.8	0.3	-	-	-	-
LOQ	10.5	2.4	0.3	0.4	0.6	1.1
# of analysis > LOQ	2	2	0	0	0	0
Phlogopite (n = 4)	**< LOQ**	**< LOQ**	**< LOQ**	**< LOQ**	**< LOQ**	**< LOQ**
S.D. (1σ)	-	-	-	-	-	-
LOQ	33	6.2	1.5	3	3	4
# of analysis > LOQ	0	0	0	0	0	
Ilmenite (n = 2)	**34**	**18.3**	**< LOQ**	**< LOQ**	**1.4**	**20**
S.D. (1σ)	2.1	0.1	-	-	0.7	2.1
LOQ	11	2.2	0.4	0.9	0.8	2.0
# of analysis > LOQ	2	2	0	0	2	2
MARID (AJE-2422)						
Phlogopite (n = 3)	**29**	**22**	**< LOQ**	**< LOQ**	**< LOQ**	**< LOQ**
S.D. (1σ)	18	3.3	-	-	-	-
LOQ	27	5.1	0.9	1.5	1.9	3.6
# of analysis > LOQ	2	2	0	0	0	0

K-Richterite (n = 3)	**66**	**3.7**	**< LOQ**	**< LOQ**	**< LOQ**	**2.3**
S.D. (1σ)	5.3	-	-	-	-	-
LOQ	10.2	2.4	0.7	0.6	0.8	1.5
# of analysis > LOQ	3	1	0	0	0	1
Zircon (n = 2)	**43400**	**42650**	**3.2**	**-**	**1737**	**59.8**
S.D. (1σ)	4525	5162	0.4	-	194	8.7
LOQ	30	5.6	1.2	-	2.1	3.2
# of analysis > LOQ	2	2	2	-	2	2
MARID (KDB-20)						
Phlogopite (n = 5)	**< LOQ**	**< LOQ**	**1.8**	**< LOQ**	**< LOQ**	**< LOQ**
S.D. (1σ)	-	-	0.6	-	-	-
LOQ	16	3.2	0.5	3.6	2.7	9.1
# of analysis > LOQ	0	0	2	0	0	0

B.3.2 Precious Metal Mineral Chemistry in Sulphide Phases

"-" in S.D. indicates <2 successful analyses. Concentrations and limits of quantitation (LOQ) are mean values. All concentrations are in parts per million (ppm)

Mineral	Ru	Ag	Pd	Re	Os	Ir	Pt	Au
GPP (JAG1)								
Pentlandite-Magnetite (mixed) (n = 5)	**13.4**	**7.4**	**18.8**	**0.43**	**5.7**	**4.4**	**6.4**	**0.4**
S.D. (1σ)	9.65	4.53	17.9	0.31	5.10	4.14	9.76	0.29
LOQ	0.5	2.5	2.9	0.02	0.09	0.2	0.08	0.03
# of analysis > LOQ	5	4	5	5	5	5	5	5
Pentlandite (n = 1)	**10.4**	**9.7**	**5.7**	**0.31**	**16**	**15.1**	**0.2**	**0.8**
S.D. (1σ)	-	-	-	-	-	-	-	-
LOQ	0.3	1.7	0.3	0.01	0.01	0.009	0.02	0.03
# of analysis > LOQ	1	1	1	1	1	1	1	1
PP (17MON 004)								
Pentlandite (n = 5)	**2.0**	**12.5**	**0.57**	**0.04**	**0.31**	**0.54**	**1.6**	**< LOQ**
S.D. (1σ)	0.52	1.9	0.32	0.002	0.02	0.04	1.26	-
LOQ	0.5	8.4	0.3	0.01	0.07	0.1	0.7	0.03
# of analysis > LOQ	5	4	3	5	4	4	5	0
Spinel Lherzolite Host (LZM-001)								
Pentlandite (n = 8)	**16.5**	**0.59**	**9.0**	**0.94**	**8.4**	**3.3**	**1.2**	**0.05**
S.D. (1σ)	15.4	0.39	3.2	1.61	3.42	2.63	2.76	0.027

LOQ	0.2	0.2	0.4	0.01	0.01	0.006	0.08	0.03
# of analysis > LOQ	8	7	8	7	8	8	8	4
Mineral	Ru	Ag	Pd	Re	Os	Ir	Pt	Au
Spinel Lherzolite Vein (LZM-001)								
Pentlandite (n = 7)	**0.83**	**1.4**	**0.49**	**< LOQ**	**0.05**	**0.03**	**0.2**	**< LOQ**
S.D. (1σ)	0.37	2.08	0.52	-	0.031	0.01	-	-
LOQ	0.2	0.2	0.3	0.04	0.01	0.007	0.02	0.3
# of analysis > LOQ	7	7	3	0	4	5	1	0
PIC (UIB-2)								
Pentlandite (n = 2)	**2.4**	**53.8**	**< LOQ**	**0.06**	**< LOQ**	**< LOQ**	**< LOQ**	**0.05**
S.D. (1σ)	0.2	20.1	-	0.03	-	-	-	-
LOQ	0.3	0.3	0.5	0.02	0.02	0.007	0.03	0.04
# of analysis > LOQ	2	2	0	2	0	0	0	1
Pentlandite-Chalcopyrite (mixed) (n = 2)	**0.94**	**14.1**	**< LOQ**	**0.03**	**< LOQ**	**< LOQ**	**< LOQ**	**0.04**
S.D. (1σ)	0.06	1.84	-	0.003	-	-	-	-
LOQ	0.2	0.2	0.5	0.01	0.02	0.01	0.04	0.037
# of analysis > LOQ	2	2	0	2	0	0	0	1
MARID (AJE-326, AJE-335, AJE-2422, KDB-20)								
Pentlandite-Heazlewoodite (Mixed) (n = 3)	**0.32**	**3.5**	**0.48**	**0.014**	**0.07**	**0.04**	**0.94**	**0.13**
S.D. (1σ)	0.28	3.44	0.64	0.016	0.05	0.01	1.44	0.16
LOQ	0.04	0.07	0.07	0.003	0.003	0.003	0.004	0.007
# of analysis > LOQ	3	3	3	3	3	3	3	2

B.4 Whole Rock Geochemistry and Modelling

B.4.1 Major Elements

Sample	SiO_2	TiO_2	Al_2O_3	Cr_2O_3	FeO_T	MnO	MgO	CaO	Na_2O	K_2O	P_2O_5	H_2O	Total
GPP (JAG1)													
XRF	45.6	0.03	3.37	0.33	7.91	0.13	39.4	2.45	0.24	0.19	0.06	-	99.4
Reconstructed	45.9	0.03	5.92	0.52	7.21	0.16	36.3	2.8	0.16	0.07	-	0.02	99.3
PP (17MON004)													
XRF	49.3	0.11	1.02	0.65	7.95	0.14	32.9	6.75	0.76	0.34	0.02	-	99.2
Reconstructed	46.7	0.03	0.58	0.88	8.11	0.15	35.2	6.44	0.67	0.13	-	0.19	99.1
Spinel Lherzolite Host (LZM-001)													
XRF	45.1	0.15	3.71	0.42	8.49	0.12	38.4	3.17	0.33	0.01	0.01	-	100.1
Reconstructed	41.8	0.19	3.11	0.38	8.89	0.13	42.0	1.82	0.26	0.03	-	0.05	99.0
Spinel Lherzolite Vein (LZM-001)													
XRF	43.1	4.05	12.9	0.22	5.39	0.06	20.6	9.56	2.58	1.31	0.06	-	100.0
Reconstructed	40.9	4.71	14.6	0.38	3.93	0.05	16.2	10.1	2.89	1.98	-	0.11	98.2
PIC (UIB-2)													
XRF	-	-	-	-	-	-	-	-	-	-	-	-	-
Reconstructed	37.2	14.5	3.05	1.17	9.32	0.12	17.8	11.2	0.63	2.41	-	0.98	98.5
MARID (AJE-326)													
XRF	47.2	4.88	4.48	0.06	8.07	0.05	21.7	5.3	1.62	6.16	0.1	-	99.7
Reconstructed	48.3	3.0	4.01	0.22	5.36	0.05	22.6	4.32	2.32	6.38	-	2.68	99.3
Fitzpayne *et al* (2018) recon.	46.5	6.73	3.22	0.31	4.88	0.03	21.7	4.7	2.52	5.87	-	2.81	99.3

Sample	SiO_2	TiO_2	Al_2O_3	Cr_2O_3	FeO^T	MnO	MgO	CaO	Na_2O	K_2O	P_2O_5	H_2O	Total
MARID (AJE-335)													
XRF	44.1	4.05	8.1	0.08	8.63	0.05	21.13	5.08	0.35	7.98	0.07	-	99.7
Reconstructed	42.7	5.44	8.2	0.08	7.64	0.05	20.3	2.9	0.26	8.5	-	3.43	99.5
Fitzpayne *et al* (2018) recon.	45.1	3.11	7.58	0.09	7.28	0.07	20.06	4.52	0.32	7.65	-	3.13	99.0
MARID (AJE-2422)													
XRF	48.6	2.87	4.15	0.20	6.79	0.06	24.9	5.32	1.63	5.04	0.08	-	99.7
Reconstructed	45.8	8.28	2.55	0.09	7.10	0.06	19.9	4.62	2.12	5.76	-	2.29	98.7
Fitzpayne *et al* (2018) recon.	41.1	6.04	8.09	0.1	7.3	0.03	22.2	0.77	0.45	9.23	-	3.62	99.0
MARID (KDB-20)													
XRF	44	1.92	3.39	0.24	7.84	0.13	28.9	7.43	1.18	3.92	0.76	-	99.8
Reconstructed	37.4	6.67	9.41	0.18	8.23	0.09	23.8	0.01	0.18	9.48	-	3.74	99.3

B.4.2 Trace Elements

Sample	Rb	Ba	Nb	La	Ce	Pb	Pr	Sr	Nd	Zr	Hf	Sm
GPP (JAG1)												
XRF	6.3	86	1.6	1	5	3	-	89	-	21	-	-
Reconstructed	1.3	28.3	0.8	1.9	4.9	0.4	0.7	38.9	2.73	8.33	0.2	0.5
PP (17MON004)												
XRF	22.4	123	7.1	2.5	20	1.3	-	211	-	48.5	-	-
Reconstructed	5.9	31.6	2.2	8.2	20.8	0.6	2.7	189	10	14.3	0.2	1.6
Spinel Lherzolite Host (LZM-001)												
XRF	0.3	14	0.3	1	1	0.5	-	18	-	16	-	-

Reconstructed	2.7	19.5	0.6	0.5	1.4	0.6	0.2	21.8	1.2	21.6	0.5	0.4
Spinel Lherzolite Vein (LZM-001)												
XRF	2.9	68	34.9	11	37	2	-	463	-	96	-	-
Reconstructed	6.5	151	33.8	6.1	20.4	0.4	3.4	518	18.3	78.8	2.6	5.5
PIC (UIB-2)												
XRF	-	-	-	-	-	-	-	-	-	-	-	-
Reconstructed	89.7	96.5	733	1.9	7	0.2	1.3	102	6.5	270	8.6	1.6
MARID (AJE-326)												
XRF	198	556	139	16	17	4	-	581	-	3326	-	-
Reconstructed	185	161	198	1.2	3.5	0.8	0.5	530	2.0	46.7	1.6	0.3
Fitzpayne *et al* (2018) recon.	146	120	503	1.1	3.4	1.0	0.5	602	2.1	159	5.7	0.3

Sample	**Rb**	**Ba**	**Nb**	**La**	**Ce**	**Pb**	**Pr**	**Sr**	**Nd**	**Zr**	**Hf**	**Sm**
MARID (AJE-335)												
XRF	413	308	30	22	24	3	-	215	-	67	-	-
Reconstructed	442	301	7.8	4.3	16.3	0.4	2.7	121	12.6	36.7	1.2	2.3
Fitzpayne *et al* (2018) recon.	437	268	11.8	7.1	28.1	2.3	4.9	192	22.2	18.9	0.8	4.0
MARID (AJE-2422)												
XRF	169	1327	124	1	0.5	1	-	573	-	88	-	-
Reconstructed	139	128	88.1	1.8	5.8	3.4	0.8	419	3.3	45.5	1.5	0.5
Fitzpayne *et al* (2018) recon.	454	468	292	0.4	1.2	0.6	0.2	75	0.6	91	3.2	0.1
MARID (KDB-20)												

XRF	171	420	87.1	31.5	61	5.2	-	633	-	159	-	-
Reconstructed	497	423	171	0.1	0.2	0.1	0.02	3	0.1	26	0.7	0.01
Sample	**Eu**	**Gd**	**Tb**	**Dy**	**Ho**	**Y**	**Sc**	**Er**	**Tm**	**Yb**	**Lu**	**Ga**
GPP (JAG1)												
XRF	-	-	-	-	-	3	9	-	-	-	-	0.5
Reconstructed	0.2	0.5	0.1	0.6	0.1	3.9	22.4	0.5	0.1	0.6	0.1	-
PP (17MON 004)												
XRF	-	-	-	-	-	2.5	13	-	-	-	-	0.9
Reconstructed	0.4	1.0	0.1	0.6	0.1	2.2	15.1	0.2	0.02	0.1	0.02	-
Spinel Lherzolite Host (LZM-001)												
XRF	-	-	-	-	-	3.8	10	-	-	-	-	3.3
Reconstructed	0.1	0.4	0.1	0.4	0.1	2.2	6.9	0.2	0.03	0.2	0.03	-

Sample	Eu	Gd	Tb	Dy	Ho	Y	Sc	Er	Tm	Yb	Lu	Ga
Spinel Lherzolite Vein (LZM-001)												
XRF	-	-	-	-	-	24.6	30	-	-	-	-	8
Reconstructed	1.9	5.7	0.8	4.8	0.9	22.1	34.3	2.3	0.3	1.8	0.2	-
PIC (UIB-2)												
XRF	-	-	-	-	-	-	-	-	-	-	-	-
Reconstructed	0.5	1.2	0.1	0.6	0.1	2.0	50.4	0.2	0.02	0.1	0.01	-
MARID (AJE-326)												
XRF	-	-	-	-	-	2.0	21	-	-	-	-	12.7

Reconstructed	0.1	0.2	0.02	0.07	0.01	0.2	20.5	0.02	0.002	0.01	0.002	-
Fitzpayne *et al* (2018) recon.	0.1	0.2	-	0.06	-	0.2	21.2	0.01	-	0.01	-	-
MARID (AJE-335)												
XRF	-	-	-	-	-	0.3	7	-	-	-	-	22.1
Reconstructed	0.6	1.4	0.2	0.7	0.1	2.2	10.1	0.2	0.02	0.1	0.01	-
Fitzpayne *et al* (2018) recon.	1.0	2.5	-	1.2	-	3.9	14.3	0.4	-	0.2	0.02	-
MARID (AJE-2422)												
XRF	-	-	-	-	-	0.3	14	-	-	-	-	25.5
Reconstructed	0.1	0.3	0.03	0.1	0.02	0.4	25.6	0.04	0.004	0.03	0.005	-
Fitzpayne *et al* (2018) recon.	0.03	0.05	-	0.02	-	0.1	7.8	0.01	-	0.01	-	-
MARID (KDB-20)												
XRF	-	-	-	-	-	4.5	15	-	-	-	-	8.9
Reconstructed	0.01	0.01	0.001	0.005	0.001	0.03	0.8	0.002	0.0002	0.002	0.001	-

Sample	Cu	Zn	Co	V
GPP (JAG1)				
XRF	1.0	51	101	45
Reconstructed	0.2	-	88.9	-
PP (17MON 004)				
XRF	3.5	44.5	77	54
Reconstructed	0.05	-	101	-
Spinel Lherzolite Host (LZM-001)				
XRF	12	56	100	65
Reconstructed	0.42	-	89.6	-

Spinel Lherzolite Vein (LZM-001)				
XRF	109	21	58	188
Reconstructed	0.7	-	38.7	-
PIC (UIB-2)				
XRF	-	-	-	-
Reconstructed	3	-	70	-
MARID (AJE-326)				
XRF	80	55	74	239
Reconstructed	0.8	-	46.4	-
Fitzpayne *et al* (2018) recon.	0.9	29	-	201
MARID (AJE-335)				
XRF	137	70	82	178
Reconstructed	1.5	-	72	-
Fitzpayne *et al* (2018) recon.	7.0	81	-	253

Sample	Cu	Zn	Co	V
MARID (AJE-2422)				
XRF	47	41.8	62	118
Reconstructed	0.5	-	48.5	-
Fitzpayne *et al* (2018) recon.	3.2	69	-	300
MARID (KDB-20)				
XRF	54	54	65	131
Reconstructed	0.1	-	76	-

B.4.3 Precious Metals and Re-Os Isotopes

$^{*187}Os/^{188}Os_i$ and $*\gamma Os_i$ are initial values calculcated to the age of eruption or massif emplacement and a chondritic $^{187}Os/^{188}Os$ of 0.1262 (Walker* et al.*, 2002) corrected to the same age. Concentrations are in ppb

Sample	Os	Ir	Ru	Pt	Pd	Re	$^{187}Re/^{188}Os$	$^{187}Os/^{188}Os$	$^{*187}Os/^{188}Os_i$	γOs	$*\gamma Os_i$
GPP (JAG1)											
Value	5.59	5.21	17.67	7.35	6.25	0.189	0.163	0.1222	0.1219	-3.21	-2.92
S.D. (2σ)	0.044	0.217	1.33	0.26	0.43	0.008	0.0066	0.0002	0.0003	0.14	0.16
PP (17MON 004)											
Value	1.39	1.62	4.40	29.07	1.32	0.044	0.132	0.1157	0.1155	-8.34	-8.05
S.D. (2σ)	0.008	0.05	0.185	4.09	0.05	0.002	0.005	0.0004	0.0005	0.28	0.33
Spinel Lherzolite Host (LZM-001)											
Value	3.68	3.03	7.17	7.09	6.02	0.32	0.417	0.1266	0.1258	0.31	0.28
S.D. (2σ)	0.03	0.11	0.26	0.26	0.46	0.02	0.022	0.0002	0.0003	0.15	0.24
Spinel Lherzolite Vein (LZM-001)											
Value	0.761	0.70	1.41	1.87	1.69	0.058	0.371	0.1404	0.1397	11.28	11.35
S.D. (2σ)	0.005	0.02	0.24	0.04	0.04	0.001	0.009	0.002	0.005	1.67	2.34
MARID (AJE-326)											
Value	0.014	0.013	0.10	0.54	0.57	0.166	60.22	0.3668	0.2712	190.6	115.97
S.D. (2σ)	0.001	0.003	0.07	0.013	0.014	0.004	6.62	0.001	0.003	1.05	3.43
MARID (AJE-335)											
Value	0.027	0.241	0.24	3.84	3.89	0.181	4.20	0.1465	0.1404	16.1	11.78
S.D. (2σ)	0.002	0.007	0.07	0.08	0.095	0.004	0.11	0.0003	0.0005	0.2	0.8

Sample	Os	Ir	Ru	Pt	Pd	Re	$^{187}Re/^{188}Os$	$^{187}Os/^{188}Os$	$*^{187}Os/^{188}Os_i$	γOs	$*\gamma Os_i$
MARID (AJE-2422)											
Value	1.559	1.50	4.03	2.63	1.65	0.147	0.45	0.1163	0.1156	-7.85	-7.95
S.D. (2σ)	0.008	0.04	0.77	0.06	0.04	0.003	0.01	0.0002	0.0003	0.13	0.84
MARID (KDB-20)											
Value	1.061	0.93	2.55	1.43	1.55	0.245	1.11	0.1122	0.1106	-11.1	-11.97
S.D. (2σ)	0.006	0.02	0.61	0.03	0.04	0.006	0.03	0.0002	0.0003	0.14	0.81

B.5 Zircon U-Th-Pb and Lu-Hf Isotope Geochemistry

B.5.1 Zircon U-Th-Pb Data

*F_{206} (%) refers to the fraction of common ^{206}Pb in the total measured ^{206}Pb and was calculated based on the two-step model of Stacey and Kramers (1975). * indicates a common Pb correction has been applied.*

Analysis	U (ppm)	Th (ppm)	Th/U	Pb (ppm)	F_{206} (%)	$^{*206}Pb/^{238}U$ ± 2σ	$^{*206}Pb/^{238}U$ Age ± 2σ
AJE-2422-02_Zir1-01	37	16	0.42	3	2.40	0.0144 ± 0.0004	92.3 ± 2.5
AJE-2422-02_Zir1-02	24	10	0.43	3	4.55	0.0149 ± 0.0006	95.4 ± 3.5
AJE-2422-02_Zir1-03	77	31	0.4	7	3.02	0.0148 ± 0.0004	94.5 ± 2.5
AJE-2422-02_Zir1-04	10	5	0.50	>1	2.98	0.0146 ± 0.0007	93.6 ± 4.4
AJE-2422-02_Zir1-05	51	24	0.47	3	1.16	0.0142 ± 0.0004	90.9 ± 2.4
AJE-2422-02_Zir2-01	73	30	0.40	5	2.82	0.0151 ± 0.0005	96.5 ± 2.9
AJE-2422-02_Zir2-02	60	34	0.56	7	4.47	0.0145 ± 0.0005	92.9 ± 3.0
AJE-2422-02_Zir2-03	84	33	0.40	1	1.40	0.0149 ± 0.0004	95.2 ± 2.5
AJE-2422-02_Zir2-04	32	15	0.45	>1	1.50	0.0141 ± 0.0004	90.5 ± 2.8
AJE-2422-02_Zir3-01	83	32	0.39	8	2.30	0.0191 ± 0.0006	122.3 ± 3.7
AJE-2422-02_Zir3-02	69	25	0.37	5	1.27	0.0197 ± 0.0008	125.9 ± 4.9
AJE-2422-02_Zir3-03	118	57	0.48	9	2.01	0.0152 ± 0.0005	97.3 ± 3.0
AJE-2422-02_Zir3-04	159	93	0.59	13	1.07	0.0161 ± 0.0004	103.1 ± 2.8
AJE-2422-02_Zir3-05	50	15	0.30	4	5.50	0.0147 ± 0.0005	94.1 ± 2.9
AJE-2422-02_Zir3-06	63	21	0.34	4	2.02	0.0173 ± 0.0006	110.8 ± 3.5
AJE-2422-01_Zir1-01	32	20	0.63	1	2.64	0.0142 ± 0.0004	90.9 ± 2.7
AJE-2422-01_Zir1-02	13	12	0.91	>1	0.76	0.0150 ± 0.0005	96.0 ± 3.0
AJE-2422-01_Zir1-03	44	44	0.99	2	2.90	0.0141 ± 0.0004	90.3 ± 2.3
AJE-2422-01_Zir1-04	11	6	0.58	>1	2.71	0.0147 ± 0.0005	94.4 ± 3.3

AJE-2422-01_Zir1-05	29	35	1.53	>1	2.39	0.0135 ± 0.0004	86.2 ± 2.3
AJE-2422-01_Zir2-01	34	13	0.39	>1	2.05	0.0140 ± 0.0004	89.7 ± 2.4
AJE-2422-01_Zir2-02	53	22	0.42	1	2.79	0.0140	89.8 ± 2.3

B.5.2 Zircon Lu-Hf Data

εHf values are based on crystallization at time (T) equal to the $^{206}Pb/^{238}U$ age of the analytical spot.

Analysis	$^{176}Lu/^{177}Hf$	$^{176}Lu/^{177}Hf$ 2σ	$^{176}Hf/^{177}Hf$	$^{176}Hf/^{177}Hf$ 2σ	$\varepsilon HF_{(T)}$	$\varepsilon Hf_{(T)}$ 2σ
AJE-2422-02_Zir1-01	0.000084	0.000002	0.28226	0.00002	-16.5	0.71
AJE-2422-02_Zir1-02	0.0000451	0.0000002	0.28222	0.00002	-17.8	0.71
AJE-2422-02_Zir1-03	0.000137	0.000002	0.28224	0.00002	-17.1	0.71
AJE-2422-02_Zir1-04	0.0000138	0.0000003	0.28226	0.00002	-16.4	0.71
AJE-2422-02_Zir1-05	0.0000732	0.0000002	0.28224	0.00002	-17.2	0.71
AJE-2422-02_Zir2-01	0.0000859	0.0000003	0.28223	0.00001	-17.5	0.35
AJE-2422-02_Zir2-02	0.000068	0.000002	0.28224	0.00004	-17.2	1.40
AJE-2422-02_Zir2-03	0.0000972	0.0000003	0.28223	0.00002	-17.5	0.71
AJE-2422-02_Zir2-04	0.0000694	0.0000004	0.28223	0.00002	-17.6	0.71
AJE-2422-02_Zir3-01	0.000156	0.000003	0.28224	0.00002	-16.5	0.71
AJE-2422-02_Zir3-02	0.0000864	0.0000003	0.28224	0.00001	-16.5	0.35
AJE-2422-02_Zir3-03	0.0000968	0.0000004	0.28222	0.00002	-17.9	0.71
AJE-2422-02_Zir3-04	0.0001157	0.0000008	0.28224	0.00003	-17.0	1.06
AJE-2422-02_Zir3-05	0.0000666	0.0000003	0.282224	0.00002	-17.2	0.71
AJE-2422-02_Zir3-06	0.0001250	0.0000009	0.28223	0.00002	-17.1	0.71
AJE-2422-01_Zir1-01	0.0000899	0.0000006	0.28222	0.00002	-17.9	0.71
AJE-2422-01_Zir1-02	0.0000322	0.0000008	0.28222	0.00002	-17.8	0.71
AJE-2422-01_Zir1-03	0.000082	0.000004	0.28222	0.00002	-17.9	0.71
AJE-2422-01_Zir1-04	0.0000228	0.0000009	0.28224	0.00002	-17.1	0.71
AJE-2422-01_Zir1-05	0.0000449	0.0000003	0.28225	0.00002	-16.9	0.71

AJE-2422-01_Zir2-01	0.0000697	0.0000004	0.28223	0.00002	-17.6	0.71
AJE-2422-01_Zir2-02	0.000130	0.000001	0.28223	0.00002	-17.6	0.71

Appendix C: Sample Imagery

Appendix C.1: Sample Imagery

GPP (JAG1)

Above: Thick section of GPP xenolith sample JAG 1 (ppl)

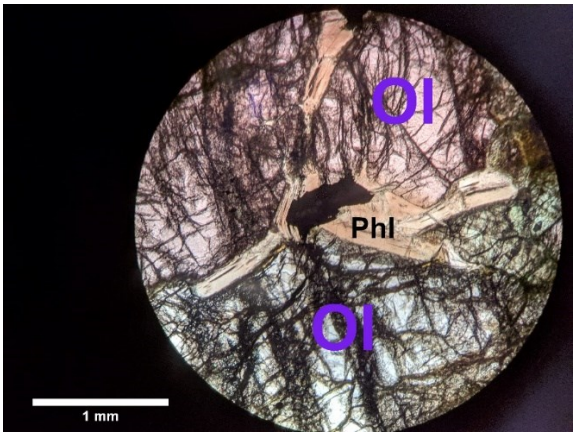

Above: metasomatic phlogopite interstitial to olivine. Sulphide (black blob) occurring in close proximity to phlogopite is common in JAG1

PP (17MON 004) (PPL)

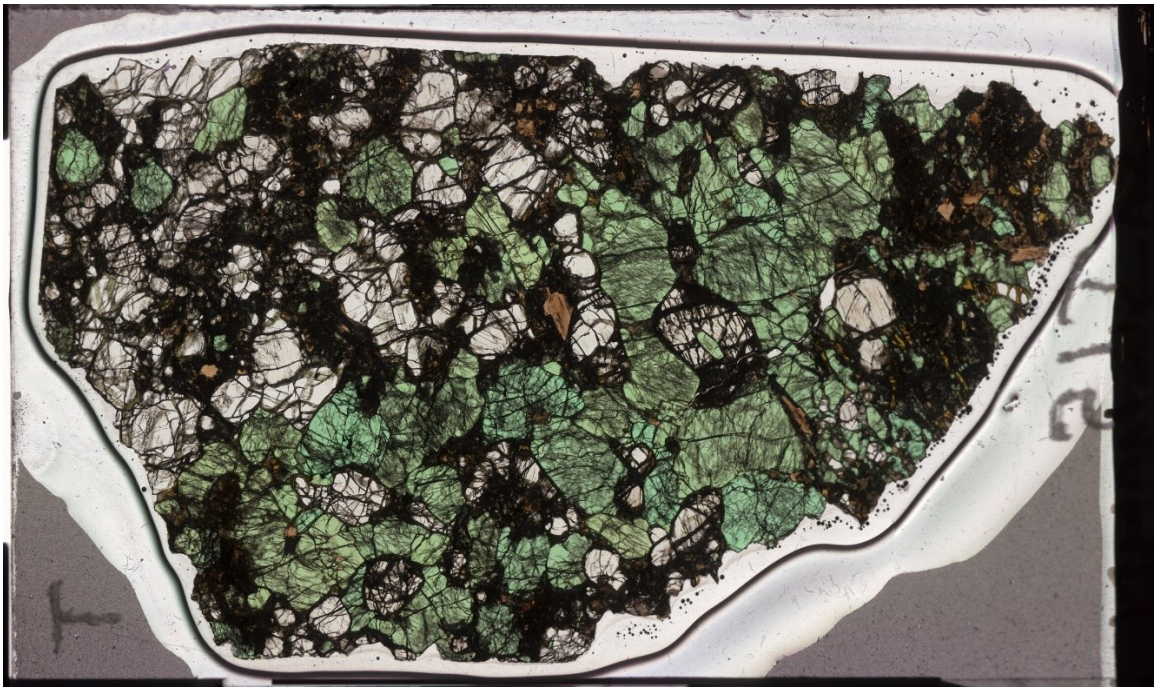

Above: Thick section of PP xenolith sample 17MON 004 (ppl). Black areas are channels altered by a fluid/melt

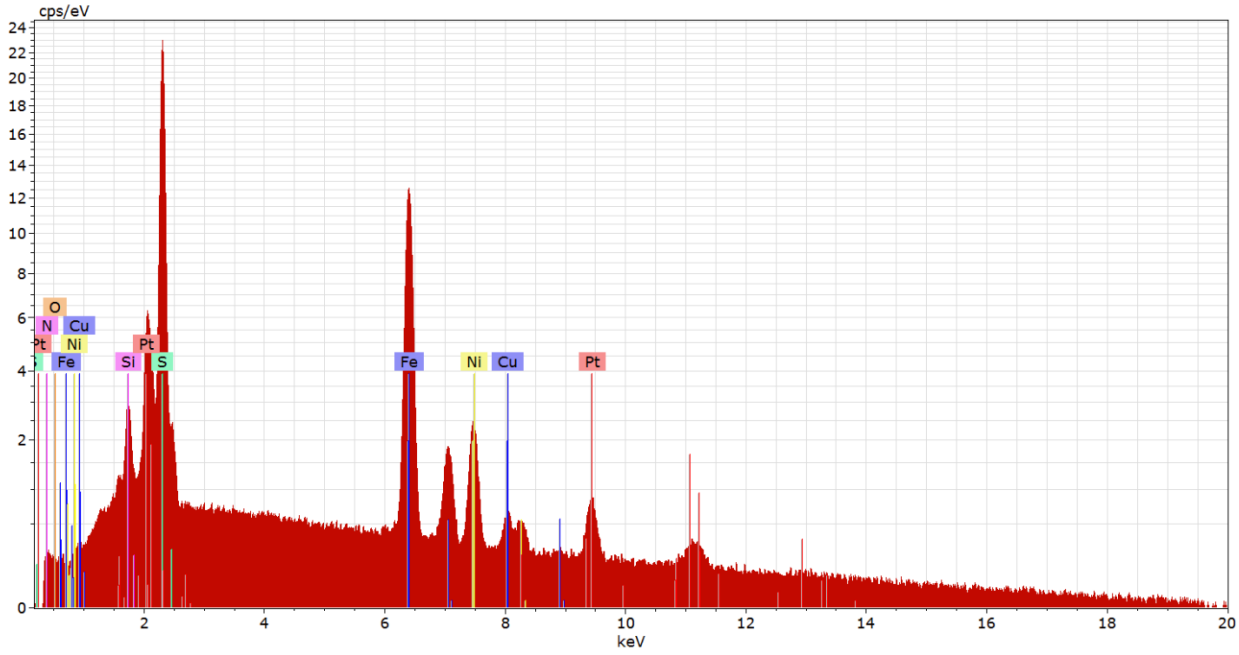

Above: EDS spectra of Pt inclusions in pentlandite of 17MON 004

Spinel Lherzolite (LZM-001) (PPL)

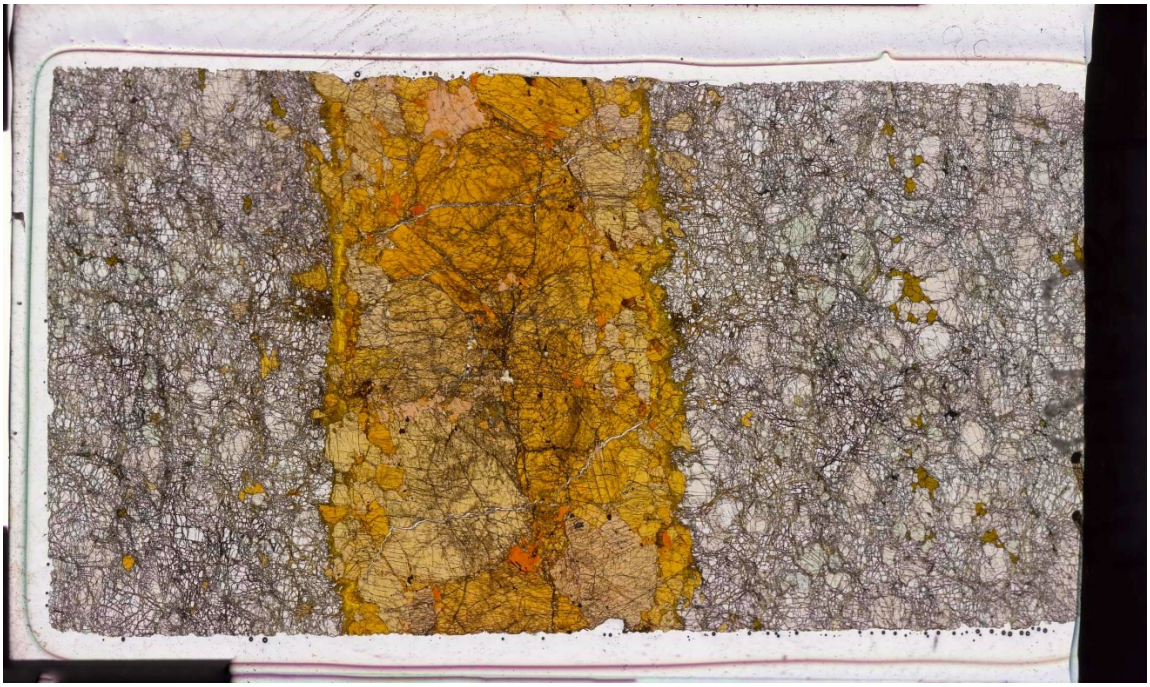

PIC (UIB-2) (PPL)

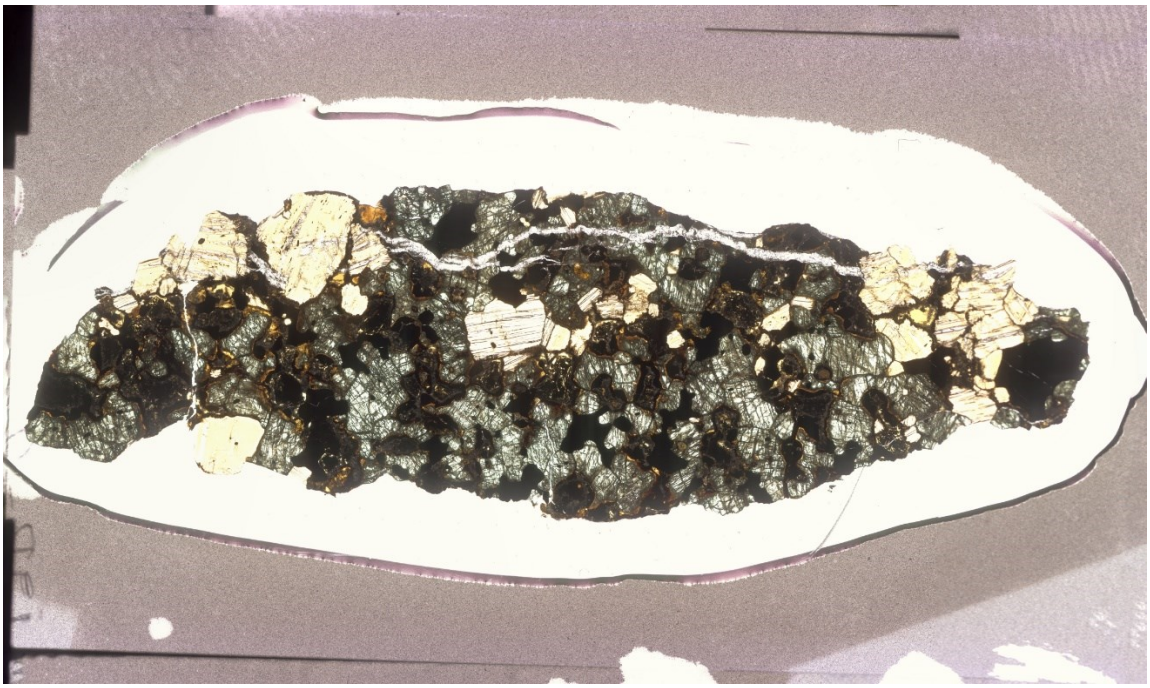

MARID (AJE-326) (PPL)

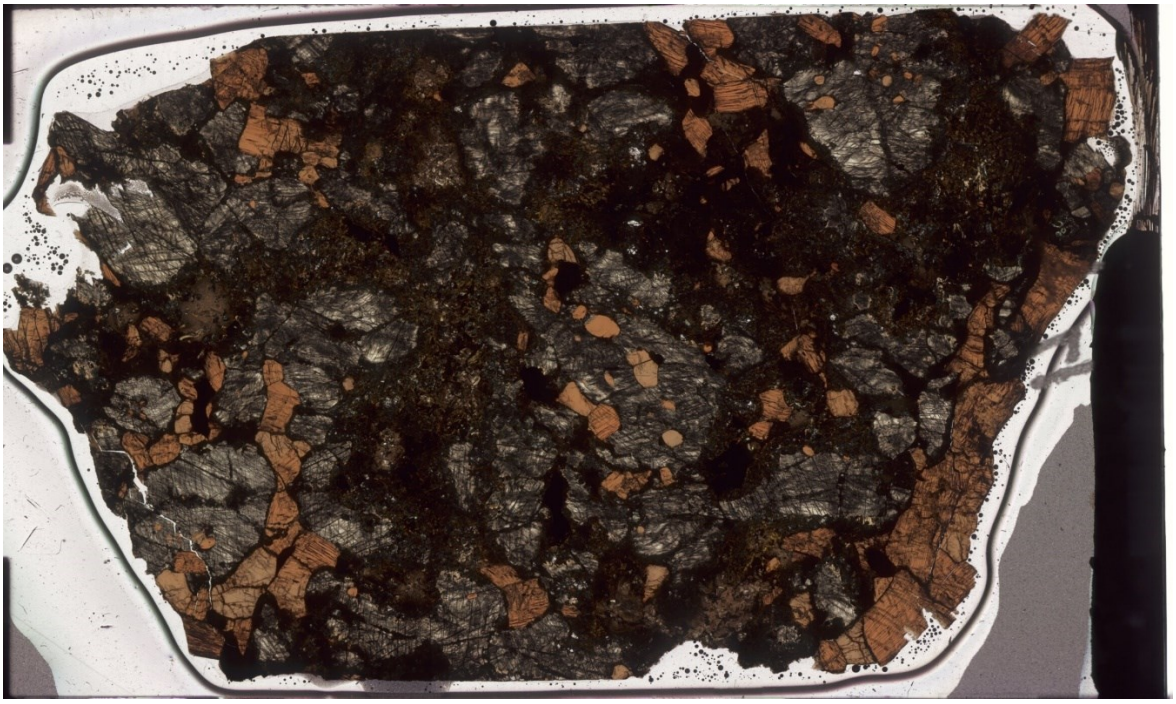

MARID (AJE-335) (PPL)

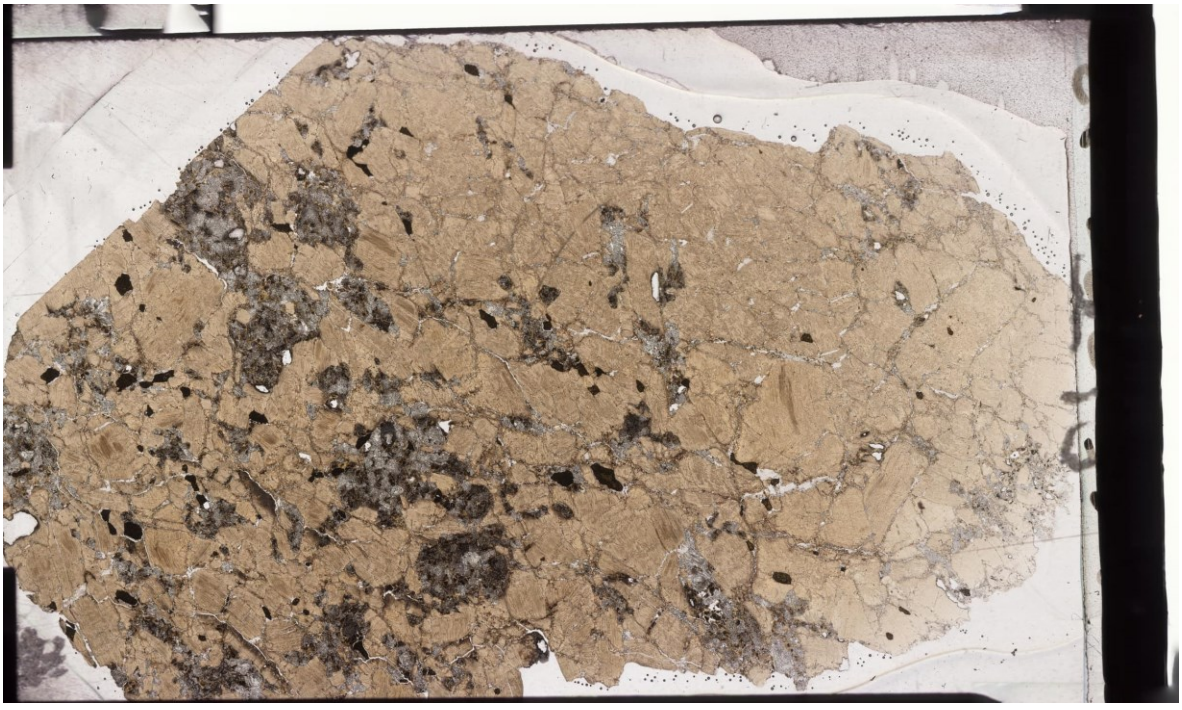

MARID (AJE-2422) (PPL)

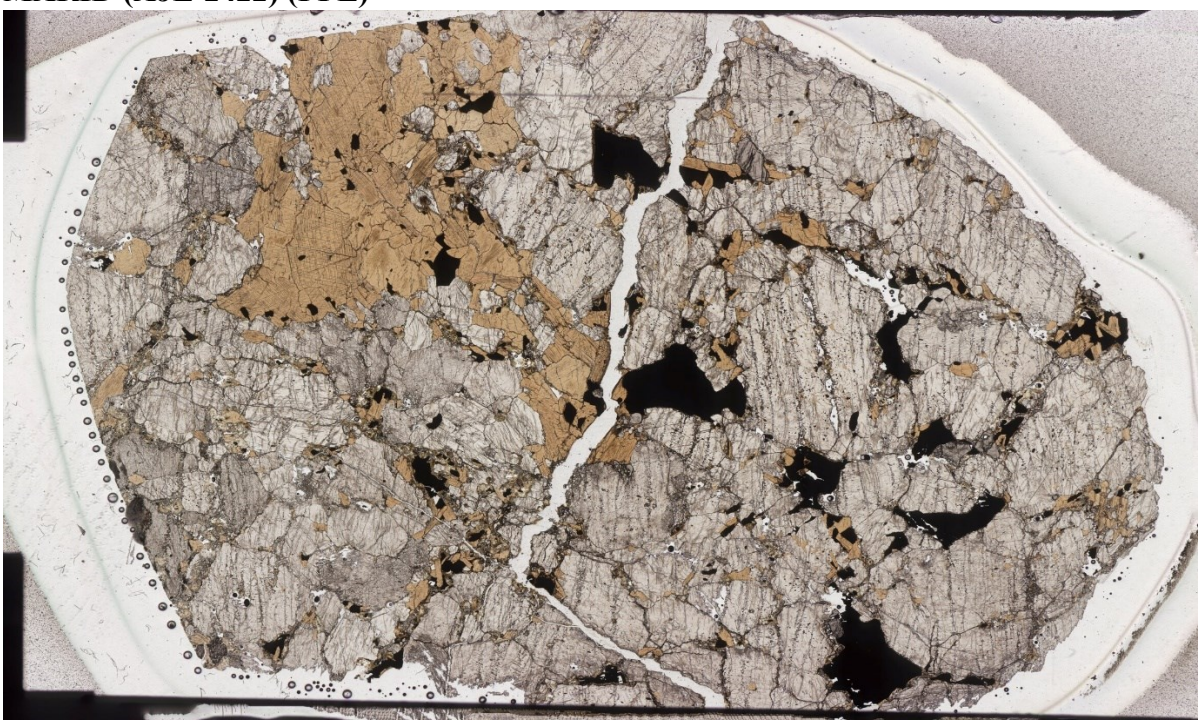

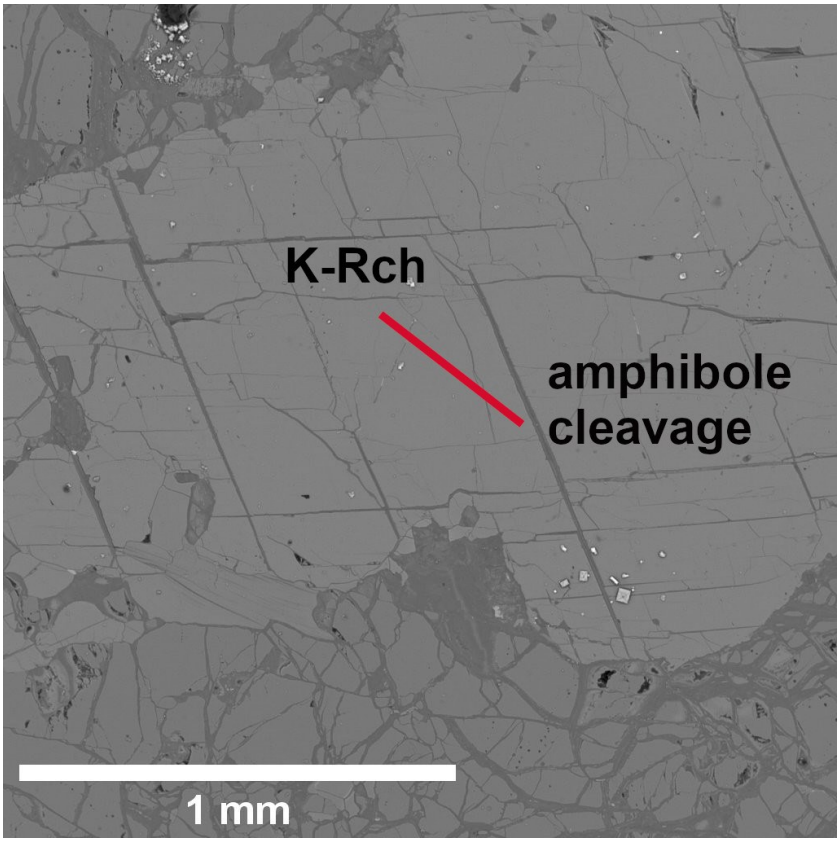

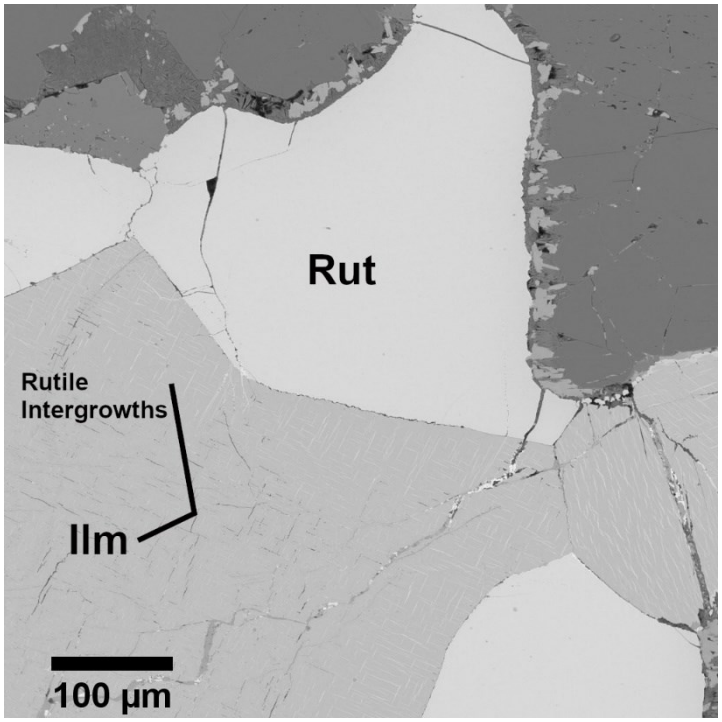

MARID (KDB-20) (PPL)

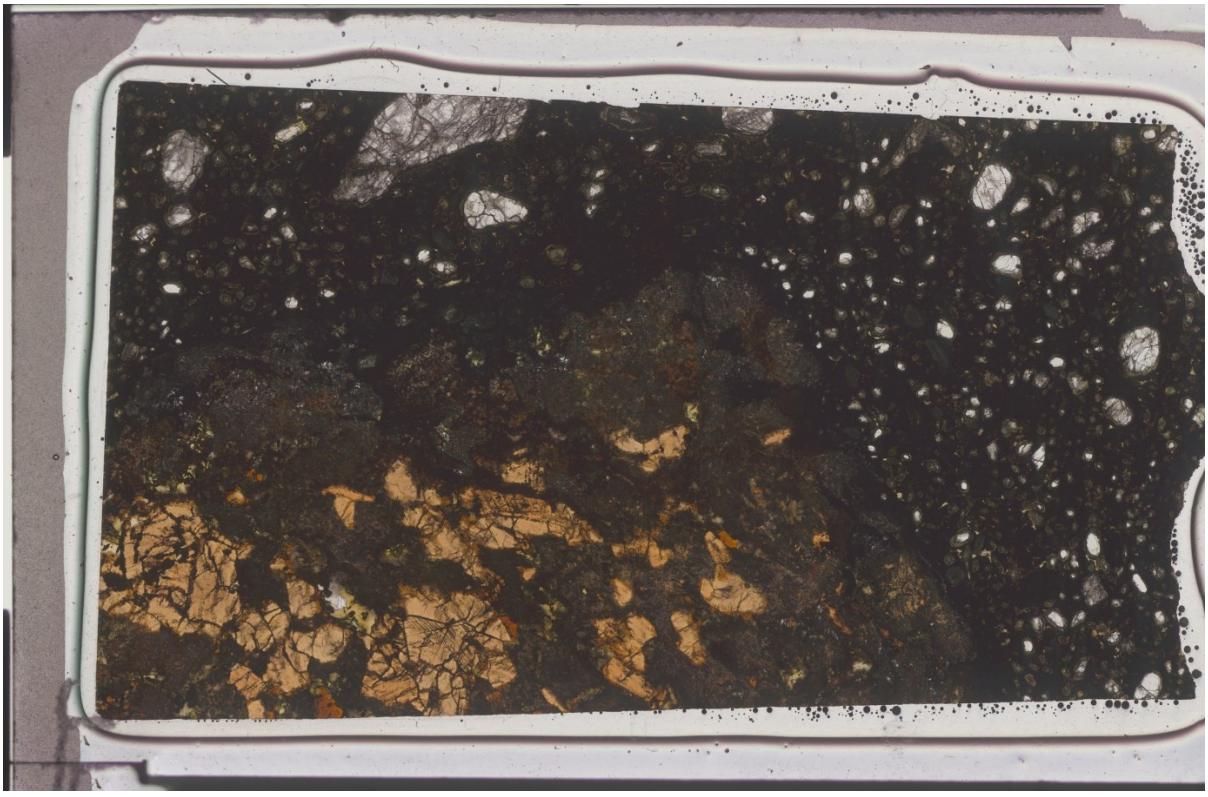

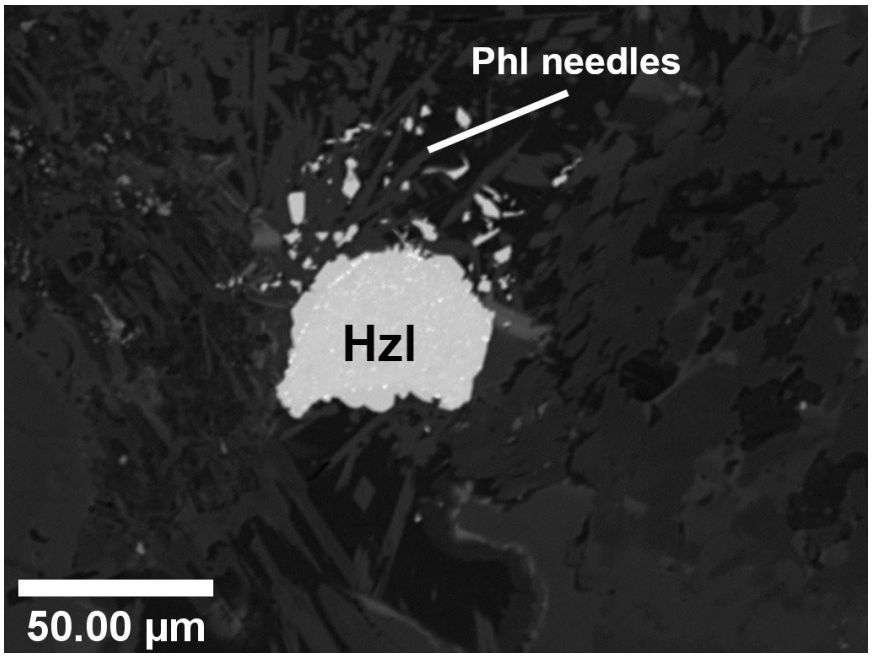

Appendix C.2 Zircon BSE Imagery

AJE-2422-01 Zir 1

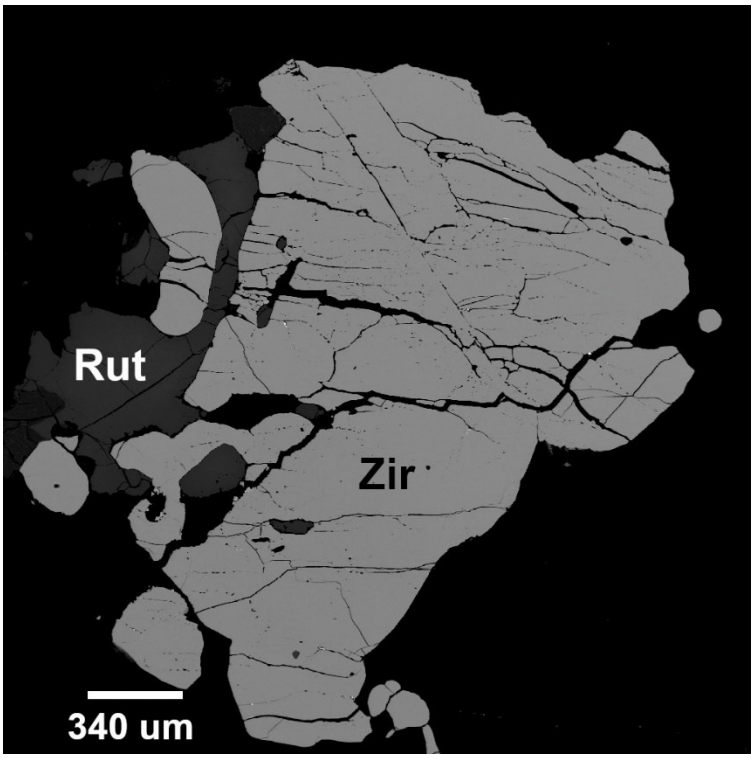

AJE-2422-01 Zir 2

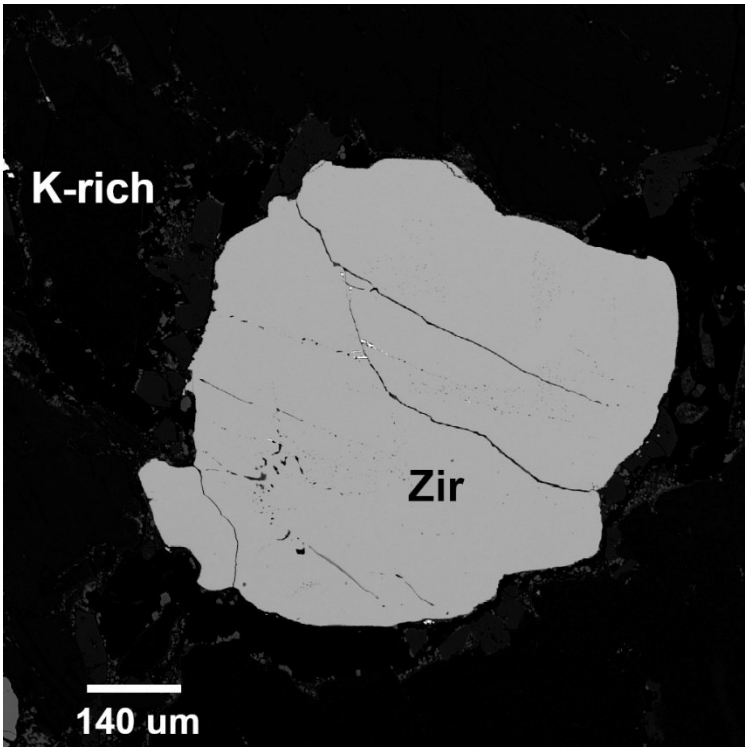

AJE-2422-02 Zir 1

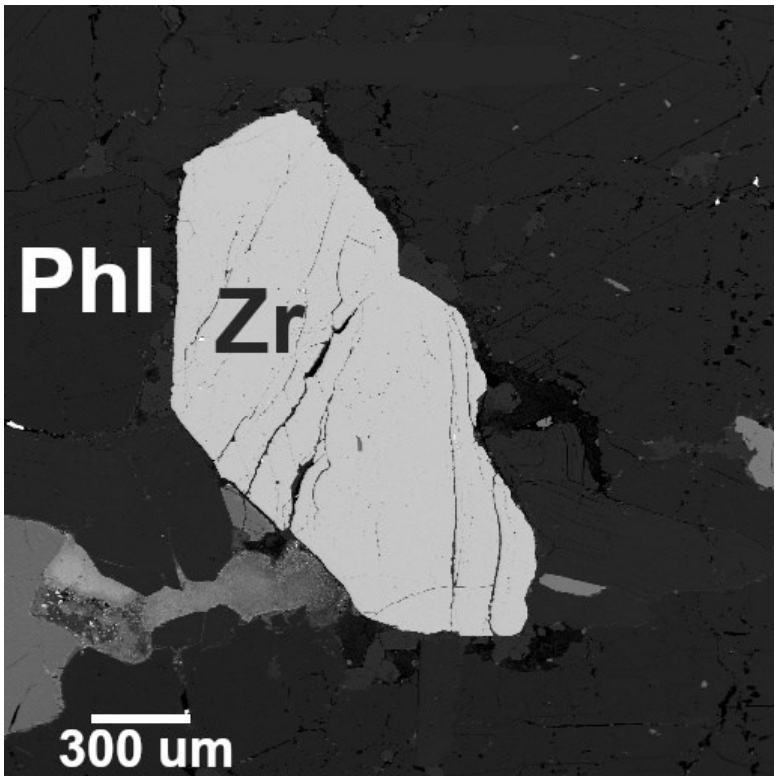

AJE-2422-02 Zir 2 and 3

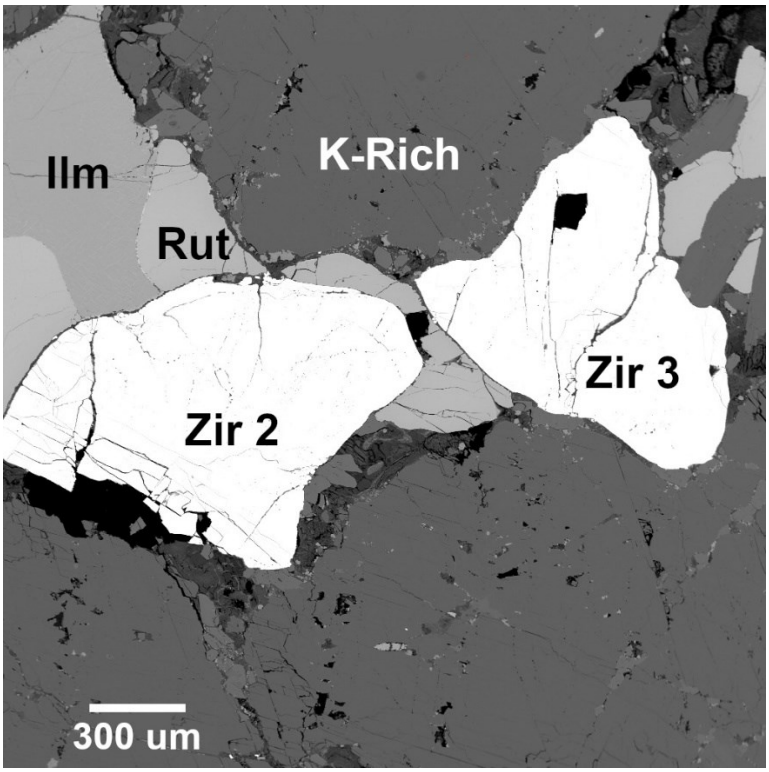
Ilm
K-Rich
Rut
Zir 3
Zir 2
300 um